Investigation of Structures Featuring Curvilinear Anisotropy: Application to Electrostatic Problem and Mechanical Response

Sean Eunsik Phenisee

A dissertation
submitted in partial fulfillment of the
requirements for the degree of

Doctor of Philosophy

University of Washington

2023

Reading Committee:

Marco Salviato, Chair

Jinkyu Yang

Richard Wiebe

Program Authorized to Offer Degree:
Aeronautics and Astronautics

University of Washington

Abstract

Investigation of Structures Featuring Curvilinear Anisotropy: Application to Electrostatic Problem and Mechanical Response

Sean Eunsik Phenisee

Chair of the Supervisory Committee:
Marco Salviato
Department of Aeronautics and Astronautics

This study examines the impact of curvilinear reinforcement in a composite structure. The key areas covered include two main applications: 1) enhancing functional properties in electrostatic problems and 2) improving the mechanical strength and fracture resistance of composite structures.

Depending on the arrangement of reinforcement, the conductivity of the composites can be adjusted. The overarching goals towards the electrostatic application are twofold. First, this study aims to provide the computational framework of obtaining optimal fiber configuration maximizing conductivity for structures with finite domain. To that end, an analytical solution of the Poisson equation is derived through conformal mapping, revealing insights such as the optimal alignment of fiber orientation with field lines under specific conditions. The concept of curvilinear transverse isotropy is introduced, and its application to electrostatic problems is demonstrated. This theoretical foundation helps to extends to practical scenarios in finite domains. The finite element method is used to determine the optimal reinforced configuration for a notched specimen. The second objective is to assess the ability of optimal reinforced configuration in the application of damage detection or health monitoring by measuring the change of conductivity. Finite element method is used to compute the change in conductivity at the source after a crack is inserted, representing a breakage of fibers from a localized damage.

Subsequently, the investigation on the influence of curvilinear reinforcement on mechanical performance is provided. Isogeometric analysis with spline basis functions for enhanced continuity is employed to evaluate the mechanical performance of composite structures with multiple variants of curvilinear reinforcement on a notched plate. An optimization study with polynomials describing orientation distribution on a given structure is carried on to determine the optimal fiber path that enhances structural properties like stress distribution and stiffness. As a result, the stress concentration factor was reduced to 1.28. This result highlights a substantial 82 % decrease when compared to the conventional longitudinal fiber reinforcement. To extend isogeometric approach suitable for a general types of trimmed surfaces, in-house IGA software is developed which employs LR B splines in a model generation and the numerical analysis. A data-driven optimization approach is used to find the optimial reinforcement configuration for improved damage tolerance. Two types of geometry used in this study are a plate with a semi-circular notch and T-shaped joint structure. A cross-ply layup sequence is assumed for each laminate. As a result for the first optimization study, the maximum principal stress is reduced by a factor greater than 7 for the rectangular plate and is reduced by a factor of 3 for T-joint. The other optimization result highlights the reduction of the energy release rate close to zero which implies that the crack is not likely to form at the notch.

Lastly, a new discrete modeling method is proposed to predict damage initiation and progression in fiber-reinforced composites. Fibers are explicitly modeled using Timoshenko beams which are embedded in a tetrahedral conforming mesh that characterizes the matrix. The facet-based formulation enables discrete fracture modeling, and prevents the element erosion. Furthermore, the explicit representation of fibers and matrix allows a simple and distinct definition of material parameters thanks to the constitutive laws grounded in physics rather than in empirical curve fitting.

TABLE OF CONTENTS

Page

LIST OF FIGURES

LIST OF TABLES

LIST OF ALGORITHMS

ACKNOWLEDGMENTS

I would like to express sincere appreciation to the William E. Boeing Department of Aeronautics and Astronautics at University of Washington for providing opportunity to work with amazing scholars and colleagues. I deeply appreciate the financial support from College of Engineering with the award, College of Engineering Dean's Fellowship for 2016-2017.

First, I would like to thank my advisor, Professor Marco Salviato, for his guidance during my Ph.D. journey. His passion towards academic endeavor and mentoring students has always been inspirational to me. Amidst his demanding schedules, he always gives priority to his students, exemplifying genuine leadership. He taught me on cultivating an awareness of prior knowledge, taking initiative in the present, and anticipating the future to navigate the path ahead. I deeply appreciate his kind dedication to my academic and personal growth to become a researcher and a better self.

I also appreciate kind support from the doctoral committee members, Prof. Richard Wiebe, Prof. Jinkyu Yang, Prof. Dana Dabiri, and Prof. Eli Livne. I would like to thank prof. Wiebe to serve as GSR in my committee. I would like to thank prof. Dabiri for teaching me the joy of learning fluid mechanics. I would like to thank prof. Livne for providing unparalleled insight on aircraft structures and design. I would like to thank prof. Yang for providing me the opportunity to work as a undergraduate intern in his lab. It was my first experience in research, and it motivated me to further pursue the career as a researcher in aerospace structures. I would also like to thank prof. Eunho Kim for providing me the mentorship during the internship.

Many thanks to my fellow colleagues in MAMS Lab and GUG 307 members: Yao Qiao, Seunghyun Ko, Antonio Alessandro Deleo, Troy Nakagawa, Shiva Goutham Kumar, Kenta Suzuki, Wei-Hong Li, Jiacheng Chen, Abhiram Aithal, Pablo Trefftz Posada, Gustavo

Fujiwara, Minh Hoang Nguyen, Dawei Lu, Maxine Tan and many others. Everyone was supportive and treated me like a family member.

Also, thanks to the industry professionals from ES3: Daniele Pelessone, Shawn Huff, Derek Shelley, and Ed Moffett for the helps on programming, manufacturing and testing in the collaborative projects.

I would also like to thank all the staff, academic advisors, facility managers: David Fray, Bill Kuykendall, George Eliot, Ed Connery, Winnie Lin, Nancy Lou Polk, Paul Neubert, Betsy Winter, Sean Krewson, David Wilson, Khalid Mohamed, Amy Sprague and many others from the University of Washington. Thank you for smoothing out the process in my Ph.D. journey.

I would also like to thank prof. Matthew Knepley for helping me on developing a numerical solver, and so many unknown intellectuals in Stack Overflow for providing collective knowledge regarding programming and algorithms.

DEDICATION

to my dear family, David Phenisee, Kyong Phenisee, Sarah Phenisee, Grace Bae, Joseph Phenisee for their endless love and support.

나를 낳아 주시고 길러주신, 언제나 사랑으로 함께하는 한국에 계시는 부모님께:

공명희, 신조우

마지막으로 보이진 않지만, 항상 의로운 길로 인도하시는 하나님께 이 시간을 바칩니다.

Chapter 1

INTRODUCTION AND RESEARCH STATEMENT

1.1 Brief history of materials in aeronautical structures

For about a decade after the aerial age launched by the historic flight of Wright brothers in 1903, woods and fabric materials were main constituents of aircraft structures. These light-weight material were widely available, the prior knowledge in manufacturing techniques made them convenient in construction, and the low speed operation did not require a high material strength and accurate streamlining on the skin. However, wooden aircraft deteriorates rapidly; therefore, hard to sustain a good quality for a long period [12].

As more airplanes were operated in faster speed, a monocoque or semi-monocoque design, that provides a better specific strength compared to truss-like structures in the previous design, were introduced and preferred for a fuselage construction. Along with the maintenance issue of a wooden structures, advancements of structural requirements (needs of higher strength and stiffness) shifted the main constituent of aircraft from woods to metals or alloys; they became the main materials used in the aircraft construction by 1950s [13].

After WWI ended, commercial flights started to increase. The development of a jet engine during WWII further contributed to the surge of commercial flights, leading to the introduction of the de Havilland DH.106 Comet, known as the world's first commercial jet airliner. While the advancement in engineering and technology promoted the new material development to improve the structural performance, there are also the social and environmental issues that further encourage the reduction in the weight of aircraft [13].

Global market kept expanding, and the trade agreement between countries started to settle. Globalization of political, social, and economic interaction throughout the world had a synergistic effect with the growth in aviation industry. By 2003, it was estimated that the air transport occupied about 40% of global freight trade by value. Moreover, point-to-point or one-stop flight services started to increase, inducing the growth in the low-cost

carrier market which targets more frequent non-stop services. Online reservation made the air travel more accessible and affordable. By early 2000s, there was a increasing trend of number of people utilizing the flight for the leisure and business with lower cost [14].

However, as flourish as the industry became, there is an increasing concern regarding the sustainability of air transport. As Greene and Wegener [15] states, the sustainable transport needs to satisfy the following conditions: "(a) its rates of use of renewable resources do not exceed their rates of regeneration; (b) its rates of use of non-renewable resources do not exceed the rate at which sustainable renewable substitutes are developed; and (c) its rates of pollution emission do not exceed the assimilative capacity of the environment." Followed by the exponential increase in the air traffic, the cost of fuel consumption increases without alternatives. Aircraft emission includes the atmospheric pollutants such as carbon dioxide and nitrogen oxide. These are known for the greenhouse gas causing the climate change across the globe [16]. As a consequence, it became inevitable to push a design of lightweight and fuel-efficient aircraft, making the advanced composite materials more attractive as main constituents in aircraft structure.

1.2 Composites, what and why?

In general, a composite material system is referred to the composition of two or more constituent materials. Mechanical performance of a composite material is superior as a union in macroscopic scale compared to the properties of constituent materials acting independently. There are mainly three distinct phases that defines the material composition as illustrated in Fig. 1.1. First is the reinforcement which has much higher stiffness and strength compared to the second phase called the matrix, which has relatively weaker mechanical property. The main role of the matrix is to provide the support of the meso-scale material structure and to transfer the load between reinforcements. Third phase is the interphase between reinforcement and matrix. Although the region occupied by the interphase is minimal compared to other two phases, it can still play an important role in determining the failure mechanism of a composite material. [17]

The mechanical and functional properties of a composite material highly depends on the properties of the constituent materials. Moreover, the geometry, distribution (or packaging

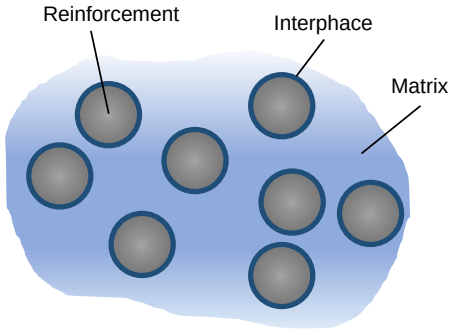

Figure 1.1: Schematic for three phases of composite materials: Reinforcement, matrix, and interphase

method), and volume fraction of a reinforcement can influence the property range.

There can be found of naturally occurring composite material systems such as woods, bones, and fish scales. Other examples, close to the definition of "engineered" material, are concrete, continuous / discontinuous fiber reinforced composite, and nanocomposites where the reinforcements are in nano-scale such as carbon nanotube and graphene nano-platelets.

For the primary structures that requires a significant amount of load bear capacity, carbon fiber reinforced composites are the popular choice due to the outstanding mechanical properties driven from the fiber reinforcement. Major stiffness and strength of the composite follows the direction of the fibers whereas the transverse properties, orthogonal to the fiber reinforcement axis, are relatively weak, resulting an orthotropy in the system. Interestingly, the idea of using fiber reinforcement dates far back to Before Christ era. In the book of Exodus (5:7), there is a reference of using straw-reinforcement for clay bricks. Coming back to modern period of time, invention of iron rods in 19th century to reinforce masonry. For the aviation industry, the development of graphite fiber and boron fiber in 1960s lead to the advanced fiber reinforced polymers that are widely used in aircraft construction [18].

Main advantages of using fiber reinforced composite materials lies in the outstanding specific property - high stiffness or strength to density ratio. While maintaining the high structural performance, engineer can reduce the total weight of the structure. Thanks to this desirable characteristics, more aircraft components are getting made out of composite materials, leading to the environmental-friendly and energy-saving design. The Boeing 787,

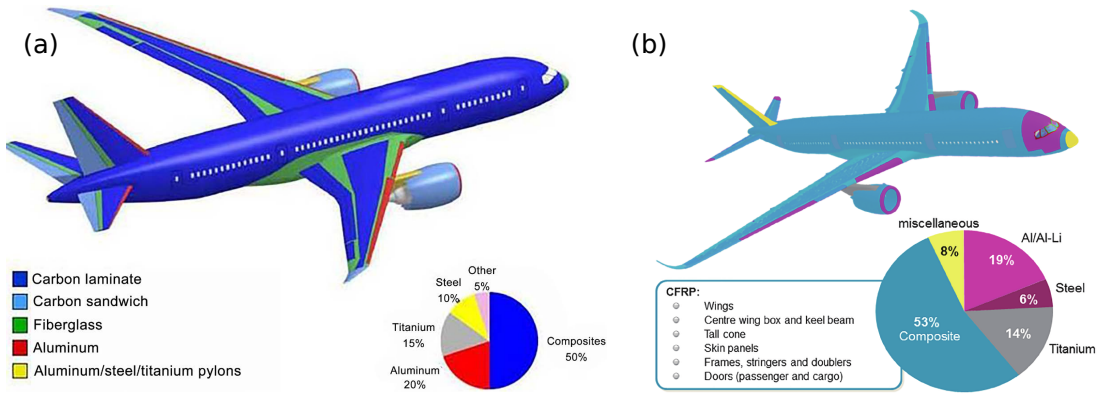

Figure 1.2: Usage of composite materials in commercial airplanes is exponentially increased over the years; (a) Boeing 787, "Dreamliner" (image from [19]); (b) Airbus, A350 XWB (image from [20])

"Dreamliner" consists of 50% composite materials by weight. Airbus, A350 XWB is made of 53% of composite materials by weight. Material composition schematics for both planes are shown in Fig. 1.2.

1.3 Current composite laminate design and limitation

1.3.1 Common practice of composite laminate design

Thanks to the outstanding specific mechanical properties, fiber reinforced polymers have wide range of applications: aerospace, automobile industry, wind power, constructions, biomedical, etc. Since the introduction of the fiber reinforcements, most of the composite structures in a laminate form shares the similar layup composition. A quasi-isotropic laminate (for an example, $[0, \pm 45, 90]_s$) provides uniform material property in the plane of isotropy. This is a convenient prevention of creating a matrix dominant, weak spots in the structure. This approach can simplify the design and manufacturing process of composite materials. As a result, a quasi-isotropic layup using four standard orientations has been widely employed; Composite Materials Handbook [21] suggests to use at least 10 percent of each element in the standard orientations set: $\{0°, \pm 45°, 90°\}$. However, this standard practice for designing any laminate structures undermines the advantage of a tailorability

of mechanical properties unique to composites compared to the metal counterparts.

There has been several works on investigating a mechanical performance from non-standard layups. Kim et al. [22] employed a thin-shallow angle ply (specifically $\pm 25^\circ$) in the composite wings construction. The authors demonstrated that the switching the layup composition of bottom skin from $\pm 45^\circ$ to $\pm 25^\circ$ improved the span-wise stiffness of the structure by 40% compared to the base-line cross-ply configuration consisting of $\pm 45^\circ$ angle group. Another group also explored to discover a new species of laminate configurations that can replace the standard quad laminate - composition using the standard four orientation angles. Double-Double, introduced by Tsai et al. [23], consists of only two angular components: $\pm\Phi$ and $\pm\Psi$. It does not require the laminate to be symmetric across the mid-plane since it can be easily homogenized after few numbers of repeat in sub-laminates. Homogenized laminate with a few angular components without symmetry requirement reduces the number of lamina to produce the part. It becomes much simpler to design a tapered structure to reduce the total weight. Less thickness reduces the danger of delamination. Furthermore, a high strength of double-double configuration compared to quad laminate legacy can be found using the first-ply failure theory such as Tsai-Wu failure criterion. Using this advantages of double-double, authors developed an searching algorithm called "Lam search" that systematically finds the optimal double-double configuration given a stress profile of a structure.

1.3.2 Limitation of current laminate designs

So far, the mechanical property of the composite laminates were tailored by changing the layup configuration. Double-Double definitely expanded the design space for the composite structures; however, it does not fully utilize the potential of the tailorability of composite materials using variable orientation of reinforcements. All the layups, mentioned so far, have the linear reinforcement. Orientation of fiber reinforcement may vary across the thickness; however, the orientation at lamina level is uniform across the plane. This implies that the properties may differ in each direction due to the orthotropic nature of composite material, but the anisotropy still does not vary across the laminate. No matter the location on the

laminate, the property in the specific direction is identical.

When the geometry of a structure is simple, uniform orientation distribution does not complicate the stress contour over the structure given that the loading and the boundary condition are simple. However, these conditions are rare in real-world applications. Structures often have geometric features such as holes and notches. Load distribution over the surface can get complex with a possible discontinuity. Thus, the stress contour can easily become non-uniform. The classical example is a plate with a central hole under a uniform traction. When the size of a plate approaches to infinity, it is well-known that the stress concentration becomes three at a neighborhood of the hole for an isotropic material. Under the same conditions, the stress concentration can be much higher and localized when the reinforcement is introduced. This localized stress raiser can cause premature damage initiation, requiring more reinforcement and increasing unnecessary weight to the structural design.

1.4 Variable anisotropy through curvilinear reinforcement

The idea of introducing reinforcement to the load-bearing sheet dates back to early 1950s. When the aircraft had a stress-bearing skin with cut-outs, strength and the stiffness reductions were problematic. Reissner and Morduchow [24] came up with the idea of reinforcing circular cut-outs in plane sheets so that the stress distribution is not affected and stayed uniform as if there is no cut-outs. However, the result of the reinforcement was not practical because the reinforcing material required such a high bending stiffness typically incompatible with the required tensile stiffness in the solution. Further study on a reinforcement method was carried out and improved by Mansfield [25] who introduced the term, neutral hole as "reinforced hole which does not affect the stress distribution in the remainder of the sheet, and therefore gives the same strength and stiffness as the replaced sheet." Mansfield demonstrated that the shape of neutral hole can be represented as a level curve that the superposition of the airy stress function and any linear function of x and y equal to zero. Assuming the reinforced material is identical to the one used in a plane sheet, the concept of neutral hole cannot be used as a weight saving method because the weight added by the reinforcement is usually greater compared to the one removed by cut-outs; however,

the idea of neutral hole provides a great reinforcement method to maintain the mechanical performance of a structure with a cut-outs such as a fuselage with multiple windows.

Concept of reinforcement is inherent in composite materials. Instead of adding extra reinforcement to the main structure, a structure with composite materials can be designed to avoid a high stress concentration region by tuning the local orientation of reinforcement. Although the presence of stress raiser is somewhat natural for a general structures made with isotropic materials, the degree of concentration significantly depends on the orientation of the reinforcement for a structures made with composite materials. As opposed to the isotropic materials, unidirectional fiber-reinforced composite materials are capable of changing orientations throughout the structure. Orientation as a function of local coordinate over a structure induces a variable anisotropy across the domain. In the structural point of view, main idea, and the main theme of the thesis, is to place the curvilinear reinforcement such that the stress distribution approaches smoothly to uniformity. Moreover, composite materials are multi-functional; carbon fibers have superior electric and heat conductivity. Fiber orientations across a structure can drastically change the overall conductivity. Therefore, tuning the reinforcement orientation of composites broadens up the multi-functional applications such as health monitoring and heat or electric shielding.

1.5 Lessons from nature

Before proceeding to the variable anisotropic design of composite structures, it is worthwhile to explore how the nature has been producing its own composite structures using natural selection. Examples of natural composite structures include human bones, fish scale, and stomatopod dactyl club. Main constituents of bio-composite materials are mineral crystallines (e.g. carbonated apatite, hydroxyapatite, etc) which mostly carry load and provide rigidity and and natural polymers (e.g. cellulose, chitin, collagen, etc) which transfer loads through shear [26].

Structures found in nature are often architected in a hierarchical manner. The examinations using scanning electron microscopy and transmission electron microscopy showed that the bones exhibits the six or seven levels of hierarchical organization. Main constituents of this composite structure are collagen molecules and minerals, which compose the first level

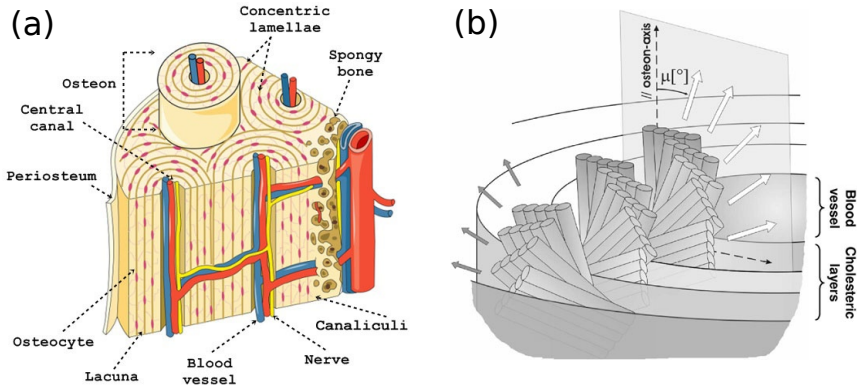

Figure 1.3: Diagram of bone structure: (a) Haversian system in a compact bone (image from [30]); (b) Helicoidal arrangements of mineralized fibrils in a concentric lamellae layers. (image from [29])

hierarchy. Collagen molecules arrange close to each other into fibrils in a staggered fashion. There are gaps and overlaps between neighboring molecules where the crystals are formed and grow to a platelet, producing mineralized fibrils which are the main building blocks of bones. Further moving up the hierarchy, minerialzed fibrils assemble themselves to the fiber bundles, which arrange into a parallel pattern and form a lamella. A compact bone is essentially a group of the Harversian systems and interstitial lamellae that fills up the remaining spots. Haversian system, also known as osteon, is a cylindrical structure which there is a central canal, that contains nervous system and blood vessels, and surrounding lamellae layers as a protection [27]. Gao et al. [28] demonstrated the relation between the nano-scale composite structure and the superior strength of bone. However, it is noteworthy to examine the lamination configuration of lamellae surrounding the central canal in an osteon. Wagermaier et al. [29] observed the helicoidal arrangement of mineralized fibrils through X-ray microscopy. The type of spiral shape stacking, also referred to Bouligand-type, sequence is common in other natural composite structure such as fish scale. Detailed illustration of Haversian system and helicoidal arrangement are shown in Fig. 1.3.

Arapaima gigas, largest fresh water fish living in the Amazon Basin, is covered with strong and tough scales to be protected from piranhas. Arapaima scales have two distinct layers. Outer layers are highly mineralized and provide high strength, stiffness, and

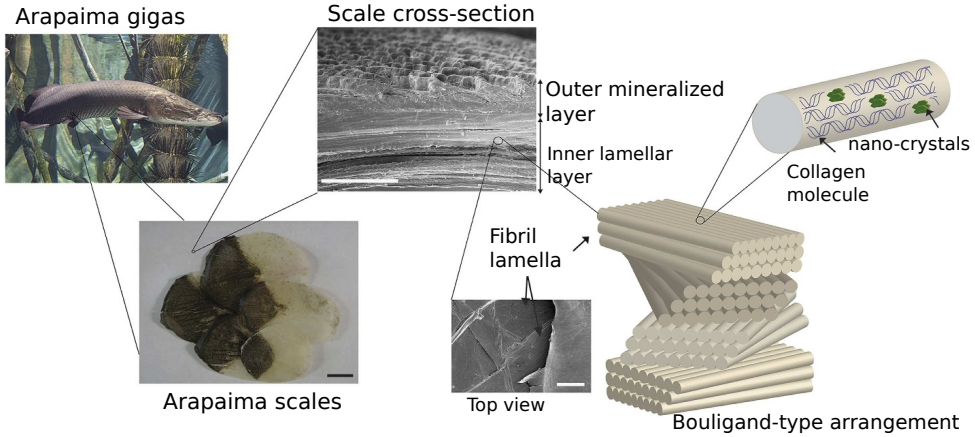

Figure 1.4: Inner lamellar layers composed of mineralized fibrils in arapaima gigas scales show Bouligand-type arrangements (Image from [31]).

penetration resistance. Inner layers consists of mineralized fibrils which are arranged in a Bouligand-type structure as illustrated in Fig. 1.4. This configuration allows to reorient the lamellae in response to the loading conditions. Adaptive property of meso-scale structure enhances the fracture toughness of the fish scale [31, 32]. Nature architects the material with nano-scale composites to provide high strength and utilize the method of meso-scale structural arrangement to supplement the fracture resistance. Bouligand-type structure takes advantage of the stacking sequence of laminate structures to achieve high performance. However, nature does not stop here to fully exploit the capability of bio-composite materials.

Bouligand-type arrangement of organic matrix embedded with natural fibers is also observed in the dactyl club of stomatopods, commonly known as mentis shrimp. They hunt preys such as mollusk, crab, and small fish by smashing the exoskeletons. They are able to accelerate the clubs to the speed of 25 m/s in water (speed of train is about 50 m/s) and generate the forces greater than 700 N [33] from the impact. It is noteworthy that the stomatopod dactyl clubs exhibit outstanding damage resistance considering that they can impose significant damage to their prey's highly mineralized exoskeletons from the powerful blow. The microstructure of a dactyl club contains three distinct regions. The

impact region is the outer most layer that is highly mineralized and directly absorbs impact. After a sharp transition of mineral composition, the periodic region is consist of bundle of mineralized chitin fibrils stacked in spiral pattern. Initially, Weaver et al. [34] showed that the helicoidal structure caused the rotation of crack front following the fibers, resulting a creation of larger surface area in the direction of crack propation and, consequently, increasing the total energy dissipation during the damage formulation. Recently, Yaraghi et al. [35] investigated micro-structural architecture in the impact region and discovered that the impact region also includes the helicoidal arrangement of minerialized chinin fiber layers. However, the lateral compaction creates the herringbone pattern, which shapes triangular periodic waves as illustrated in Fig. 1.5. This type of arrangement induces twisting of a crack front and prevents the coalescence of multiple micro-cracks. Furthermore, the bridging of curvilinear fibers on micro-cracks induces a volumetric arrest of crack nucleation and propagation. Following the observation, they manufactured the 3-D printed cylindrical specimens made of polymer that feature helicoidal and herringbone structures as shown in Fig. 1.6 and tested under uni-axial compression. The experiment demonstrated the surpassing capability of the herringbone structure in distributing strain and absorbing more energy from the deformation. The impact region is the layer which directly absorb the impact from the strike compared to the periodic region. This example shows the further adaptation of nature from stacking sequence of 2-D linear reinforcement to 3-D curvlinear fiber arrangement in the response of an extreme loading condition.

1.6 Practicality of curvilinear reinforcement: advancement in manufacturing methods

As the use of composite materials increase exponentially across the applications, effort of improving the composite layup manufacturing process emerged. Furthermore, conventional layup procedures include manual labors that can increase the time consumption in production, manufacturing defects, and irregularities from human error [36]. These reasons motivate the automation in the composite manufacturing. This section presents two main automated technology that enable a curvilinear reinforcement.

Automated Fiber Placement (AFP) uses a mechanical equipment in either gantry style or

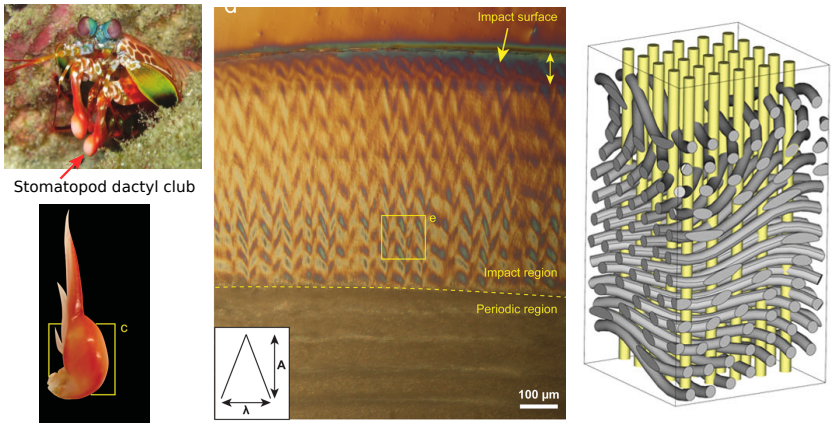

Figure 1.5: Herringbone pattern of compact mineralized fibrils is observed at the impact region in stomatopod dactyl club. Schematic illustrate the sinusoidal reinforcement of fibers (Image is re-created from figures in [35]).

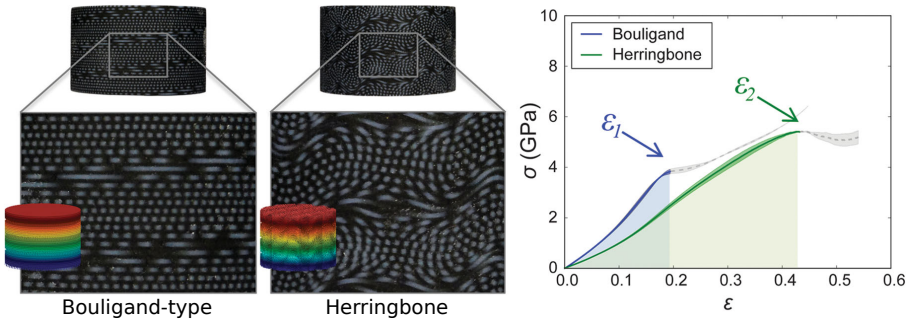

Figure 1.6: Mechanical testing of Bouligand-type and Herringbone pattern reinforcement. Herringbone pattern reinforcement provides surpassing fracture toughness along with a slight decrease in the stiffness (Images are from [35]).

robotic-arm setup (as shown in Fig. 1.7 (a)) to place narrow tapes on a tooled surface. The width of a narrow tape typically ranges from 3.2 mm to 12.7 mm. A machine feeds the tapes to the head, which can place more than 30 independent tapes on the surface. A machine can stop and cut the tapes individually restricted by a minimum cutting length. Heat source installed on the head improve the quality of the layup stacking, and the compaction roller press down the tapes to remove the air pocket and gaps between layers. Configuration of a typical machine head is illustrated in Fig. 1.7 (b). The presence of curvature on a surface or path of the reinforcement, one needs to be cautious of the turning radius. Because the rectangular tape has a finite width, high curvature can cause winkles and pull-up in the tow. Besides, other manufacturing defects using AFP include gaps and overlaps between tows, missing tow, and twisted tow rotated during the placement [36, 37].

Since the manufacturing defects reduce the mechanical performance of a part, there have been a number of studies focused on the effect of manufacturing defects. Sawicki and Minguet [38] examined the reduction in a compressive strength due to the out-of-plane waviness caused by intraply overlaps and gaps; Croft et al. [39] introduced four main defects in AFP specimens at the symmetry axis and their effect on the strength under tension, compression and in-plane shear; Fayazbakhsh et al. [40] implemented degradation of Elastic modulus and increase in effective thickness of local strips to represent gaps and overlaps, respectively, to capture the in-plane stiffness and buckling load of a composite laminate; Falcó et al. [41] showed the effect of tow-angle discontinuity and gap coverage in the laminate on tensile strength of both unnotched and open-hole specimens; Mukhopadhyay et al. investigated numerically and experimentally the influence of the artificially created fiber-wrinkle on both compressive strength [42] and tensile strength [43], exploring the failure modes and interaction in the region of the wrinkle; Xu et al. [44] further explored the effect of the out-of-plane wrinkles on out-of-plane properties with a four point bending test on curved beam specimens followed by numerical investigations to show their failure modes; Lan et al. [45] extended the effect of embedded defects of AFP laminates on their shear and compressive properties with the experiments; Nguyen et al. [46] provided a comprehensive and systematical experimental study of a failure progression and modes induced by imperfections produced by AFP and their effect on stiffness and strength of the

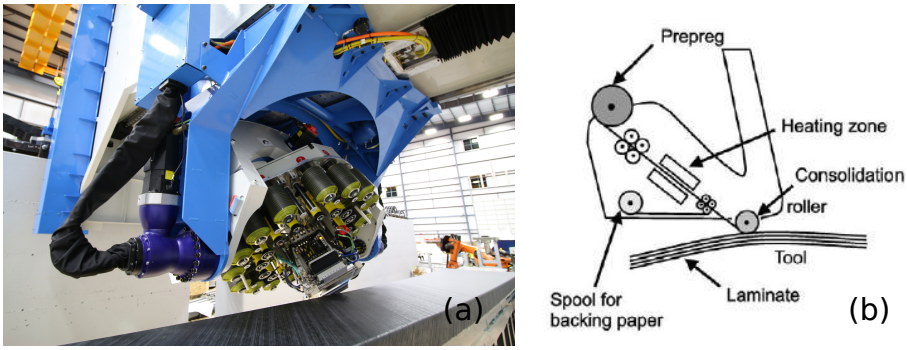

Figure 1.7: Automated Fiber Placement: (a) image of Electroimpact AFP machine (Source: Electroimpact Inc.); (b) Schematic of the machine head of AFP equipment (image from [37]).

laminate.

Additive manufacturing (AM) became popular for a rapid prototyping the product. However, affordable 3-D printers are limited with the choice of materials can be printed, and materials are all isotropic [36]. To improve the mechanical performance of the 3-D printed parts, fillers such as millimeter-size glass whiskers (developed by Stratasys Inc.) are utilize to toughen the polymer system [47]. Recently, there have been several efforts to print continuous fiber bundles with polymer matrix. Following are the examples of currently available 3-D printing research of continuous fiber reinforcement.

Markforged Inc. [48], additive manufacturing company, developed "Mark One" printer (claimed to be the first) that can print in continuous cabon fiber reinforcement with polylactic acid (PLA). Van Der Klift et al. [49] demonstrated the capability of 3D printing continuous carbon fiber reinforced thermoplastic with Mark One printer and evaluated the tensile strength of the printed specimen. Matsuzaki et al. [50] developed 3D printing method for continuous fiber-reinforced thermoplastic with PLA using fused-deposition modeling. Diagram of the 3-D printer and the image of printing process is shown in Fig. 1.8 (a). Tensile specimens with Carbon fiber and jute fiber reinforcements are printed, and their mechanical properties (modulus and strength) are compared with pure PLA and other reinforcements found in literature. Tian et al. [51] similarly developed a FDM-based printer capable of manufacturing 3-D print carbon fiber reinforced PLA composite. Five

parameters (Temperature of liquifier, layer thickness, feed rate, hatch spacing and transverse speed of extruder head) were investigated to see the influence on printing process. To evaluate the mechanical performance of 3D printed specimen, flexural strength and stiffness were measured. Interface between fiber and PLA and fiber content are important in mechanical performance. Sugiyama et al. [52] successfully manufactured 3D printed sandwich structures with continuous carbon fiber. Multiple core shape were printed as shown in Fig. 1.8 (b), and three-point bending test are conducted. Poor adhesion between core and skins were observed, and the printing errors produced lower experimental flexural modulus and strength compared to the theoretical calculation. However, flexibility in printing various type of core shape with continuous fiber allows convenient way to manufacture and to directly compare core shape design for sandwich structures. Parandoush et al. [53] developed additive manufacturing method for pre-preg composites with laser assisted curing and cutting process. This method provide outstanding inter-facial bonding from the peel test and the single lap shear test. This results lead to outperforming mechanical behavior compared to FDM printing method, comparable to compression molding method. They showed promising potential of incorporating laser assisted bonding technology to additive manufacturing.

3-D printing technology of a continuous fibers can improve the curvature limitation of AFP-based design and further provide the flexibility of producing a structure with variable anisotropy using the curvilinear reinforcement.

1.7 Research Statement

In this work, a systematic exploration on the effect of curvilinear reinforcement in a composite structure is presented. The main topics covered in this work are schematized in a flow chart shown in fig. 1.9. The effect of a curvilinear reinforcement is investigated in two main applications: 1) improving functional property in electrostatic problem and 2) improving mechanical performance focusing on the fracture resistance of composite structures.

In chapter 2, the investigation on electrostatic problem is presented. Carbon fibers have a high thermal and electrical conductivity, which makes them highly applicable as a functional material. Depending on the reinforcement orientation, it is capable of tuning

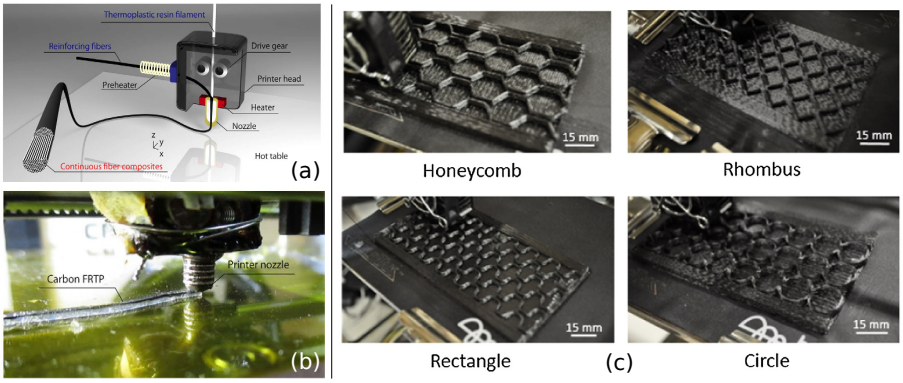

Figure 1.8: Additive manufacturing of continuous fiber: (a) FDM method of printing continuous fiber reinforcement (image from [50]); (b) 3-D printed sandwich structures with continuous carbon fiber reinforcement (image from [52]).

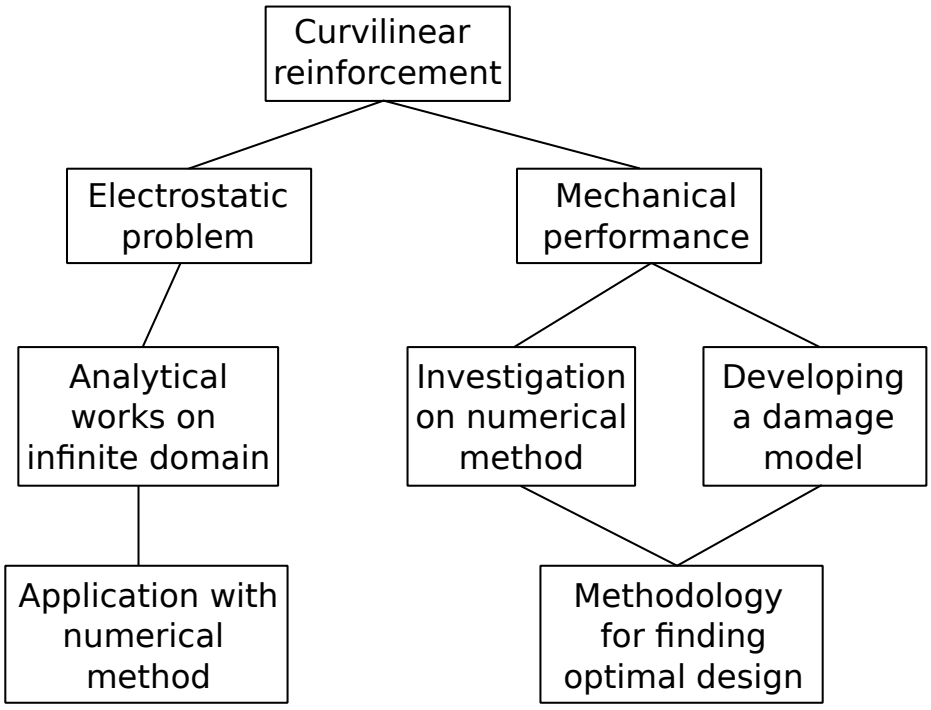

Figure 1.9: Flow chart of the research plan.

conductivity of composite structures. Poisson equation describes the electrostatic behavior of composite materials; therefore, it is possible to obtain an analytical solution with a set of simple boundary and loading conditions in a proper domain. First, the concept of curvilinear transverse isotropy (CTI) is introduced, and a simple electrostatic problem in an infinite domain is formulated. The analytical solution is obtained utilizing the conformal mapping and highlights significant findings such as the optimal fiber orientation is aligned with the field lines in an isotropic material under the identical electrostatic boundary condition. These findings in a theoretical work extend our investigation to a finite domain that can actually be applied to real world examples. Finite element method is used to obtain the optimal reinforcement configuration of a single edge notch specimen, and evaluate the capability of damage detection using the conductivity differential as a measure of damage progression. Lastly, the examination on the capability of health monitoring feature utilizing the piezoresistive property of conductive fibers concludes our exploration in the functional side composites featuring CTI.

Subsequently, the effect of curvilinear reinforcement on the mechanical performance is investigated. The literature review on the topic of curvilinear reinforcement applied to the mechanical problems is presented in chapter 3 to provide the previous studies that set the foundation to this study. The chapter 4 present the investigation on the mechanical performance of a rectangular composite laminate with a semi-circular notch featuring CTI. First, a numerical method of modeling a composite structure featuring a curvilinear reinforcement is introduced. In this effort, the isogeometric analysis with spline basis functions provide high continuity over the analysis domain. Furthermore, the augmented numerical integration scheme is proposed to account for a variation of fiber orientation inside the element. The mechanical behavior of some representative curvilinear paths are explored for a plate with a semi-circular notch. The optimization method is proposed to obtain the optimal fiber path optimizing the structural properties such as stress concentration, stiffness and principal stress value. In order to proceed to the analysis of fracture behavior, an appropriate spline technology for the isogeometric analysis suitable for modeling a trimmed surface for an arbitrary notched specimen is determined and presented in chapter 5. The investigation of mechanical performance utilizing a data driven optimization method in order to attain

the optimal reinforcement configuration for the outstanding damage tolerance is carried on with the proposed approach as discussed in chapter 6. Lastly, a novel discrete approach of modeling fiber reinforced composite materials is proposed in chapter 7. This novel modeling framework predicts a damage initiation and progression of composite structures.

The summary of findings and concluding remarks are provided in chapter 8. Future works that can be extended from this work are also provided.

Chapter 2

CURVILINEAR TRANSVERSE ISOTROPY IN ELECTROSTATIC PROBLEM: PRESENCE OF ELECTRIC SOURCES

2.1 Isotropic and homogeneous media

In this section, the electrostatic problem is stated with Poisson equation with a set of boundary and loading condition. The analytical solution of a homogeneous and isotropic material is provided to obtain the insight of electric field on the structure to identify a potential reinforcement direction.

2.1.1 Continuity equation in Cartesian coordinates in the presence of electric charges

Let us consider the 2D domain $\Omega \cup \partial\Omega$ subjected to the electric potential difference depicted in Fig. 2.1. Such domain is assumed to be made of a homogeneous and isotropic, linear electrostatic material.

$$\frac{\partial J_x}{\partial x} + \frac{\partial J_y}{\partial y} + \sum_{i=1}^{N_s} Q^{(i)} \delta \left[\boldsymbol{x} - \boldsymbol{x}^{(i)} \right] = -\frac{\partial \rho}{\partial t} \tag{2.1}$$

where $J_i \, (i = x, y) =$ components of the current density in the $x-$ and $y-$directions, $\rho =$ electric charge density, and $Q^{(i)}$ with $i = 1, ...N_s$ represents an electric point source located in $\boldsymbol{x}^{(i)}$. The Dirac function $\delta \left[\boldsymbol{x} - \boldsymbol{x}^{(i)} \right] = \delta \left[x - x^{(i)} \right] \delta \left[x - x^{(i)} \right]$ is zero everywhere except at $\boldsymbol{x} = \boldsymbol{x}^{(i)}$, where is infinite and satisfies the following condition:

$$\int_{\boldsymbol{a}}^{\boldsymbol{b}} \delta \left[\boldsymbol{x} - \boldsymbol{x}^{(i)} \right] \mathrm{d}\boldsymbol{x} = \int_{a_x}^{b_x} \int_{a_y}^{b_y} \delta \left[y - y^{(i)} \right] \delta \left[x - x^{(i)} \right] \mathrm{d}y \mathrm{d}x = 1 \tag{2.2}$$

$\forall \boldsymbol{x}^{(i)} \in (\boldsymbol{a}, \boldsymbol{b})$. The current density is related to the electric field, $\boldsymbol{E}$, through Ohm's law: $E_i = k^{-1} J_i$ where $k = k_x = k_y$ represents the electrical conductivity of the material, treated as homogeneous and isotropic. Further, the conservativeness of the electric field leads to the following link to the electric potential ρ: $E_x = -\partial\rho/\partial x$ and $E_y = -\partial\rho/\partial y$. Substituting

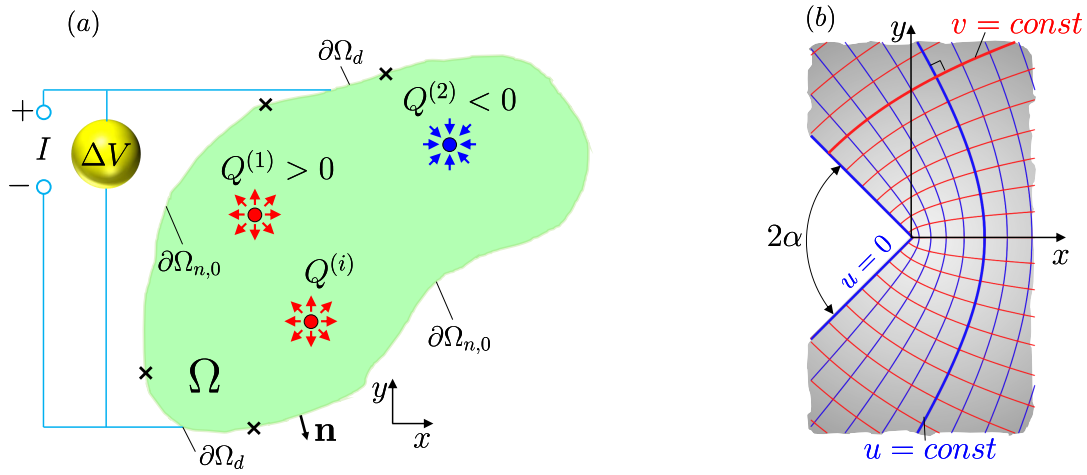

Figure 2.1: (a) 2D domain $\Omega \cup \partial\Omega$ subjected to an electric potential and a set of electric sources, $Q^{(i)}$ and (b) example of a conformal mapping $z(\xi) = \xi^q$ with $q \in \mathbb{R}$.

the foregoing expressions into Eq. (2.1) and focusing on the steady-state solution of the problem, one gets the following two-dimensional Poisson's equation for the electric potential:

$$\nabla^2 \rho = -\sum_{i=1}^{N_s} \frac{Q^{(i)}}{k} \delta\left[\boldsymbol{x} - \boldsymbol{x}^{(i)}\right] \tag{2.3}$$

where $\rho = \rho_0$ in $\partial\Omega_d$, $\partial\rho/\partial n = \nabla\rho \cdot \boldsymbol{n} = 0$ in $\partial\Omega_{n,0}$, $\partial\Omega = \partial\Omega_d \cup \partial\Omega_{n,0}$, and $\nabla^2 = \partial^2/\partial x^2 + \partial^2/\partial y^2$ is the laplacian operator. The solution of Eq. (2.3) in the two-dimensional domain $\Omega \cup \partial\Omega$ subjected to Dirichlet or von Neumann boundary conditions on the boundary $\partial\Omega$, allows the complete characterization of the electric potential and the related current density.

2.1.2 Continuity equation in curvilinear coordinates in the presence of electric charges

To facilitate the application of the boundary conditions in domains of complex shapes, it is often convenient to employ a transformation of coordinates. In this work, only conformal mappings are considered, i.e. transformations that can be described by means of a complex analytic function [54, 55, 56]. In such as case, the change of coordinates $z = z(\xi)$ with $z = z + \boldsymbol{i}y$ is always bijective, satisfies the Cauchy-Riemann (C-R) conditions: $\partial u/\partial x = \partial v/\partial y$,

$\partial u/\partial y = -\partial v/\partial x$ in Ω, and transforms the governing equation to an expression that is formally identical to the Cartesian case:

$$\frac{\partial^2 \rho}{\partial u^2} + \frac{\partial^2 \rho}{\partial v^2} = -\left\|\xi'(z)\right\|^2 \sum_{i=1}^{N_s} \frac{Q^{(i)}}{k} \delta\left[\boldsymbol{x} - \boldsymbol{x}^{(i)}\right] = \sum_{i=1}^{N_s} \frac{Q^{(i)}}{k} \delta\left[\boldsymbol{\xi} - \boldsymbol{\xi}^{(i)}\right] \tag{2.4}$$

where $\left\|\xi'(z)\right\|^2 > 0$ according to Dini's theorem and:

$$\delta\left[\boldsymbol{x} - \boldsymbol{x}^{(i)}\right] = \frac{\delta\left[\boldsymbol{\xi} - \boldsymbol{\xi}^{(i)}\right]}{\left\|\xi'(z)\right\|^2} = \frac{\delta\left[\boldsymbol{\xi} - \boldsymbol{\xi}^{(i)}\right]}{h^2} \tag{2.5}$$

transforms the Dirac's function in the new coordinate system. In the foregoing expressions, $\xi'(z) = \mathrm{d}\xi/\mathrm{d}z$ is the first derivative of the conformal mapping linking the Cartesian and the curvilinear domains and $\left\|\xi'(z)\right\|$ refers to its magnitude. Further, the metric coefficients $h_u = \sqrt{(\partial x/\partial u)^2 + (\partial y/\partial u)^2}$ and $h_v = \sqrt{(\partial x/\partial v)^2 + (\partial y/\partial v)^2}$ were implicitly introduced. Since a conformal map is isometric, $h_u = h_v = h = \left\|\xi'(z)\right\|$, this latter condition leading to Eqs. (2.4) and (2.5). In this work, the focus is on conformal maps in which the condition $u = u_b$ or $v = v_b$ (with u_0, v_0 being real constants) describes the boundary $\partial\Omega_{n,0}$, where the condition $J_n = \boldsymbol{J} \cdot \boldsymbol{n} = 0$ is satisfied. Finally, in the curvilinear coordinate system the electric field can be calculated as follows:

$$\boldsymbol{E} = -\nabla\rho = -\frac{1}{h}\frac{\partial \rho}{\partial u}\boldsymbol{e}_u - \frac{1}{h}\frac{\partial \rho}{\partial v}\boldsymbol{e}_v \tag{2.6}$$

where $\{\boldsymbol{e}_u, \boldsymbol{e}_v\}$ represent the orthonormal basis of the curvilinear system.

2.1.3 Green's function in curvilinear coordinates

As shown in the foregoing sections, the conformal transformation leaves the governing Poisson's equation formally invariant. Accordingly, considering the case in which $u = u_b$ describes $\partial\Omega_{n,0}$, the Green's function, G, associated to Eq. (2.4) satisfies the following equa-

tions:

$$\frac{\partial^2 G}{\partial u^2} + \frac{\partial^2 G}{\partial v^2} = \delta\left(u - u_0\right)\delta\left(v - v_0\right) \tag{2.7}$$

$$G = 0 \qquad \text{in } \partial\Omega_d \tag{2.8}$$

$$\frac{\partial G}{\partial u} = 0 \qquad \text{in } \partial\Omega_{n,0} \tag{2.9}$$

As can be noted, while the governing equations remains unchanged, the boundary conditions can be imposed via a very simple set of equations.

2.1.4 General solution in curvilinear coordinates by the method of images

The equation defining the fundamental solution, Eq. (2.8), is identical to the Cartesian problem, for which the fundamental solution is well known. Accordingly, the general fundamental solution of the curvilinear problem must take the same form:

$$G\left(u, v, u_0, v_0\right) = \frac{1}{2\pi}\ln\sqrt{\left(u - u_0\right)^2 + \left(v - v_0\right)^2} + \text{const} \tag{2.10}$$

Then, leveraging the foregoing expression, it is possible to use the method of images to impose the desired boundary conditions. In contrast to the Cartesian case, however, the use of conformal mapping now allows the easy application of the boundary conditions even to complex boundaries.

Since in this work, the focus is the electric field close to notches, the part on the boundary $\partial\Omega_d$ is reached for $\|\xi\left(z\right)\| \to \infty$. Accordingly, the only condition on the Green's function is that $\partial G/\partial n = 0$ on $u = u_b$. This condition can be achieved easily by adding a second unit source that is reflected with respect to the $u = u_b$ plane. Such a unit source is outside the domain of interest so, the Green's function results to be:

$$G\left(u, v, u_0, v_0\right) = \frac{1}{2\pi}\ln\sqrt{g\left(u - u_0, v - v_0\right) g\left(u + u_0 - 2u_b, v - v_0\right)} \tag{2.11}$$

where the function $g\left(u, v\right) = u^2 + v^2$ was introduced. As can be noted, the foregoing

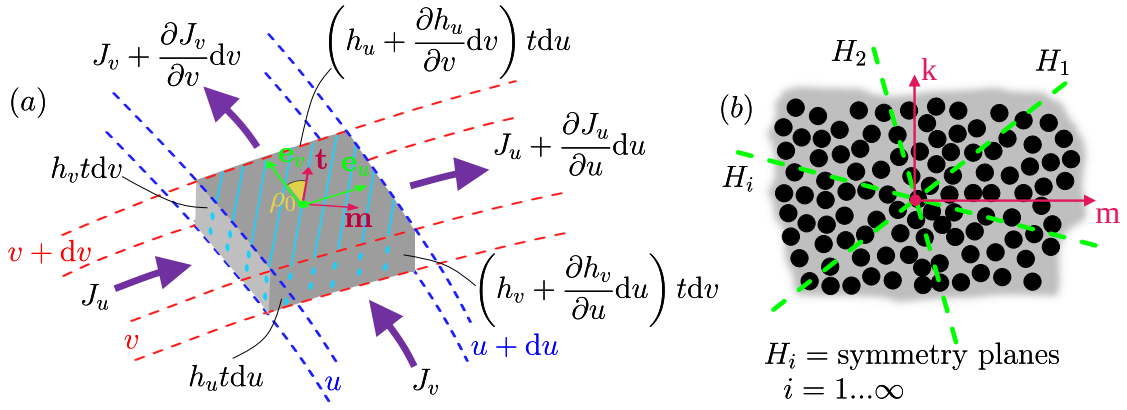

Figure 2.2: (a) Infinitesimal material element featuring curvilinear orthotropy in $(\mathbf{e}_u, \mathbf{e}_v, \mathbf{k})$ and the related current densities; (b) schematic representation of the microstructure as cut by the plane $\pi : \pi \perp \mathbf{t}$. As can be noted, an infinite number of symmetry planes H_i exist supporting the assumption of *curvilinear transverse isotropy* in $(\mathbf{t}, \mathbf{m}, \mathbf{k})$.

equations satisfies the boundary conditions:

$$\left.\frac{\partial G\left(u, v, u_0, v_0\right)}{\partial u}\right|_{u_b} = \frac{1}{2\pi}\left[\frac{u - u_0}{g\left(u - u_0, v - v_0\right)} + \frac{u + u_0 - 2u_b}{g\left(u + u_0 - 2u_b, v - v_0\right)}\right]_{u_b} = 0 \tag{2.12}$$

Once the Green's function, $G\left(\boldsymbol{\xi}, \boldsymbol{\xi}_0\right)$, is found, one can determine the solution for any distribution of sources leveraging the additivity property of the Poisson's equation. Using Green's identity:

$$\iint_{\Omega} \left(\rho \nabla^2 G - G \nabla^2 \rho\right) \mathrm{d}\Omega = \oint_{\partial\Omega} \left(\rho \nabla G - G \nabla \rho\right) \cdot \boldsymbol{n} \mathrm{d}s \tag{2.13}$$

and finally, taking advantage of Eq.(2.8), the electric potential can be expressed by the following equation:

$$\rho\left(\boldsymbol{\xi}_0\right) = -\sum_{i=1}^{N_s} \iint_{\Omega} \frac{Q^{(i)}}{k} G\left[\boldsymbol{\xi}^{(i)}, \boldsymbol{\xi}_0\right] \mathrm{d}\Omega \tag{2.14}$$

2.2 Media featuring Curvilinear Transverse Isotropy (CTI)

2.2.1 Curvilinear Transverse Isotropy (CTI)

Let us consider a material reinforced by fibers following a family of curvilinear paths $\gamma(s, u_c, v_c)$. The paths are constructed such that their tangent, $\mathbf{t}$ is rotated of a constant angle ρ_0 with respect to field lines. In the particular case in which $\rho_0 = 0$, the fiber paths coincide with the field lines of the problem. For each material point, a curvilinear orthonormal basis $(\mathbf{t}, \mathbf{m}, \mathbf{k})$ can be defined such that $\mathbf{m} \times \mathbf{t} = \mathbf{k}$ with $\mathbf{k}$ being the unit vector of the $z-$direction. Now, considering the material microstructure, it is easy to note that any plane $H : \mathbf{t} \in H$ is a symmetry plane (Figure 2.2b). Accordingly, in each material point the transverse plane $\pi : \pi \perp \mathbf{t}$ is a plane of isotropy and the material exhibits *curvilinear transverse isotropy* [57]. Assuming that each material point is reinforced by a sufficiently large number of curvilinear fibers, the material can be treated as homogeneous. Then, the anisotropic Ohm's equation can be written in matrix form as follows:

$$\begin{Bmatrix} J_t \\ J_m \end{Bmatrix} = - \begin{bmatrix} k_{tt} & 0 \\ 0 & k_{mm} \end{bmatrix} \begin{Bmatrix} E_t \\ E_m \end{Bmatrix} \tag{2.15}$$

where J_t, J_m, E_t, E_m represent the components of the current density and electric field respectively in the orthonormal basis $(\mathbf{t}, \mathbf{m}, \mathbf{k})$. The electric conductivities k_{tt} and k_{mm} in the curvilinear system can be measured experimentally or estimated by means of micromechanics [58, e.g.] and depend on the electric conductivities of the fibers and the matrix as well as the volume fraction of fibers. Assuming that the electric conductivity of the fibers is significantly larger than the matrix and considering that fibers and matrix are in parallel coupling along $\mathbf{t}$ and in series coupling along $\mathbf{m}$, one can conclude that generally $k_{tt} \geq k_{mm}$.

Although the orthonormal basis $(\mathbf{t}, \mathbf{m}, \mathbf{k})$ guarantees the simplest description of the constitutive behavior, it is convenient to recast Eq. (2.15) in the curvilinear coordinate system $(\mathbf{e}_u, \mathbf{e}_v, \mathbf{k})$ which enables the simplest application of the boundary conditions without affecting the continuity equation significantly. Considering the case in which $u = u_0$ provides the description of $\partial\Omega_{n,0}$ and recalling that $\mathbf{t} = \cos\rho_0 \mathbf{e}_v + \sin\rho_0 \mathbf{e}_u$ and $\mathbf{m} = -\sin\rho_0 \mathbf{e}_v +$

$\cos\rho_0\mathbf{e}_u$, the constitutive behavior can be written as follows:

$$\begin{Bmatrix} J_v \\ J_u \end{Bmatrix} = - \begin{bmatrix} k_{vv}\left(\rho_0, k_{tt}, k_{mm}\right) & k_{uv}\left(\rho_0, k_{tt}, k_{mm}\right) \\ k_{uv}\left(\rho_0, k_{tt}, k_{mm}\right) & k_{uu}\left(\rho_0, k_{tt}, k_{mm}\right) \end{bmatrix} \begin{Bmatrix} E_v \\ E_u \end{Bmatrix} \tag{2.16}$$

where:

$$\begin{cases} k_{vv}\left(\rho_0, k_{tt}, k_{mm}\right) = \cos^2\left(\rho_0\right) k_{tt} + \sin^2\left(\rho_0\right) k_{mm} & \text{(2.17a)} \\ k_{uu}\left(\rho_0, k_{tt}, k_{mm}\right) = \sin^2\left(\rho_0\right) k_{tt} + \cos^2\left(\rho_0\right) k_{mm} & \text{(2.17b)} \\ k_{uv}\left(\rho_0, k_{tt}, k_{mm}\right) = \left(k_{tt} - k_{mm}\right) \cos\rho_0 \sin\rho_0 & \text{(2.17c)} \end{cases}$$

It is worth mentioning that Eqs (2.17a), (2.17b) and (2.17c) can be obtained noting that $\mathbf{K}^{(u,v)} = \mathbf{T}^\top \mathbf{K}^{(t,m)} \mathbf{T}$ with $\mathbf{T}$ being the rotation matrix linking $(\mathbf{t}, \mathbf{m}, \mathbf{k})$ to $(\mathbf{e}_u, \mathbf{e}_v, \mathbf{k})$ and $\mathbf{K}^{(t,m)}$, $\mathbf{K}^{(u,v)}$ being the conductivity matrices in the two orthonormal bases respectively.

In case that $v = v_0$ provides the description of $\partial\Omega_{n,0}$, $\mathbf{e}_u$ becomes the unit tangent vector of the field lines and ρ_0 represents the angle between $\mathbf{t}$ and $\mathbf{e}_u$. It can be shown that the constitutive behavior can be obtained from Eq. (2.16) simply by switching the diagonal terms in $\mathbf{K}^{(u,v)}$.

In this work, it focus on cases in which the fibers follow the field lines of the isotropic case. In such condition, $\rho_0 = 0$, $k_{vv} = k_{tt}$, $k_{uu} = k_{mm}$, and $k_{uv} = 0$. As demonstrated by Salviato and Phenisee [57], this condition represents the configuration optimizing the electrical conductivity of the material.

2.2.2 Continuity equation in media featuring CTI

To solve for the electric potential and prove the invariance of the solution to the isotropic case, it is convenient to rewrite the continuity equation of the material system schematically shown in Figure 2.2 in curvilinear coordinates. The energy balance for an infinitesimal time increment $\mathrm{d}t$ reads:

$$-J_v \frac{\partial h}{\partial v} - h\frac{\partial J_v}{\partial v} - J_u \frac{\partial h}{\partial u} - h\frac{\partial J_u}{\partial u} = -h \sum_{i=1}^{N_s} Q^{(i)} \delta\left[\boldsymbol{\xi} - \boldsymbol{\xi}^{(i)}\right] \tag{2.18}$$

Finally, introducing the constitutive equations and the relation between the electric field and electric potential, the continuity equation can be finally written as follows:

$$k_{vv}\frac{\partial^2\rho}{\partial v^2}+k_{uu}\frac{\partial^2\rho}{\partial u^2}=-\sum_{i=1}^{N_s}Q^{(i)}\delta\left[\boldsymbol{\xi}-\boldsymbol{\xi}^{(i)}\right] \tag{2.19}$$

2.2.3 Closed-form solution: electric potential, field lines and current density

Introducing the change of variable $\psi=\alpha u$ with $\alpha=\sqrt{k_{vv}/k_{uu}}$, one can write:

$$\frac{\partial^2\rho}{\partial v^2}+\frac{\partial^2 G}{\partial\psi^2}=-\sum_{i=1}^{N_s}\frac{Q^{(i)}}{k_{vv}}\frac{\delta\left[v-v^{(i)}\right]\delta\left[\psi-\psi^{(i)}\right]}{\alpha} \tag{2.20}$$

$$\rho=\rho* \qquad \text{in } \partial\Omega_d \tag{2.21}$$

$$\frac{\partial G}{\partial\psi}=0 \qquad \text{in } \partial\Omega_{n,0} \tag{2.22}$$

The foregoing expressions take the same form as the curvilinear and Cartesian cases investigated before except for the change of coordinate and the presence of the term α dependent on the orthotropic electric conductivities. Accordingly, the fundamental solution reads:

$$G\left(v,\psi,v_0,\psi_0\right)=\frac{1}{2\pi}\ln\sqrt{g\left(\psi-\psi_0,v-v_0\right)g\left(\psi+\psi_0-2\psi_b,v-v_0\right)} \tag{2.23}$$

From Green's theorem one gets:

$$\rho\left(\psi_0,v_0\right)=-\sum_{i=1}^{N_s}\iint\limits_{\Omega}\frac{Q^{(i)}}{k_{vv}}\frac{G\left[\psi_0,v_0,\psi^{(i)},v^{(i)}\right]}{\alpha}\mathrm{d}\psi\mathrm{d}v \tag{2.24}$$

By transforming the coordinates back to the original curvilinear system, the following result is obtained:

$$\rho\left(u_0,v_0\right)=-\sum_{i=1}^{N_s}\iint\limits_{\Omega}\frac{Q^{(i)}}{k_{vv}}G\left[u_0,v_0,u^{(i)},v^{(i)}\right]\mathrm{d}u\mathrm{d}v \tag{2.25}$$

This result is identical to the isotropic case provided that one uses the conductivity in the fiber direction *in lieu* of the isotropic constant k.

$$\varphi(u,v) = \frac{\psi(u,v,a) + \psi(u,v,-b) - \psi(u,v,-a) - \psi(u,v,b)}{2\pi k_{vv}} \tag{2.26}$$

$$\psi(u,v,x) = -\left\{\chi(u,v,x) + 4uv\zeta(u,v,x) + \xi(u,v,x)\right\}/x \tag{2.27}$$

$$\chi(u,v,x) = x\left(x^2 + u^2 - v^2\right)\log\left[(x-v)^2 + u^2\right] \tag{2.28}$$

$$\zeta(u,v,x) = \tan^{-1}\left[(x-v)/u\right] \tag{2.29}$$

$$\xi(u,v,x) = (x-v)(x+3v) \tag{2.30}$$

2.3 Validation via FEA

In this section, theoretical framework on an infinite plate with a single edge crack is validated by comparing the analytical solutions to the finite element analyses on electrostatic problem using ABAQUS 6.17. The electric potential and current density were computed using 3-node linear coupled thermal electric elements, DC2D3E and 4-node linear coupled thermal electric elements, DC2D4E. In order to characterize the Curvilinear Transverse Isotropy, a material was defined with an orthotropic conductivity, and the user sub-routine, ORIENT was used to assign the orientation of curvilinear fiber paths. ORIENT can only prescribe a single material orientation to each element at the integration point, which limits the continuity of the fiber to C^0. This requires to have a fine mesh near the tip of a crack in order to capture smooth fiber paths in the region with a high curvature. Size of the mesh was locally refined using the bias option in ABAQUS 6.17, and the numerical convergence was investigated to determine the size of the mesh that would provide the changes in the maximum electric potential value within 1%.

2.3.1 Modeling details

In modeling the geometry of a single edge crack specimen, a finite plate with the width, $D = 500$ mm and the length, $H = 1000$ mm is created. A crack with the initial length,

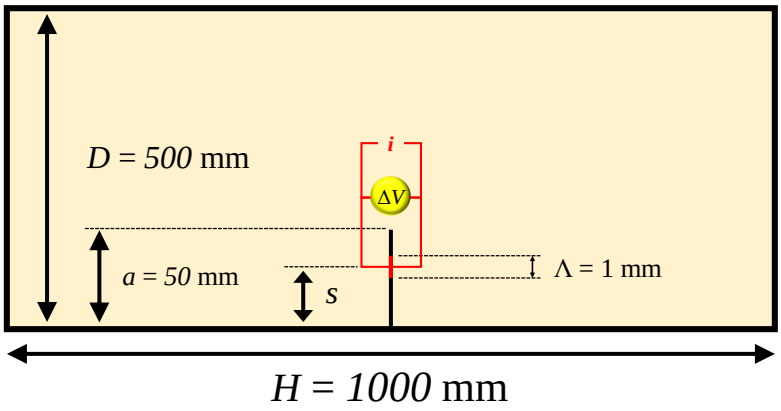

Figure 2.3: Geometry of a single edge crack specimen for a numerical validation.

$a = 50$ mm, is located at the midpoint of the bottom edge. A uniform current is applied at the small regions of the crack surfaces. The length of source strips, Λ, is 2% of the crack length, a. Two locations for the center of source strip are chosen for the validation: $s = 14.5$ mm and $s = 34.5$ mm. Summary of the geometry and the modeling detail is shown in Fig. 2.3. A CTI material system was chosen such that the conductivity in longitudinal direction, $k_f = 400$ S/mm and the conductivity in transverse direction, $k_m = 10^{-19}$ S/mm.

According to the theory, all the fibers emanate from the source location where the current flows in and converge back to the sink where the current flows out. This creates the loops of fibers in the infinite plate with the edge crack. User-subroutine, ORIENT, was used to align the fibers in the direction of the optimal path; however, the finite dimension in the finite element model intrinsically cannot capture the physical continuity of fibers at the boundary. To apply the correct boundary condition corresponding to the infinite plate, exact electric potential found in the analytical solution was directly applied to the outer boundary excluding the crack surfaces of the finite element model using the user-subroutine, DISP.

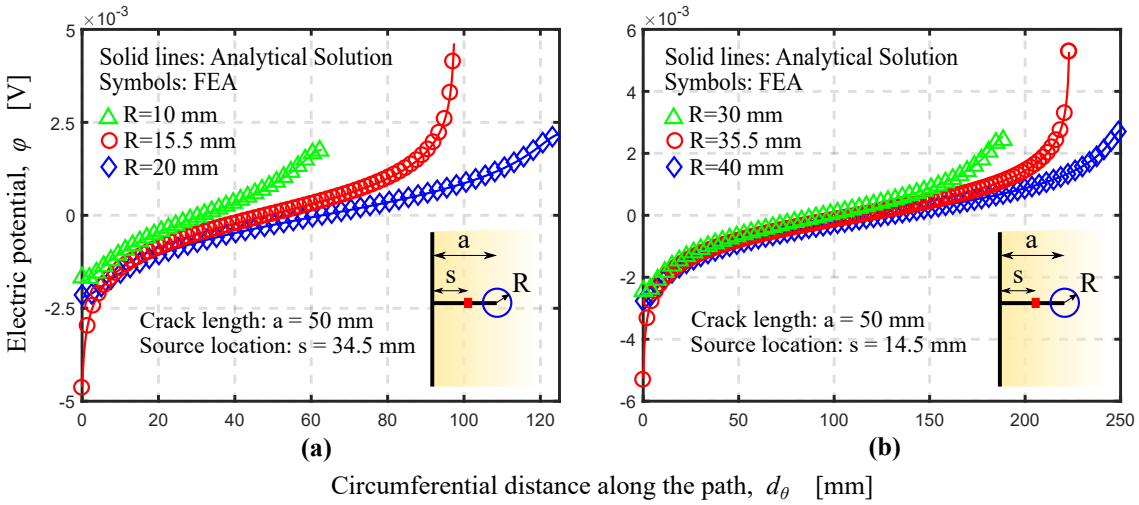

Figure 2.4: Numerical validation of the closed-form analytical solution. Plots of the electric potential along three circular paths with current sources located at (a) 34.5 mm and (b) 14.5 mm.

2.3.2 Theoretical and numerical results comparison

Comparisons between the electric potential components along three circular paths obtained by the theoretical solution and the numerical analysis are shown in Fig. 2.4. Two source locations are explored for the validation. As can be noted, the theoretical and numerical solutions are in a perfect agreement for each path in both source locations, providing a maximum difference less than 2%. Similar analysis was conducted for the current density components. Figure 2.5 shows that the theoretical and numerical results for the current density components are also in a perfect agreement for all the cases, providing a maximum difference less than 2%.

2.4 Application to damage detection in notched components

Many engineering materials and structures often include notches and reentrant corners in their design. The stress at the vicinity of a sharp notch theoretically approaches to singularity. In practice, when the curvature of the tip of a notch is large, a notch can be considered sharp and becomes a highly stress-concentrated region. This results to a

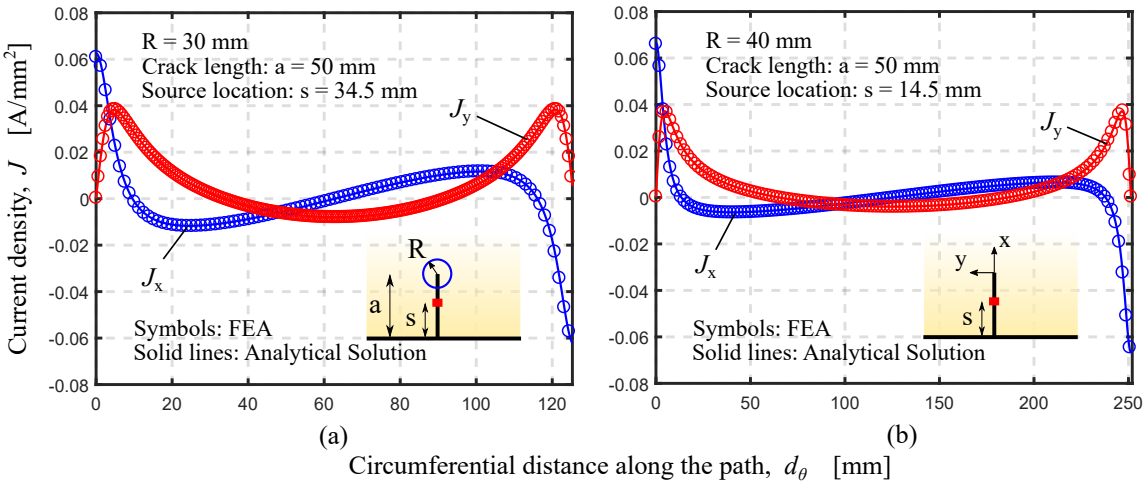

Figure 2.5: Numerical validation of the closed-form analytical solution. Plots of the electric electric current density along the circular path with current sources located at (a) 34.5 mm and (b) 14.5 mm.

significant reduction in the load bearing capacity of the structure, and often induces brittle fracture with a few precursors and a short response time before the failure. Under the cyclic loading, a crack can formulate at the tip of a notch, and it may propagate in a stable manner until the critical condition is reached, and the failure will occur dynamically. Thus, it is important to have a high resolution technique that can detect the damage initiation and propagation near stress concentrators in order to maintain the structures before the catastrophic failure.

To exemplify the application of a CTI material, the foregoing theoretical framework is extended to a finite geometry with a V-notch to examine its capability of damage detection at the vicinity of the V-notch. The foregoing analytical work on finding the closed-form solution for an infinite plate with a single edge crack can be applied to a plate with a V-notch using a proper conformal transformation. Previous work on electrostatic problems of materials featuring CTI [57] takes advantage of *Schwarz Christoffel mapping* (SCM), which provides a method for creating a conformal mapping for any polygonal geometry, to conveniently describe the optimal fiber path in a curvilinear coordinate system. However, field equations from SCM often include several gaussian hypergeometric functions that can

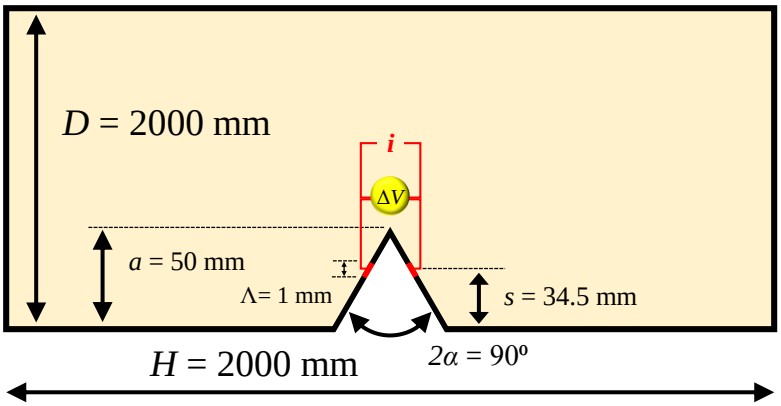

Figure 2.6: Geometry of a V-notch specimen for the numerical study. Finite strips of an unit current source are located 34.5 mm above the bottom edge. Opening angle of the V-notch is 90°.

easily increase the numerical evaluations exponentially. Furthermore, the finiteness in a geometry makes the expression of an analytical solution even more complicated. As a remedy for these practical concerns, this study proposes a numerical method to obtain the fiber orientation that provides the optimal electric conductivity of a given structure and loading condition.

2.4.1 Modeling details

In modeling the geometry of a V-notch specimen, a finite plate with the width, $D = 1000$ mm and the length, $H = 2000$ mm is created. The center of a notch with a depth, $a = 50$ mm and an angle, $2\alpha = 90°$, is located at the middle of the bottom edge. Similar to the crack case, a uniform current is applied at the source strips on the notch surfaces shown in Fig 2.6. The vertical length of source strips, Λ, is 2% of the notch depth, a. The location of the center of source strip, s, is 34.5 mm above the bottom edge. Summary of the geometry and the modeling detail is shown in Fig. 2.6. Same CTI material system used in the crack case was chosen for this study. For the case with an isotropic material, the conductivity in longitudinal direction for the CTI material was used, $k_{iso} = k_f = 400$ S/mm.

2.4.2 Methodology

From the foregoing theoretical framework, it concludes that the optimal fiber orientation is aligned with the field lines in an isotropic material under the identical electrostatic boundary condition. Leveraging on this result, identification of optimal fiber paths of any geometry comes down to solving the field lines of the equivalent problem with an isotropic material. It is worth mentioning that the material property of an isotropic material does not affect the orientation of field lines in a given geometry and boundary condition. Following steps are taken to numerically obtain the optimal fiber orientation of CTI material under the choice of geometry and boundary condition.

1. Run a finite element analysis on the electrostatic problem with an isotropic material under the choice of geometry and boundary condition.

2. Extract the both components of the current density, J_x and J_y, at the integration point of each element.

3. Compute the optimal fiber paths for each element based on the current density information, $\phi = \arctan(J_y/J_x)$.

4. Run a finite element analysis on the equivalent electrostatic problem with an orthotropic constitutive law and choose the user-defined material orientation option with ORIENT subroutine to assign computed optimal fiber orientation for each element.

It is important to notice that the mesh of a given geometry in step 4 should be same as the one used for the analysis with the isotropic material in step 1 since the fiber angle is computed for the specific location of each element. For this study, it was not a problem to keep the same mesh for both the simulations; however, if it is inevitable to regenerate the mesh, then one can use an interpolation technique to estimate the optimal fiber angle for the new element with the given set of optimal fiber angles obtained in the prior simulation with an isotropic material in step 1.

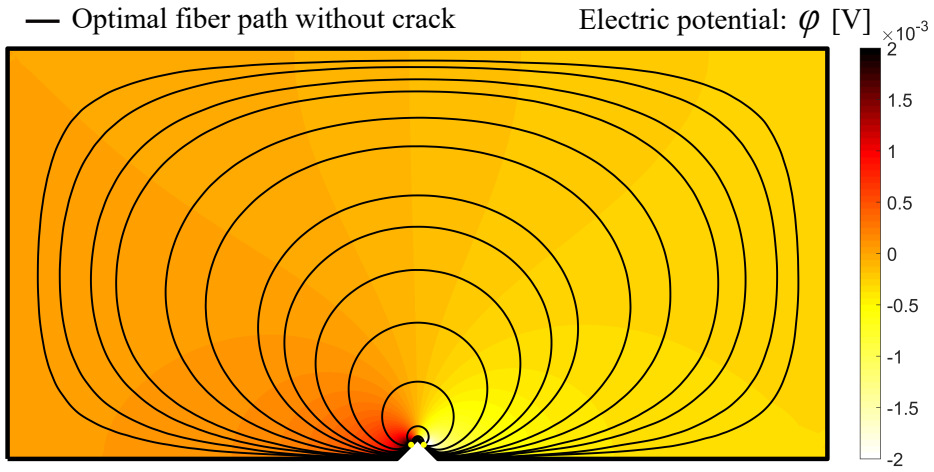

Figure 2.7: Optimal fiber paths visualized onto the solution of electrostatic problem.

2.4.3 Verification

In this section, the electric potential and current density computed with the isotropic material are compared to the ones with the CTI material in which the fiber paths are numerically calculated following the method introduced in the previous section. Visualization of fiber paths and the electric potential field of the CTI material is shown in Fig. 2.7. Leveraging on the fact that the field properties (electric potential and current density) must be identical for both material systems when the conductivity in the longitudinal direction, $k_f = 400$ S/mm is equal to the conductivity of isotropic material, $k_{iso} = 400$ S/mm, the accuracy of the numerical optimal paths is verified.

Figure 2.8(a) shows the comparison on the electric potential along the three circular paths between the isotropic material and optimized CTI material system. As can be noted, the electric potential values obtained in the isotropic material and CTI material system are in a perfect agreement for each path, providing a maximum difference well less than 1%. The circular path with the radius of 22 mm was chosen to investigate the current density for both material systems, and the comparison is shown in Fig. 2.8(b). Similar to electric potential comparison, the current density values obtained from both material systems are in a perfect agreement, providing a maximum difference well below 1%.

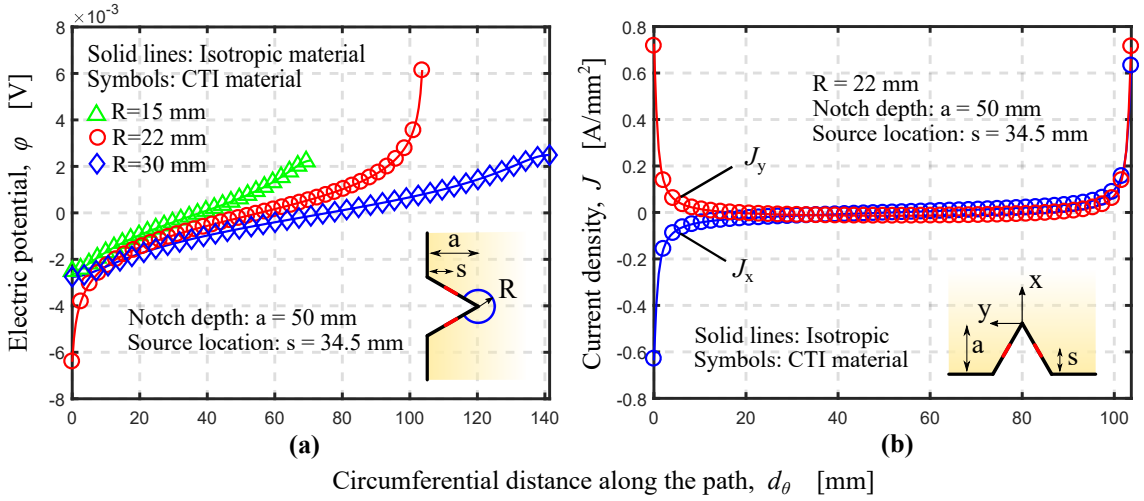

Figure 2.8: Comparison between the solutions to the electrostatic problem with the isotropic material and CTI material system with the optimal fiber orientation. (a) Plot of the electric potential along three circular paths, (b) Plot of the electric current density along the circular path, $R = 22$ mm.

This verification ensures that the preceding numerical method provides an efficient and accurate tool to compute the optimal fiber orientation. It is worth reminding that the this method can easily be extended to a more general and complicated geometry. Once the direction of the field lines of a specified geometry and boundary condition with an isotropic material are obtained, the identification of the optimal fiber paths for CTI system is completed.

2.4.4 Resistance of a CTI system with a crack propagation

In this section, the damage detection capability of the CTI system is investigated and compared to the one with an isotropic material and straight fibers. Two straight fiber cases were chosen for this study: fibers are laid 1) the orthogonal to the direction of a crack propagation and 2) the parallel to the direction of a crack propagation. Material and the Modeling detail for the V-notch specimen follow the same descriptions in the forgoing section. A crack was introduced at the tip of the notch defined by a seam. The length of the crack was ranged from 0 to 20 mm. Optimal fiber path was obtained using the

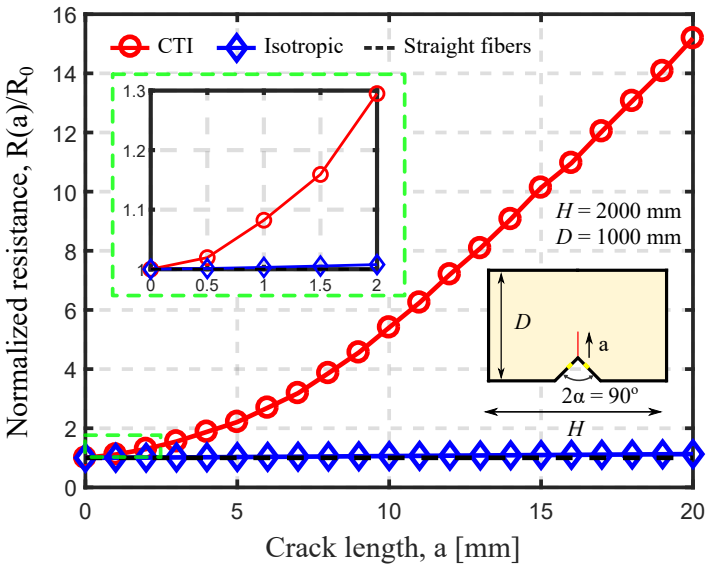

Figure 2.9: Increase in the electrical resistance of the V-notch specimens with three different material systems: 1) CTI, 2) isotropic and 3) orthotropic with straight fiber path. Region of early stage in the crack propagation, ranged from 0 to 2 mm, is magnified.

numerical method discussed in the preceding section and kept same while the crack length was changed. Resistance was computed across the source strips where the uniform current was applied for each crack length.

The comparison on the evolution of resistance from the change in crack length between the CTI material and the isotropic material is shown in Fig. 2.9. As can be noted, the change in the resistance of the CTI material is much more conspicuous compared to the one with isotropic material and the one with the straight fibers. In fact, both the straight fiber cases did not affect the resistance at the source strips because the straight fibers does not complete the closing circuit, and the electric potential at the source strips remains same as the crack propagates. The change in the resistance of the specimen with the isotropic material is negligible compared to the one with CTI material. Thanks to the noticeable change in the resistance, CTI material has an advantage on diagnosing the damage in the structure near the stress concentrator compare to an isotropic material and straight fiber cases.

For brittle and quasi-brittle materials including fiber-reinforced composites, a small propagation of a crack can lead to a dynamic failure and collapse of the structure. Therefore, it is important to have a high resolution in detecting the onset of the crack propagation. As the crack length is increased from 0 to 1 mm, the normalized resistance of the isotropic specimen is only increased by 0.3% whereas the normalized resistance of the CTI specimen is increased by 8.2%. When the crack length is increased to 2 mm, the normalized resistance of the isotropic specimen and the CTI specimen are increased by 0.8% and 29.6%, respectively, from the onset of the crack. This further exhibits the outstanding ability to detect the damage initiation and propagation of a CTI material with an optimal fiber orientation compare to other material systems.

There are two main factors for the CTI material with optimized fiber paths that contribute to the significant increase in the resistance across the source strips when the crack length increases: 1) a breakage of fibers which disconnect the closing circuit from one end of source strips to the other and 2) a deviation of the initial optimal fiber orientation from the updated field lines due to the presence of a crack as shown in Fig. 2.10.

Initially, each fiber behaves as an conductive closed-loop circuit. When the fiber is broken, the current cannot flow anymore along that fiber, and the electric potential is increased due to the high resistance caused by the fiber breakage. As more and more fibers are cut by the crack propagation, it forms a localized region at the vicinity of the notch tip and the crack where the electric potential is accumulated as shown in Fig 2.10 and behaves similar to a capacitor. It can be also noted that the region away from the notch tip and the crack still has a low electrical potential value. This region is where the fibers still form close-loop circuits where the current can flow from the source.

The increase in electric potential across the source strips is further augmented by the increase in the misalignment of the fiber orientation to the field lines in the presence of a crack. This is an unique feature that the CTI material takes advantage over an isotropic material, which automatically adapts to the new field lines for each crack length; therefore, the change in the resistance is minimal. Figure 2.10 depicts the evolution of the change in optimal fiber paths for each crack length and the deviation of the initial optimal fiber placement from them. As can be noted, the deviation becomes enlarged as the crack length

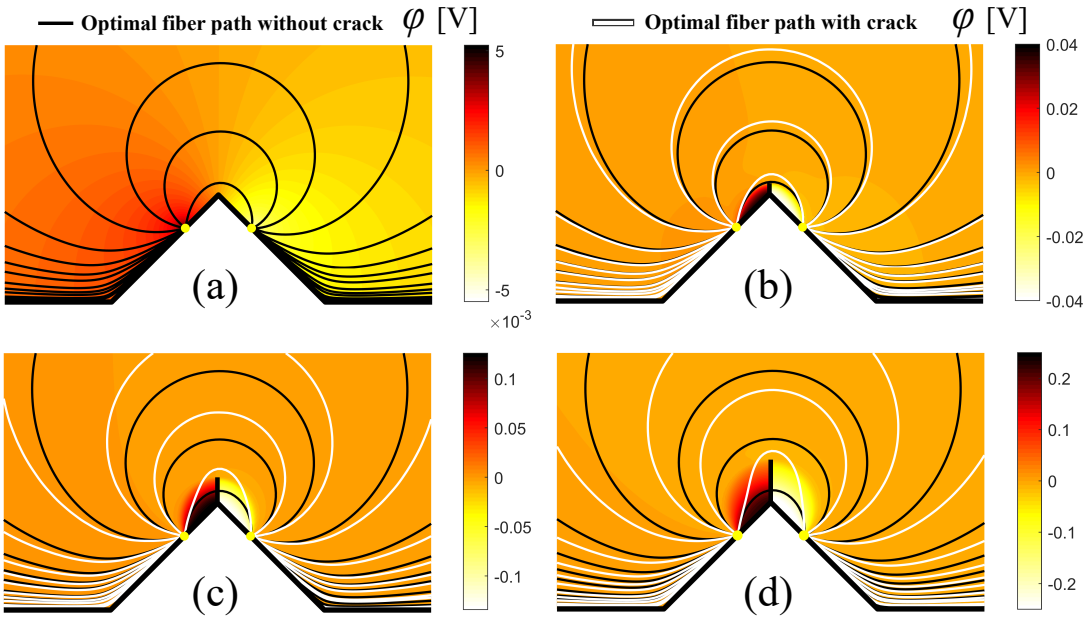

Figure 2.10: Electric potential field solutions to the electrostatic problem on the V-notched specimen with a crack length, (a) $a = 0$ mm, (a) $a = 5$ mm, (a) $a = 12$ mm, (a) $a = 20$ mm located at the tip of V-notch. Fiber path optimized for the conductivity of V-notch with no crack is shown in red and starts to deviate from the true optimum shown in yellow dashed line as the crack is initiated.

is increased, which further contribute to the increase in the electric potential in the whole structure.

2.5 Piezoresistive behavior of CTI: application to health-monitoring

In the last decades, it has been shown that the smart materials, which utilize electrical properties for a sensing capability on the structural health monitoring, are effective to inspect and diagnose the damage or strain field. Early works on the self-monitoring technique of fiber reinforced composites leveraged on the change in the resistivity measure of conductive fibers and showed the promising results on a self-monitoring capability utilizing piezoresistive behavior of fibers under multiple loading conditions [59, 60, 61, 62, 63, 64].

In this section, the piezoresistive behavior of the CTI material is explored and compared to the behavior of a woven composite. Geometry and the boundary condition are same as the ones in the foregoing section, and same optimal fiber path obtained from the electrostatic problem is assigned for the CTI material. Mechanical and piezoresistive properties of an unidirectional fiber-reinforced (UD) composite and a woven composite are selected accordingly to the ones used in the work from Boschetti-de-Fierro et al [63], which nicely characterized the piezoresistive response of both UD and woven matrix-carbon fiber composites under a tension. Material properties of carbon fiber fabric used for each reinforcement type is identical to each other. Summary of mechanical and electrical properties of both fiber-reinforced composites are shown in Table 2.1. The relative change in electrical resistance from the increase in the longitudinal strain is shown in Fig. 2.11. The relative change in electrical resistance is defined as follows:

$$\%\Delta R/R_0 = \frac{R_c - R_0}{R_0} \times 100 \tag{2.31}$$

where R_c is resistance value at each time, and R_0 is the initial resistance value without any deformation.

Table 2.1: Material properties of carbon fiber-reinforced composites with different type of reinforcement

	Mechanical properties				Electrical conductivity	
Reinforcement Type	E_1 [GPa]	E_2 [GPa]	ν_{12}	G_{12} [GPa]	k_1 [S/mm]	k_2 [S/mm]
Unidirectional fiber	64.0	5.7	0.3	3.0	7.7	0.004
Woven	33.2	33.2	0.1	12.77	4.17	4.17

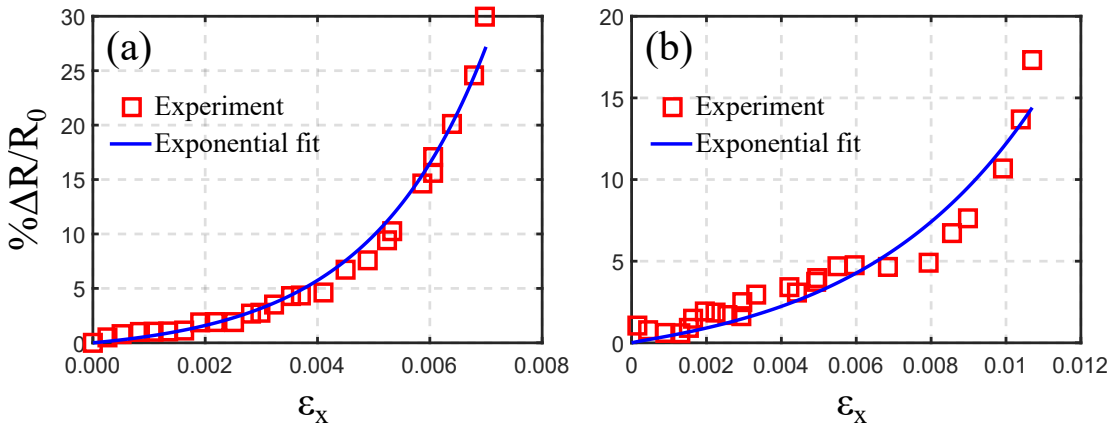

Figure 2.11: Increase in the relative electrical resistance from the increase in longitudinal strain under a tension for (a) unidirectional fiber-reinforced composite and (b) woven composite. Exponential functions were used for characterizing the relation between electrical resistance and longitudinal strain.

2.5.1 Numerical implementation

Leveraging on the fact that the governing equation of the steady-state heat transfer problem is equivalent to the one of electrostatic problem, coupled mechanical and heat transfer analyses were conducted in ABAQUS 6.17 Standard. In this case, temperature field and heat flux are equivalent to potential field and current density, respectively. This choice was made such that the strain dependent conductivity can be assigned to the material property using the subroutine called UMATHT. However, UMATHT does not allow users to access the current strain information during a computation. Therefore, it had to be called in conjunction with another subroutine, USDFLD, which allows users to access field variables such as current strain values at the integration points in each element. For the future users of subroutine USDFLD, selection of the user defined field option in the material module alone does not activate the subroutine, USDFLD. Users need to add an Initial Conditions statement in the correct location of the input file. The temperature and heat flux were computed using 3-node linear displacement and temperature element, CPE3T. A numerical convergence study was performed to determine the size of the mesh that would provide the changes in the maximum temperature value within 1%.

In the process of assigning the piezoresistive behavior of UD and woven carbon fiber composites under tension, the experimental data from Boschetti-de-Fierro et al. [63] were approximated with the following exponential functions:

$$R_{UD} = R_{0,UD}\left(0.99 + 0.01\exp\left(477\langle\varepsilon_1\rangle\right)\right) \tag{2.32}$$

$$R_{woven} = R_{0,W}\left(0.99 + 0.01\exp\left(135.4\langle\varepsilon_1\rangle^{0.86}\right)\right) \tag{2.33}$$

where $R_{0,UD}$ and $R_{0,W}$ are the initial resistance of UD and woven composites, respectively, and ε_1 is a strain in longitudinal direction at each time. Macaulay brackets, $\langle x\rangle = \max(0, x)$, are used for exponents to exclusively take the contribution of positive longitudinal strain. Exponential fitting to the experimental data is shown in Fig 2.11. Changes in the resistance along the transverse direction of UD composite is negligible compared to the one in longitudinal direction. Furthermore, the conductivity in transverse direction is 2000 times

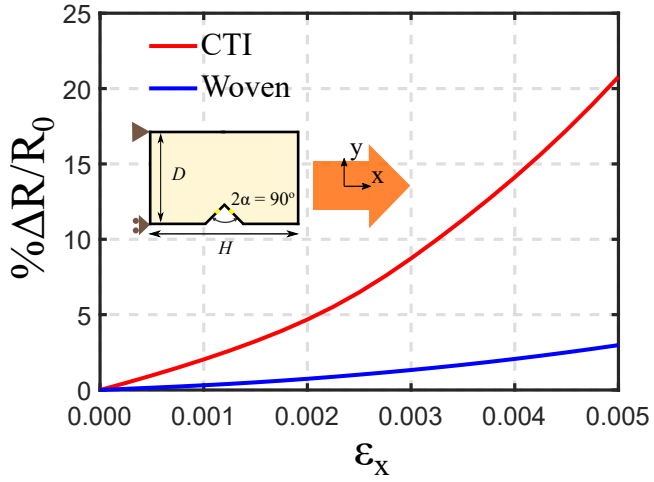

Figure 2.12: Comparison on the relative change in electrical resistance across the source between the CTI material and the woven composite under a longitudinal tension.

lower than the one in longitudinal direction. Therefore, the piezoresistive behavior of UD composites in transverse direction is neglected in the constitutive behavior. For the woven composite, the piezoresistive behavior in both longitudinal and transverse direction are assigned identically. For both types of reinforcement, a resistance change due to a local compression was ignored.

2.5.2 Results and discussion

The comparison on the change of resistance due to the tension between the CTI material with optimized fiber path for the conductivity and the woven composite is shown in Fig. 2.12. As can be noted, the increase in the resistance of CTI material is about 7 times larger. This result indicates that CTI material is more attractive in using piezoresistive behavior to monitor the local strain field near a stress concentrator before the onset of crack propagation. This is an outstanding performance considering that the fiber path is not optimized for magnifying the piezoresistive response under tension.

2.6 Conclusions

This study extended a general theoretical frame work for the exact, closed-form solution on the electrostatic problem with the finite source of an electric current in a CTI material system. Moreover, the numerical method to obtain the optimal fiber paths given any geometry is proposed to exemplify the application of CTI material in a damage detection. Based on the results obtained in this study, the following conclusions can be elaborated:

1. Leveraging on the fact that the fiber paths should align with the field lines of the equivalent electrostatic problems in an isotropic medium to maximize the conductivity, the numerical methods of finding the optimal fiber orientation for any finite geometry is simple, convenient and can easily verified.

2. It is shown that the damage detection capability of CTI media is superior to isotropic and straight fiber material systems thanks to 1) fiber breakage by crack propagation and 2) deviations in an original fiber paths from the updated field lines due to a crack propagation.

3. Furthermore, health monitoring ability of CTI material systems near a stress concentrator utilizing piezoresistive behavior of fiber is outstanding compare to a conventional fiber-reinforcement such as a woven composite. This provides an interesting multi-objective optimization problem to a CTI material system in health monitoring and damage detection application.

Chapter 3

CURVILINEAR TRANSVERSE ISOTROPY IN MECHANICAL PROBLEM: LITERATURE REVIEW

The idea of adding a reinforcement is not so new in the structural engineering. Rebars have been added to the concrete structures to increase the tensile strength. Stringers in aircraft structures prevent the buckling of skin. In contrast to this type of reinforcing application where an additional structural component provides extra support at the weak region, fiber reinforced composite material inherently exhibits the reinforcing feature along the direction of fibers.

The superior specific mechanical properties were the initial driving factor for substituting metal components at the pursuit of lighter aircraft. As Mansfield [65] demonstrated the potential performance gain of curvilinear reinforcements via the concept of neutral hole, further advancement in the reinforcement design of composite materials can optimize the balance between the weight saving and mechanical objective. Despite this fact, limitation in the manufacturing technology discouraged researchers due to the lack of practicality.

In recent years, the advent of Automated Fiber Placement (AFP) and Additive Manufacturing (AM) with continuous fibers have widen the range of design space of composite materials and allowed the production of more sophisticated reinforcement design in a good quality [66, 67, 68]. Thanks to the advancement in manufacturing technology, several works have explored the concept of variable stiffness over a composite structure to attain desired mechanical properties.

Hyer and Charette [69] were the first to investigate the curvilinear fiber reinforcement in the whole structure. They were able to demonstrate the attainment of a superior loading capacity in tension compared to unidirectional composites. Later, they extended their study of curvilinear fiber reinforcement design to achieve a high buckling resistance of composite plates with a central hole [70].

Parnas et al. [71] also used the curilinear fiber reinforcement and varying thickness to reduce the weight of composite laminates under various loading conditions. Both bi-cubic spline functions and bi-cubic NURBS surfaces are used to describe the fiber paths and the thickness of the plate, respectively. Sequential quadratic programming was used in optimizing the composite configuration, and the Tsai-Hill failure criterion [72] was used in constraining the stress distribution in the structure below the critical value.

Somewhat different approach of finding optimal reinforcement design was introduced by Setoodeh et al. [73]. They utilized the lamination parameters to introduce variable stiffness over the structure and minimize the compliance of a composite plate under in-plane and out-of-plane loading conditions. Thanks to the convex nature of lamination parameters, the optimization with the sequential quadratic programming was very efficient and guaranteed to find the global optimum in the objective function. However, it was not so straightforward to retrieve the fiber paths from the distribution of lamination parameters. Further studies from the same authors on the effect of variable stiffness on a flat composite plates succeeded in capturing the post-buckling behavior [74] and examining the in-plane and buckling load under compression [75, 76]. In both studies, the fiber paths were assumed to vary in one-dimension as introduced in [77].

For balanced and symmetric laminates under compression, Nik et al. [78] showed that plates featuring optimized curvilinear reinforcement simultaneously outperform quasi-isotropic laminates in terms of both buckling load and in-plane stiffness. Cho and Rowlands [79, 80] demonstrated the capability of CTI of reducing the stress concentration of perforated media. Further studies on the stress concentration of laminated composite plates were carried out by Honda et al. [81], who later extended their methodology to allow for multi-objective optimization of the structural performance [82].

Recently, Malakhov and Polilov [83] showed a significant reduction in the stress concentration in plates with a central hole by aligning the fibers with the maximum principle stress direction. Akhavan and Ribeiro demonstrated [84] demonstrated that the curvilinear fiber plates provide more flexibility of tuning frequencies and mode shapes compared to straight fibers. Frequencies are sensitive to the path of fiber. In this study, fiber paths are restricted to shifts of reference fiber path defined in linearly varying angles in 1-D as introduced in

[77]. Variation in fiber path can lead to a meaningful change in vibration mode and in natural frequencies.

Zamani et al. [85] investigated the improvement in the failure load under various loading conditions of thin-walled beams. Variable stiffness was induced by means of curvilinear fiber configuration following the paths defined in [77]. Governing equations are derived using the extended Hamilton's Principle, and the extended Galerkin method was used to attain the solution. Optimization study was carried on finding both straight and curvilinear fiber configuration that maximize the failure load under various loading conditions. The sequential quadratic programming was used in the process. Optimization results show that there is a reasonable performance increase in introducing variable stiffness feature in the plate. Extending this work, Haddadpour and Zamani [86] studied the aeroelastic stability improvement of thin-walled composite wings with the variable stiffness resulting from fibers which the angles vary linearly along the span. The result demonstrates that instability speed can be further increased using the variable stiffness idea in the composite wings. Murugan and Friswell [87] further studied the benefits of a curvilinear fiber design on a morphing wing structure. Genetic algorithm was used to obtained the Pareto front for well-balanced design that can simultaneously minimize the in-plane stiffness and maximize out-of-plane stiffness to retain aerodynamic performance. Fiber paths are restricted to shifts of reference fiber path defined in linearly varying angles in 1-D as introduced in [77].

In recent works on the variable stiffness concept, Montemurro and Catapano introduced the multi-scale two-level (MS2L) optimization method on minimizing the compliance [88] and maximizing strength [89] of composite laminates. Their procedure involves two stages: 1) setting up the objective function with point-wise varying laminate polar parameters (PPs) interpolated by B-spline surfaces and 2) retrieving the fiber paths based on the optimal distribution of PPs obtained in the first stage. Fiordilino et al. further improved the method to obtain optimal configurations maximizing buckling loads of the benchmark problems with outstanding results [90]. One of the remarkable advantages of the approach proposed by Montemurro *et al.* of using a set of B-spline surfaces to represent the distribution of the laminate polar parameters over a structure are that it ensures continuity of polar parameters and fiber paths, and it also reduces the number of design variables.

The idea of curvilinear reinforcement extends to the stiffeners on panels. Dang et al. [91] found optimal configuration of stiffener following curvilinear path on panels with cutouts under multiple loading conditions. The similar approach is further extended to the minimization of weight on shells with stiffeners under compression and shear loads [92]. Devarajan et al. [93] employs the isogeometric finite element analysis to investigate the effect of the curvilinear stiffeners on the thermal buckling behavior of plates with complex cutouts.

In the following chapters, a proper numerical method to analyze the mechanical behavior of composite structures featuring CTI is first selected. In this effort, a comparison between the standard numerical methods used in the literature study and the particular choice of numerical method is presented to provide a reason behind the particular choice suitable for analysis on composites exhibiting CTI. Then, the mechanical performances of several different curvilinear fiber reinforcements are presented. The elastic behavior includes a stress concentration and the stiffness of a structure, and the first order failure analysis is performed using a polynomial strength criterion. Lastly, the optimization study is performed to find the superior reinforcement design based on the choice of design objectives.

Chapter 4

NUMERICAL ANALYSIS ON A PLATE WITH A SEMI-CIRCULAR NOTCH FEATURING CTI: ISOGEOMETRIC FRAMEWORK

This chapter includes the work done with the fellow colleague, Kenta Suzuki for his master thesis [94, 95].

Isogeometric Analysis introduced by Hughes et al. [1] is a trending numerical methods in the world of computational mechanics. This new method utilizes spline as a basis function inspired from Computer Aid Design (CAD) in Finite Element Method (FEM), providing a novel framework for solving governing equations in various physics and engineering disciplines: e.g. fluid, solids and structures.

Interestingly enough, FEM was introduced in the field of engineering around 1950s and 1960s [96]. Aerospace engineering was at the forefront of developing this numerical method to solve partial differential equations that describe dynamic and aeroelastic problems. At the present time, its use is widespread throughout the computational mechanics and all the engineering disciplines. On the other side, CAD was introduced later in 1970s and 1980s [97]. Although the geometrical description is important in FEM, CAD had a much later origin. This gives us an insight on the discrepancy in the geometric representation between them. Unlike the FEM elements in which the basis functions are defined with polynomial functions, CAD relies on the splines, piece-wise polynomials, to represent a geometry.

Today, it is common to generate the geometry and mesh using a CAD software and import them into a FEM program to carry on the analysis. According to Hughes et al. [1], 80% of the time spent in overall analysis process is devoted to the mesh generation in the automotive, aerospace and ship building industries. In many circumstances, modeling a geometry and a mesh of the full structure of a vehicle can take several months due to the discrepancy in CAD and FEM. This can disrupt the productivity since the design changes can be made on a daily basis. Furthermore, the analysis process is iterative and often

requires mesh refinements. In most circumstances, there is no linkage between CAD and FEM software that allows communication between them, and this causes the difficulty in an interactive process.

Another problem that rises from the geometric approximation in FEM is accuracy. Thin-shell structures are extremely sensitive to the imperfection in the geometry. Buckling load of a geometrically perfect cylindrical shell can be substantially weakened by embedding geometric imperfections [1]. Not restricted to structural problems, the quality of mesh generation is also crucial to capture the boundary layer in computational fluid dynamics and provide accurate computation of quantities such as pressure, velocities and friction coefficient.

In conclusion, the motivation of developing IGA is to reduce the cost of mesh generation and prevent the inherent accuracy problem from the geometric representation in standard FEM. Moreover, it can serve as a channel that will allow the communication between FEM and CAD software during mesh refinement leading to a more efficient and proficient design tool in the engineering field.

The word "Isogeometric" in IGA refers to the "exact (Iso-)" geometric representation during the analysis. This is done by borrowing the identical parametric definition of the geometry model for the analysis. In other words, same basis functions that defines the geometry are used as shape functions of the element during the analysis. Therefore, IGA mesh from the definition grants the exact CAD geometry regardless of mesh size. Exact representation of a geometry provides the solutions to the preceding problems. First, it reduces the cost of mesh generation. Geometry modeling defined by splines becomes part of mesh generation, so there is no need for a step transforming the geometry to the analysis-suitable mesh. Moreover, modifications in the geometry are automatically updated in the mesh; therefore, there is no need for a mesh re-generation. These advantages significantly reduces the cost of mesh generation and modification process in the design. Second, the exact geometric representation means there is no compromise in the geometric accuracy; therefore, IGA can prevent the inherent accuracy problem from the approximate geometric representation in standard FEM. Lastly, IGA can serve as a channel that will allow the smooth communication between analysis and CAD software leading to a more efficient and

proficient design tool in the engineering field.

In addition to those advantages, it is convenient to control the continuity between spline elements by the implementation of order elevation [1, 9]. This is in contrast to standard FEA which always provides C^0 continuity between elements. Flexibility in controlling the continuity of spline basis functions allows to implement high-order deformation plate theories without any shear correction factor such as an inverse tangent shear deformation theory demonstrated by Thai et al. [98]. Furthermore, higher continuity in spline basis functions can efficiently prevent shear locking as highlighted by Da Veiga et al. [99] and Valizadeh et al. [100].

Producing an accurate field solution in a numerical analysis of a structure requires a fine mesh refinement near the regions of high stress concentration. For a structure with an uniform stiffness, a stress concentration generally occurs in the presence of geometric features such as holes and notches given that the loading and boundary conditions are simple. For a structure with a variable stiffness, a stress concentration can occur at the location of high gradient in the material properties, which can be realized with a high radius of curvature in fiber reinforcement. To capture this phenomenon, standard FEM requires several levels of mesh refinements. This may not be the case for the IGA mesh with higher inter-continuity between elements. In this study, investigation on the effect of high inter-continuity between elements and the effect of variation diminishing property (i.e. the maximum number of intersections that a plane has with a spline curve is equal to the number of intersections that the plane has with the control polygon) to the convergence is carried on by comparing to numerical performance provided by a standard FEM mesh.

In this work, representation of curvilinear anisotropy into an element stiffness matrix is introduced following the IGA framework defined with NURBS (Non-Uniform Rational B-Spline). Then, its performance is examined by comparing it to standard FEA in terms of error of the stress measured in L^2-norm. The performance of IGA is compared to the performance of a standard FEA in terms of computational efficiency by measuring the time consumption and accuracy by computing the error in the stress field using the L^2-norm. Then, the exceptional mechanical behavior of curvilinear fiber composites is explored in terms of in-plane stiffness and stress concentration using a plate weakened by a semi-circular

notch as a case study. Finally, the optimal fiber paths minimizing the stress concentration factor and the Tsai-Wu failure index is identified using the Sequential Quadratic Programming (SQP). Similarly, the fiber paths that minimize the maximum principal stress and maximize stiffness of a more complex structure are found.

4.1 Mathematical background

In the standard FEA framework, Lagrangian basis functions define the physical space [101]. On the contrary, in the IGA framework, spline functions, such as Non-Uniform Rational B-Spline basis functions, define the parameter space [1, 9]. Thus, in the following sections, a brief introduction on NURBS is provided. Then, the method to impose continuous fibers following curvilinear paths under the isogeometric framework is introduced.

4.1.1 B-spline parametric space

NURBS are extension of B-splines. A knot vector is non-decreasing sequence of real number that forms a set of coordinates in the B-spline parametric space. Let $\Xi = [\xi_1, \xi_2, ..., \xi_{n+p+1}]$ be the knot vector, then ξ_i is the ith knot where i is the knot index, $i = 1, 2, ..., n + p + i$. p is the degree of polynomial, and n is the number of B-spline basis functions. Uniform knot vectors have equally spaced knots; otherwise knot vectors are said to be non-uniform if knots are spaced unequally. Knots that are present more than one are referred to as repeated knots. If the first and last knots are repeated $p+1$ times, then the corresponding knot vector is said to be open. Open knots are widely used in the CAD due to their interpolatory at the ends of a curve or corners of patches in a higher dimension. However, B-spline geometry is not interpolatory in the interior knots. In contrast, all the nodes in FEM elements are interpolatory, which is the inherent trait of a polynomial approximation.

4.1.2 B-spline basis function

B-spline basis functions can be calculated in many different ways. Most convenient way to compute B-spline basis function is to use recurrence formula [102] in Eq. 4.2. This can be obtained employing the divided difference in the definition of the basis functions [103].

Recurrence formula builds from zeroth degree ($p = 0$) piece-wise constant, which is defined in Eq. 4.1.

$$N_{i,0}(\xi) = \begin{cases} 1 & \text{if} \quad \xi \leq \xi < \xi_{i+1} \\ 0 & \text{otherwise.} \end{cases} \tag{4.1}$$

For $p = 1, 2, 3, ...$, B-spline basis function is recursively defined as follows:

$$N_{i,p}(\xi) = \frac{\xi - \xi_i}{\xi_{i+p} - \xi_i} N_{i,p-1}(\xi) + \frac{\xi_{i+p+1} - \xi}{\xi_{i+p+1} - \xi_{i+1}} N_{i+1,p-1}(\xi) \tag{4.2}$$

Different order of basis functions with a uniform knot vector are shown in Fig. 4.1. As can be noted, the basis functions with degree $p = 0$ and $p = 1$ are equivalent compare to a standard FEM basis function of piece-wise constant and linear elements.

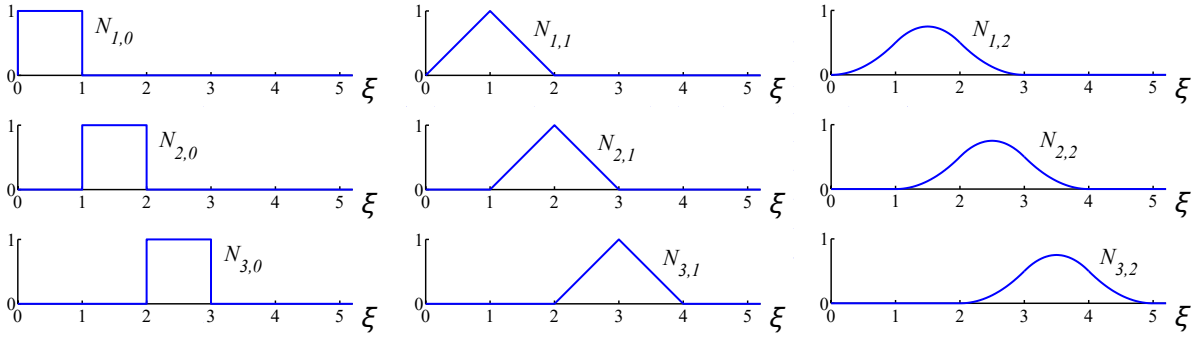

Figure 4.1: Basis functions of degree 0, 1, 2. The knot vector is uniform (image from [1]).

A multiplicity of knots is related to the continuity of the geometry. Basis functions of degree p obtains C^{p-1} continuity, and it decreases by k as a knot is repeated k-times. An example of a quadratic basis functions with open knot vector is illustrated in Fig. 4.2a. As it can be noted, C^1-continuity is attained everywhere except at $\xi = 4$ where it's C^0-continuous due to a repetition.

Important properties of B-spline basis function are listed below:

1. Partition of unity,

$$\sum_{i=1}^{n} N_{i,p}(\xi) = 1 \tag{4.3}$$

2. Each $N_{i,p}(\xi)$ has a compact support meaning that it is zero outside of the interval, $[\xi_i, \xi_{i+p+1}]$.

3. All the basis functions are non-negative.

Derivative of B-spline basis function can also be computed recursively following Eq. 4.4, which can be proved by induction [102].

$$N'_{i,p}(\xi) = \frac{p}{\xi_{i+p} - \xi_i} N_{i,p-1}(\xi) - \frac{p}{\xi_{i+p+1} - \xi_{i+1}} N_{i+1,p-1}(\xi) \tag{4.4}$$

B-spline curve of a degree, p is defined as:

$$C(\xi) = \sum_{i=1}^{n} N_{i,p}(\xi) B_i \tag{4.5}$$

where the coefficients, B_i are called *control points*. The B-spline curve constructed with previous knot vector example is show in Fig. 4.2b. An affine transformation such as translation, scale, shear, and rotation can be applied to the curve by transforming the control points.

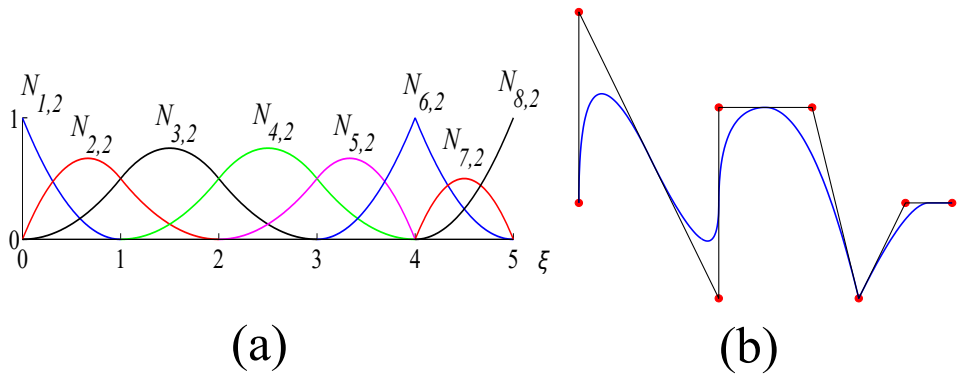

Figure 4.2: (a) Basis functions of degree 2 for a knot vector: $\Xi = \{0, 0, 0, 1, 2, 3, 4, 4, 5, 5, 5\}$, (B) B-spline curve with the corresponding knot vector (image from [1]).

4.1.3 Refinement methods

Knot insertion

Knots can be inserted into knot vectors without modifying the curve geometrically and parametrically. This process is analogous to h-refinement in a standard FEM. Given a knot vector $\Xi = [\xi_1, \xi_2, ..., \xi_{n+p+1}]$, let $\bar{\xi} \in [\xi_k, \xi_{k+1}]$ be inserted. The $n+1$ basis functions can be computed from recursion formula given in Eq. 4.1 and 4.2. The $n+1$ control points, $\bar{B}_i$, are placed to conserve the curve geometrically and parametrically from the original n control points, B_i, as follows:

$$\bar{B}_i = \alpha_i B_i + (1 - \alpha_i) B_{i-1} \tag{4.6}$$

where

$$\alpha_i = \begin{cases} 1, & 1 \leq i \leq k-p \\ \frac{\bar{\xi} - \xi_i}{\xi_{i+p} - \xi_i}, & k-p+1 \leq i \leq k, \\ 0, & k+1 \leq i \leq n+p+2. \end{cases} \tag{4.7}$$

This relation can be proven by induction using the property of a divided difference [104].

Degree elevation

The Degree of polynomial in basis functions can be increased without modifying the curve geometrically and parametrically. Multiplicity of each distinct knot increases to restrain the continuity of the curve. Number of new control points added depends on multiplicity of the original knots. This process of increasing the degree of polynomial is analogous to p-refinement in a standard FEM.

K refinement

In IGA, a combination of knot insertion and degree elevation can be applied to refine a mesh. It is worth to notice that the order of these two processes does not commute. This concept seems a little ambiguous; however, it will be much clear with the following example.

Given a open knot vector, $\Xi = [0, 0, 1, 1]$, and the associated linear basis functions, lets first insert the knots, $\xi_1 = 1/3$ and $\xi_2 = 2/3$. The new knot vector becomes $\Xi = [0, 0, \frac{1}{3}, \frac{2}{3}, 1, 1]$. The order of the continuity is maintained as C^0. In the next step, the degree elevation is applied such that $p = 2$. Resultant knot vector is $\Xi = [0, 0, 0, \frac{1}{3}, \frac{1}{3}, \frac{2}{3}, \frac{2}{3}, 1, 1, 1]$. Each unique knot value is repeated to preserve the C^0-continuity, and the total number of knots are 10. Now, lets flip the order of refinement process and start with the original knot vector, $\Xi = [0, 0, 1, 1]$. After a degree elevation, $\Xi = [0, 0, 0, 1, 1, 1]$ and $p = 2$. Lastly, $\xi_1 = 1/3$ and $\xi_2 = 2/3$ are inserted to the new knot vector, resulting $\Xi = [0, 0, 0, \frac{1}{3}, \frac{2}{3}, 1, 1, 1]$ as a final product with C^1-continuity for the internal knots, and the total number of knots is 8. The geometry and parametrization of each curve obtained from each procedure are identical. However, the latter case provides advantage over the first by providing a higher interior continuity (smoother derivative) with the smaller number of knots (less basis functions). For this reason, latter refinement process referred to k-refinement.

4.1.4 Rational B-spline

In this section, more general way to represent the geometry will be introduced by defining a rational B-spline. It can be shown that the polynomials cannot exactly represent the conic sections such as an ellipse, a parabola, and a hyperbola. These curves can be precisely represented with rational functions.

A NURBS curve with the degree p is defined as:

$$C(\xi) = \frac{\sum_{i=1}^{n} N_{i,p}(\xi) w_i B_i}{\sum_{\hat{i}=1}^{n} N_{\hat{i},p}(\xi) w_{\hat{i}}} \tag{4.8}$$

where $N_{i,p}$ is pth-degree B-spline basis function, w_i is a associated weight, and B_i is a corresponding control point. Rational basis function, $R_i^p(\xi)$, can be defined as:

$$R_i^p(\xi) = \frac{N_{i,p}(\xi) w_i}{\sum_{\hat{i}=1}^{n} N_{\hat{i},p}(\xi) w_{\hat{i}}} \tag{4.9}$$

This allows to rewrite a NURBS curve as:

$$C(\xi) = \sum_{i=1}^{n} R_i^p(\xi) B_i \tag{4.10}$$

A NURBS curve can be interpreted as a projection of four-dimensional B-spline curve to the hyperplane ($W = 1$) [102]. Given a point, $B = (x, y, z)$, in three-dimensional Euclidean space, it can be transformed to the 4-tuple with a weight, W, as fourth quantity. This results $B^w = (wx, wy, wz, w) = (X, Y, Z, W)$. By introducing a perspective mapping, H at the center of the origin, the relation between B and B^w can be established as follows:

$$B = H\{B^w\} = H\{(X, Y, Z, W)\} = \begin{cases} \left(\frac{X}{W}, \frac{Y}{W}, \frac{Z}{W}\right) & \text{if } W \neq 0 \\ (X, Y, Z) & \text{if } W = 0 \end{cases} \tag{4.11}$$

Then, a four-dimensional B-spline curve is defined as:

$$C^w(\xi) = \sum_{i=1}^{n} R_{i,p}(\xi) B_i^w \tag{4.12}$$

A three-dimensional NURBS can be computed by employing the perspective map, H, to $C^w(\xi)$. This is illustrated in Fig. 4.3.

$$C(\xi) = H\{C^w(\xi)\} \tag{4.13}$$

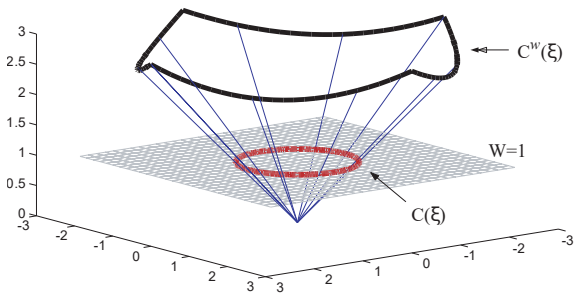

Figure 4.3: Projection of a three-dimensional B-spline curve, $C^w(\xi)$ on the hyperplane, $W = 1$ to form a two-dimensional rational B-spline curve, $C(\xi)$ (image from [1]).

Given a control net, $\{B_{i,j}\}$ where indices, $i \in [1, n]$ and $j \in [1, m]$, and knot vectors, $\Xi = [\eta_1, \eta_2, ..., \eta_{m+q+1}]$ and $\eta = [\eta_1, \eta_2, ..., \eta_{m+q+1}]$, a NURBS surface is defined by a tensor product:

$$R^{p,q}_{i,j}(\xi, \eta) = \frac{N_{i,p}(\xi) M_{j,q}(\eta) w_{i,j}}{\sum_{\hat{i}=1}^{n} \sum_{\hat{j}=1}^{m} N_{\hat{i},p}(\xi) M_{\hat{j},q}(\eta) w_{\hat{i},\hat{j}}} \tag{4.14}$$

$$S(\xi, \eta) = \sum_{i=1}^{n} \sum_{j=1}^{m} R^{p,q}_{i,j}(\xi, \eta) B_{i,j} \tag{4.15}$$

A NURBS solid can be defined similarly by a tensor product with an additional knot vector, and the corresponding control points are three-dimensional object.

4.1.5 Derivative of NURBS

Starting from the derivative of B-Splines, the derivative of NURBS functions simply follow the quotient rule such that:

$$\frac{d}{d\xi} R^{p}_{i}(\xi) = \omega_i \frac{W(\xi) N'_{i,p}(\xi) - W'(\xi) N_{i,p}(\xi)}{[W(\xi)]^2}, \tag{4.16}$$

where

$$W'(\xi) = \sum_{\hat{i}=1}^{n} N'_{\hat{i},p}(\xi) \omega_{\hat{i}}. \tag{4.17}$$

Further properties and techniques for B-Splines and NURBS can be found in [103, 105, 106, 107] and [108, 109, 110, 111], respectively. For detailed theoretical framework and the implementation in IGA, the reader is referred to Hughes et al. [1, 9].

4.1.6 Refinements in NURBS

Knot insertions and degree elevations used for B-splines can be applied with similar manner since NURBS can be expressed as a weighed B-splines. Weight values of control points for a NURBS are not necessarily equal to one; therefore, control points need to be transformed to projective coordinate system before applying the refinement methods. Once a new set of control points are computed in projective coordinate system, they can be transformed back to physical coordinate system.

4.1.7 Curvilinear fiber description for simple optimization studies

Commonly, the depiction of curvilinear fiber paths involves assigning a constant tangent vector to each segment and treating the orientation of each segment as a variable within the parameter space [69, 70, 79, 80]. While this approach offers a comprehensive framework for defining potential fiber arrangements, it can easily lead to a substantial rise in computational expenses due to the extensive number of design variables (equivalent to the count of elements). Conversely, certain investigations [73, 88, 89, 90] have pursued optimization to identify the optimal distribution of mechanical parameters, such as lamination and polar parameters. These methodologies also yield promising outcomes, despite they necessitate a secondary step to recover the corresponding fiber paths aligned with the distribution established in the initial phase. In order to limit the number of design variables to a reasonable value while retaining the desired space of fiber configurations, a simplified approach using the following functions are proposed:

1. 5^{th}-order complete polynomials proposed in [81, 82]

2. Himmelblau's polynomials

A level-set function [81, 82] is used to illustrate a subset of potential fiber arrangements within the selected domain. This approach additionally guarantees the following important attributes for manufacturability: 1) the smooth continuation of fiber trajectories, and 2) the avoidance of any intersections among fibers. Consequently, in this study, the curvilinear fiber pathways are described utilizing either 5th-order complete polynomials or Himmelblau's polynomials, which mirror the form of Himmelblau's function. These two polynomial level-set functions are defined in Eq. 4.18 and Eq. 4.19, respectively.

$$\begin{aligned} f(x,y) = C_{00} &+ C_{10}x + C_{01}y + C_{20}x^2 + C_{11}xy + C_{02}y^2 \\ &+ C_{30}x^3 + C_{21}x^2y + C_{12}xy^2 + C_{03}y^3 \\ &+ C_{40}x^4 + C_{31}x^3y + C_{22}x^2y^2 + C_{13}xy^3 + C_{04}y^4 \\ &+ C_{50}x^5 + C_{41}x^4y + C_{32}x^3y^2 + C_{23}x^2y^3 + C_{14}xy^4 + C_{05}y^5, \end{aligned} \tag{4.18}$$

$$f(x,y) = (C_1x^2 + C_2y - C_3)^3 + (C_4x + C_5y^2 - C_6)^3 \tag{4.19}$$

The coefficients, C in each level-set functions are the design variables that determine the fiber paths over the two-dimensional structure. The fiber orientations θ are calculated by partially differentiating the level set function of Eq. (4.18) and (4.19) with respect to x and y as:

$$\theta(x,y) = \tan^{-1}\left(-\frac{\partial f/\partial x}{\partial f/\partial y}\right) \tag{4.20}$$

4.1.8 Element implementation of the elastic behavior for CTI materials

In finite element framework, each element need to consider the local fiber orientation at each integration point to properly compute the elemental stiffness matrix. The constitutive relations for a linear elastic problem can be expressed as:

$$\{F\} = [K]\{d\} \tag{4.21}$$

where $\{F\}$, $\{d\}$, and $[K]$ are the loading vector, the displacement vector, and the global stiffness matrix, respectively. Then, the element stiffness matrix in the physical domain $\Omega^{(e)}$ can be written in the form:

$$[K]^{(e)} = \int_{\Omega^{(e)}} [B]^T [\overline{C}]^{(\theta)} [B]\, d\Omega^{(e)}, \tag{4.22}$$

where $[B]$ is the strain-displacement matrix generated from the NURBS basis functions, and

$$[\overline{C}]^{(\theta)} = [T_\sigma^{-1}(\theta)][C][T_\epsilon(\theta)], \tag{4.23}$$

where $[T_\sigma^{-1}(\theta)]$ and $[T_\epsilon^{-1}(\theta)]$ are transformation matrices for the stress and strain, respectively, and $[C]$ is the in-plane stiffness coefficients matrix depending on three engineering moduli (E_1, E_2, and G_{12}), and the Poisson's ratio (ν_{12}) [112, 113]. Then, the element

stiffness is calculated by Gauss quadrature such that:

$$[K]^{(e)} = \sum_{m=1}^{N_p} w_{\tilde{\xi}_m} w_{\tilde{\eta}_m} [B_m]^T [\overline{C_m}]^{(\theta_m)} [B_m] J_m, \tag{4.24}$$

where N_p is the number of integration points, $w_{\tilde{\xi}_m}$ and $w_{\tilde{\eta}_m}$ are the corresponding weighs for the each direction, and J_m is the determinant of the Jacobian which maps from physical space to parent space. Detailed derivation and calculation of the element stiffness in the isogeometric framework can be found in [114].

In prior research [69, 70, 81, 82, 79, 80], the investigation of CTI media involved the utilization of a consistent constitutive relationship for the integration points within each element as depicted in Fig. 4.4. This means that $\theta = \theta^{(n_e)}$ where n_e is an element number, i.e., $[K]^{(e)} = [K^{(e)}\{\theta^{(n_e)}\}]^{(e)}$. Conversely, in this study, a constitutive relationship varies depending on the position of integration points within the element when calculating the element stiffness matrix, denoted as $\theta = \theta(x, y)$, where x and y are the coordinates of the integration points. i.e., $[K]^{(e)} = [K\{\theta(x, y)\}]^{(e)}$ [94]. In this way, the effects of the gradient in fiber curvature is implemented in the calculation of the element stiffness.

4.2 Optimization method

4.2.1 Sequential quadratic programming method

For the optimization study, Sequential Quadratic Programming (SQP) method is used assuming that the object function is twice differentiable. It enables to achieve a rate of convergence using 2^{nd}-order derivatives of Lagrange polynomial [115, 116].

In this work, the SQP utilizes the Constrained Steepest-Descent (CSD) approach through two primary steps: 1) establishing the Quadratic Programming (QP) subproblem, and 2) implementing a line search algorithm. Further detail on this method is provided in in [115, 116].

4.2.2 Optimal fiber design problem

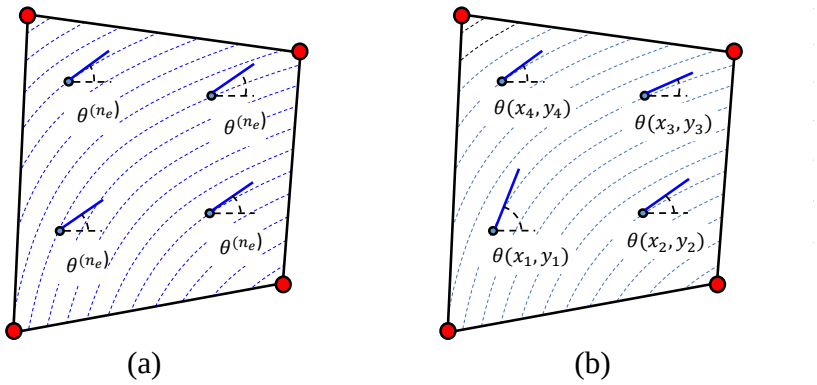

Figure 4.4: Schematic representation of 4-node, isoparametric, quadrilateral element with material orientations assigned to each integration point. As can be noted, fiber orientations are assigned as constant in previous works: (a). In this work, the fiber orientation depends on the location of integration points during the computation of element stiffness matrix: (b) (image from [94, 95]).

The optimization study aims to derive the optimal curvilinear fiber paths that yield favorable mechanical behaviors (specifically, low stress concentration, minimal maximum principal stress, low Tsai-wu failure index, and high structural stiffness). Therefore, considering the objective function F, which fine-tunes the fiber paths to enhance one of the mentioned characteristics, and assuming it is a twice differentiable nonlinear function, the formulation of the optimal design problem is as follows:

Minimize

$$F(\mathbf{C}), \tag{4.25}$$

where $\mathbf{C} \in \mathbb{R}$ is the coefficient vector of the level-set functions defined in Eq. (4.18) and (4.19). Thus, the objective functions are subject to the fiber orientations in Eq. (4.20). In this study, the SQP method implemented in the MATLAB environment is performed by utilizing the built-in function called *fmincon* with an option of *SQP* algorithm [117].

4.3 Results and discussion

This section involves the application of IGA to model fiber-reinforced semi-circular notched plates using NURBS functions. The IGA solver, based on [114], is adapted to MATLAB for simulating orthotropic media. Additionally, Finite element approach is employed for studying semi-circular notched plates with various fiber configurations. The FEA solver is developed within the MATLAB environment and validated against the analytical solution for an infinite plate containing a circular hole. The accuracy of both IGA and FEA is confirmed by assessing the convergence rates from the simulation of an elastic, isotropic plate as shown in Fig. 4.5. Stress errors, computed using L2-norm, are plotted against the maximum diagonal length within the mesh using a double-logarithmic scale. The slopes observed in Fig. 4.6 are both approximately equal to 2 for the quadratic element, aligning precisely with the theoretical values [9].

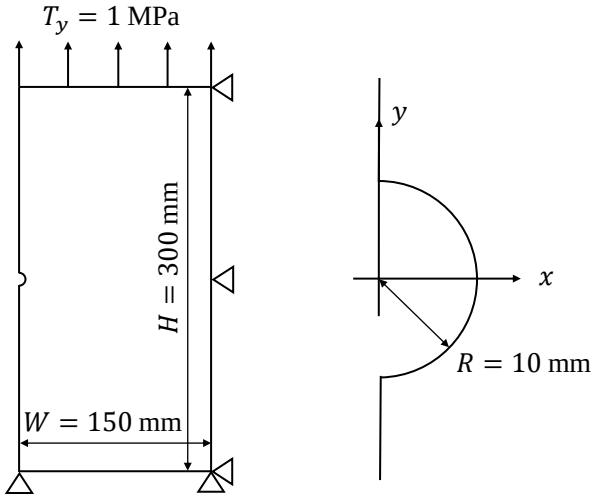

Figure 4.5: Case I: Elastic plate featuring curvilinear transverse isotropy weakened by a 10-mm semi-circular hole notch (image from [95]).

4.3.1 Problem setup

Stress analysis of a plate with a semi-circular notch is carried out using two methods: NURBS-based IGA and classical FEA, both assuming linear elastic behavior, as shown in

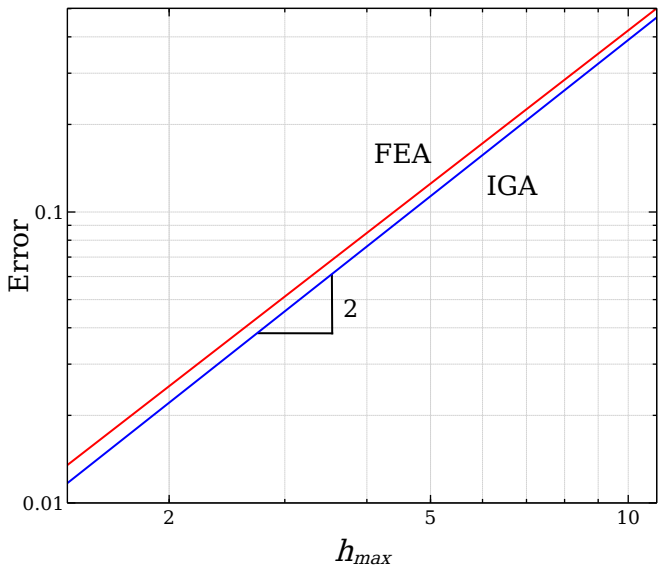

Figure 4.6: Error measured in L^2-norm of the stress against the maximum diagonal length found in the mesh h_{max} (image from [95]).

Fig. 4.5. The plate is subjected to a uniform tension of $T_y = 1$ MPa along its upper edge and is assumed to experience plane stress conditions. It is constrained along its bottom edge and right-hand side edge in the y- and x-directions, respectively. In the IGA simulations, the elastic plate is represented using quadratic NURBS basis functions, utilizing two knot vectors $\boldsymbol{\Xi} = [0, 0, 0, 0.25, 0.5, 0.5, 0.75, 1, 1, 1]$ and $\boldsymbol{H} = [0, 0, 0, 1, 1, 1]$. Mesh refinement is achieved through knot insertion [1, 9]. For conventional FEA, simulations utilize 9-node quadrilateral elements (Q9), employing the same node coordinates as in IGA to ensure a fair convergence comparison. The semi-circular notched plate with several fiber configurations is examined considering the following properties:

1. Stress concentration factor K_t:

$$K_t = \sigma_y^{max}/T_y, \quad \sigma_y^{max}\text{: Maximum longitudinal stress found in the body,} \tag{4.26}$$

2. Average in-plane stiffness $\bar{K}$:

$$\bar{K} = \frac{P_{tot}}{\bar{v}}, \quad \text{with} \quad P_{tot} = \int_0^L \sigma_{yy} d\,x \quad \text{and} \quad \bar{v} = \frac{1}{L}\int_0^L v d\,x, \tag{4.27}$$

where σ_{yy} and v are the longitudinal stress and displacement along the top edge, respectively, and L is the length of the top edge.

3. Tsai-Wu failure index Φ assuming Transverse Isotropy under plane-stress condition [118]:

$$\Phi = F_1\sigma_1 + F_2\sigma_2 + F_{11}\sigma_1^2 + F_{22}\sigma_2^2 + F_{66}\tau_{12}^2 + 2F_{12}\sigma_1\sigma_2, \tag{4.28}$$

where

$$\begin{aligned} F_1 &= \frac{1}{\sigma_{1t}^f} - \frac{1}{\sigma_{1c}^f}, \qquad F_2 = \frac{1}{\sigma_{2t}^f} - \frac{1}{\sigma_{2c}^f}, \qquad F_{66} = \frac{1}{\tau_{12}^f}, \\ F_{11} &= \frac{1}{\sigma_{1t}^f\sigma_{1c}^f}, \qquad F_{22} = \frac{1}{\sigma_{2t}^f\sigma_{2c}^f}, \qquad F_{12} = -\frac{1}{2}\sqrt{F_{11}F_{22}}. \end{aligned} \tag{4.29}$$

The choice of this criterion is motivated by its effectiveness and accuracy in capturing the failure condition of composite laminates featuring smooth or slightly notched surfaces. However, for more complex structural configurations and loading conditions, the emergence of large Fracture Process Zones (FPZs) can lead to significant size effects. This is typically the case of structures featuring sharp notches and other stress raisers. In such a case, a quasibrittle fracture mechanics framework should be preferred over a stress-based failure criterion [119, 120, 121, 122, 123].

All the required material properties such as longitudinal and transverse elastic moduli E_1 and E_2, shear modulus G_{12}, Poisson's ratio ν_{12}, and the ply strengths: σ_{1t}^f, σ_{1c}^f, which are tensile and compressive strengths in the fiber direction, σ_{2t}^f, σ_{2c}^f, which are tensile and compressive strengths perpendicular to the fiber directions, and τ_{12}^f, that is shear strength are respectively assigned and tabulated in Table 4.1.

Table 4.1: Elastic material properties

Symbol		Unit	Property
E_1	181	GPa	Longitudinal modulus
E_2	10.3	GPa	Transverse modulus
G_{12}	7.17	GPa	Shear modulus
ν_{12}	0.28	-	Poisson's ratio
σ_{1t}^f	1500	MPa	Longitudinal strength in tension
σ_{1c}^f	1500	MPa	Longitudinal strength in compression
σ_{2t}^f	40	MPa	Transverse strength in tension
σ_{2c}^f	246	MPa	Transverse strength in compression
σ_{12}^f	68	MPa	Shear strength

4.3.2 Initial fiber configurations investigated

In this work, four distinct fiber arrangements are explored, as outlined in Fig. 4.7: a) traditional longitudinal fibers in straight paths, b) conventional transverse fibers in straight paths, c) concentric fibers aligned along a semi-circular notch, and d) curvilinear fibers following the holomorphic path described by the conformal mapping detailed in [124]. The four fiber orientations described with reference to the global coordinate system are defined as follows:

(a) Conventional longitudinal straight fibers: $\theta(x, y) = \pi/2$,

(b) Conventional transverse straight fibers: $\theta(x, y) = 0$,

(c) Concentric fibers following the semi-circular hole:

$$\theta(x, y) = \frac{\pi}{2} + \cos^{-1}\frac{x}{a}, \quad a = \sqrt{x^2 + y^2},$$

(d) Curvilinear fibers following the holomorphic function presented in [124]:

$$\theta(x, y) = \tan^{-1}\left[\frac{1 + \frac{R^2}{x^2+y^2}\cos\left(2\tan^{-1}\left(\frac{y}{x}\right)\right)}{-\frac{R^2}{x^2+y^2}\sin\left(2\tan^{-1}\left(\frac{y}{x}\right)\right)}\right].$$

where $\theta(x, y)$ represents the spatial distribution of the angle of the tangent to the fiber path from the x-axis.

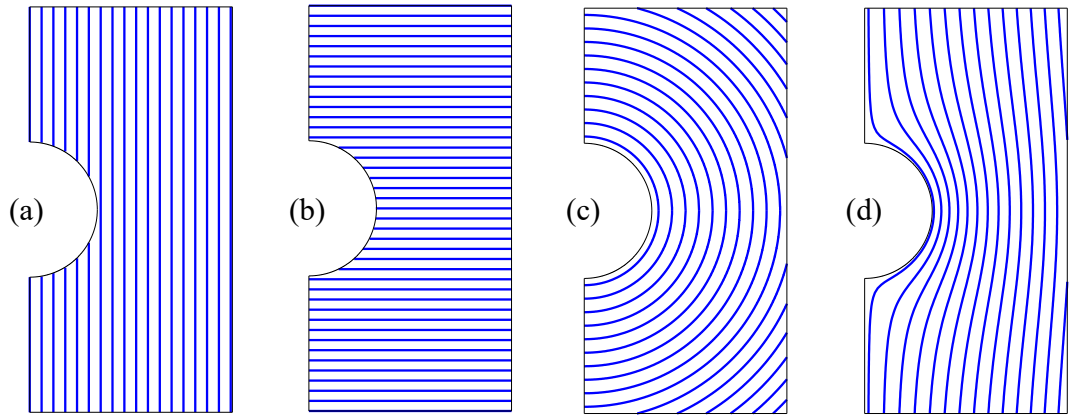

Figure 4.7: Composites reinforced by different fiber configurations: (a) Longitudinal straight fiber paths, (b) Transverse straight fiber paths, (c) Concentric fiber paths following the semi-circular notch, (d) Curvilinear fiber paths following the semi-circular notch (image from [95]).

4.3.3 Investigation of the performance of IGA

Figure 5.20 shows the error computed in L^2-norm of stresses for each of the fiber configurations presented in Fig. 4.7. The error for each component is defined by the following:

$$\boldsymbol{\epsilon} = \sqrt{\oint_V \boldsymbol{\epsilon}_\sigma \boldsymbol{\epsilon}_\sigma \, dV}, \tag{4.30}$$

where V is the domain of the whole material, and the $\boldsymbol{\epsilon}_\sigma$ is the vector of the difference between the converged stress field (change in the K_t less than 0.5%) and the current stress field. Then, the error ϵ, the root-mean-value of the Eq. (4.30) is taken as:

$$\epsilon = \sqrt{\frac{\boldsymbol{\epsilon} \cdot \boldsymbol{\epsilon}}{n}} \tag{4.31}$$

where n is the number of components for the stress field. The errors are plotted in double-logarithmic scale as a function of the number of degrees-of-freedom for both IGA and FEA.

Figure 2.8 illustrates the outstanding convergence performance of IGA over standard FEA approach. It is particularly evident when considering specimens with fibers following curved trajectories. To understand this behavior, the continuity of basis functions in IGA

and standard FEA is addressed. For the FEA approach in this study, quadratic Lagrange polynomials serve as the basis functions, resulting in C^0-continuity between elements at all times. Conversely, NURBS-based IGA employs bi-quadratic NURBS basis functions, ensuring C^1-continuity everywhere except along the x-axis due to multiplicity at $\xi = 0.5$.

To minimize the influence of mesh configurations, such as element size, aspect ratio, and element count, an equivalent FEA mesh resembling the physical IGA mesh is generated. Eight refinement iterations were conducted for the convergence analysis. Figure 4.9 shows mesh refinements #2 and #4 for both IGA and standard FEA. The Q9 and bi-quadratic NURBS elements consist of 9 associated nodes and control points, respectively. In this 2D analysis, each element incorporates 18 nodal variables and 18 control variables for FEA and IGA, respectively. A detailed summary of the meshes used for IGA and FEA is provided in Tables 4.2 and 4.3.

In IGA, the enhanced inter-element continuity appears to provide more precise field variables and improved numerical performance for a given degree of freedom compared to classical FEA. Furthermore, as shown in Figure 5.20 (d), the discrepancy in errors between IGA and FEA is notably larger than the one in cases involving conventional fiber configurations (Figure 5.20 (a) and 5.20 (b)). This difference suggests that IGA demonstrates higher efficiency when modeling CTI specimens characterized by sophisticated fiber paths.

Table 4.2: Mesh refinements and parametrization information for IGA

# h-refinement	Elements	DoFs	Unique knots; ξ	Unique knots; η	p	q
0	4	42	5	2	2	2
1	16	88	9	3	2	2
2	64	228	17	5	2	2
3	256	700	33	9	2	2
4	1,024	2,412	65	17	2	2
5	4,096	8,908	129	33	2	2
6	16,384	34,188	257	65	2	2
7	65,536	133,900	513	129	2	2
8	262,144	529,932	1,025	257	2	2

It is worth mentioning here that the same linear system solver was used for both IGA and standard FEA. To assess computational efficiency, the actual run-times for all four

Table 4.3: Mesh refinements information for standard FEA

# h-refinement	Elements	DoFs	Element Type
0	4	54	Q9
1	16	170	Q9
2	64	594	Q9
3	256	2,210	Q9
4	1,024	8,514	Q9
5	4,096	33,410	Q9
6	16,384	132,354	Q9
7	65,536	526,850	Q9
8	262,144	2,102,274	Q9

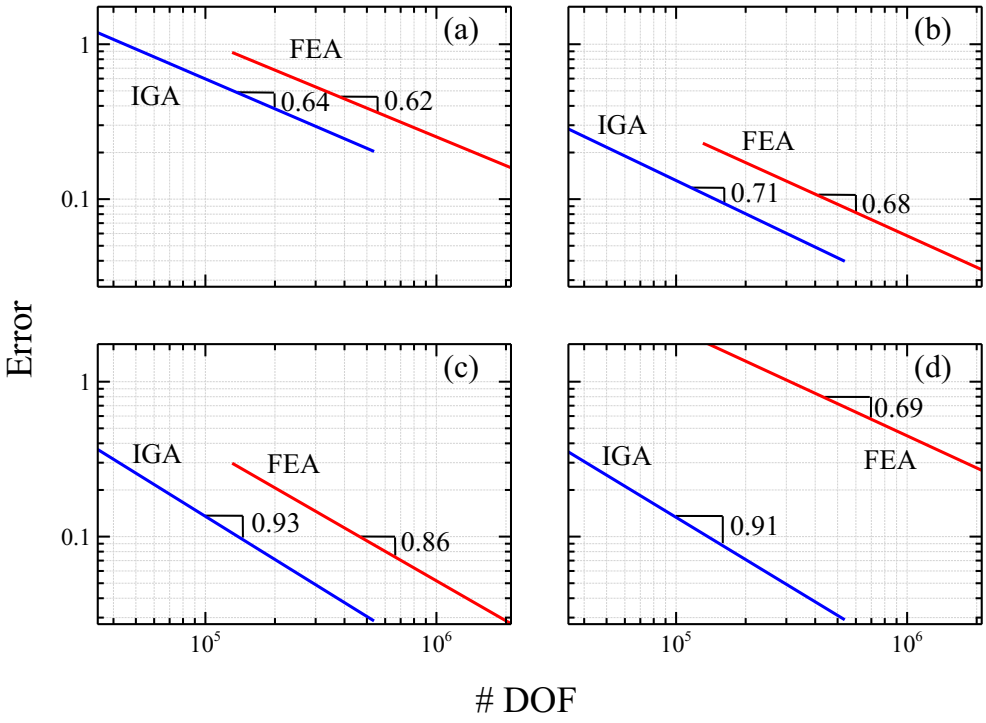

Figure 4.8: Error measured in L^2-norm of the stress against the number of degrees-of-freedom (# DOF): (a) Longitudinal straight fiber paths, (b) Transverse straight fiber paths, (c) Concentric fiber paths following the semi-circular notch, (d) Curvilinear fiber paths following the semi-circular notch (image from [95]).

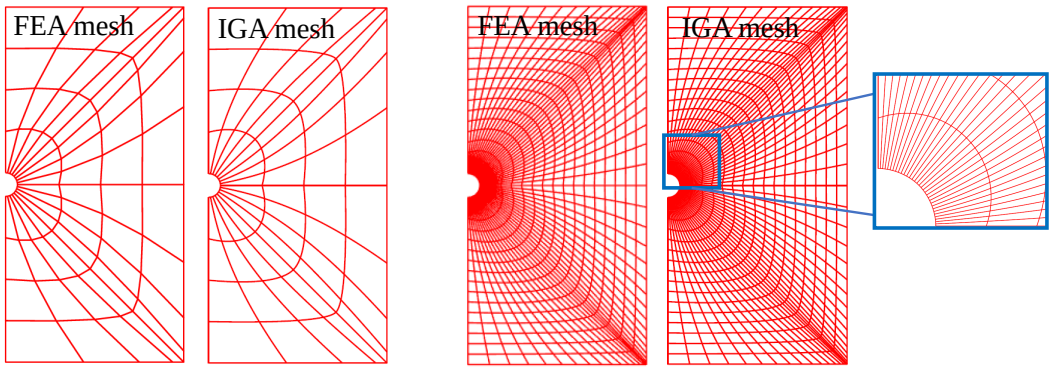

(a) Refinement #2 (b) Refinement #4

Figure 4.9: Visualization of (a) mesh refinement # 2 for both FEA and standard IGA and (b) mesh refinement # 4 for both FEA and standard IGA with the magnification near the semi-circular notch. IGA mesh has bi-quadratic elements ($p = 2, q = 2$) which do not necesarily have straight edges; (b) FEA mesh is created from IGA mesh and has Q9 elements (image from [95]).

distinct fiber paths were calculated for both methods, employing the highest level of mesh refinement (refinement 8) used within this study. All the simulations were performed on an AMD Ryzen 5 2600 processor running at 3.4 MHz using 32 GB of RAM. Table 4.4 includes the results along with the percentage reduction defined as:

$$\Delta t\% = \frac{|t_{IGA} - t_{FEA}|}{t_{FEA}} * 100 \tag{4.32}$$

where t represents the running time elapsed each numerical method, and the numerator is given as an absolute value (See Fig. 4.10). The running time of IGA is approximately 35-40% lower than conventional FEA. This means that not only IGA can reduce the time from Computer-Aided Design (CAD) to analysis, but also enables a significant reduction of the running time of an analysis. This result becomes more significant when the size and complexity of the analysis increases.

In summary, IGA provides:

1. time reduction
2. computational efficiency

Table 4.4: Run-time difference in refinement # 8 between IGA and standard FEA on four different fiber paths

	t [sec], IGA	t [sec], FEA	Δ t [%]
Longitudinal Straight Fiber	65.7	104.0	36.8
Transverse Straight Fiber	65.6	108.9	39.7
Concentric path	67.8	105.3	35.6
Curvilinear path	68.1	105.3	35.3

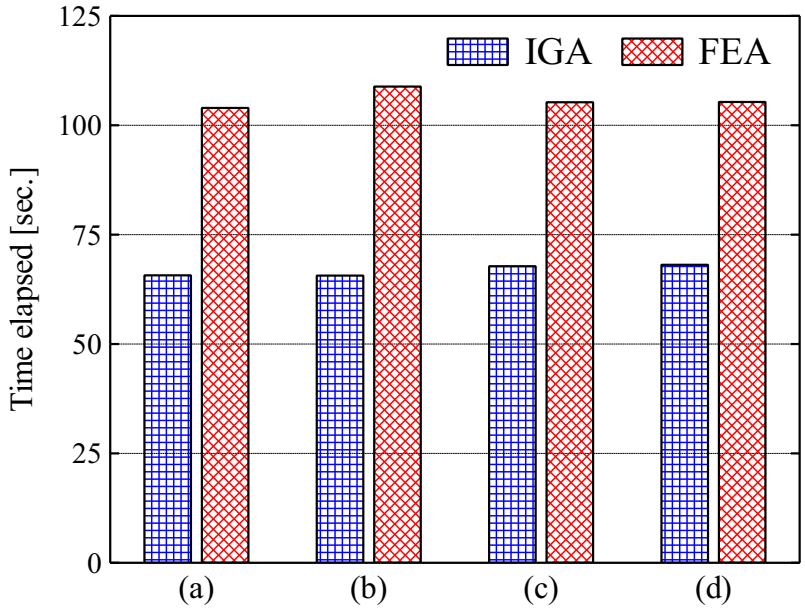

Figure 4.10: Running time in seconds elapsed to obtain convergence for each fiber configuration: (a) Longitudinal straight fiber paths, (b) Transverse straight fiber paths, (c) Concentric fiber paths following the semi-circular notch, (d) Curvilinear fiber paths following the semi-circular notch. (image from [95])

3. more accurate description of the field variables for a given number of degrees-of-freedom, compared to classical FEA

It is worth mentioning here that similar performance advantages of IGA over FEA where reported in several other studies focusing e.g. on computational electromagnetics [125] and mechanics [1, 126, 127, 128]. These features make IGA a valuable tool for the simulation of structural and electrostatics problems in media featuring curvilinear anisotropy [124, 69, 70, 75, 79, 80, 81, 82, 129, 130].

4.3.4 Investigation of the effects of curvilinear anisotropy on the elastostatic behavior

As indicated by the data presented in Table 4.5, conventional longitudinal fiber-reinforced composites tend to exhibit high in-plane stiffness with significant stress concentration around notches and similar stress raisers. Conversely, composites reinforced with straight transverse fibers exhibit reduced stress concentrations and low in-plane stiffness. Exploiting the advantages in IGA, the impact of various curvilinear fiber paths outlined in Fig. 4.7 on stress concentration and stiffness are examined. All stress concentration factors and Tsai-Wu failure indices derived from simulations are listed in Table 4.5.

Table 4.5: Table of the stress concentration factor K_t, the average stiffness on the top edge $\bar{K}$, and the maximum Tsai-Wu failure index Φ of: (a) Longitudinal straight fiber path (Fig. 4.5a), (b) Transverse straight fiber path (Fig. 4.5b), (c) Concentric fiber path (Fig. 4.5c), (d) Curvilinear fiber path following the semi-circular notch (Fig. 4.5d).

	(a)	(b)	(c)	(d)
K_t	7.18	2.38	5.02	3.49
$\bar{K}$ [GN/mm]	88.20	5.11	10.78	86.72
Φ	0.004	0.050	0.051	0.026

Concentric fibers following semi-circular paths

One of the fiber configurations involves concentric paths encircling the semi-circular notch as shown in Fig 4.7 (c). In this case, the fibers placed above and below the notch exhibit transverse orientations to the applied load, resulting in relatively compliant regions. This

contrast becomes apparent upon comparing the contour plots of in-plane stress components for the concentric fiber paths (Fig. 4.11) with those of the longitudinal (Fig. 4.12) and transverse (Fig. 4.13) fiber cases. The noticeable outcome is that the compliant regions provide a mild shielding effect around the notch, and the highest stress concentration factor, approximately 5.02, is obtained at the midpoint along the right-hand side edge of the plate. This is contrasting to the other two cases with linear fibers, where the peak stress consistently occurs at the tip of the notch. Despite the presence of compliant regions, the stress contour surrounding the semi-circular notch remain high valued compared to the nominal value (Ty = 1 MPa), and the stress concentration factor remains approximately 4.

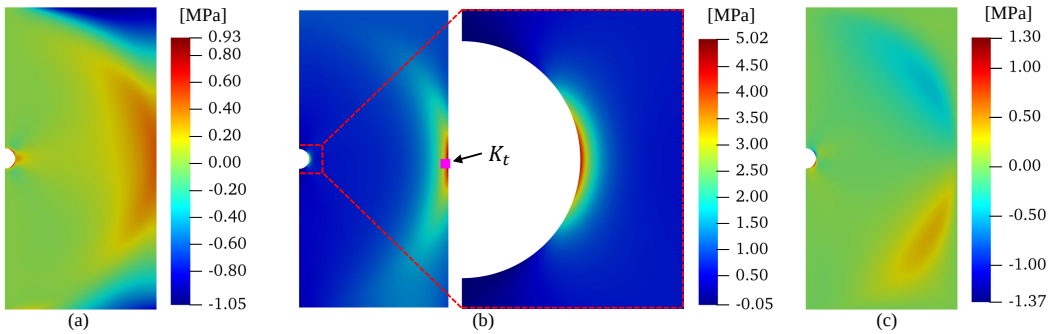

Figure 4.11: Stress fields of composites reinforced by concentric fibers following the semi-circular notch: (a) stress in the x-direction σ_{xx}, (b) stress in the y-direction σ_{yy} and the magnification around the semi-circular notch with the location of the stress concentration factor K_t marked by the magenta square, (c) shear stress in the x-y plane τ_{xy} (image from [95]).

When examining the stress concentration relative to the cases of linear fibers, an intriguing observation for the concentric path can be made: K_t value is approximately 30 % lower than that of the longitudinal fiber case, while it is approximately 111 % higher compared to the transverse fiber case. Conversely, the overall stiffness of the plate is roughly one-eighth of the longitudinal fiber case and approximately twice that of the transverse fiber case. Consequently, in this configuration, the curvilinear anisotropy does indeed lead to a reduction in stress concentration in comparison to the longitudinal fiber case. However, this improvement comes at the expense of structural stiffness, which notably decreases in com-

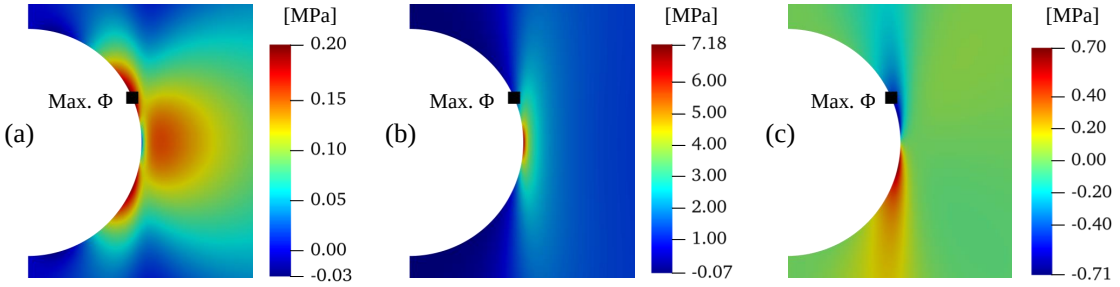

Figure 4.12: Stress fields of composites reinforced by longitudinal straight fibers with the maximum Tsai-Wu index Φ marked by the black square: (a) stress in the x-direction σ_{xx}, (b) stress in the y-direction σ_{yy}, (c) shear stress in the x-y plane τ_{xy} (image from [95]).

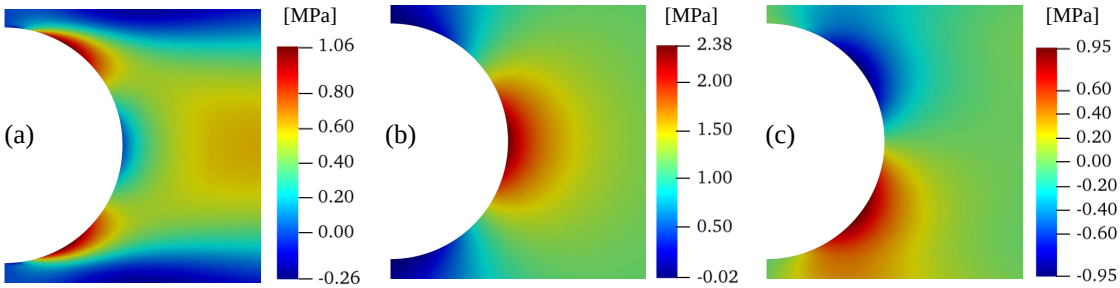

Figure 4.13: Stress fields of composites reinforced by transverse straight fibers: (a) stress in the x-direction σ_{xx}, (b) stress in the y-direction σ_{yy}, (c) shear stress in the x-y plane τ_{xy} (image from [95]).

parison to the longitudinal fiber case (although it still remains higher than the transverse fiber case).

Within the set of linear fiber cases, the transverse straight fiber path (Fig. 4.7 (b)) exhibits the highest Tsai-Wu index value: 0.050. This is induced by the dominance of resin strength in the direction of loading. Although the stress concentration associated with the concentric fiber configuration is less pronounced than that of the conventional longitudinal fiber composite, the maximum failure index, 0.051, is similar to the value observed for the transverse fiber configuration. Consequently, choice of this particular curvilinear fiber path might not be as favorable in terms of damage tolerance due to shear-related damage.

Curvilinear fibers following holomorphic paths

Figure 4.14 provides the stress contour plots for each in-plane stress component, specifically for the plate reinforced with fibers following the holomorphic paths as defined in [124]. These contour patterns resembles the traditional longitudinal straight fiber composite (Fig. 4.12), featuring a notable stress concentration at the notch tip. However, the stress concentration factor K_t stands at 3.49, which is roughly half of that observed in the case of the longitudinal straight fiber composite. Concurrently, the average stiffness $\bar{K}$ for the curvilinear fiber layer is close to 86.7 GN/mm, a value close to the 88.2 GN/mm computed for the longitudinal straight fiber case. This indicates that despite the nearly identical stiffness between the two materials, the stress distribution σ_{yy} around the semi-circular notch is considerably less concentrated in the curvilinear fiber case than in the longitudinal straight fiber case.

The maximum Tsai-Wu failure index recorded for the curvilinear holomorphic fibers stands at 0.026, which is lower compared to those observed in other fiber paths as depicted in Figs. 4.7 (b), 4.7 (c). Nonetheless, the maximal Tsai-Wu index for the longitudinal straight fibers is notably smaller (approximately six times lower) yet the stress concentration is considerably high. As evident in Fig. 4.12 and 4.14, the maximum Tsai-Wu indices coincide with the regions around the peak stress points for both cases in the vicinity of the x- and shear stress components. This alignment suggests that the structural failures could potentially arise due to a combination of resin and shear damage.

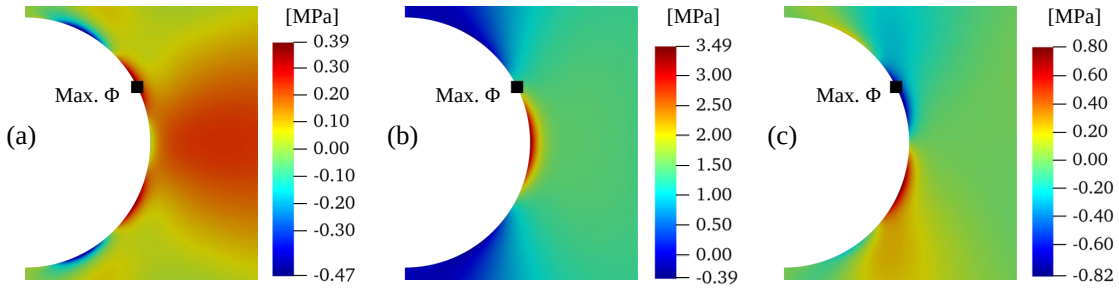

Figure 4.14: Stress fields of composites reinforced by curvilinear fibers following holomorphic paths with the maximum Tsai-Wu index Φ pointed marked by the black square: (a) stress in the x-direction σ_{xx}, (b) stress in the y-direction σ_{yy}, and (c) shear stress in the x-y plane τ_{xy} (image from [95]).

4.4 Optimization study

In the preceding section, it was demonstrated that curvilinear reinforcement shows promising result for enhancing various mechanical properties. The subsequent portion of this study involves conducting optimization studies aimed at identifying optimal fiber paths to address the following problems:

1. minimizing the stress concentration factor, Eq. (4.26)
2. minimizing the maximum the principal stress, Eq. (4.33)
3. Tsai-Wu failure index, Eq. (4.28)
4. maximizing average stiffness Eq. (4.27)

Note that maximum principal stress is defined by

$$max \left[\left(\frac{\sigma_x + \sigma_y}{2} \right) \pm \sqrt{\left(\frac{\sigma_x + \sigma_y}{2} \right)^2 + \tau_{xy}^2} \right]. \tag{4.33}$$

4.4.1 Problem statement

The optimization scheme based on the SQP method is used in this section to optimize the fiber paths of the geometries shown in Fig. 4.5 and Fig. 4.15. As initial condition, the parameter $\mathbf{C}$ of the level-set functions describing the family of fiber paths, Eq. (4.18) and (4.19), are chosen to take unit values. It is necessary to re-state that these fiber describing

level-set functions above does not guarantee the whole design space of the possible fiber paths, and might results in local minimum.

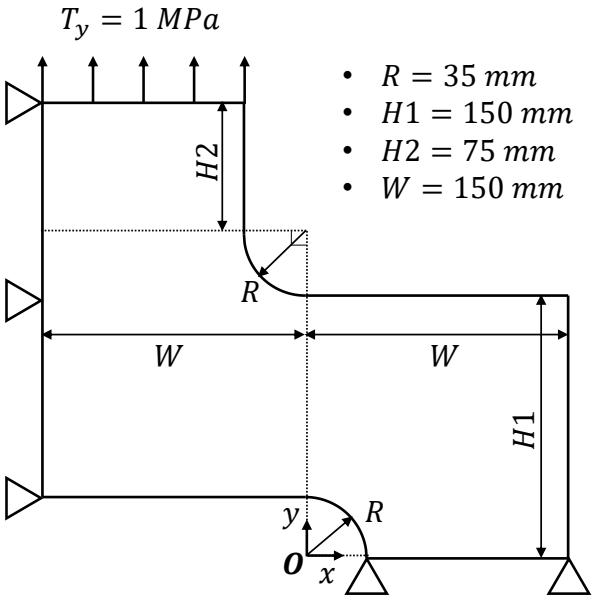

Figure 4.15: Case II: Elastic plate featuring curvilinear transverse isotropy (image from [95]).

4.4.2 Optimization of the fiber paths for case I

As a demonstration of the Isogeometric modeling of curvilinear fiber-reinforced composites, the optimization framework described in the previous section has been implemented on the simple semi-circular notched plate (Fig. 4.5). The design space of the possible fiber paths is defined by the 5^{th}-order complete polynomial, Eq. (4.18) in order to describe the fibers with high rate of curvature.

Stress concentration factor minimization

The optimal fiber paths found using SQP are presented in Fig. 4.16 (a), and an overview of the outcomes in terms of stress concentration, failure index, and overall stiffness is pro-

vided in 4.6. Stress contours are shown in Fig. 4.16 (b)-(d). Remarkably, the optimized configuration provides a stress concentration of 1.28 (Table 4.5 (a)), which shows 82 % reduction compared to the longitudinal fiber case, and even surpassing the performance of the isotropic case. This suggests that leveraging curvilinear anisotropy can produce a substantial reduction in notch sensitivity.

It is worth mentioning that the stress concentration in the optimal case is lower than that in the transverse fiber case, which has the lowest observation among the preceding investigation. In fact, the stress concentration for the optimal fiber path case (Table 4.5 (a)) is lower by 46 %.

To conclude, the utilization of curvilinear anisotropy holds the potential to notably alleviate stress concentration, surpassing even the levels seen in isotropic materials. When considering the increase in strength and stiffness contributed by the fibers reinforcements, it is evident that material featuring CTI can surpass the mechanical performance of conventional composites.

Table 4.6: Table of the stress concentration factor K_t, the average stiffness on the top edge $\bar{K}$, and the Maximum Tsai-Wu failure index Φ of: (1) optimal fiber path for the minimum K_t, (2) the optimal fiber path for the minimum Φ.

	(1)	(2)
K_t	1.28	7.18
$\bar{K}$ [GN/mm]	33.38	88.20
Φ	0.020	0.004

Minimization of the Tsai-Wu failure index

The optimization study for the minimum Tsai-Wu index is also implemented under the same condition for the minimum stress concentration.

The initial design variable vector $\mathbf{C}$ is decided as the longitudinal straight fiber path

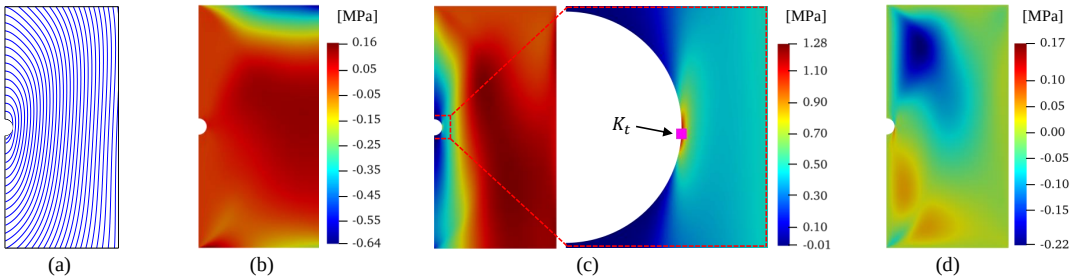

Figure 4.16: Optimal fiber path for the minimum stress concentration factor: (a), and the contour plots of: (b) the stress in the x-direction σ_{xx}, (c) the stress in the y-direction σ_{yy} and the magnification around the semi-circular notch with the location of the stress concentration factor K_t marked by the magenta square, (d) the shear stress in the $x-y$ plane τ_{xy} (image from [95]).

shown in Fig. 4.7a such that:

$$C_{ij} = \begin{cases} 1 & \text{if } (i,j) = (1,0), \\ 0 & \text{otherwise} \end{cases} \tag{4.34}$$

where i, j are the subscripts of the coefficients shown in Eq. (4.18),

because this fiber path provides the minimum Tsai-Wu failure index based on the four different fiber configurations (Fig. 4.7a and Table 4.5).

As a result of the optimization, the design variables remained as same as the initial conditions indicating that the longitudinal straight fiber case is the one minimizing the failure index (Table 4.5). In terms of Tsai-Wu index, conventional longitudinal straight fiber path is the best option, however, the stress concentration is very significant compared to the optimal fiber case of the minimum stress concentration. Thus, it is interesting to make a comparison between the two focusing on Tsai-Wu index as discussed next.

Damage initiation analysis

Referring to Table 4.6, the maximum Tsai-Wu failure index is identified as 0.020 for the fiber path with the minimum stress concentration, located at the upper-left node. This value is approximately five times greater than the value associated with the longitudinal

straight fiber path, which is the optimal configuration for minimizing the Tsai-Wu index. Table 4.7 presents the local stresses for each component, along with the local dominance of the ply strength at the points of the maximum Tsai-Wu failure index. The local ratios between stresses to the lamina strength such that:
For the longitudinal fiber direction:

$$\sigma_1/\sigma_1^f = \begin{cases} \sigma_1/\sigma_{1t}^f & \text{if } \sigma_1 \geq 0 \\ \sigma_1/\sigma_{1c}^f & \text{if } \sigma_1 < 0 \end{cases} \tag{4.35}$$

For the transverse fiber direction:

$$\sigma_2/\sigma_2^f = \begin{cases} \sigma_2/\sigma_{2t}^f & \text{if } \sigma_2 \geq 0 \\ \sigma_2/\sigma_{2c}^f & \text{if } \sigma_2 < 0 \end{cases} \tag{4.36}$$

while for the shear component the ratio, τ_{12}/τ_{12}^f is independent of the sign of the local shear stress.

Examining the scenario of optimal fibers for minimal stress concentration (Fig. 4.16 (a)), it is evident that the transverse stress component aligns closely with the associated strength value. This observation suggests that a probable matrix failure, such as splitting at the upper-left region of the plate (Fig. 4.17(a)), represents the most plausible damage mechanism. However, any resultant crack is likely to advance along a curvilinear fiber trajectory and eventually be arrested by fibers. Consequently, although the plate initiates damage, an immediate and abrupt failure might not occur. In the medium optimized for achieving the minimum Tsai-Wu index, the transverse and shear components of strength exhibit large values when contrasted with their respective strengths. This phenomenon indicates the splitting crack as a dominant failure mode. Notably, as depicted in Fig. 4.17 (b), the initiation of a splitting crack will occur in close proximity to the notch tip, progressing undisturbed along the longitudinal fiber path until it traverses the plate's entire span.

Hence, accurately predicting which fiber configuration will achieve the highest load-bearing capacity is challenging. Apparently, the Tsai-Wu failure criterion is suitable to

predict damage progression, and quasibrittle fracture mechanics models is necessary in future works to investigate the highly nonlinear progressive damage followed by initiation [123, 120, 131, 132, 133].

Table 4.7: Table of the local stresses and the local stress dominance of ply strengths at the points of the maximum Tsai-Wu failure index for: (1) optimal fiber path for the minimum K_t, (2) the optimal fiber path for the minimum Tsai-Wu failure index Φ.

	σ_1 [MPa]	σ_2 [MPa]	τ_{12} [MPa]	σ_1/σ_1^f	σ_2/σ_2^f	τ_{12}/τ_{12}^f
(1)	0.061	0.941	0.238	$4.0E-5$	$2.4E-2$	$3.5E-3$
(2)	1.112	0.205	0.480	$7.4E-4$	$5.1E-3$	$7.1E-3$

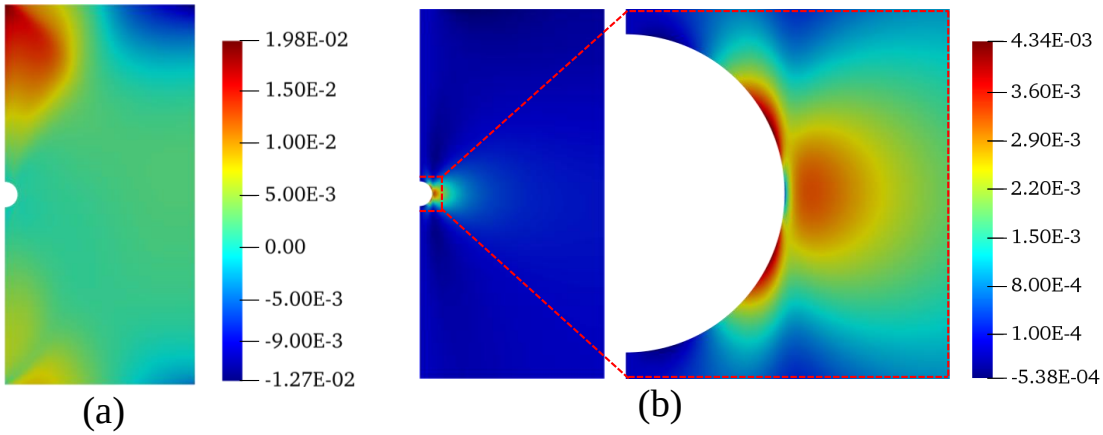

Figure 4.17: Contour plots of the Tsai-Wu failure index of the optimal fiber paths: (a) for the minimum stress concentration factor, and (b) for the minimum Tsai-Wu failure index and the magnification around the semi-circular notch (image from [95]).

4.4.3 Optimization of the fiber paths for case II

The focus of this optimization study is to extend the exploration of the potential gain in mechanical performance (reduction in the maximum principal stress and increase in the stiffness of the structure) via cuvilinear fiber reinforcement described by a simple polynomial level-set function.

Minimization of the maximum principal stress

In this study, the optimal fiber paths are illustrated in Fig. 4.18, and the outcomes are listed in Table 4.8. The fiber paths presents a certain degree of resemblance to the contour of the structure. As can noticed, the minimum principal stress is about 8.62, reflecting a remarkable 74 % reduction in comparison to the conventional longitudinal fiber reinforcement. Notably, this value surpasses that of the conventional transverse fiber reinforcement, measuring 13.41, which is considered as the minimum principal stress in traditional straight fiber layups.

Conversely, the Tsai-Wu failure index and average stiffness values suggest that this particular setup might not yield significant improvement in structural stiffness and strength. Nevertheless, it still presents the challenges to accurately predict the ultimate strength of the structure in the absence of a progressive damage model. Keeping this in mind, one can still speculate about the possible mechanical response of the structure. When locally off-axis fibers are introduced, the point of maximum principal stress might serve as the initiation site for a splitting crack. This optimal configuration could potentially be a suitable candidate for reinforcement in the design of a structure that is less susceptible to splitting cracks.

Maximization of the in-plane stiffness

Figure. 4.19 shows the the optimal fiber path that maximizes the average stiffness. A comprehensive summary of the maximum stiffness and other mechanical properties are listed in Table 4.8. The fiber paths exhibit similarities with those discussed in the preceding section, although it features a more pronounced vertical descent on the right-half segment. As highlighted in Table 4.8, the average stiffness is approximately 4.3 GN/mm, which presents a substantial 31 % increase over the traditional longitudinal straight fiber case and about 71 % increase compared to the transverse fiber case.

Moreover, the Tsai-Wu index is comparably low, close to the value seen in the configuration reinforced by longitudinal fibers and the fiber path that achieves the minimum Tsai-Wu index as derived from our optimization approach. This optimal fiber configuration not only yields a notable average stiffness but also maintains material strength, concurrently.

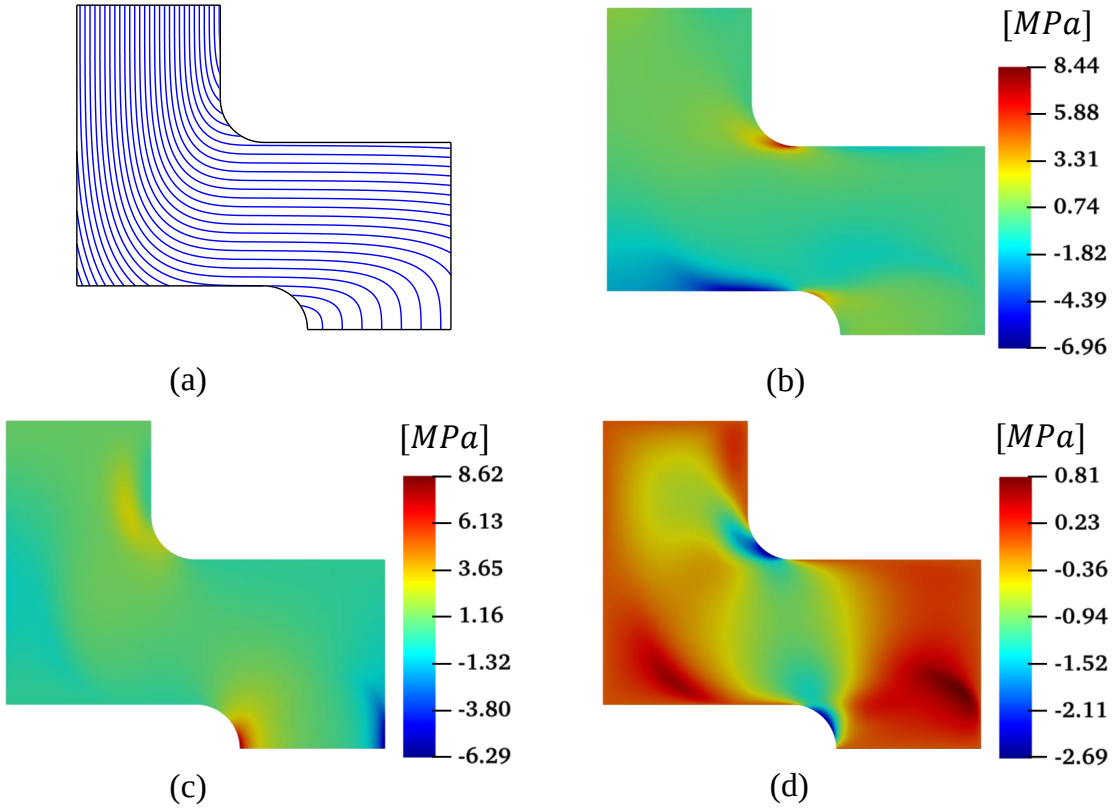

Figure 4.18: Optimal fiber path for the minimum principal stress: (a), and the contour plots of: (b) the stress in the x-direction σ_{xx}, (c) the stress in the y-direction σ_{yy}, and (d) the shear stress in the $x-y$ plane τ_{xy} (image from [95]).

However, it is important to acknowledge that our current parameters may not provide the ultimate strength of a given structure. To substantiate these findings, a more in-depth exploration using quasibrittle fracture mechanics is necessary.

Table 4.8: Table of the maximum principal stress Σ_1, the average stiffness on the top edge $\bar{K}$, and the Maximum Tsai-Wu failure index Φ of: (1) optimal fiber path for the minimum Σ_1, (2) the optimal fiber path for the maximum $\bar{K}$, (3) the conventional longitudinal fiber path, and (4) the conventional transverse fiber path.

	(1)	(2)	(3)	(4)
Σ_1	8.62	23.58	32.86	13.41
$\bar{K}$ [GN/mm]	2.44	4.33	3.30	2.54
Φ	0.149	0.049	0.040	0.083

4.5 Conclusion

In this work, (IGA) computational framework is utilized to numerically investigate the media featuring curvilinear anisotropy on their mechanical performance. Based on the results, the following conclusions are made related to the numerical aspect of the problem:

1. thanks to the exact geometric representation and the enriched continuity between elements, NURBS-based IGA outperforms classical FEA in terms of computational efficiency, run time, and accuracy in the description of field variables for the same number of degrees-of-freedom;
2. for the configurations investigated in this work, the use of IGA resulted in an average reduction of the total simulation time of about 40% compared to FEM given the same error in the estimation of the maximum stress and solution scheme of the reduced system of equations;
3. the higher efficiency of IGA makes it an interesting alternative to FEM for the simulation of large and complex structures made of materials featuring curvilinear anisotropy. Further, this characteristic makes it particularly suitable for optimization studies which generally require several simulations before reaching the optimal solution;

The following conclusions are made related to the mechanical performance of plates featuring curvilinear anisotropy:

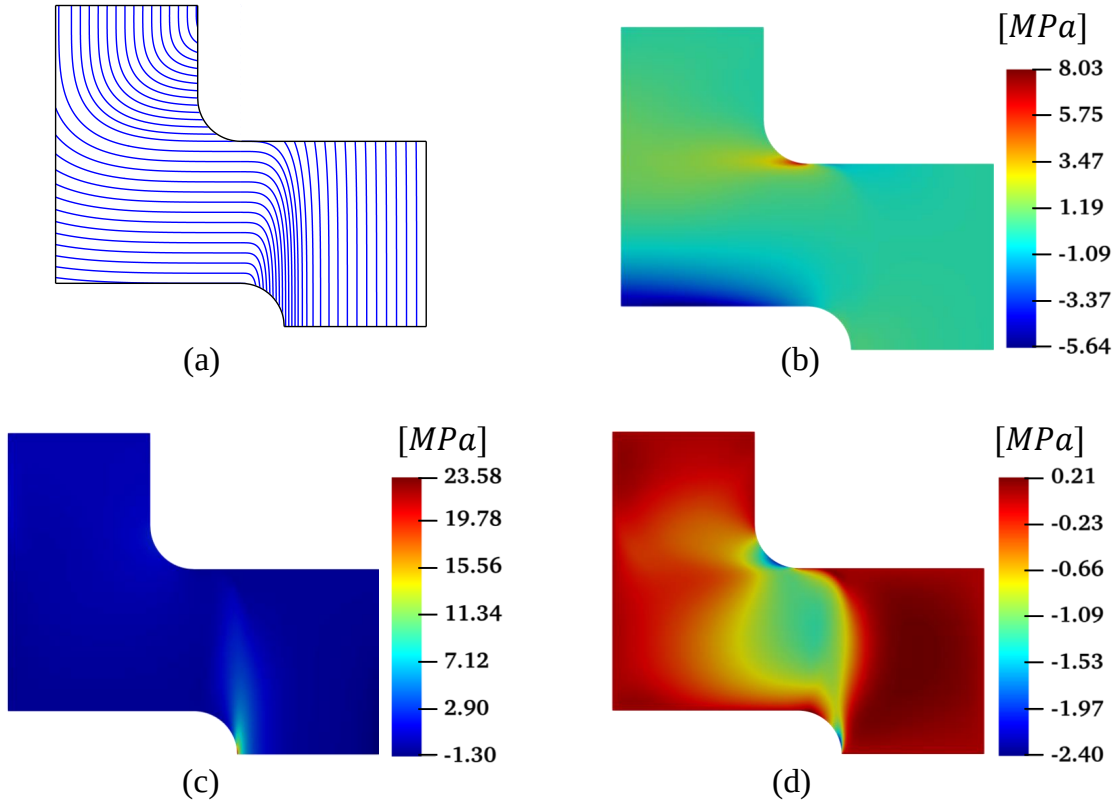

Figure 4.19: Optimal fiber path for the maximum average stiffness: (a), and the contour plots of: (b) the stress in the x-direction σ_{xx}, (c) the stress in the y-direction σ_{yy}, and (d) the shear stress in the $x-y$ plane τ_{xy} (image from [95]).

4. as expected, curvilinear anisotropy has a significant effect on the elastic stress and strain fields as well as the overall stiffness of the plate;
5. in curvilinear anisotropic media, the regions of high stress concentration can be widely distributed over the domain. Hence, when performing optimization studies, it is important to utilize a uniform refinement instead of a local refinement around the notch. Guaranteeing a uniform accuracy throughout the domain may become very computational expensive with FEM. In contrast, IGA significantly mitigates this problem thanks to the higher accuracy and efficiency;
6. by optimizing the fiber paths in the plate with a semi-circular notch, the stress concentration factor, K_t, is reduced to 1.28 with the maximum stress located at the notch tip. This represents a reduction of about 82% compared to the classical longitudinal linear fiber case and a reduction of 58% compared to the isotropic case;
7. by optimizing the fiber paths in the geometry shown in Fig. 4.15, the optimal configuration improves the average stiffness of 71% compared the transverse fiber path. Furthermore, the configuration that reduces the maximum principal stress of 74% compared to the longitudinal fiber path is obtained.
8. on the other hand, it was identified that the longitudinal linear fiber path provides the minimum Tsai-Wu failure index, with damage initiation in the form of a mode II splitting crack close to the tip of the notch. In contrast, the path minimizing the stress concentration gives a failure index about five times larger, with damage initiation as mode I splitting crack. However, this result does not allow significant conclusions on the ultimate capacity of the plates since this depends on the progressive damage evolution up to failure. It is likely that, after initiation, the splitting crack in the curvilinear anisotropic case will be significantly slowed down and arrested by the fibers before final failure. On the other hand, the splitting crack in the longitudinal fiber case will propagate unstably until reaching the top and bottom boundaries of the plate. To investigate damage progression in curvilinear anisotropic media, future works will focus on the use of quasibrittle fracture mechanics computational models [123, 120, 131, 132, 133]. These are quintessential to capture the formation of large Fracture Process Zones (FPZs) and distributed damage in composites which are a

significant source of size effects [121, 122, 133];

9. another interesting result is that the curvilinear fiber paths designed to optimize the electric conductivity of the plate [124] showed also an outstanding mechanical performance. In fact, the stress concentration factor was found to be 3.49, about 51% lower than the longitudinal linear fiber case with similar levels of plate stiffness. This result is particularly promising because it shows that it is possible to harness curvilinear anisotropy not only to obtain superior mechanical performance compared to traditional composites, but also to introduce novel multi-functional properties. Future works will focus on the formulation of novel multi-objective optimization schemes within the IGA framework to take advantage of this new design space;
10. in order to improve the optimization scheme, a broader definition of fiber paths should be used to ensure that the design space does not restrict the potential optimal outcome. A different optimization method such as Bayesian optimization and genetic algorithms can be applied to ensure that the optimal result is not a local minimum.

Chapter 5

MODELING A TRIMMED SURFACE AND A GEOMETRIC DISCONTINUITY IN THE ISOGEOMETRIC FRAMEWORK

In the previous chapter, the NURBS-based isogeometric analysis of composite plates featuring CTI is presented. Parametrization using NURBS exactly represents the semi-circular notch in a plate regardless of mesh refinement levels. However, there is a limitation to this tensor-product surfaces representing an arbitrary topology. The word, "complex", may not apply to the visual complexity in a geometry. Even a simple and common geometry of interest in structural engineering such as a plate with a central hole cannot be parametrized in a single patch NURBS tensor-product surface. This may sound ironic since the spline technology has been widely utilized in the CAD industry.

Engineered surfaces often include geometric features such as holes, notches, chamfer, and fillets. To add these features to a structure, CAD utilize the trimming techniques in a software. A typical procedure of constructing a complex surface involves Boolean operations on a much simpler geometric entity. Boulean operation is an efficient method of visualizing cut-outs in a geometry; however, it does not modify the parametrization. Thus, a numerical solver does not see the cut-outs in the physical domain during the analysis without any treatment in the mesh generation.

A solution to avoid such operation is to use multiple NURBS patches. However, this method requires creating multiple compatible NURBS surfaces and numerically attaching the patches so that the solver recognize as a single domain. It is not so straightforward to generate compatible patches for arbitrary topology and numerical treatment can increase the computational cost. Therefore, there have been efforts to develop treatments so that the trimmed surfaces can be transformed in to analytically-suitable objects.

In the following sections, literature study on some of representative methods of treating trimmed spline surfaces for isogeometric analysis is provided. Then, a brief introduction on

the theory of LR B-splines is followed by the method of defining crack to the mesh used for analysis. Lastly, the development of in-house 3D IGA software package which includes preprocessor, a linear solver, and postprocessor is discussed.

5.1 Literature review of IGA on trimmed surface

In order to model an arbitrary topology, it is necessary to utilize a non-tensor based spline technology. T-spline [2] is a generalized representation of B-spline formulation that allows parametrization in a relative reference frame. T-spline consists of T-mesh, which is a control grid where the local paramatrization can be deduced from knot interval. An example of T-mesh is shown in Fig. 5.1. Unlike NURBs, T-splines can have T-junctions at which one s-edge and two t-edges coincide, or one t-edge and two s-edges are coincide. s-edge is a linear segment of constant s-value. Same idea applies to t-edge. T-junctions allows a flexible local control in mesh refinement. When T-mesh simplifies to a structured grid, T-spline representation becomes identical to B-spline. Detail characteristics of T-spline technology is referred to the work by Sederberg et al. [2]. Thanks to the localized framework, vertices in T-mesh can be shared by more than 4 edges. Vertices that have valence number other than 4 and is not T-junctions is called extraordinary nodes.

Placing extraordinary nodes in right places can model the complex geometric feature induced by trimming operation. However, it is not so straight forward where to locate the extraordinary points given an arbitrary geometry as pointed out by Nguyen [3]. An example of modeling complex geometry with T-spline and extraordinary nodes is shown in Fig. 5.2. In analytical point of view, continuity between neighbor elements centered around extraordinary point decreases depending on the treatment on the extraordinary point, but this is rather a minor issue since the neighboring region is minimal compared to the whole domain. Therefore, modeling dimensioned parts, most of engineered parts, becomes quite sophisticated with T-splines although it is definitely possible. Some method of going around this issue is to convert a mesh to T-mesh. Wang et al. [4] introduced a method of converting quadrilateral mesh to a T-mesh. This method starts from an unstructured quadrilateral mesh and goes through two stages. First, it generate a T-mesh with regular and extraordinary nodes and goes through templates based on the classification of quadrilateral

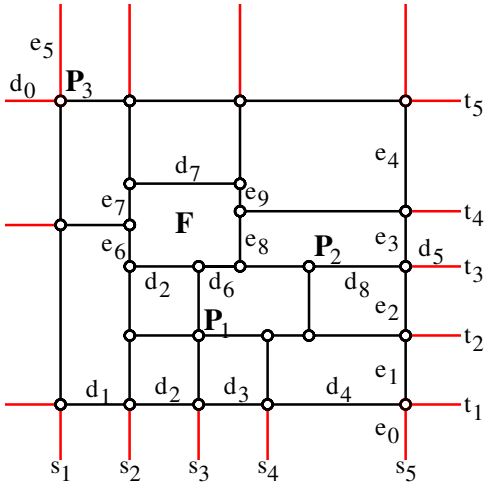

Figure 5.1: Example of T-mesh (image from [2]) in a parametric space (s, t); F and P refer to facet and control point, respectively. d and e are knot intervals in s and t direction, respectively

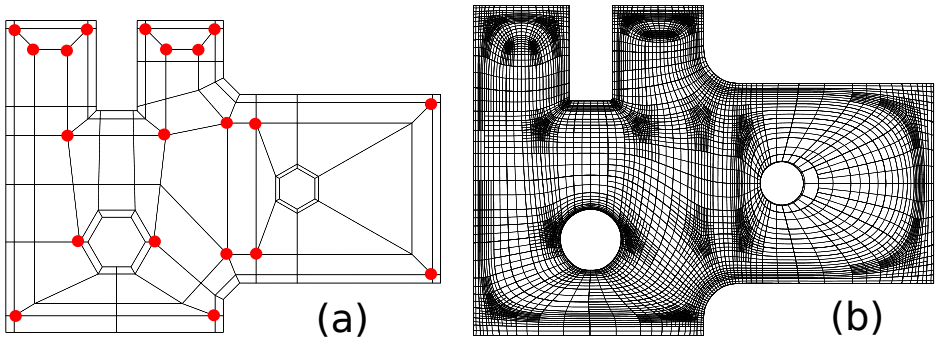

Figure 5.2: T-spline modeling of a machine part (reconstructed image from [3]): (a) Control polygon from T-mesh; red dots are extraordinary nodes; (b) T-spline elements.

elements to finalize gap-free T-mesh. Last stage involves relocation of control points to preserve geometric accuracy. The example of converting the unstructured mesh of the knee model is shown in Fig. 5.3. Similar approach is introduced by Liu et al. [134], in which they improved a method of handling extraordinary nodes using the weighted T-spline functions. They are able to improve the surface continuity and simplify the process of converting an unstructured mesh. This approach resembles the idea of reverse engineering. Although this method provides a clear procedure of modeling a dimensioned complex parts, it is not suited for our idea of isogeometric framework since it starts from an unstructured mesh and exact modeling may require optimization process for an arbitrary topology. This method is more appropriate for the application of converting a mesh from a 3-D scanned object for IGA.

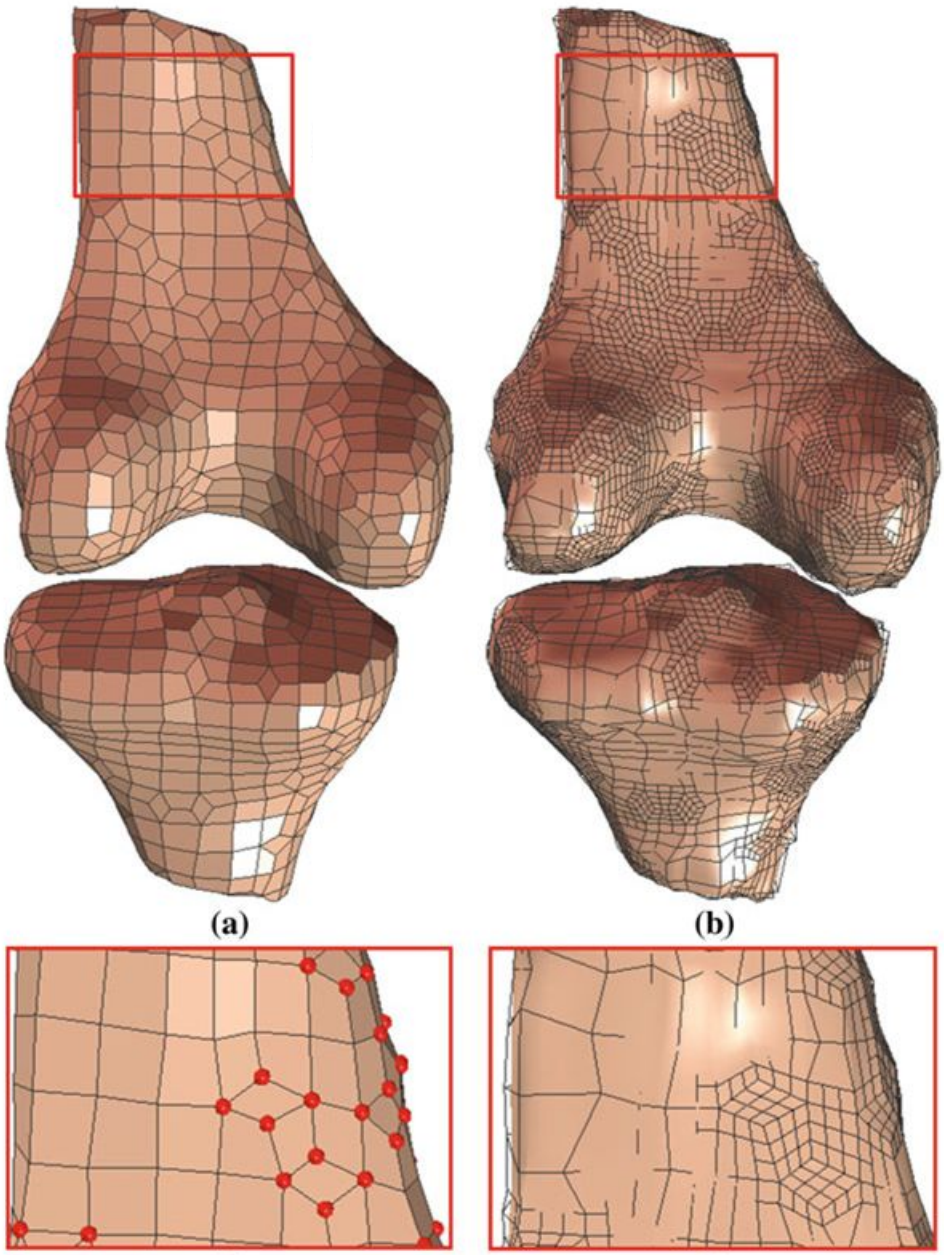

Figure 5.3: The knee model conversion (image from [4]): (a) initial unstructured mesh input; red dots are extraordinary nodes; (b) gap-free validated T-mesh converted from the initial mesh.

Another approach of modeling trimmed surface is to utilize a local reconstruction. This method actually modifies the parametrization to reconstruct the physical trim boundary.

It involves the modification of the knot spans and control points for the trimmed elements. This method seems promising and provides interesting application on arbitrary shape load design on a surface. However, there are several concerns on adapting this method. First, implementation aspect was not so clear in the paper, especially for the presence of multiple closed trim curves. Second, it requires another modeling steps for reconstructing trimming boundary that may require optimization to reduce the error of construction. It seems to require additional mesh refinement for the close approximation of trim boundary when the curvature of trimming curve is high. Considering that this method is provided in NURBS which does not have flexibility in local refinement, it may present some possible complications for a complex trimming domain. Physical matching of trim boundary is desirable; however, reconstruction does not seem so attractive compared to T-spline design since T-spline can produce an accurate single patch model without reconstruction.

There are other type of approach to modeling trimmed surfaces. That is to numerically identify the cut-out region by introducing the penalty in the integration process. Kim et al. [5, 135] provide the method of identifying trimmed elements using trimming curves given in CAD files. Then, they modify the integration scheme for trimmed elements to improve the accuracy of the numerical solution. Control points in the cut-out domain are deactivated so that the solver virtually recognize the cut-out region. The integration scheme subdivide a trimmed element into two region: normal triangular integration cell and curve triangular integration cell. The integration process of the normal triangular cell region is identical to the standard integration process of isogeometric analysis with the triangular Gauss quadrature points. For the curve triangular cell, NURBS-enhanced integration method [136] is used to improve the accuracy. This numerical treatment of the trimmed surface is simple and does not require parametric modification. Additionally, CAD modeling of the domain is straight forward. The example of rectangular surface with two trimming curve is shown in Fig. 5.4.

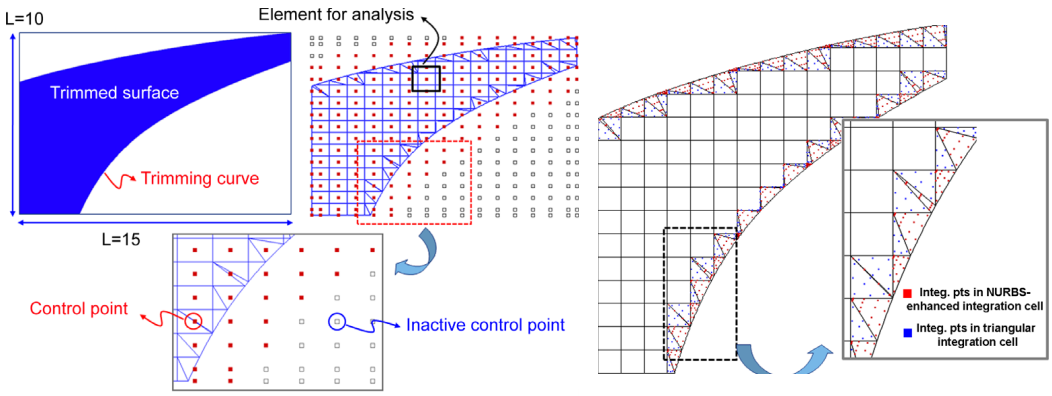

Figure 5.4: Elements for analysis is shown in blue line (image from [5]). Control points that has the span of influence outside the analysis domain is deactivated. Trimmed elements have two distinct partition for integration scheme: NURBS-enhanced integration cell and triangular integration cell.

Similar approach of numerical treatment is applying the Finite Cell Method (FCM) in the isogeometric framework [137, 138]. FCM is embedded domain method which appends a fictitious domain to the physical domain to form a simpler embedding domain where the analysis is performed. Schematic of FCM approach is shown in Fig. 5.5. During the integration process, elements in the fictitious domain is penalized so that the material is extremely compliant. Capturing the physical boundary in a good resolution directly correlates to the accuracy of the simulation result. Therefore, an adaptive integration scheme of finite cells is mostly implemented in the FCM. Advantages in the FCM are: exponential convergence rates in energy norm given that a problem is smooth and the simplification of mesh generation in the analysis domain. Most meshes are rectilinear cell grids. Main difference between the FCM and the one proposed by Kim et al. is that the FCM uses adaptive integration scheme that simply improves the accuracy of the solution as the refinement level increases without introducing a complication in the Gauss Quadrature point selection. However, any adaptive integration requires a local mesh refinement techniques. Schillinger et al. [6] and Ruess et al. [139] utilize the subdivision method in hierarchical NURBS to implement the adaptive integration scheme as illustrated in Fig 5.6. Since subdivisions only occur in trimmed elements, it is well suited for adaptive integration method.

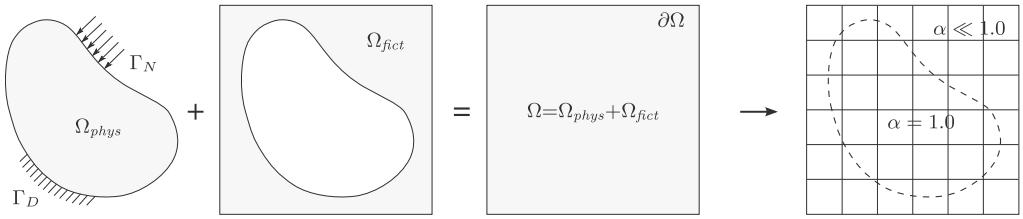

Figure 5.5: FCM extend physical domain, Ω_{phys}, combined by a fictitious domain, Ω_{fict}, to an embedded domain, Ω, which is easier to generate in CAD (image from [6]). Fictitions domain is penalized with a small value of α.

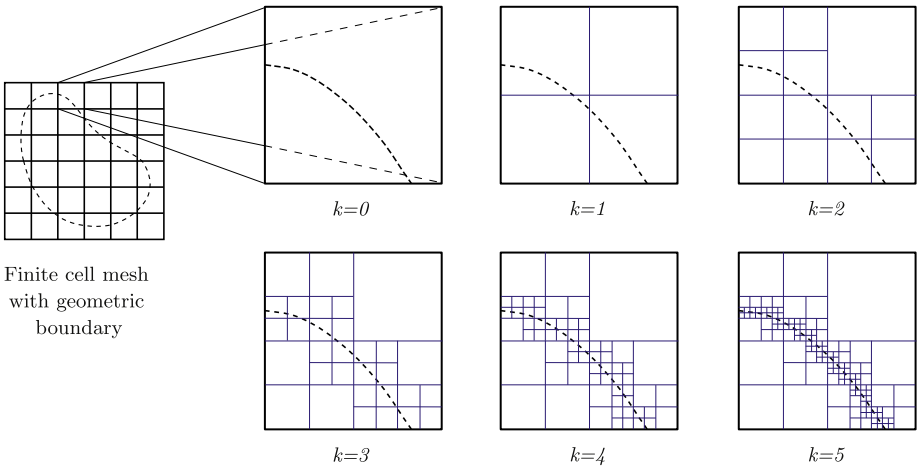

Figure 5.6: Adaptive integration for FCM (image from [6]); Only the elements on the boundary goes through subdivision, resulting a true local refinement.

5.2 LR B-spline for modeling a general trimmed surface

For non-CAD experts, it is challenging to come up with a complex spline parametrization for an arbitrary geometry. Given that one is determine to use T-spline, it is not so apparent where to place T-junctions and extraordinary nodes to correctly dimension the trimmed feature in a geometry. Therefore, the FCM provides a well-compromised approach in modeling a surface with an arbitrary trimmed feature. It simplifies modeling an analysis domain, which leads to a simple parametrization and mesh generation.

As discussed in the previous section, it is somewhat inevitable to adapt a local refinement technique to utilize FCM. Hierarchical NURBS is an option, but it inherently does not capture the local representation of cells like other locally defined splines. T-spline is a suitable option but there is another local parametrization technique that are simpler and closer to the B-spline.

Locally refined B-splines, denoted as LR B-splines [7] present a better local control and a direct operation on a spline space. In the following section, introduction of LR B-splines is presented followed by the implementation detail on the development of in-house IGA suite.

5.2.1 LR B Spline

This sub-section is a brief introduction to the theory of LR B-spline, which is a generalization of a tensor-product based B-spline. It provides a capability to adapt a true local refinement technique.

A conventional tensor product B-spline shows a limitation on generating a mesh with a true local refinement. In order to produce a biased mesh (descending or ascending trend of the size of elements), new internal knots can be inserted with a non-uniform distance. However, this results a mesh with elements with high aspect ratio and significant increase in unnecessary elements. Figure 5.7 illustrates this issue of tensor product refinement compared to the desired local refinement. Therefore, conventional B-spline is not suitable for an adaptive mesh refinement, which presents synergistic effect with a true local refinement that only refine the neighborhood of a selected region. Recently, Dokken et al. [140] proposed locally refined B-splines (LR B-splines) that is a generalization of conventional B-splines

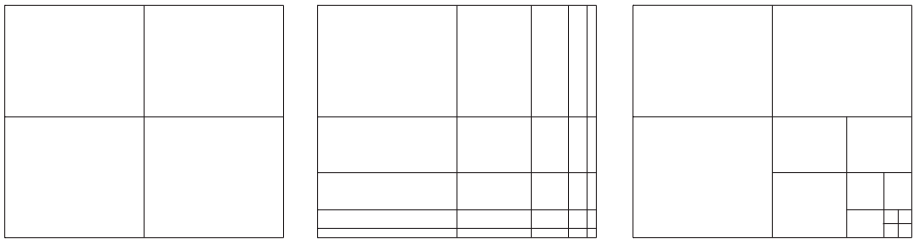

Figure 5.7: Tensor product refinement procedure to provide a small elements on the bottom-right corner generates undesired elements with high aspect ratio unlike the desired true local refinement (images from [7]).

with the extended local control. Johannessen et al. [7] further adapted LR B-splines in IGA framework and demonstrated their capability of usage in adaptive refinement.

A geometry represented in a conventional B-spline requires knot vectors that provide a parametric space. In the case of clamped B-spline which the end points are interpolated, a knot vector has $n+p+1$ knots where n is the number of linearly independent basis functions with the degree of p. The evaluation of each basis function only depends on $p+2$ knots. In LR B-splines, local knot vectors consist of $p+1$ non-decreasing knots that is associated to a single basis function. As an example, consider the knot vector, Ξ, associated with a quadratic basis function in Eq. 5.1. Ξ can be separated into 6 local knot vectors, $\Xi_1, ..., \Xi_6$.

$$\begin{aligned}
\Xi &= [0,0,0,1,2,2,3,3,3] \\
\Xi_1 &= [0,0,0,1] \\
\Xi_2 &= \quad [0,0,1,2] \\
\Xi_3 &= \qquad [0,1,2,2] \\
\Xi_4 &= \qquad\quad [1,2,2,3] \\
\Xi_5 &= \qquad\qquad [2,2,3,3] \\
\Xi_6 &= \qquad\qquad\quad [2,3,3,3]
\end{aligned} \tag{5.1}$$

Utilizing the local knot vectors, a two-dimensional B-spline, $B(\xi)$, is defined as in Eq. 5.2 where $B_\Xi(\xi)$ and $B_H(\eta)$ are univariate B-spline functions in each parametric direction.

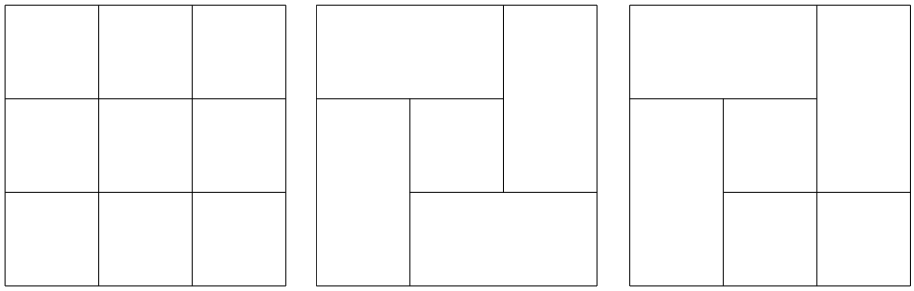

Figure 5.8: Different types of meshes (images from [7]).

$$B(\xi, \eta) = B_{\xi}(\xi) B_H(\eta) \tag{5.2}$$

There are several candidates for the type of mesh to be considered in the parametric space. A box mesh is a two-dimensional partition where a rectangular domain, $[\xi_0, \xi_n] \times [\eta_0, \eta_n]$ is divided into rectangular sub-domains by multiple horizontal and vertical lines. A tensor mesh is a box mesh where all the horizontal and vertical lines span the entire length across the whole domain. Lastly, an LR-mesh is a box mesh resulting from the sequence of single line insertion. In each sequence, a new line must start from an edge and traverse to the other end; it cannot stop in the middle of the box domain. From the definition, the mesh resulting from a subsequence of the mesh line insertions is also LR-mesh. Examples of all three meshes are shown in fig. 5.8.

The span of influence of a B spline basis function is identified by its support, which is defined as a set of ordered pair of parameters, (ξ, η), where the B spline basis function is defined. As an example, the support of a two dimensional B spline basis, $B : \mathbb{R}^2 \mapsto \mathbb{R}$ where

$$\begin{aligned} B(\xi, \eta) &= B_{\Xi}(\xi) B_H(\eta) \\ \Xi &= [\xi_0, ..., \xi_{p+1}] \\ H &= [\eta_0, ..., \eta_{q+1}] \end{aligned} \tag{5.3}$$

is $\{(\xi, \eta) : (\xi, \eta) \in [\xi_0, \xi_{p+1}] \times [\eta_0, \eta_{q+1}]\}$.

A horizontal line, $\varepsilon = [\xi_0^*, \xi_1^*] \times \eta^*$, is said to traverse the support of a B-spline with the associated local knot vectors, $[\xi_0, ..., \xi_{p+1}], [\eta_0, ..., \eta_{q+1}]$, when the following conditions are satisfied: 1) $\xi_0^* \leq \xi_0, \quad \xi_{p+1} \leq \xi_1^*$ and 2) $\eta_0 \leq \eta^* \leq \eta_{q+1}$. Similar idea applies to the vertical lines.

For a B-spline to be called an LR B-spline on an LR mesh, all the knot lines in all the dimension must be in the LR mesh. Moreover, the B-spline needs to have a minimal support, which leads to the formation of an unique set of LR B-spline functions given a LR mesh.

A B-spline is said to have minimal support on an LR mesh when the following conditions are satisfied. First, every horizontal knot line, $\varepsilon = [\xi_0^*, \xi_1^*] \times \eta^*$, of multiplicity n traversing the interior of the support can find n number of η^* in the local knot vector associated with the B-spline in η direction. Second, every horizontal edges, $\varepsilon = [\xi_0^*, \xi_1^*] \times \eta^*$, of the support can find at least one η^* in the local knot vector associated with the B-spline in η direction. Similar argument applies to the every vertical knot lines traversing the interior and the edges of the support.

Refinement in LR mesh is done by inserting a new knot line. Knot insertion process is derived from the one in the conventional B-splines. One notable difference is that the number of increase in the set of basis functions is identical to the number of increase in the set of local knot vectors. When a new knot is inserted, the length of the extended local knot vector of degree, p, is equal to $p + 3$. Therefore, the extended local knot vector must be split in two local knot vectors of length equal to $p + 2$. As an example, consider that a new knot, $\hat{\xi}$ in Eq. 5.4, is inserted between the knots ξ_{i-1} and ξ_i in the knot vector, Ξ, resulting two knot vectors, Ξ_1 and Ξ_2.

$$\begin{aligned} \Xi &= [\xi_1, \xi_2, ..., \xi_{i-1}, \quad \xi_i, ..., \xi_{p+1}, \xi_{p+2}] \\ \Xi_1 &= [\xi_1, \xi_2, ..., \xi_{i-1}, \hat{\xi}, \xi_i, ..., \xi_{p+1} \quad\quad\ ] \\ \Xi_2 &= [\quad \xi_2, ..., \xi_{i-1}, \hat{\xi}, \xi_i, ..., \xi_{p+1}, \xi_{p+2}] \end{aligned} \tag{5.4}$$

Then, the new basis functions, $B_{\Xi_1}(\xi)$ and $B_{\Xi_2}(\xi)$, associated with the knot vectors, Ξ_1 and Ξ_2, have the relation with the original basis function, $B_{\Xi}(\xi)$, shown in Eq. 5.5.

$$B_{\Xi}(\xi) = \alpha_1 B_{\Xi_1}(\xi) + \alpha_2 B_{\Xi_2}(\xi), \quad \text{where}$$

$$\alpha_1 = \begin{cases} 1, & \xi_{p+1} \le \hat{\xi} \le \xi_{p+2} \\ \frac{\hat{\xi}-\xi_1}{\xi_{p+1}-\xi_1}, & \xi_1 \le \hat{\xi} \le \xi_{p+1} \end{cases} \tag{5.5}$$

$$\alpha_2 = \begin{cases} \frac{\xi_{p+2}-\hat{\xi}}{\xi_{p+2}-\xi_2}, & \xi_2 \le \hat{\xi} \le \xi_{p+2} \\ 1, & \xi_1 \le \hat{\xi} \le \xi_2 \end{cases}$$

Refining process of LR-mesh often involves the sequence of multiple meshline insertions. In this case, any B-spline goes under the check whether the new meshline traverses the interior of the B-spline. If so, the B-spline need to be split. After this process, all new B-splines go under the check whether any existing meshline traverses the support of any B-splines in the updated spline space. Any traversed B-splines in the new spline space also needs to be split. When the new basis functions are created from the splitting process, there can be preexisting basis functions identical to one or both of new functions. In this case, the control point of the preexisting basis function is updated in two steps and the new function is simply ignored. First, transform the pair of control points into projective coordinate system. Second, sum the two control points and transform back to the original coordinate system. On the other hand, any new basis functions without any identical pair is simply added to the new spline space.

As can be noted, all the discussion up to this point can be easily extended to a three dimensional parametric space. As an example, three dimensional LR B spline basis will be a tensor product form shown in Eq. 5.3 except there is one more term for the third parameter. The following list shows some noticeable properties of LR B-spline:

1. Partition of unity: the sum of LR B-spline basis functions for any parameter value is equal to 1.
2. The result of a refinement procedure in LR B-splines is order independent.
3. The set of LR B-spline basis functions forming a spline space does not guarantee the linear independence.

Linear independence of a set of basis functions is crucial element deciding whether the spline

is analysis suitable. Johannessen et al. [7] do not provide the analytical proof; however, they observed that there were no linearly dependent set by checking with the peeling algorithm when the meshes were generated following the full span and the structured refinement techniques. They also conjecture that those two refinement techniques inherently produce a linearly independent set of basis functions, similar to the analysis suitable T-splines utilized for IGA [141].

5.2.2 Bézier extraction

The shape of standard finite element basis functions based on polynomial functions of a fixed degree does not change from element to element. In contrast, the shape of the spline basis functions depends on the knot vectors associated with them, and the span of influence can reach multiple elements. The evaluation of the spline basis functions often rely on the recurrence formula, resulting a difficulty in incorporating the IGA implementation into the existing finite element framework. This issue can be resolved by introducing the Bézier extraction for evaluating the basis functions, resulting a smooth and compatible implementation in accordance with the existing finite element framework.

The Bézier extraction is an operation that provides a mapping from a piecewise Bernstein polynomial onto a B-spline function. Thus, it sets a relation between piecewise C^0 Bézier elements to spline elements. As a result, it allows to use piecewise C^0 Bézier elements, which have consistent polynomial shape functions, as a building block of the finite element representation of a spline mesh.

The Bézier extraction for the LR B-spline used in our In-house IGA package follows the same procedure proposed by Scott et al [142]. developed for T-splines. Essentially, every LR B-spline, $N_a^e(\xi)$, associated with a set of local knot vectors is expressed in a linear combination of piecewise Bernstein polynomials, $\boldsymbol{B}(\xi)$, over element, e, as shown in Eq. 5.6 where $\boldsymbol{C^e}$ is a extraction operator row-vector of size $1 \times m$ with Bézier coefficients. m is number of Bernstein polynomials in a single knot span. There is always same number of Bernstein polynomials in a Bézier element; however, this is not the case for the LR B-spline elements, especially when a local refinement is performed in the LR mesh.

$$N_a(\xi) = \boldsymbol{C}^{\boldsymbol{e}}\boldsymbol{B}(\xi) \tag{5.6}$$

The Bernstein polynomials of degree, p over the domain $[-1, 1]$ is defined as in Eq. 5.7.

$$\begin{aligned} B_{i,p}(\xi) &= \frac{1}{2^p}\binom{p}{i-1}(1-\xi)^{p-(i-1)}(1+\xi)^{i-1}, \quad \text{where} \\ \binom{p}{i-1} &= \frac{p!}{(i-1)!(p+1-i)!}, \quad 1 \le i \le p+1 \end{aligned} \tag{5.7}$$

In CAD, the Bernstein polynomials are often evaluate in the domain of $[0, 1]$; however, it is preferred to be computed in bi-unit domain to utilize Gauss quadrature in finite element framework.

A Bézier extraction procedure for LR B-splines in our case is identical to the one for T-splines. First, the local knot vectors of degree, p are extended by inserting the first and last knots until their multiplicity reaches to $p + 1$. For example, consider the local knot vector of quadratic degree, $[0, 1, 2, 3]$ to be extended. After the extension, the local knot vector becomes $[0, 0, 0, 1, 2, 3, 3, 3]$. Extension process adds the unnecessary basis functions, so it is important to keep track of which function is the original LR B-spline function to be used in extraction. If the basis functions are numbered following the ascending order of knot, the LR B-spline has the number of $n_t + 1$ where n_t is the number knots added to the left end. After the extended knot vector is obtained, it goes through univariate extraction. The extraction operation is similar to the one for NURBS [143]. Main difference is that coefficient matrix, $\boldsymbol{C}$, from the operation has other rows associated to the newly added basis functions. Therefore, the row vector corresponding to the original LR B-spline function is needed. This work can be done with the connectivity array. Finally, the extraction operator vector for multivariate knot vectors is computed using tensor product of each row vector attained from univariate extraction in each parametric direction.

In the finite element formulation, the weak form of the governing equation requires the computation of shape functions, $\boldsymbol{R}(\boldsymbol{\xi})$, and their derivatives, $\frac{\partial \boldsymbol{R}(\boldsymbol{\xi})}{\partial \xi_i}$. Numerical integration is performed in element level. When Gaussian quadrature is used, shape functions and their derivatives are evaluated in parent domain, and it is necessary to compute the Jacobian

determinant, J^e.

The LR B-spline functions in each element are computed following Eq. 5.8, which employs the Bezier coefficients matrix, $\boldsymbol{C}^e$, for element e and the column vector of control point weights, $\boldsymbol{w}^e$, associate to the element.

$$\begin{aligned} \boldsymbol{R}^e(\boldsymbol{\xi}) &= \boldsymbol{W}^e\boldsymbol{C}^e\frac{\boldsymbol{B}(\boldsymbol{\xi})}{W^e(\boldsymbol{\xi})}, \quad \text{where} \\ W^e(\boldsymbol{\xi}) &= (\boldsymbol{w}^e)^T\boldsymbol{C}^e\boldsymbol{B}^e(\boldsymbol{\xi}) \end{aligned} \tag{5.8}$$

The first order derivatives with respect to the parent coordinates are computed as follows in Eq. 5.9.

$$\frac{\partial \boldsymbol{R}^e(\boldsymbol{\xi})}{\partial \xi_i} = \boldsymbol{W}^e\boldsymbol{C}^e\frac{\partial}{\partial \xi_i}\left(\frac{\boldsymbol{B}(\boldsymbol{\xi})}{W^e(\boldsymbol{\xi})}\right) = \boldsymbol{W}^e\boldsymbol{C}^e\left(\frac{1}{W^e(\boldsymbol{\xi})}\frac{\partial \boldsymbol{B}^e(\boldsymbol{\xi})}{\partial \xi_i} - \frac{\partial W^e(\boldsymbol{\xi})}{\partial \xi_i}\frac{\boldsymbol{B}(\boldsymbol{\xi})}{(W^e(\boldsymbol{\xi}))^2}\right) \tag{5.9}$$

The derivatives with respect to the physical coordinates are computed simply applying the chain rule to the the derivatives in parent coordinates as in Eq. 5.10

$$\frac{\partial \boldsymbol{R}^e(\boldsymbol{\xi})}{\partial x_i^e} = \sum_{j=1}^{dim}\frac{\partial \boldsymbol{R}^e(\boldsymbol{\xi})}{\partial \xi^j}\frac{\partial \xi^j}{\partial x_i^e} \tag{5.10}$$

where $\frac{\partial \boldsymbol{\xi}}{\partial \boldsymbol{x}^e} = \left(\frac{\partial \boldsymbol{x}^e}{\partial \boldsymbol{\xi}}\right)^{-1}$.

The jacobian determinant of the element e, J^e is computed as in Eq. 5.11.

$$J^e = \left|\frac{\partial \boldsymbol{x}^e}{\partial \boldsymbol{\xi}}\right| \tag{5.11}$$

Further detail procedure on computing Bezier coefficients is referred to [143, 142].

5.2.3 Local refinement techniques with LR B splines

There are three types of local refinement scheme suggest by Johannessen et al [7] as shown in fig 5.9: full span, minimum span, and structured mesh. Structured mesh is obtained by splitting all the knot spans of one of the basis functions affecting the element. This method prevents the production of elements with a bad aspect ratio and the case of generating

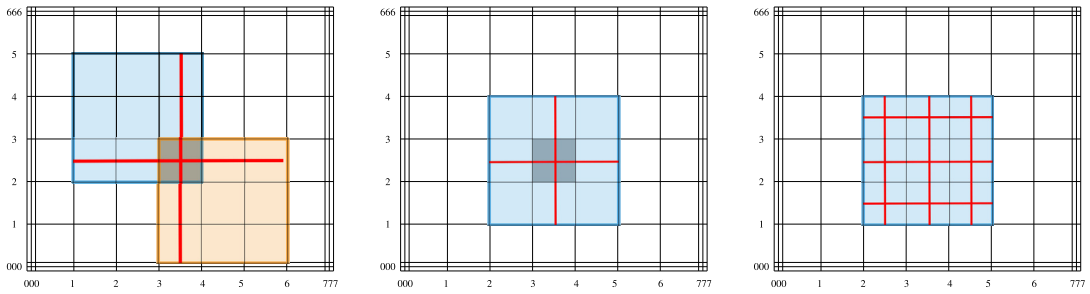

(a) Full span refinement (b) Minimum span refinement (c) Structured mesh

Figure 5.9: Full span method (a) inserts the meshlines that split all basis functions on the element. Minimum span methods (b) inserts two meshlines that split one of the basis functions on the element. Structured mesh method (c) inserts the meshlines that split all the knot spans of the selected basis function on the element (images from [7]).

linearly dependent set of basis functions. Therefore, this scheme was chosen for the adaptive integration method in our in-house IGA package. One uncertain step is the selection of a basis function that leads the splitting process. When the order of the spline is even, it is somewhat clear which basis function has the parametric center of its support closest to the center of the knot span of the element. When the order of the spline is odd, there can be multiple basis functions that has same distance from their parametric center to the center of the knot span of the element. In this case, a random selection of the basis function can be done.

With these local refinement technique, it is possible to locally refine a set of elements to improve the accuracy of finite element analysis. A common approach to this type of adaptive refinement process aims to minimize the global energy error leading to the mesh with more or less an uniform error distribution. This is a nice way to finalize the analysis mesh represented by LR B spline.

In this study, most of geometric feature such as a circular notch and a crack are represented exactly with a proper placement of control points. Therefore, the local refinement is mainly used at the location of stress concentration to improve the accuracy of analysis without having too many degrees of freedom. This helps to reduce the computation time, especially helpful for an optimization study that can easily require thousands of simulations.

As an example, a quarter plate with a semi-circular notch is modeled with bi-quadratic B spline basis functions as shown in Fig. 5.10 (a). In the figure, blue lines shows the boundary of elements, and the red circular points are control points. The initial mesh has a total of 36 elements. The midpoint of the circular arc is chosen to be the point of interest which leads to the local refinement in the example mesh. The first step is to identify the nearest neighboring elements, which are colored in light green in Fig.5.10 (b). Next step is to choose the basis functions supporting the identified elements. Following the structured refinement technique, two basis functions that are closest to the center of knot span of the identified elements are selected as shown in Fig. 5.10 (c). Last step is to insert meshlines that split all the knot spans of selected basis functions. This can be done by identifying the union of the supports as shown in blue in Fig. 5.10 (c) and defining meshlines that subdivide the support. The result of the local refinement process is shown in Fig. 5.11. As can be seen, only the region of interest has refined elements by subdivision from inserting meshlines. Moreover, a meshline insertion does not change the spline mesh, parametrically nor geometrically; therefore the continuity of the spline mesh is not disturbed. The theoretical detail on the local refinement technique is referred to [7]. In this framework, LR B spline can provide an efficient approach to improving accuracy of analysis without significantly raising the computational cost.

5.3 Modeling a crack with LR B-spline

The capability in LR B splines to locally refine the mesh can be utilized to model local discontinuities on a geometry such as cracks. To simulate a linear elastic fracture mechanics problem, a crack is often inserted to a mesh as a geometric discontinuity. In this case, the continuity across a line crack is C^0. When a geometry is modeled with linear spline functions, there is no need to reduce the continuity at the boundary of each element since it is already C^0. However, when higher degree spline functions are used to model a geometry, it is necessary to insert a meshlines where the crack is about to be defined in order to enforce the C^0 continuity across the crack. This work only focuses on modeling two dimensional cracks. Modeling a two dimensional crack, the multiplicity of at a specific knot in both parametric direction need to be increased when the degree of splines are higher than one.

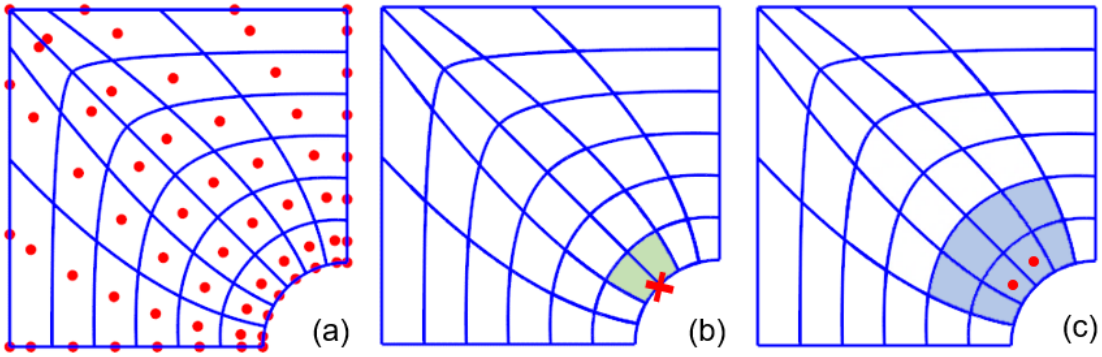

Figure 5.10: A quarter plate with a semi-circular notch modeled with bi-quadratic B splines; (a) initial mesh before a local refinement; (b) X-mark shows the location where the local refinement is applied; elements colored in light green are nearest elements to the refinement point; (c) two control points are selected from the nearest elements; blue region shows the union of the supports of two LR B spline basis.

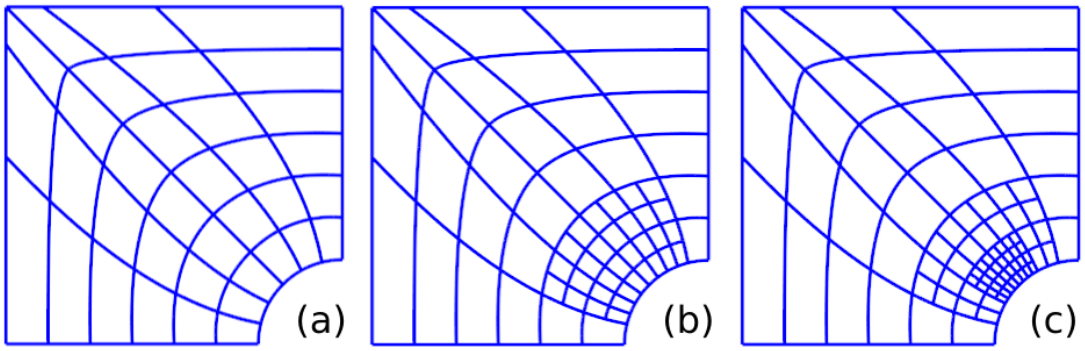

Figure 5.11: The example pregression of local refinement on a quarter plate with a semi-circular notch model; (a) initial mesh; (b) mesh after a first level of local refinement; (c) mesh after a second level of local refinement.

Let us assume that the crack which traverses a mesh is represented by the knot line, $\xi^* \times [\eta_0, \eta_1]$, and this crack is inserted on a quarter plate with a semi-circular notch as shown in Fig. 5.12 (a). If non-local splines such as NURBS are used in modeling a geometry, two internal knots, $\xi = \xi^*$ and $\eta = \eta_1$, associated with the green lines in Fig. 5.12 (b) are inserted to reduce the continuity. Since $\eta = \eta_0$ is at the boundary of the mesh, there is no need to insert a knot there. As discussed in the previous section, a knot insertion is a global refinement technique; therefore, the knot lines where the continuity is reduced span the entire mesh. After the insertion, control points lying on the crack line needs to be duplicated. At the final step, the pairs of coincident control points on the crack line needs to be properly assigned to adjacent elements to induce the discontinuity across the crack line.

On the other hand, the meshlines inserted in a LR B spline mesh does not necessarily span the entire mesh. The meshline, $\xi^* \times [\eta_0, \eta_1 + q\Delta\eta]$ where $q = 2$ is the degree LR B spline in η direction, is inserted to reduce the continuity across $\xi = \xi^*$. The meshline traverses $q\Delta\eta$ distance from the tip of the crack in η direction so that it completely splits the support of basis functions near the tip of the crack. The other meshline, $[\xi^* - p\Delta\xi, \xi^* + p\Delta\xi] \times \eta_1$ where $p = 2$, is inserted to enforce C^0 continuity at the crack tip. This meshline traverses $p\Delta\xi$ distance from the tip of the crack in ξ direction so that it completely splits the support of basis functions near the tip of the crack in ξ direction. The result of the insertion process is shown in Fig. 5.12 (c). As can be noted, meshlines do not fully span the entire domain of the mesh. Consequently, it localize the region of low continuity. Although it is not so apparent in this example since the mesh is relatively coarse for the demonstration purpose, once can easily deduce that the localized region of lower continuity by meshline insertions can be significantly smaller compared to the one in tensor mesh when the element sizes are much smaller. This can be further improved when the local refinement technique is used near the crack tip.

In this approach of defining cracks in a mesh, the lower bound of the length of a crack depends on the size of elements in a mesh. When NURBS is used, elements with high aspect ratio can be easily produced as a result of knot insertions. However, meshline insertions followed by a local refinement near the crack in LR B spline mesh can prevent such a highly

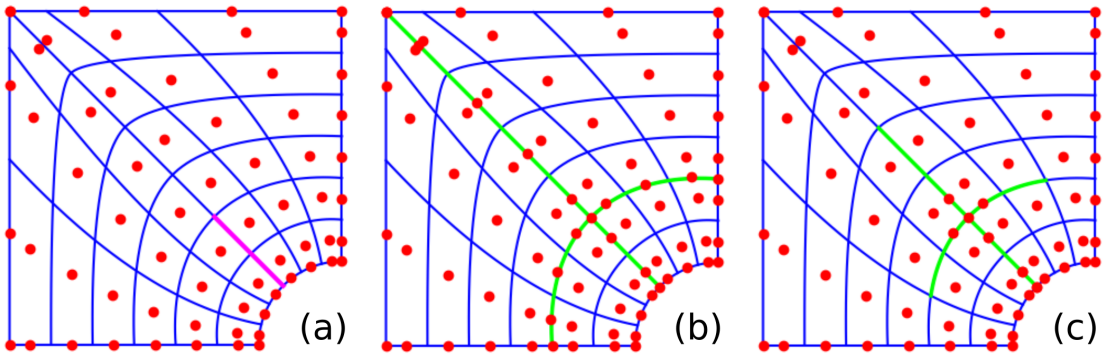

Figure 5.12: Modeling a crack on a quarter plate with a semi-circular notch; (a) magenta line is the crack that is about to be inserted; (b) Green lines which are inserted to reduce the continuity in the mesh spans whole domain; (c) Meshlines in LR B spline framework only affect the local continuity of the mesh.

biased mesh.

5.4 Development of an IGA package: LRSFEM

In the beginning of this project, there were no IGA software openly available that utilizes LR B spline to model composite structures. In this project, in-house IGA package, called LRSFEM (Locally Refined Spline Finite Element Method), with features discussed in the previous sections are developed in order to proceed to the next phase. LRSFEM has three main constituent: 1) preprocessing module, 2) linear solver, and 3) postprocessing module. All three modules are written in *C++* to take the advantage of Objected Oriented Programming framework in addition to the high computational performance. Instead of using a text-based input file format that common commercial FEM software adapt, LRSFEM uses *pybind11* to provide a dynamic library for *Python* so that users can directly use main functionality such as model generation, solver, and post-processing along with visualization in *Python*. By providing *Python* API, it becomes very efficient to utilize other modules provided in *Python* along with LRSFEM. Following subsections provide brief discussion on each ingredient of the in-house IGA package.

5.4.1 Preprocessing module: geometry and mesh generation

The main purpose of the preprocessing module is to provide objects that are used for a spline geometry generation and for a LR mesh suitable for IGA.

"OpenNurbs" object is used to generate an open NURBS geometry. Input parameters are knot vectors, coordinate values of control points, dimension of parameter space, and degrees of spline basis functions. These are the basic set of information needed to define a NURBS. "OpenNurbs" object has some basic methods such as knot insertion and degree elevations to operate on spline basis functions. These methods are implemented closely following the "igakit" [144], which is a python library that has the Fortran implementation of the NURBS routines in Piegl's book [108].

Once an elementary NURBS object is created, "LRMesh" object can be instantiated and initialize a LR B spline mesh consisting of three main constituent: "Vertex", "Facet" and "Cell". Each vertex object contains each control point data along with the parametric information of associated LR B spline basis function such as knot vectors and degrees. Facets are building block of a two dimensional mesh. Each facet object holds information on knot spans and a set of pointer addresses of vertices which include the area of the facet as part of their support. Similarly, cells are building block of a three dimensional mesh. Each cell object holds information on three dimensional knot spans and a set of pointer addresses of vertices which include the volume of the facet as part of their support. The set of vertices that either a cell or a facet has as an attribute provides covering relation when a mesh is represented as a simple two layered Directed Acyclic Graph (DAG). The discretization data management library for unstructured grids from Portable Extensible Toolkit for Scientific Computation (PETSc) [145, 8] treats mesh components such as vertex, edge and face as a point with an identification integer value. A mesh is represented as a Hasse Diagram that displays a partially ordered set using the covering relation. An example of a simple triangular mesh and its representation in the Hasse diagram is shown in Fig. 5.13 (a). As an example of a covering relation, the left face in Fig. 5.13 (b) is covered by edges numbered 6, 7, and 8. The edge number 6 is covered by two vertices numbered 2 and 3.

In "LRMesh" object, there is no convenient way to define edges since the vertices repre-

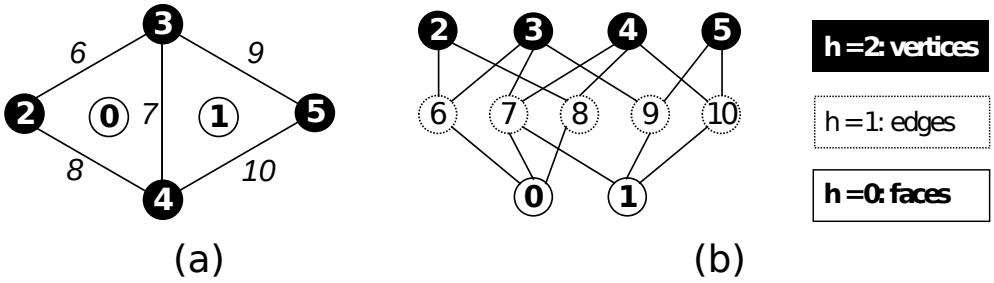

Figure 5.13: An example of a 2D doublet mesh. (images are from [8]) (a) two triangular facets are sharing the edge in the middle and two vertices on top and bottom; (b) The Hasse diagram for the mesh displays the covering relation.

sent control points which are not necessarily interpolatory. So, it becomes easier to define a covering relation of either facets or cells directly with vertices, of which their support contains the area or the volume of a facet or a cell. In this mesh structure, it is efficient to operate on the local data on a mesh. One can identify a set of vertices that have non-zero spline basis functions that are affecting a particular facet or cell. "LRMesh" object stores a set of vertices as a *C++* vector object. The same approach applies to the storage of a set of facets and a set of cells. This subsection is intended to provide the implementation of a local refinement method and the implementation of a crack insertion method in "LRMesh" object.

Before working on the insertion process of meshlines to a mesh for a refinement, facets or cells that are neighboring the region of interest need to be identify. In the proceeding discussion, it is assumed that the region of interest is defined as a point location defined in a parametric coordinate, and a mesh is in a two dimensional parametric space; therefore, facets are the main building block. It is possible to iterate on a set of facets stored in a mesh to identify whether each facet area contains the point location; however, this process is computationally not efficient and easily slows down the refinement process. In LRSFEM, *Multimap* objects which is a dictionary-like data structure that stores pairs of key and value are created during the initialization process of "LRMesh" object. A nice feature of *Multimap* is that multiple values can be paired with a same key, and *Multimap* can use keys to sort its sequence of data when an ordering relation is provided. Without going too much in detail, a

LR B spline mesh can produce a *Multimap* which keeps pairs of pointer addresses of facets as a set of values and associated knot values for facets as a set of keys. Because facets are sorted in order, it becomes computationally efficient to find a set of facets identified with specific knot keys. The *equal range* method defined in *Multimap* object can be used to find a set of neighboring facets provided a knot values of a point location. Once the set of neighboring facets are identified, a single vertex from each facet is chosen. From those selected vertices, meshlines are computed so that they splits the union of the supports of vertices. As a final step, these meshlines are inserted following the method introduced by Johannessen et al. [7], and the all the steps repeat for each refinement level. At the end, a new set of facets and vertices are created. They are stored in "LRMesh" object and *multimap*s are updated with new facets. The local refinement implementation is summarized in Alg. 1.

ALGORITHM 1: 2D Local refinement method in LRMesh object

Data: Knot coordinates of a point location and refinement level are inputted
Result: New facets and new vertices are produced after meshline insertions

```
for Each refinement level
    Find neighboring facets using multimap
    Gather vertices from found facets
    Define set of meshlines which splits the union of the supports of vertices
    for Each meshline
        Identify facets that needs to be subdivided
        Subdivide those facets
        Split vertices that the meshline splits their support
        Append new vertices to "LRMesh" object
        Append new facets to "LRMesh" object
        Update multimaps Update the covering of facets by either removing association to old
          vertices or adding new vertices to the covering relation
    end
    Remove old subdivided facets from the mesh object
    Remove old split vertices from the mesh object
end
```

"LRMesh" object has a method to insert a two dimensional crack. The process of crack insertion is similar to the local refinement since it requires the meshline insertion; however, meshlines are on the edges on facets rather than they traverse across the facets in order to subdivide like in the local refinement process. The information on meshlines that need to be inserted to a mesh is provided user as a set of ranges for each knot direction. Furthermore, meshlines do not subdivide existing facets; therefore, there is no need to create a new facets.

Once the vertices that the meshlines split their support are identified, they go through the refining process described by Johannessen et al. [7] to produce the new set of vertices. Identifying these vertices involves two steps. First, facets that are adjacent to the crack line is found using *multimap* in "LRMesh" object. Since the sequence of data are sorted in *multimap*, this process is quick. Each facet stores a set of vertices as a *C++* vector object. The support of each vertex includes the area of the facet. Therefore, the second step only requires to loop through these vertices to identify the ones that the meshlines split their support. When the meshline insertions are complete to achieve proper discontinuity over a crack line, next step is to duplicate the control points on the crack. In a two dimensional spline surface, adjacent facets are either in one side or the other from the crack line. Pairs of coincident vertices need to decide which facet it will belong to. At this point, it does not matter which one needs to be in which facet since two vertex are identical in a physical location and parametrization. It just need to be made sure that the if one is in one facet than the other pair belongs to the facet in the opposite side. Summary of the crack insertion process is shown in Alg. 2.

5.4.2 Bi-harmonic solver

In the isogeometric analysis, identical basis representing a geometry is used to form a solution space of the numerical method. This idea of using isoparametric basis is an important building block of finite element framework. Traditional elements such as Lagrangian elements utilize polynomial functions as the basis, thanks to their simplicity and well known approximation properties and theorems. In IGA, the identical set of spline basis used in modeling a geometry forms the solution space. It is important that spline basis functions satisfy the sufficient conditions to provide the convergence in the analysis [146]: 1) a basis is at least C^1 inside the element, 2) a basis is at least C^0 on the boundary of the element, and 3) the set of basis can represent all linear functions (completeness). First two conditions are not restrictive to splines. Third condition is satisfied by a partition of unity. Therefore, a spline basis with a partition of unity can ensure the convergence in the finite element framework.

ALGORITHM 2: 2D crack insertion method in LRMesh object

Data: Meshlines for 2D crack are provided
Result: Continuity across the crack line is C^0, and new vertices are created on the crack line.

```
Identify facets adjacent to the crack line using multimaps
From adjacent facets, gather vertices need to be refined
for Each meshlines
    Split vertices that the meshline splits their support
    Append new vertices to "LRMesh" object
    Update the covering of facets by either removing association to old vertices or adding new
      vertices to the covering relation
end
Remove old split vertices from the mesh object
Create a set of adjacent facets in side A from the crack line
Create a set of adjacent facets in side B from the crack line
for Each facet in side A
    for Each vertex in covering relation
        Remove association to the new vertex from duplication to keep only one vertex in
          coincident vertex pair
    end
end
for Each facet in side B
    for Each vertex in covering relation
        Remove association to the original vertex from duplication keep only one vertex in
          coincident vertex pair
    end
end
```

The strong form of a linear elastostatic problem is stated as follows. Given $f_i : \Omega \to \mathbb{R}$, $g_i : \Gamma_{D_i} \to \mathbb{R}$, and $h_i : \Gamma_{N_i} \to \mathbb{R}$, find $u_i : \overline{\Omega} \to \mathbb{R}$ such that

$$\begin{aligned} \sigma_{ij,j} + f_i &= 0 \quad \text{in}\Omega, \\ u_i &= g_i \quad \text{on}\Gamma_{D_i}, \\ \sigma_{ij} n_j &= h_i \quad \text{on}\Gamma_{N_i}, \end{aligned} \tag{5.12}$$

where $\overline{\Gamma_{D_i} \bigcup \Gamma_{N_i}} = \Gamma$ and $\Gamma_{D_i} \bigcap \Gamma_{N_i} = \emptyset$.

By multiplying weighting function, w_i and taking the integration by part, the weak form is formulated. Given $f_i : \Omega \to \mathbb{R}$, $g_i : \Gamma_{D_i} \to \mathbb{R}$, and $h_i : \Gamma_{N_i} \to \mathbb{R}$, find $u_i \in S_i$ such that for all $w_i \in V_i$

$$\int_\Omega w_{(i,j)} c_{ijkl} u_{(k,l)} d\Omega = \int_\Omega w_i f_i d\Omega + \int_{\Gamma_{N_i}} w_i h_i d\Gamma, \tag{5.13}$$

where c_{ijkl} is elastic coefficient, and u_i satisfies the Dirichlet boundary condition on Γ_{D_i}. The weak form can be visually simplified with bilinear and linear functional notation.

$$\begin{aligned} a(\mathbf{w}, \mathbf{u}) &= L(\mathbf{w}), \quad \text{where} \\ a(\mathbf{w}, \mathbf{u}) &= \int_\Omega w_{(i,j)} c_{ijkl} u_{(k,l)} d\Omega \\ L(\mathbf{w}) &= \int_\Omega w_i f_i d\Omega + \int_{\Gamma_{N_i}} w_i h_i d\Gamma. \end{aligned} \tag{5.14}$$

In order to solve the problem numerically, Galerkin's method is used to turn the weak form into a system of linear equations. In Galerkin's method, the finite dimensional subspaces is explored to find a trial solution, $\mathbf{u}^h$ and weighting function, $\mathbf{w}^h$ and assume that there exist a lifting g^h which satisfy $g_i^h = g_i$ at Γ_{D_i} in the finite dimensional trial solution space. Therefore, the trial solution has a following decomposition: $\mathbf{u}^h = \mathbf{v}^h + \mathbf{g}^h$ where $\mathbf{v}^h$ in finite-dimensional weighting functional space. As a result, the following expression is obtained

$$a(\mathbf{w}^h, \mathbf{v}^h) = L(\mathbf{w}^h) - a(\mathbf{w}^h, \mathbf{g}^h). \tag{5.15}$$

From the isoparametric formulation, $\mathbf{u}^h$ is expressed as

$$u_i^h = \sum_A N_A d_{iA} + g_i^h, \tag{5.16}$$

where N_A is a basis, and d_{iA} is a i-th component of control variable corresponding to the basis, N_A. After the substitution, a linear system can be built as follows

$$\begin{aligned} \mathbf{Kd} &= \mathbf{F}, \quad \text{where} \\ K_{PQ} &= a(N_A \mathbf{e}_i, N_B \mathbf{e}_j), \\ F_P &= L(N_A \mathbf{e}_i), \quad d_Q = d_{jB}. \end{aligned} \tag{5.17}$$

The flow chart of a standard finite element implementation is shown in fig. 5.14. The steps colored in green are places where the formulation needs to be modified to be compatible with IGA. Main difference implementing IGA comes from storing parametric data for spline object and building connectivities along with the mesh information. After the assembly, the size of a structural stiffness matrix can be large; however, many components in the matrix will be zero. To reduce the memory usage, a structural stiffness matrix is stored as a sparse matrix following CSR format. For high performance computing capability, MUMPS (MUltifrontal Massively Parallel sparse direct Solver), a parallel sparse direct solver library, is used [147, 148]. To solve a linear system, MUMPS uses LU decomposition for an unsymmetric matrix and uses cholesky decomposition for a symmetric matrix. Since MUMPS is a parallel solver, it allows to solve a large scale linear system using MPI framework.

In LRSFEM, "Mechanical3D" object provides a method called "solve" to solve a linear elastic problem after it is initialized with a "LRMesh" object. As a result, it stores a control variables such as nodal forces and nodal displacements in *C++* vectors, which can be accessible as a *numpy* array in *Python*. Once the control variables are obtained as a solution, stress and strain at each integration points can be computed.

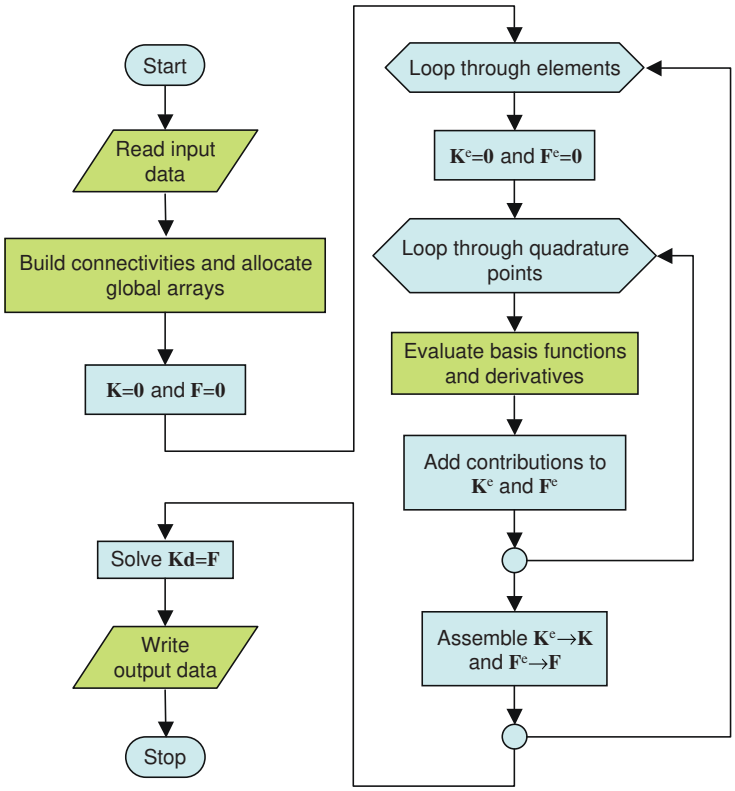

Figure 5.14: Flow chart of a standard finite element framework. Steps colored in green can be modified to make it compatible with IGA (image is from [9]).

5.4.3 Postprocessing module: stress/strain extrapolation and visualization

There is no simple library in *C++* or in *Python* that allows to visualize LR B splines surfaces. A wireframe plot can be used to represent a two dimensional spline surfaces. In this case, smooth edges of spline facets are segmented in a straight lines. Computing a set of points on the edge of spline surface is not so challenging since the knot values are already known, and is not so expensive. To visualize the actual faces on a spline surface or volume, each spline facets need to be discretized in to a mesh. The number of evaluations on a spline object increase exponentially to capture the smoothness of the geometry. *Python* implementation of a visualization module seems to be okay for a wireframe plots; however, it was not proficient to visualize 3D contour plots. Therefore, the development in postprocessing visualization is implemented in *OpenGL* written in *C++*.

OpenGL is a specification for functions used in programming to modify graphics. It is a rule for API developers that tells what the outcomes are supposed to be and how they are performed. There are multiple API libraries that allows to use *OpenGL* implementation. In LRSFEM, *Qt* is used to provide a visualization of spline objects and graphical interface to it such as panning, zoom, and rotation features in a visualization window. Compared to other libraries, *Qt* provides some functionality that makes it more convenient to manipulate colors in *OpenGL* framework.

There is an open tutorial available in online called "LearnOpenGL" [149], which covers all the necessary components needed to develop this visualization module using *OpenGL*. It is referred to this resource for detail on *OpenGL* graphics programming. The graphics pipeline of *OpenGL* performs necessary works to visualize a 3D models in to a 2D representation on a window, and these steps are be parallelizable. This is one of the reasons why GPUs contains a multitude of small processing cores. The visualization module in LRSFEM directly uses *OpenGL* functionality which allows to use the graphics unit. Therefore, it takes much less time to visualize a 3D spline object and manipulate the graphics.

A building block of a graphical mesh is triangle since a GPU is particularly good at drawing thousands of triangles in parallel. As a result, each facet in a LR B spline mesh is discretized into a triangular mesh. Computing the 3D coordinates of each triangles are

not difficult; however, computing the stress or strain values at the arbitrary location on a spline object is not straight forward since stress and strain vectors are calculated on integration points. In a standard finite element approach, stress values are extrapolated to the node using polynomial basis functions. For LR B spline functions, it is not clear how to extrapolate. The number of control points spanning an element can often be larger than the number of integration point after local refinements.

In LRSFEM, the number of integration points and the number of Bezier control points in an element are the same. A linear system can be set up to enforce that the stress values at Bezier control points so that the interpolated result provide correct stress values at the integration points. In this way, an approximation field of stress contour at each spline object is provided for visualization.

5.4.4 Verification

For a verification, the NURBS-based isogeometric analysis is performed on an infinite plate with a circular hole under an uniform tension. This is a classical elasticity problem that has an analytical solution to be compared. The analyses are performed with bi-quadratic ($p = q = 2$) and bi-cubic($p = q = 3$) NURBS elements followed by h-refinement to examine the convergence with $L - 2$ norm error of stress [150] following the Eq. 5.18,

$$L^2(\Omega) = \left(\int_{\Omega} |\boldsymbol{\sigma_{exact}} - \boldsymbol{\sigma_{numerical}}| d\Omega \right)^{1/2} = \mathcal{O}(h^k), \tag{5.18}$$

where Ω is the whole domain of the structure, and h refers to the diameter of an element.

The infinite plate is modeled with the finite quarter plate with symmetry boundary conditions and correct traction applied following the exact solution. The schematic of the quarter plate is shown in fig. 5.15. Modeling details are referred to [9]). The analytical solution shown in Eq. 5.19 is from [151].

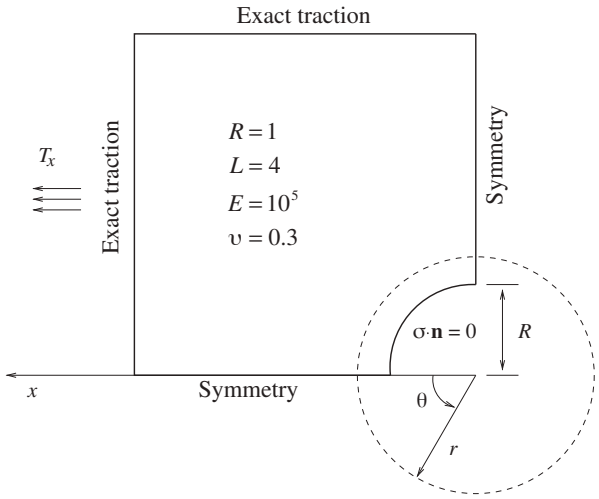

Figure 5.15: Quart plate model with applied boundary conditions (image is from [9]).

$$\begin{aligned}
\sigma_{rr}(r,\theta) &= \frac{T_x}{2}\left(1-\frac{R^2}{r^2}\right)+\frac{T_x}{2}\left(1-4\frac{R^2}{r^2}+3\frac{R^4}{r^4}\right)\cos 2\theta,\\
\sigma_{\theta\theta}(r,\theta) &= \frac{T_x}{2}\left(1+\frac{R^2}{r^2}\right)-\frac{T_x}{2}\left(1+3\frac{R^4}{r^4}\right)\cos 2\theta,\\
\sigma_{r\theta}(r,\theta) &= -\frac{T_x}{2}\left(1+2\frac{R^2}{r^2}-3\frac{R^4}{r^4}\right)\sin 2\theta,
\end{aligned} \tag{5.19}$$

In the numerical analysis, T_x is assumed to be 10; therefore, the stress contours were expected to converge with the stress concentration of $\sigma_{xx} = 30$ at the vicinity of the hole boundary.

Examples of bi-quadratic and bi-cubic meshes for the quarter plate model is shown in fig. 5.16. As can be seen, higher degree spline elements have more control points around each element.

Contour plot of stress value in $x-$direction is shown in fig. 5.17 for both bi-quadratic and bi-cubic meshes. Convergence plot of $L2$-norm error against the largest diameter in the mesh is shown in fig. 5.20. As can be seen, rate of convergence is close to the degree of splines in the NURBS surface.

To evaluate the FCM, a quarter plate is modeled in rectangular domain, and adaptive refinements up to 4^{th} order are applied for both bi-quadratic and bi-cubic meshes as shown

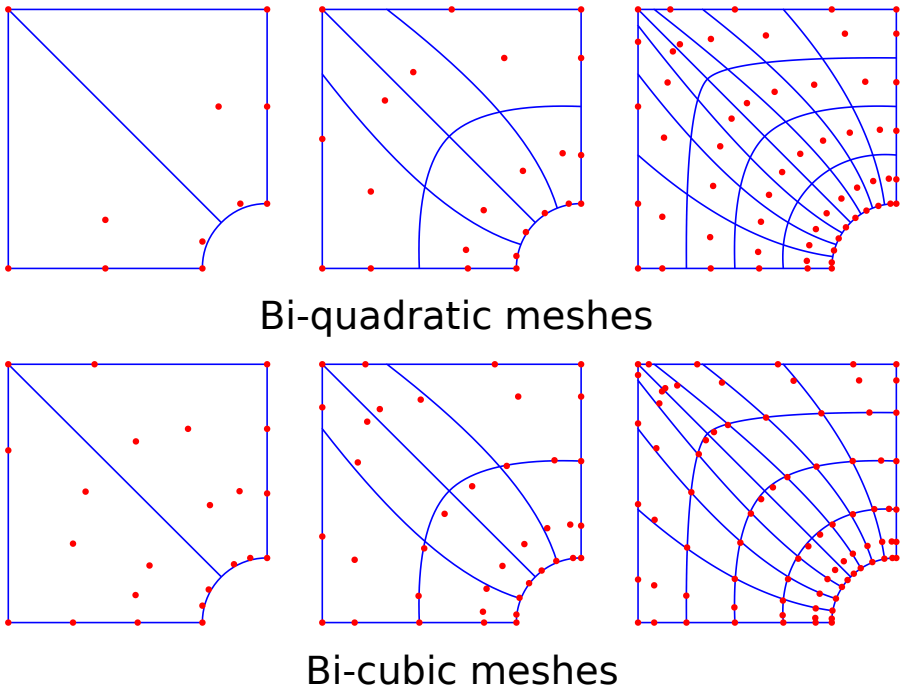

Figure 5.16: Examples of bi-quadratic and bi-cubic meshes for the quarter plate model. Red dots are control points where the control variables are evaluated. Higher degree NURBS elements have more control variable compared to lower degree elements.

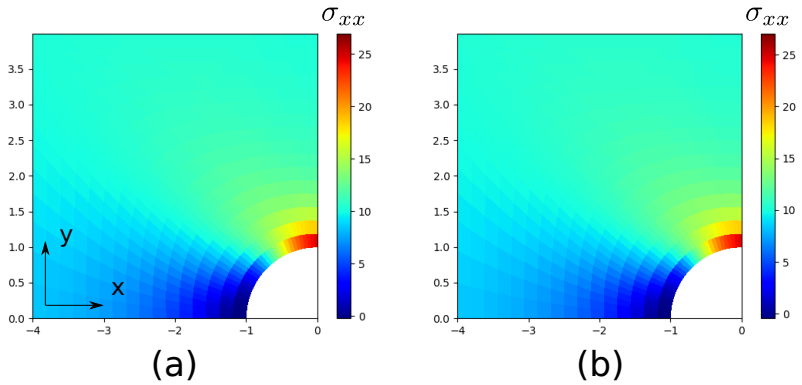

Figure 5.17: Contour plot of σ_{xx} for (a) bi-quadratic mesh and (b) bi-cubic mesh.

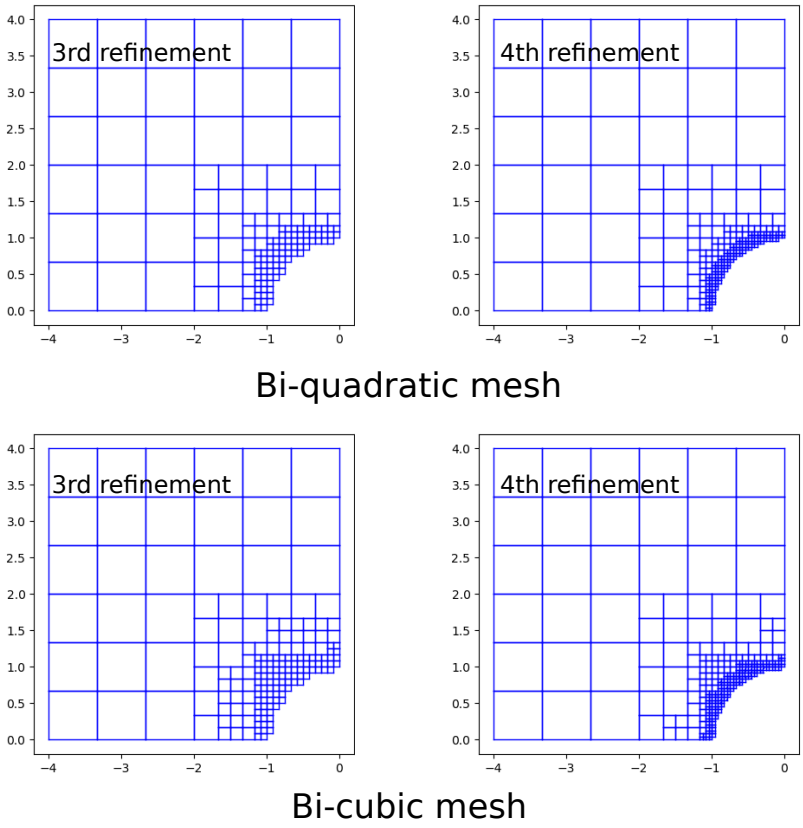

Figure 5.18: Examples of bi-quadratic and bi-cubic meshes for the quarter plate model using structural adaptive refinement.

in fig. 5.18.

Contour plot of stress value in $x-$direction is shown in fig. 5.19 for both bi-quadratic and bi-cubic meshes in 4^{th} order refinement. As can be seen, stress concentrations for both degree are converging to the correct value. The convergence plot of $L2$-norm error against the degrees of freedom is shown in fig. 5.21 and compared to the exact model using NURBS. As can be seen, the precision in FCM up to 4^{th} order is not as good compared to the exact model. For the curvature of a given hole, it is expected to provide better precision with a higher order of adaptive refinement.

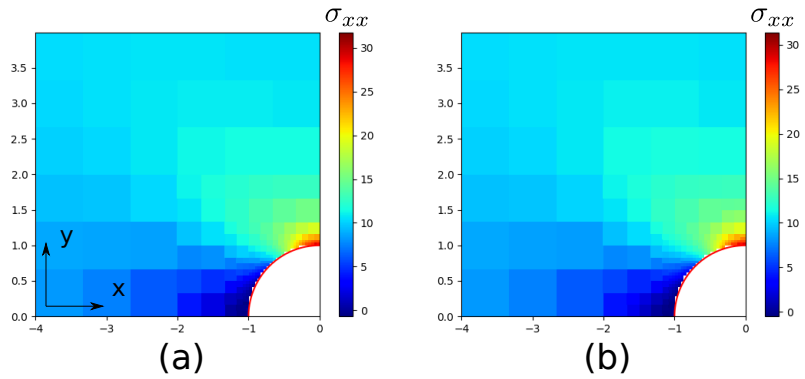

Figure 5.19: Contour plot of σ_{xx} using FCM for (a) bi-quadratic mesh and (b) bi-cubic mesh. Both are in 4^{th} refinement.

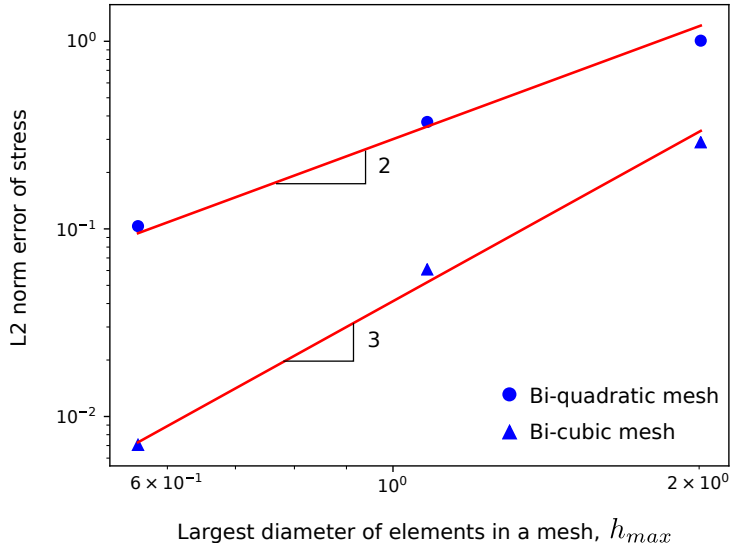

Figure 5.20: Convergence behavior of NURBS elements. Rate of convergence matches with the degree of spline surfaces.

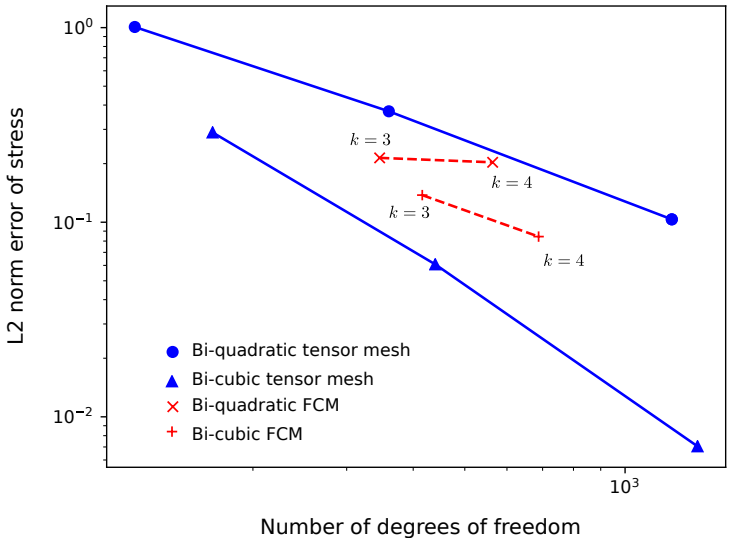

Figure 5.21: Convergence behavior of FCM compared to the exact NURBS meshes. k refers to the order of adaptive refinements.

Chapter 6

ISOGEOMETRIC APPROACH TO OPTIMIZE A FRACTURE RESISTANCE OF COMPOSITE STRUCTURES

The preceding chapter sets a nice numerical tools for analyzing structural response of composite parts featuring CTI with and without a geometric discontinuity such as a crack. In this chapter, IGA framework is utilized to simulate a fracture behavior of composites featuring CTI. Furthermore, optimization study is performed to identify the optimal fiber paths for two main geometries, 1) a rectangular plate with a semi-circular notch and 2) T-joint with filleted corners, that maximize their fracture resistance. In order to set up a proper simulation of fracture mechanics simulations on those structures, it is necessary to understand how composites fracture. In the following sections, the fracture behavior of composite materials is briefly introduced. Then, a method of providing a smooth distribution of fiber path over a structure is discussed. Next, two main optimization methods that are used in this work are briefly introduced. Lastly, optimization results on two geometries are presented with discussion on their mechanical implication.

6.1 Fracture mechanics of composites

Structures exhibit three types of fracturing behavior: 1) brittle, 2) ductile and 3) quasibrittle [10].

The first type, so called brittle fracture, is often observed in fine-grained ceramics, glass polymers. In the presence of a crack or notch, there is a region of highly nonlinear stress state called a fracture process zone (FPZ). Materials exhibiting a brittle fracture has a negligible size of FPZ in front of a crack compared to the structural size as illustrated in Fig. 6.1 (a). where the discontinuity in stress distribution from stress-free crack boundary to the front of crack tip is shown below the schematics. In this case, we can fairly assume that the most of domain on the structure behaves linearly; therefore, the linear elastic fracture mechanics (LEFM) provides a good analytical solutions to predict the failure behavior of

brittle materials. Since the FPZ of a brittle type is negligible, the size of a structure does not affect the analysis.

The second type is referred to ductile fracture. Most of metals and plastic polymeric materials are representative materials that exhibit ductile fracture. In these materials, the size of FPZ is still small, but there is a non-negligible size of yielding zone in front of the tip of crack or notch compare to the size of the structure. As can be noted in Fig. 6.1 (b), there is a plateau region of stress after a sudden development stress concentration at the crack tip. The non-negligible size of plastic region brings the characteristic length to the analysis of ductile fracture and induces the effect of structural size on the formation of a crack.

The third type is quasiBrittle fracture [152, 153, 154], which is most relevant to composite materials. In this case, the size is FPZ in front of the crack tip is substantial compared to the structural size as illustrated in Fig. 6.1 (c). The nonlinearity in FPZ does not come from a plastic deformation. Instead, a progression of microscale damages such as randomly distributed microcracking, frictional micro-slips, and grain interlocks cause a cohesive softening in which the stress decreases to zero value from the boundary of FPZ to the tip of the crack. The quasi-brittleness in composite materials comes from the heterogeneity of material constituents. For example, carbon fibers are extremely brittle. On the other hand, polymeric matrix are ductile. The length scale of the heterogeneity depends on the type of composites and affect the scale of FPZ on a structure. When designing a structure with a material that exhibits a quasibrittle fracture mechanics, the size of a structure needs to be carefully considered in the analysis. At one extreme, FPZ can span almost the entire region of a structure. In this case, the structure will exhibit a quasi-plastic failure, similar to the second type. On the other extreme, the size of FPZ may be negligible. In this case the failure behavior of the structure will be similar to the brittle failure. If the size of a structure is in between these two extreme, the nonlinear behavior induced by the cohesive softening needs to be considered in the analysis to properly characterize the failure. As can be noted, the structural length scale is significant to analyze the fracture behavior of materials that exhibits quasi-brittleness.

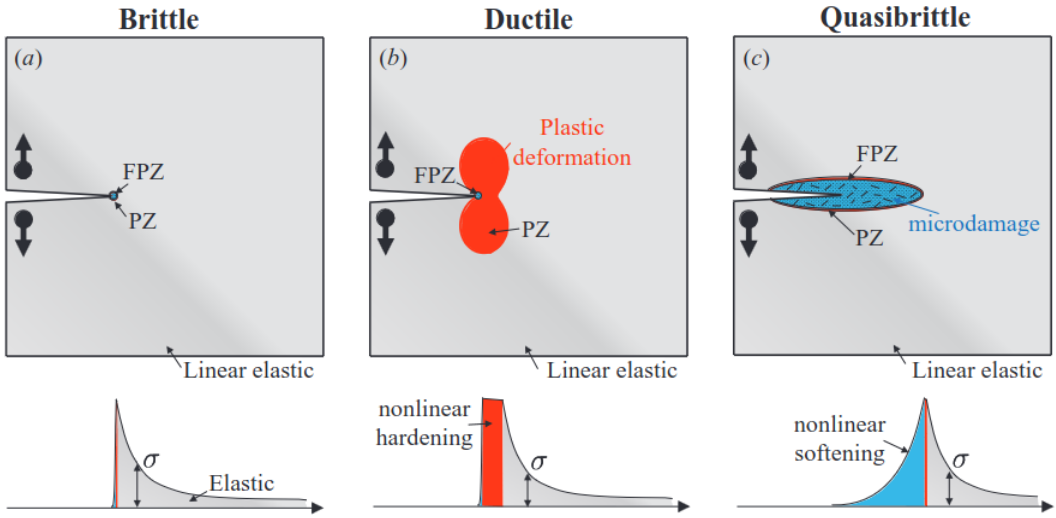

Figure 6.1: Visualization of three different structural fracture behavior denoted as (a) brittle, (b) ductile and (c) quasibrittle; stress distribution along the crack line is shown at the bottom of each types, characterizing different nonlinearity at the tip of a crack (image is from [10]).

6.2 Type II size effect

Structures with a notch or crack as a geometric feature (not as a defect) follows the type II size effect in which the localized crack after failure initiation is deterministic. The cohesive crack in a structure is represented as an equivalent LEFM crack. The length of an equivalent LEFM crack, $a = a0 + cf$, is the sume of the original crack length, a_0, and the characteristic length of FPZ, cf.

In mode I fracture, the stress intensity factor has the following form:

$$K_I = \frac{P}{b\sqrt{D}} k(\alpha) \tag{6.1}$$

where P is the applied load, D is the width of a structure, b is the thickness, and $k(\alpha)$ is the dimensionless stress intensity factor as a function of normalized crack length, $\alpha = a/D$, and $k(\alpha)$ depends on a geometrical shape. Further modification of Eq. 6.1 by introducing Irwin's relation, $K_I^2 = E'G$ when $G = G_f$, and substituting nominal strength defined as

$\sigma_N = P/(bD)$, results the following expression:

$$\sigma_N = \sqrt{\frac{E^{'} G_f}{D g(\alpha)}} \tag{6.2}$$

where $g(\alpha) = k^2(\alpha)$ is the dimensionless energy release rate as a function of normalized crack length. From Eq. 6.2, Bažant's type II size effect law [155, 156, 157] can be derived by expanding the dimensionless energy release rate into Taylor series at $\alpha_0 = a_0/D$:

$$g(\alpha) = g(\alpha_0) + g^{'}(\alpha_0)\frac{cf}{D} + ... \tag{6.3}$$

After substituting first two terms of Taylor series of $g(\alpha)$, Bažant type II size effect law (SEL) has the form as expressed in Eq. 6.4.

$$\sigma_N = \sqrt{\frac{E^{'} G_f}{cf g^{'}(\alpha_0) + D g(\alpha_0)}} \tag{6.4}$$

The SEL can be expressed in a simplified form to represent a relation between normalized quantities as shown in Eq. 6.5.

$$\frac{\sigma_N}{\sigma_0} = \left(1 + \frac{D}{D_0}\right)^{-1/2} \tag{6.5}$$

where $\sigma_0 = cf g^{'}(\alpha_0)/g(\alpha_0)$ and $D_0 = \sqrt{E^{'} G_f / cf g^{'}(\alpha_0)}$. The normalized version of SEL is plotted in Fig 6.2 with experimental data points obtained for IM7/977-3 material system [11]. As can be noted, SEL exhibits two asymptotic behaviors. As the structural size decreases ($D << D_0$), the fracture behavior of a quasibrittle materials approaches to the pseudo-plastic limit at which the strength determines the fracture behavior of the structure. As the structural size increases ($D >> D_0$), the fracture behavior of a quasibrittle materials approaches to LEFM. Figure 6.2 implies that the prevalent size effect behavior of a single material system, IM7/977-3. The quasibrittleness of a composite depends on layup configurations, mode of fracture, size of structure and loading direction (inter-laminar vs. intra-laminar). Therefore, the analysis of fracture behavior is not only challenging but also requires to carefully assume many different aspect.

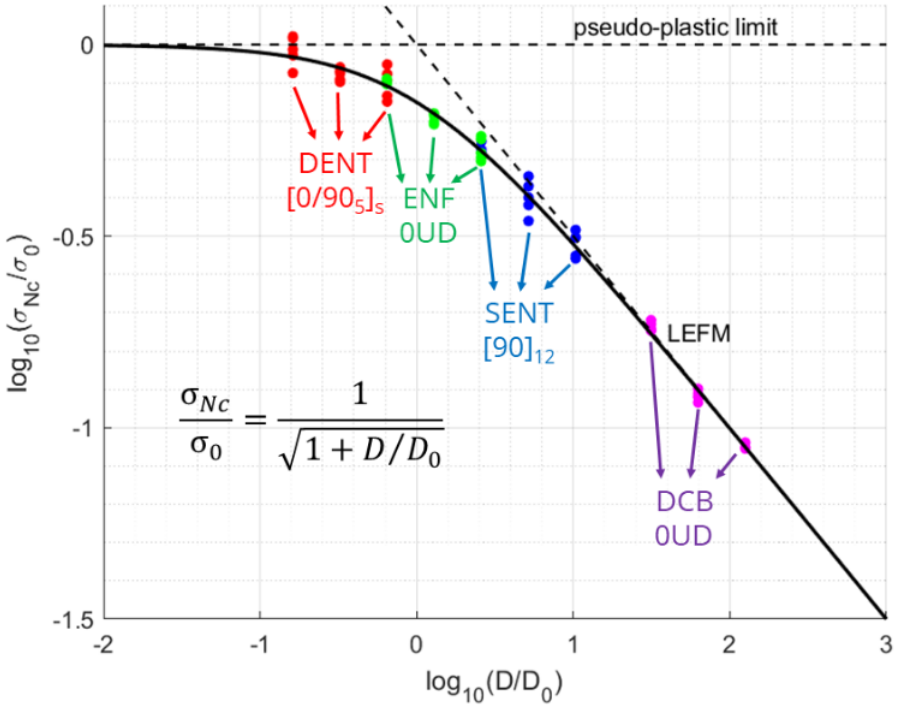

Figure 6.2: Normalized type II size effect plot from a comprehensive testing of IM7/977-3 material system (image is from [11]).

In this work, a tensile load is applied in in-plane direction of structures with a notch to induce a intra-laminar mode I crack near the notch. These structures are assumed to follow the type II SEL. Numerical analyses of composite structures assume that a structure is near either pesudo-plastic limit or LEFM regime. Therefore, a linear system solver can be used for the stress dominant analysis or for the LEFM analysis with a pre-inserted crack. To properly simulate a fracture behavior of composite structures in transition region, a more sophisticated damage modeling is required so that it can capture the nonlinear behavior in FPZ of the structure. More ideas on this subject is discussed in the next chapter.

6.3 Optimization problem

The optimization study in this work focuses on improving the fracture resistance of a structure with fiber-reinforced composites utilizing the idea of CTI. As discussed in the previous

section, the fracture behavior of a composite materials depends on the size of a structure compared to the size of FPZ. In this study, two asymptotic cases are assumed: 1) pseudo-plastic limit where the critical stress value determines the failure and 2) the regime where the theory of LEFM can be use to predict the failure of a structure. The design space for both cases are identical and are a set of paths of reinforcing fibers on the structures. Next section present the method of providing design space; however, the symbol, $\{\theta_i\}$, is used in this section to represent a general signature of fiber orientations on a structure featuring CTI. In this work, a laminate with a symmetric cross-ply layup configuration is modeled for each geometry. Although a quasi-isotropic laminate design is a common practice in composite community, a cross-ply laminate simplifies the layup sequence on a structure with CTI while it reinforces the transverse direction of each layers; therefore, it reduces the region of splitting cracks along the fiber paths. This enhancement helps the assumption that a localized crack is likely to initiate at the region of stress concentration.

For the first asymptotic case, the objective is to minimize the maximum principal stress of a given structure and loading condition. The optimization statement is expressed in Eq. 6.6.

$$\begin{aligned} \min_{\{\theta_i\}} \quad & \max\left(\sigma_{principal}(\{\theta_i\})\right) \\ \text{s.t.} \quad & \text{each } \theta_i \in [0, 2\pi] \end{aligned} \tag{6.6}$$

For the second asymptotic case, the objective is to minimize the energy release rate of a given structure and loading condition. In LEFM, the energy release rate, G, defines the loss of a total potential energy in the structure as it goes under fracture process, and has the expression shown in Eq. 6.7.

$$G = -\frac{d\Pi}{dS} \tag{6.7}$$

where Π is the total potential energy of a structure, and S is the surface area of a crack. According to LEFM, there is a crack growth when the energy release rate, G, reaches over the specific fracture energy of a material, G_f, This means that the energy released to be available for fracturing process is either enough or exceeds the required amount to

create an incremental crack surface. By minimizing the energy release rate of a structure given the set of a geometry and a loading condition, the possibility of the crack growth is minimize; therefore, the fracture resistance is maximized for a given condition. However, there is one crucial assumption is placed, which is that the specific fracture energy of the material remains same (or the change is negligible). If the specific fracture energy changes significantly, then it should be the ratio, G/G_f that needs to be minimize to account for the change in material toughness. Currently, there is no theoretical framework or empirical study to estimate the change in fracture energy of fiber reinforced composites based on the change in fiber orientations. In this work, the optimization study was performed assuming that the change in fracture energy along the crack propagation is negligible, and optimal fiber paths are checked to see the assumption can stay valid.

6.4 Isogeometric design space

In optimization study, it is important to define a proper design space. In this work, a design space is a set of possible fiber paths on a given geometry. Based on which additive manufacturing technology is in mind, there can be a constraint on the orientation of fibers to leave out the path that cannot be achieved due to the manufacturability. In this effort, a proper design space is the one with fibers that do not intersect with each other because there is no technology that can produce fibers that can bifurcate itself. Besides that constraint, there is no restriction on a radius of curvature and distance between fibers to generalize the possibility of local anisotropy.

In this work, isogeometric design space is proposed. The world, "isogeometric" implies that the identical representation of geometry is used; therefore, identical spline object for modeling a geometry is used to provide a design space for an optimization problem; in this case, the distribution of fiber orientations at each location of a given structure. As an example, a rectangular plate with a semi-circular notch is a geometry of interest, As shown in Fig. 6.3 (a), a basic geoemtry is modeled with a total of eight elements with NURBS. There are 28 control points that governs the shape of the spline geometry. Each control point has four components in homogeneous coordinate system. To use this spline surface as an interpolatory object for fiber orientations, the dimension of homogeneous

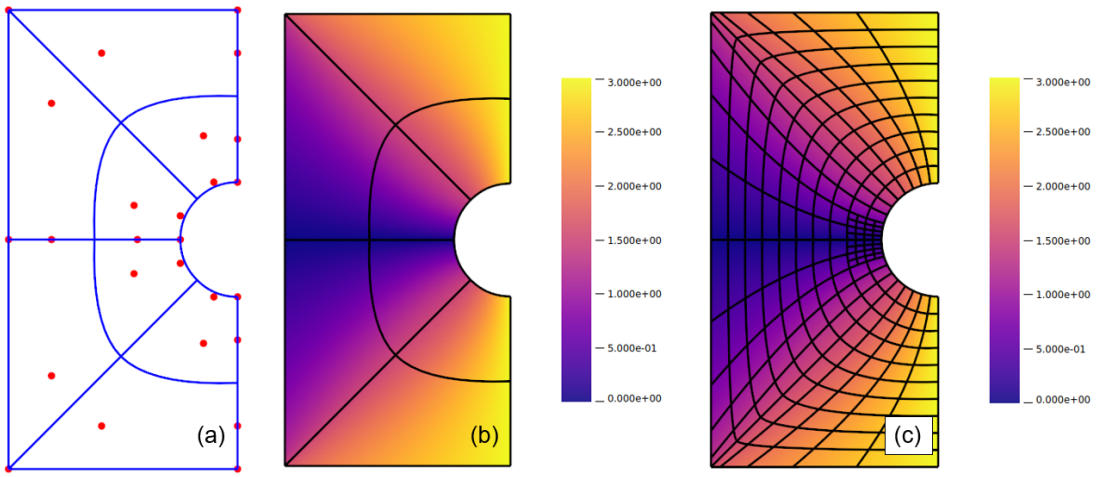

Figure 6.3: LR B spline used in modeling geometry also provides spline interpolation for design space; (a) coarsest mesh used to define a plate with a semi-circular notch; (b) orientation values are assigned to the control points as a fourth dimension, resulting a smooth orientation distribution over the geometry; (c) both global and local mesh refinement does not change the orientation distribution, parametrically and geometrically.

coordinate system can be extended. Now, each control point has fourth coordinate value as a orientation and fifth coordinate value as weight. An example spline surface representing the orientation distribution over the structure is shown in Fig. 6.3 (b). Orientation values are represented as a contour plot. In general, one may avoid such a high dimensional design space to prevent a large number computations during an optimization process. Therefore, orientation assignment to control points are done with a coarse mesh. However, the size of the mesh is not enough to provide accurate result in analysis. A big advantage of spline is that knot insertion process in both global and local framework does not change the spline object, parametrically and geometrically. As a result, orientation distribution stays same as the one defined in the beginning as can be noted in Fig. 6.3 (c). It is a mesh independent process.

This framework of providing a design space is proposed to be called “isogeometric” because the parametrically and geometrically identical spline object is used to define a geometry and to define a design space for the optimization problem. Furthermore, same spline object is used for analysis in finite element method. The obvious advantage of this

methodology is that it simplifies the modeling work since a single parametrization takes care of all the aspect of space necessary in an optimization problem such as a modeling space for geometry, a design space, and a functional space for analysis. Another advantage is that the spline interpolation can actually provide a fairly generalized fiber path space in which fibers are not intersecting each other as long as the geometry itself is not self-intersecting. If the resolution of fiber path is not good enough from the orientation distribution obtained from the spline with a coarse mesh, either global or local refinement process can be applied before the orientation coordinate is introduced to each control point on the spline object. As the size of elements becomes smaller, a more general representation of fiber paths on a geometry is obtained.

The other important benefit of using splines to define a fiber orientation is that it prevents the intersection of fibers. When the angular value is assigned to the component of control point coordinates, it produces a smooth interpolation of angles on a structure. In this study, the value of angles are limited to the range from 0 to 180 degrees. With this constraints on the domain, there is a one-to-one mapping between angular values on the spline to unit vectors that represents the local direction of fiber reinforcements. It acts as a vector field for the gradient of fibers. As a result, each location on the structure has a non-zero vector that describes a fiber path. This implies that there is no stagnation point where the fiber orientation is not defined. Furthermore, in this study, quadratic splines are used for the isogeometric approach; therefore, the orientation function defined by the quadratic splines is C^1 continuous almost everywhere except on the knot line with multiplicity equal to 2. On that line, the continuity is C^0. If fibers intersect or coincide on a vector field, the location of intersection does not have an unique vector as a fiber path. This implies that a well defined vector field where each point has an unique non-zero vector does not have fibers that intersect or coincide. Thanks to the continuity of the spline representation, isogeometric design space with a constraints on the domain of angular value provides the fiber alignments without intersections.

There is one important assumption made in the fracture simulation, and that is damage is localized in to a single crack without delamination across the thickness. However, there is a discontinuity between layers where the fiber paths of each lamina is different. Edge

effect can cause the delamination between layers and complicates the fracture behavior of composite structures. In the scope of this work, edge effect is ignored, but it is suggested to investigate this phenomenon for the future works.

6.5 Optimization methods

The design space defined with a spline function can easily have a high dimension. The example spline geometry shown in Fig. 6.3 requires 28 variables to define an orientation distribution. Both of the objective functions, maximum principal stress and the energy release rate, do not have easily computable first- and second- order derivatives. It is intended to find a global optimum, but it is not apparent to see if both the objective functions are convex and/or linear. Based on these properties of the optimization problem, it does not seem to be appropriate to solely use a gradient-method. Numerical evaluations of gradient vectors will take multitude of simulations due to the large number of variables; furthermore, it is not guaranteed to converge to a global minimum due to the lack of information on convexity of objective functions.

To improve the uncertainty on an optimal result, a surrogate method is first performed as a global optimization technique. This type of method builds an approximate model (surrogate) of the objective function to determine the next point of evaluation. Surragate methods are particularly useful when the evaluation of an objective function is expensive, there is a lack of convexity on an objective function, and the evaluation of derivatives are not clear. Therefore, it applies well to the optimization in this work.

However, the result from a surrogate method may still be a sub-optimal value if the number of iterations are not enough or the surrogate approximation does not reflect the true optimum in the real objective function. As a simple solution, a gradient-based approach can be followed up using the sub-optimal result from the surrogate method as an initial condition. In this way, the local minimum result from the gradient-based method has a higher chance of being a global minimum in the objective function. A brief introduction of a particular choice for each optimization methods is provided in the following subsections.

6.5.1 Data driven approach to find sub-optimal candidate

Bayesian optimization goes under the umbrella of surrogate method as a global optimization technique. A distinctive feature compared to other surrogate methods is that it uses Bayesian statistical inference to construct a surrogate. Bayesian interpretation of a surrogate model gives a clear reasoning on the point of evaluation in the next iteration. A basic workflow of Bayesian optimization is shown in Alg. 3.

ALGORITHM 3: Procedures in Bayesian optimization

Data: Training data, objective function, and number of iterations, N
Result: Optimal value from a given number of evaluations

```
Set a prior distribution on f.
From the training data, update the observation on the objective function at each point.
Find the best observed value and its argument.
iteration = range(0, N)
for Each iteration
    Update the posterior probability distribution on the objective function based on the
      observations.
    Find the argument that maximizes the acquisition function.
    Evaluate the objective function at the argument.
    Update the best observed value and its argument.
    Proceed to the next iteration.
end
Return the best observed result and its argument.
```

As can be noted in Alg. 3, the two main ingredients in Bayesian optimization are 1) statistical model for surrogate and 2) acquisition function that decides the next point of evaluation.

The first component is to build an approximate function to be used as a surrogate, but this brings the question of how one can represent a function in a statistical form. It is quite common to associate a function as a formula. For an example, it is easy to associate $f\frac{1}{2}x^2$ as a representation of the quadratic function, $f(x) = \frac{1}{2}x^2$. There is nothing wrong with this view, but it is somewhat restrictive in order to generalize the representation, especially in statistical approach. A function is essentially a mapping that has well-defined domain and co-domain. One constraint is that an argument in the domain is mapped to a single element in the range. Without formulating a equation for a function, the range of a function can be thought of as a collection of function evaluations, $f = \{f(x_1), f(x_2), f(x_3), ...\}$. In

this perspective, a function can be represented as a set of random variables that follows a certain statistical properties. Of course, a multivariate Gaussian distribution can be used to provide a function space if the size of domain is finite; however, a domain of continuous functions is uncountable. This is where a Gaussian process takes a place.

A Gaussian process [158, 159] is defined as a set of random variables such that any finite subset of variables are jointly Gaussian. This definition does not seem to be so helpful in the beginning but it may be thought of as self-similar object that can extended to a pretty large scale. A Gaussian process is constructed with a mean function, $m(\boldsymbol{x})$ and a covariance function $k(\boldsymbol{x}, \boldsymbol{x}')$. Consider a case where the observation comes with a noise that follows a Gaussian distribution with zero mean: $y_n = f(\boldsymbol{x}_n) + \epsilon_n$ and $\epsilon_n \sim \mathcal{N}(0, \sigma_n^2)$. The evaluation of the statistical model at the training data should be close to the observed values. Given a training set $D = \{(\boldsymbol{x}_i, y_i) : \boldsymbol{x}_i \in \boldsymbol{X},\ i = 1, 2, ..., N\}$ where $y_i = f(\boldsymbol{x}_i)$ and the prediction output $f_* = \{f(x_j^*) : x_j^* \in X_*,\ j = 1, 2, ..., N_*\}$, the joint prior distribution is expressed as shown in Eq. 6.8.

$$\begin{bmatrix} \boldsymbol{y}_X \\ \boldsymbol{f}_* \end{bmatrix} \sim \mathcal{N}\left(\begin{bmatrix} \boldsymbol{\mu}_X \\ \boldsymbol{\mu}_* \end{bmatrix}, \begin{bmatrix} \boldsymbol{K}_{X,X} + \sigma_n^2 \boldsymbol{I} & \boldsymbol{K}_{X,*} \\ \boldsymbol{K}_{*,X} & \boldsymbol{K}_{*,*} \end{bmatrix} \right) \tag{6.8}$$

where $\boldsymbol{\mu}_X = [m(\boldsymbol{x}_1), ..., m(\boldsymbol{x}_N)]$, $\boldsymbol{\mu_*} = [m(\boldsymbol{x}_1^*), ..., m(\boldsymbol{x}_N^*)]$, $\boldsymbol{K}_{X,X} = k(\boldsymbol{X}, \boldsymbol{X})$, $\boldsymbol{K}_{X,X_*} = k(\boldsymbol{X}, \boldsymbol{X}_*)$, $\boldsymbol{K}_{X_*,X} = k(\boldsymbol{X}_*, \boldsymbol{X})$, and $\boldsymbol{K}_{*,*} = k(\boldsymbol{X}_*, \boldsymbol{X}_*)$.

After applying a Bayes' rules, posterior predictive distribution can be obtained with some help from linear algebra. If a single prediction input is given, the posterior distribution simplifies as expressed in Eq. 6.9.

$$p\left(f_* | D, \boldsymbol{x}_*\right) = \mathcal{N}\left(m(\boldsymbol{x}_*) + \boldsymbol{k}_*^T \left(\boldsymbol{K}'_{X,X}\right)^{-1} (\boldsymbol{y} - \boldsymbol{\mu}_X), k(\boldsymbol{x}_*, \boldsymbol{x}_*) - \boldsymbol{k}_*^T \left(\boldsymbol{K}'_{X,X}\right)^{-1} \boldsymbol{k}_*\right) \tag{6.9}$$

where $\boldsymbol{K}'_{X,X} = \left(\boldsymbol{K}_{X,X} + \sigma_n^2 \boldsymbol{I}\right)$ and $\boldsymbol{k}_* = [k(\boldsymbol{x}_*, \boldsymbol{x}_1), ..., k(\boldsymbol{x}_*, \boldsymbol{x}_N)]$.

Typically, input data to form a Gaussian process is standardized; therefore, zero mean function is often used. For covariance functions, kernels are used. In this subsection, only two types of kernel, radial basis functions (RBF) and Matérn class functions are introduced.

RBF kernel also known as Gaussian kernel is commonly used and as the following form shown in Eq. 6.10.

$$k(\boldsymbol{x}, \boldsymbol{x}') = \alpha \exp\left(-\frac{||\boldsymbol{x} - \boldsymbol{x}'||^2}{2\ell^2}\right) \tag{6.10}$$

where $\alpha > 0$. In Eq. 6.10, α scales the magnitude of RBF kernel, and ℓ provides how fast the kernel value changes as the radius increases. A noticeable property of RBF kernel is that it is infinitely differentiable, and this leads to a very smooth shape. On the other hand, Matérn kernel exhibits high frequency oscillation. It has the following form:

$$k(\boldsymbol{x}, \boldsymbol{x}') = \alpha \frac{2^{1-\nu}}{\Gamma(\nu)} \left(\frac{\sqrt{2\nu}||\boldsymbol{x} - \boldsymbol{x}'||}{\ell}\right)^{\nu} K_\nu \left(\frac{\sqrt{2\nu}||\boldsymbol{x} - \boldsymbol{x}'||}{\ell}\right) \tag{6.11}$$

where K_ν is a modified Bessle function. In Eq. 6.11, α and ℓ describe how large and how fast the kernel changes, respectively. In contrast to RBF kernel, Matérn kernel is only differentiable up to k-times where $\nu > k$.

These two kernels are called Mercer kernels, which are positive semi-definite in nature. Mercer's theorem states that a positive definite kernel which maps from a finite measure space have positive eigenvalues and their associated eigenfunctions. Furthermore, the kernel can be expressed with its eigenfunctions as follows: $k(\boldsymbol{x}, \boldsymbol{x}') = \sum_{i=1}^{\infty} \lambda_i \phi_i(\boldsymbol{x}) \phi_i^*(\boldsymbol{x}')$ where λ_i is an eigenvalue and ϕ_i is the associated eigenfunction function. This result brings the interesting relation between a Gaussian process and Bayesian regression analysis [158, 159].

In a linear regression problem, a function is a linear combination of basis functions, $\phi_i(\boldsymbol{x})$: $y = \sum_{i=1}^{N} w_i \phi_i(\boldsymbol{x}) + \epsilon$ where $\epsilon \sim \mathcal{N}(0, \sigma_n^2)$. Assuming the weight variables follows a Gaussian prior distribution with a zero mean, the posterior distribution of weights has the following form:

$$p(\boldsymbol{w}|\boldsymbol{X}, \boldsymbol{y}) \sim \mathcal{N}\left(\frac{\boldsymbol{A}^{-1}\boldsymbol{\Phi}_X^T \boldsymbol{y}}{\sigma_n^2},\ \boldsymbol{A}^{-1}\right) \tag{6.12}$$

where ij-th component of $\boldsymbol{\Phi}_X$ matrix is $\phi_i(\boldsymbol{x}_j)$ and $\boldsymbol{A} = \sigma_n^{-2}\boldsymbol{\Phi}_X^T\boldsymbol{\Phi}_X + \boldsymbol{\Sigma}_w^{-1}$. $\boldsymbol{\Sigma}_w$ is the covariance matrix of the Gaussian prior, $p(\boldsymbol{w})$. After marginalization over the weights, the posterior predictive distribution is obtained as shown in Eq. 6.13.

$$p(\boldsymbol{f_*}|\boldsymbol{X}, \boldsymbol{y}, \boldsymbol{x}_*) \sim \mathcal{N}\left(\frac{\boldsymbol{\phi}^T(\boldsymbol{x}_*)\boldsymbol{A}^{-1}\boldsymbol{\Phi}_X^T\boldsymbol{y}}{\sigma_n^2},\ \boldsymbol{\phi}^T(\boldsymbol{x}_*)\boldsymbol{A}^{-1}\boldsymbol{\phi}(\boldsymbol{x}_*)\right) \tag{6.13}$$

According to Mercer's theorem, a kernel can be represented as follows: $k(\boldsymbol{x}, \boldsymbol{x}'_*) = \boldsymbol{\phi}^T(\boldsymbol{x})\boldsymbol{\Sigma}_w\boldsymbol{\phi}(\boldsymbol{x}')$. This means that the associated covariance matrix in the Gaussian process has the following form: $\boldsymbol{K}_{X,X} = \boldsymbol{\Phi}_X\boldsymbol{\Sigma}_w\boldsymbol{\Phi}_X^T$. Furthermore, $\boldsymbol{k}_* = \boldsymbol{\Phi}_X\boldsymbol{\Sigma}_w\boldsymbol{\phi}(\boldsymbol{x}_*)$ and $k(\boldsymbol{x}_*, \boldsymbol{x}_*) = \boldsymbol{\phi}^T(\boldsymbol{x}_*)\boldsymbol{\Sigma}_w\boldsymbol{\phi}(\boldsymbol{x}_*)$. Substituting these forms to Eq. 6.9, the predictive posterior obtained by a Gaussian process becomes identical to the one obtained from a linear regression analysis when the mean function is assumed to be a zero function.

This implies that a function approximation using a Gaussian process is equivalent of representing the function with a set of basis functions. A limitation of the regression approach is that the set of basis functions has a finite size. However, some kernels such as RBF has a infinite dimensional feature representation. Therefore, the surrogate model from a Gaussian process can reside in a fairly large function space.

Kernels have hyperparameters, $\boldsymbol{\rho}$, to be determined. For example, Matérn kernel has parameters: α and ℓ. The most popular method is to choose values that maximizes the log marginal likelihood (LML) as expressed in Eq. 6.14.

$$\log\left(p(\boldsymbol{y}|\boldsymbol{X}, \boldsymbol{\rho})\right) = \log\left(\int p(\boldsymbol{y}|\boldsymbol{X}, \boldsymbol{f})p(\boldsymbol{f}|\boldsymbol{X}, \boldsymbol{\rho})d\boldsymbol{f}\right) \tag{6.14}$$

There is analytical form for the gradient vector of LML, so a gradient-based optimization method can be used to find a local optimum. However, LML is often not convex, so it requires multiple restarts to survey other local optima.

The other major component in Bayesian optimization is acquisition function, which decides a point of evaluation in the next iteration. There are multiple acquisition functions that are designed to serve specific purpose. In this subsection, *Expected improvement* function (EI) is introduced and used in optimization problems in later sections. The main idea is to select the argument that is expected to improve the observation [160]. The improvement after making observation at $\boldsymbol{x}$ is computed as: $\langle f(\boldsymbol{x}) - f_n^{max}\rangle$ where f_n^{max} is the best observed value after n-th iteration. The Macaulay brackets represent the following notion: $\langle x\rangle = \max(x, 0)$. The problem is $f(\boldsymbol{x})$ is unknown until the evaluation is actually performed.

Instead, expected value of the improvement can be computed using the posterior predictive distribution from the Gaussian process. The EI with a single input has the following expression shown in Eq. 6.15:

$$EI_n(\boldsymbol{x}) = \langle \Delta_n(\boldsymbol{x}) \rangle + \sigma_{(n)}(\boldsymbol{x}) \varphi_0 \left(\frac{\Delta_n(\boldsymbol{x})}{\sigma_{(n)}(\boldsymbol{x})} \right) - |\Delta_n(\boldsymbol{x})| \varphi_1 \left(\frac{\Delta_n(\boldsymbol{x})}{\sigma_{(n)}(\boldsymbol{x})} \right) \tag{6.15}$$

where $\Delta_n(\boldsymbol{x}) = \mu_n(x) - f_n^{max}$ is the expected difference compared to the best observed result from previous iteration, $\sigma_{(n)}(\boldsymbol{x})$ is the variance from the posterior predictive distribution. φ_0 and φ_1 are functions of $\Delta_n(\boldsymbol{x})/\sigma_{(n)}(\boldsymbol{x})$. Equation 6.15 shows that the EI is proportional to two components: $\langle \Delta_n(\boldsymbol{x}) \rangle$ and $\sigma_{(n)(\boldsymbol{x})}$. Therefore, the optimizer is examining a potential gain from either exploiting a region with the highly expectation (high $\langle \Delta_n(\boldsymbol{x}) \rangle$) or exploring a region with the high uncertainty (high $\sigma_{(n)(\boldsymbol{x})}$). This game of exploitation versus exploration provides a nice strategy in constructing a surrogate with a few evaluation.

There are several freely available Bayesian optimization libraries. In this work, *BoTorch* from Meta Platform Inc. [161] is used. *BoTorch* provides all the necessary functionality needed to form a Bayesian optimization loop in *Python* API. It is build on top of *PyTorch* which is an open source machine learning framework developed by Meta AI and *GPyTorch* which is a Gaussian process library based on *PyTorch*. As an implementation node, "FixedNoiseGP" model is used to set up a Gaussian process with a very small noise value equal to 0.001.

6.5.2 Gradient based approach to obtain an optimal result

The optimal result from Bayesian optimization can be actually sub-optimal, especially, when the dimension of design space is big, and the number of iteration is restricted for time constraint. As discussed in the previous subsection, *expected improvement* acquisition function can ask to explore regions of high uncertainty for many iterations to build a decent surrogate approximation before exploiting a region with high expectation of improvement. Therefore, the iteration loops may end before it converges to a true optima.

This can be easily solved by performing a gradient-based optimization with the sub-optimal result obtained from Bayesian optimization step as an initial point. The theory of

gradient-based optimization is a quite mature subject; therefore, only the method used in this work is stated. The "L-BFGS-B" method which is extended version of "L-BFGS" to accepted boundary constraints is used from borrowing the implementation in *Scipy* which is scientific computing module for *Python*. "L-BFGS" is one of quasi-Nuewton methods that approximates Hessian matrix based on the gradient information in previous steps. In the name, "L" refers to limited memory because the implementation only saves gradient information up to certain point from the current evaluation for the approximation of Hessian.

The result from a gradient-based optimization should be a local optimum closest to the sub-optimal value found in Bayesian optimization which is a global method. Therefore, there is a higher chance that the local optimum from these steps is a global optima in the objective function.

6.6 Case I: a rectangular plate with a semi-circular notch

A first set of optimization studies are performed on a rectangular plate with a semi-circular notch, which is a prevalent stress riser in engineering design. The geometric detail on this structure is shown in Fig. 6.4 (a). For a numerical analysis, the bottom surface has a clamped boundary condition; all the degrees of freedom are constrained. The top surface of the laminate is constrained in x-direction so that there is no transverse motion, and it is displaced in the longitudinal direction for an uni-axial loading condition. This set of boundary and loading condition resembles a typical tensile testing on a rectangular coupon in a load frame and is illustrated in Fig. 6.4 (b).

The composite material system used in this study is IM7/977-3 graphite/epoxy. The linear elastic properties of this material is provided by Clay and Knoth [162] following standardized ASTM uniaxial tension/compression experiments. The list of properties are shown in Table 6.1.

In the model generation step, bi-quadratic NURBSs are used to generate a spline surface. Two knot vectors, $\boldsymbol{\xi} = [0, 0, 0, 0.25, 0.5, 0.5, 0.75, 1, 1, 1]$ and $\boldsymbol{\eta} = [0, 0, 0, 1, 1, 1]$ provide the parametric space. List of control points used in modeling is provided in Appendix. This creates a NURBS mesh with four elements in ξ-direction. By adding a knot, $\eta = 0.5$, the NURBS surface shown in Fig 6.5 (a) is produced. This mesh is used to provide a orientation

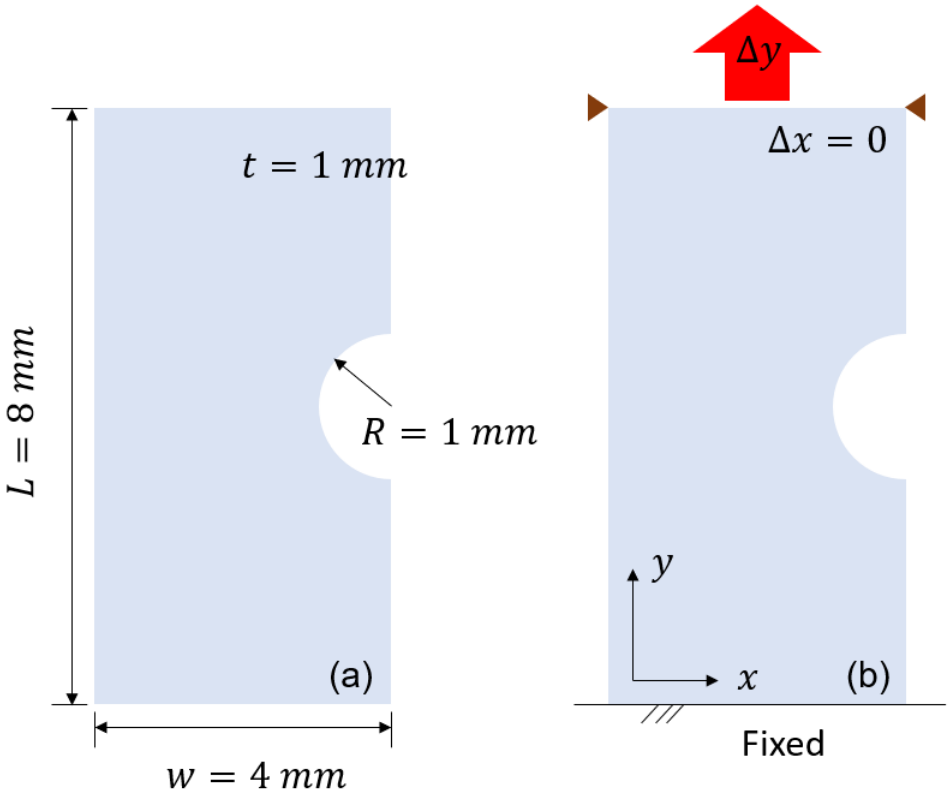

Figure 6.4: Rectangular plate with a semi-circular notch on right edge: (a) dimensions; (b) boundary condition and loading condition.

Table 6.1: Mechanical properties of IM7/977-3

Property	Value
Longitudinal modulus, E_1, (GPa)	164
Transverse modulus, E_2, (GPa)	8.98
Major Poisson's ratio, ν_{12}	0.320
In-plane shear modulus, G_{12}, (GPa)	5.010

distribution across the domain. There are a total of 28 control points. As can be noted in Fig. 6.4 (b), there is a clear geometrical symmetry line cutting through the mid-section of a plate. Moreover, applied loading and boundary condition can produce symmetrical deformation as long as the fiber orientations retain the symmetry. Therefore, the symmetry in fiber paths across the geometrical symmetry line. This condition forces the four control points in the middle to have either 0° or 90° orientation. In this work, 90° is enforced; however, the cross-ply layup sequence automatically enforce 0° in the other layer. As a consequence, only 12 control points either on the top-half or the bottom-half of the spline surface requires a orientation value to provide a smooth spline design space.

For the analysis, the mesh need to have finer elements, especially near the tip of the circular notch since the notch induces a stress concentration. After a series of global refinement and local refinement near the tip of the notch, the mesh shown in Fig. 6.5 (b) is obtained. The local refinement technique produces a result similar to that of subdivision. Therefore, the size of the element decreases fairly quickly with the refinement level, k. In this work, refinement level of $k = 2$ is chosen. Figure 6.5 (c) shows the magnified view of the mesh at the local refined region. As a last step for the model generation procedure, 2D spline surface is extruded to provide four layers on the laminate. Since the layup is symmetric, there is no bending induced from the in-plane loading condition; therefore, each lamina have one element through thickness. The knot vector in out-of-plane direction, $\boldsymbol{\zeta} = [0, 0, 1, 1]$ is used to produce a single layer thickness with two control points: $c1 = (0, 0, 0, 1)$ and $c2 = (0, 0, 1, 1)$ in homogeneous coordinate system. Then, three knots ($\zeta_1 = 0.25$, $\zeta_2 = 0.50$, and $\zeta_3 = 0.75$) are inserted to obtain four layers. The resultant mesh that are ready for analysis is shown in Fig. 6.5 (d).

Before moving on to the optimization study, the analysis was performed on the laminate with straight fibers in a cross-ply configuration. This result serves as the reference to evaluate the improvement on the fracture resistance of the optimized laminate. Figure 6.6 (a) shows the contour of the stress component in y-direction. As expected, there is a stress concentration at the tip of the semi-circular notch. A localized crack is likely to be appeared at the stress concentration. As discussed in the beginning of this chapter, the cross-ply reinforcement helps to restrict the generation of splitting cracks, which prevents a

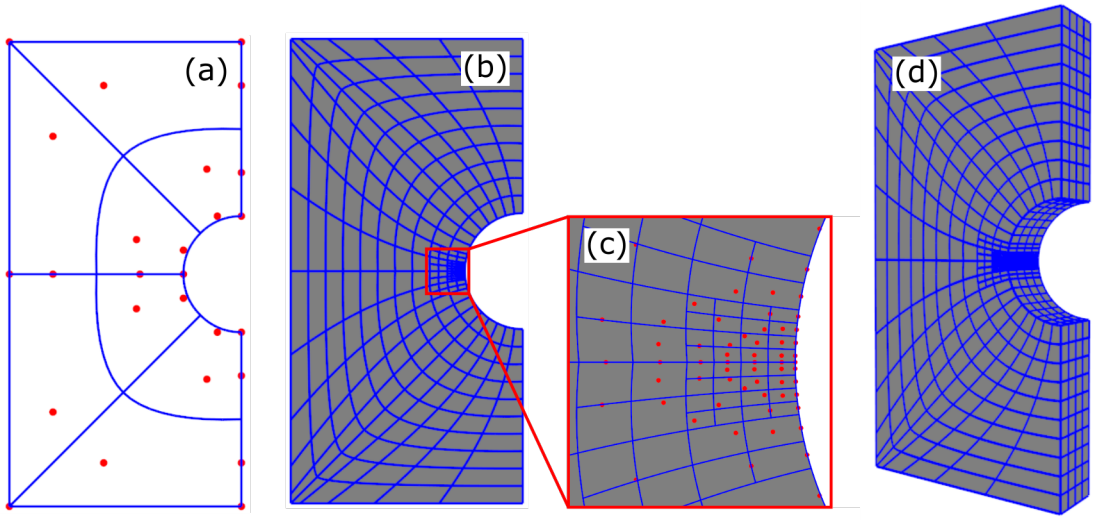

Figure 6.5: The evolution of the mesh in each steps of modeling: (a) 2D mesh where the orientation values are assigned to the control points; (b) 2D mesh after global and local refinement; (c) magnified view of locally refined area; red dots are control points; (d) 3D mesh ready for analysis after extrusion.

formation of a localized and sharp crack. This allows to proceed with a crack placement in front of the notch. Figure 6.6 (b) shows the contour of the stress component in y-direction on the same structure with the crack that has a length, $a = 0.075$ mm. As can be noted, stress is further localized near the tip of the crack.

The first optimization study is to minimize the maximum principal stress. This covers the structures of sizes that the failure is stress-dominant. To start with Bayesian optimization, a Gaussian process regression model needs to be trained with a set of initial data. In this optimization problem, an argument is a vector consisting of twelve orientation values, $\boldsymbol{\Theta} = \{\theta_1, \theta_2, ...\theta_{12}\}$, to be assigned to the control points in the spline surface shown in Fig. 6.5 (a), and the objective function, y_i is the maximum of principal stress from the simulation. To generate a random but well dispersed set of arguments, Sobol sequences were used. After simulating each cases, a total of 3000 pairs of $(\boldsymbol{\Theta}_i, y_i)$ are produced for the training data. Once the initial surrogate is prepared, 1000 iterations of Bayesian optimization loop are performed followed by a gradient-based optimization described in the previous section. All the simulations were performed on an AMD Ryzen 7 1700 eight-core

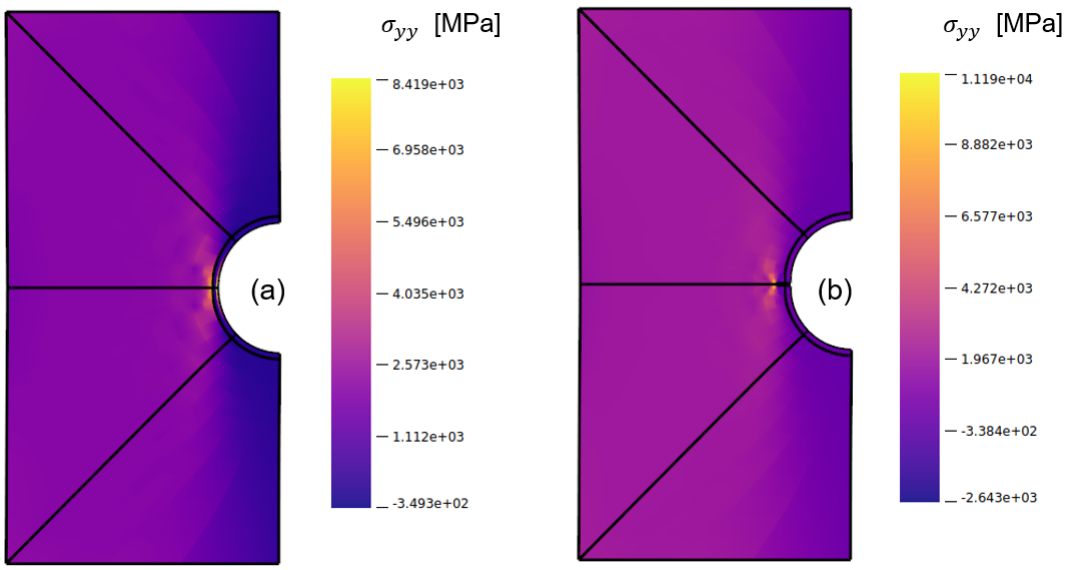

Figure 6.6: The result from isogeometric analysis on the cross-ply laminate with straight fibers: (a) contour plot of a stress component in y-direction; (b) contour plot of a stress component in y-direction after a crack is inserted at the tip of semi-circular notch.

processor with hyperthreading running at 3.0 MHz using a total 32 GB of RAM (two 16 GB DIMM DDR4 synchronous). Two simulations are ran in parallel using MPI framework implemented in *Python* ("mpi4py") to prepare training data, and simulations from the optimization iterations are ran in series. The total run time for this optimization was about 3 hours.

Figure 6.7 (a) shows the contour of maximum principal stress of the optimized result. In the reference case, the largest maximum principal stress is found to be around 8419 MPa. After the optimization, it is dropped to 1196 MPa. The largest value of the maximum principal stress is reduced by a factor greater than 7. Furthermore, stress concentration on the laminate with straight fibers is well localized at the tip of the notch. However, the stress contour exhibits a well distribution of load across the structure. This is well desired condition since the load bearing capacity of the structure is likely to be much higher. The optimal fiber paths of the cross-ply laminate is shown in Fig. 6.7 (b) and (c). One is the 90° offset from the other to form a cross-ply layup sequence. Focusing on the fiber paths

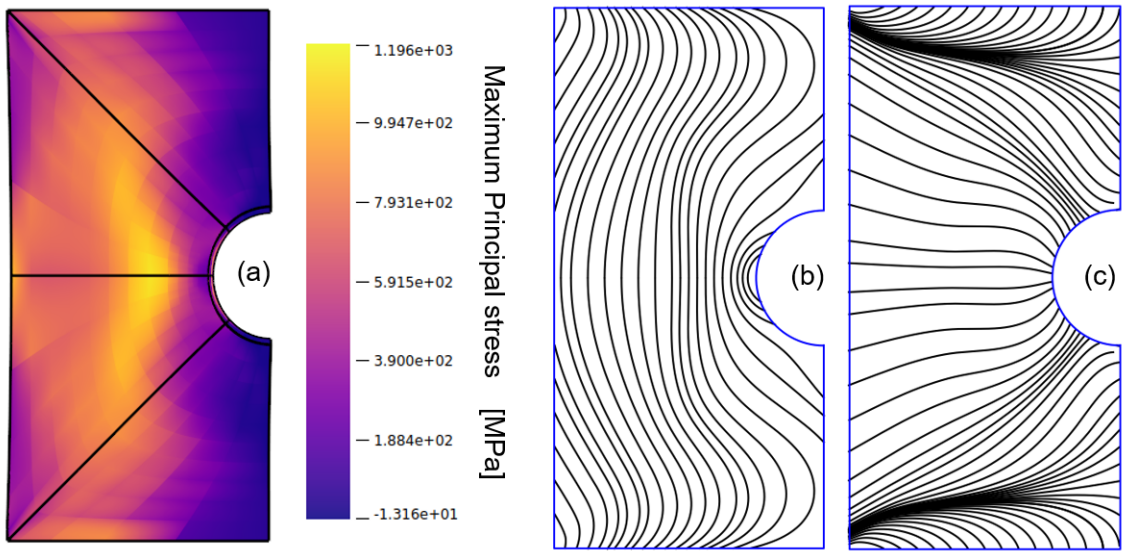

Figure 6.7: The optimization result for minimizing the maximum principal stress on the structure: (a) contour of a maximum principal stress of a laminate with optimal fiber placement; (b) optimal fiber paths in the outer layers; (c) optimal fiber paths in inner layers, which are 90° offsets of fibers in the outer layers to retain a cross-ply configuration.

in Fig. 6.7 (b), fibers near the tip of notch approximately forms a circular paths centered around the tip. This seems to make the region compliant and reduce the stress build up near the notch. Moving along the horizontal line away from the notch, fibers seem to follow the contour of the geometry, embracing the notch. However, fibers tend to curve back as they move towards either top or bottom surfaces. This also seems to make the region of relatively large cross-sectional area more compliant so that the loads are well distributed across the whole domain.

The second optimization study is to minimize the energy release rate. This covers the structure of sizes that LEFM applies to predict the fracturing behavior. For Bayesian optimization, identical procedure is used to generate initial training data. Main difference is that two simulations are performed one without a crack and one with a crack to compute the energy release rate as defined in Eq. 6.7. Similarly, a total of 3000 training data is generated using Sobol sequences. 1000 iterations of Bayesian optimization loop are performed followed by a gradient-based optimization to fine tune the optimal fiber paths. The total run time

for this optimization was about 6 hours.

Figure 6.8 (a) and (b) show the contours of stress component in y-direction from the optimized laminate without the crack and with the crack, respectively. As can be noticed, stress contour is almost identical to each other. Furthermore, there is no positive stress at the tip of notch where the crack is inserted. This implies that the optimizer finds the fiber paths that does not induce positive strain where the crack is likely to occur. This is expected behavior from the optimizer because there is no change in strain energy if the crack is not opened. As a result, outstanding result of $G = 0.027$ N/mm is obtained. For the reference case, the energy release rate is found to be 73.3 N/mm. Furthermore, this optimal laminate also removes stress concentration at the tip of the notch, and loads are well distributed. Figure 6.9 (a) and (b) show the optimal fiber paths of the cross-ply laminate. Focusing on the fiber paths in Fig. 6.9 (b), fibers near the tip of notch approximately forms a circular paths centered around the tip. This was already observed in the previous optimization study. These circular paths traps the crack, and enclosing arcs reduces the local stiffness around the crack. This mechanism eliminate the opening displacement at the tip of notch, making the crack stealthy from the tensile load. Although the fiber paths resembles the previous optimal result; however, fibers tend to straighten for those located away from the notch.

Now, it is a good time to recall that G is not the only component that determines the crack growth. The value of G in the structure needs to overcome the material property, G_f. As pointed out in the previous section, G_f depends on the fiber orientation. Looking at the longitudinally oriented layer shown in Fig. 6.9 (b), it can be noticed that the fiber paths are orthogonal to the direction of crack propagation. In this optimization problem, this happened thanks to the symmetry condition. Regardless, this condition played in favor in placing fiber that maximizes G_f at the tip of the crack; moreover, G_f stays uniform in the direction of the crack growth. Therefore, the minimization of G is relevant to the increase of fracture resistance in this optimal laminate.

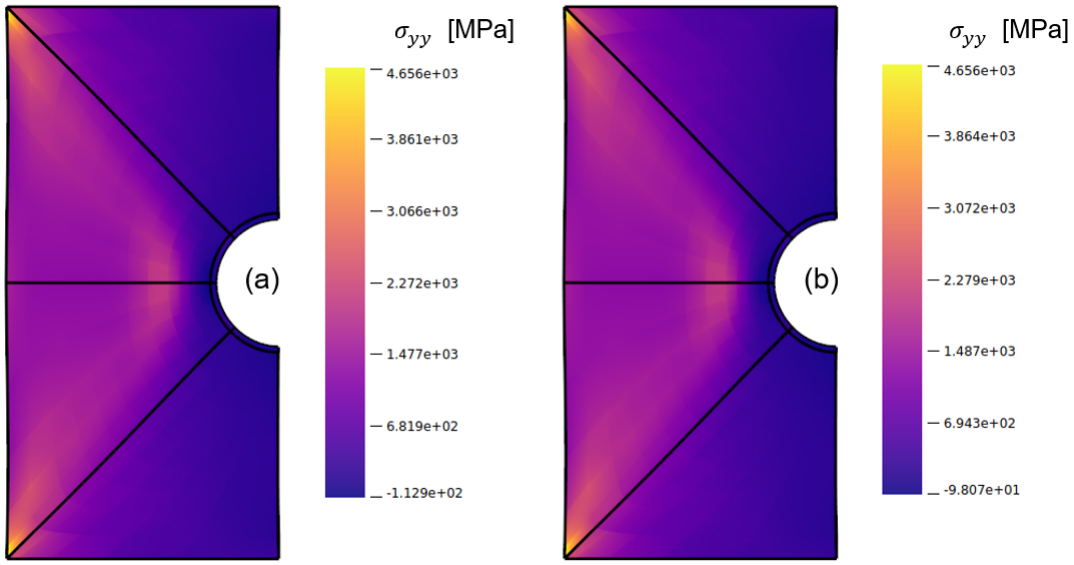

Figure 6.8: The optimization result for minimizing the energy release rate of the structure: (a) contour of the stress component in y-direction without a crack; (b) contour of the identical stress component with the crack at the tip of the semi-circular notch.

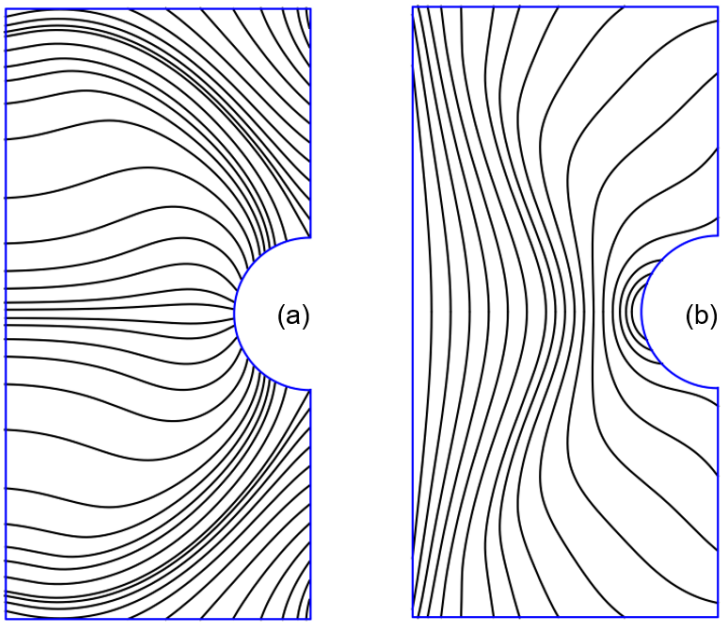

Figure 6.9: The optimal fiber paths for minimizing the energy release rate of the structure: (a) placed in the outer layers; (b) placed in inner layers which are 90° offsets of fibers in the outer layers to retain a cross-ply configuration.

6.7 Case II: T-joint under a tension

The other set of optimization studies are performed on a T-joint structure under a tensile load. The geometric detail on this structure is shown in Fig. 6.10 (a). For a numerical analysis, left and right arms are clamped so that all the degrees of freedom are constrained at this boundary. The bottom surface of the laminate is constrained in x-direction so that there is no transverse motion, and it is pulled downward for an uni-axial loading condition as illustrated in Fig. 6.10 (b). The same composite material system, IM7/977-3 graphite/epoxy, is used.

There is no simple tensor spline parametrization to represent this shape, so two inverted L-shape objects are merged together in the model generation shape. The left half of the T-joint is parametrized with bi-quadratic NURBSs: $\boldsymbol{\xi}_L = [0, 0, 0, 0.125, 0.125, 0.25, 0.375, 0.375, 0.5, 0.5, 0.5]$ and $\boldsymbol{\eta}_L = [0, 0, 0, 0.5, 0.5, 0.5]$. The right half of the T-joint is modeled with the other set of bi-quadratic NURBSs: $\boldsymbol{\xi}_R = [0.5, 0.5, 0.5, 0.625, 0.625, 0.75, 0.875, 0.875, 1, 1, 1]$ and $\boldsymbol{\eta}_R = [0.5, 0.5, 0.5, 1, 1, 1]$. The set of control points for both left and right parts of the T-joint model is listed and provided in Appendix. After putting them together, the coarse mesh consisting of 8 elements is produced as shown in Fig. 6.11 (a). This mesh is used to provide a orientation distribution across the domain. There are a total of 48 control points.

As can be noted in Fig. 6.10 (b), there is a clear geometrical symmetry line where to parts are joined. Moreover, applied loading and boundary condition can produce symmetrical deformation as long as the fiber orientations retain the symmetry. Therefore, the symmetry in fiber paths across the geometrical symmetry line. This condition forces the four control points in the middle to have either 0° or 90° orientation. Similar to the previous geometry, 90° orientation is enforced along the symmetry line. As a consequence, only 19 control points either on the left-half or the right-half of the spline surface requires a orientation value to provide a smooth spline design space.

For the analysis, the mesh need to have finer elements, especially near the corners since the concavity induces a stress concentration. After a series of global refinement and local refinement near the tip of the notch, the mesh shown in Fig. 6.11 (b) is obtained. The local

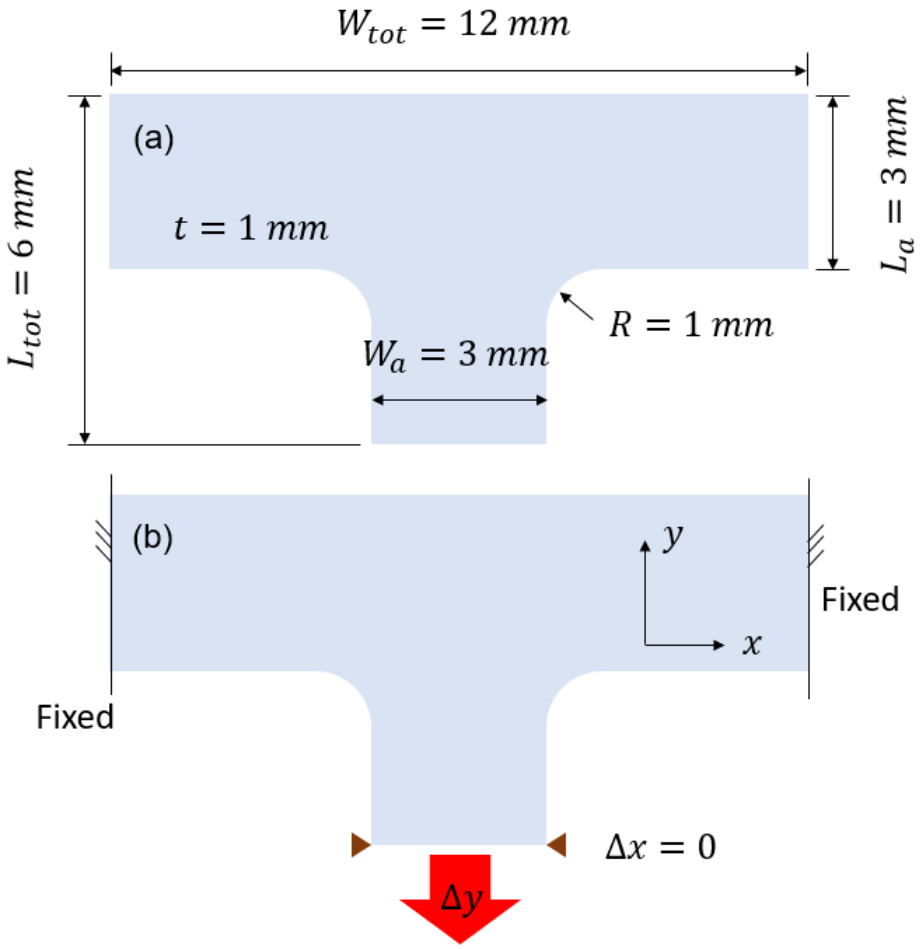

Figure 6.10: T-joint with a circular fillets: (a) dimensions; (b) boundary condition and loading condition.

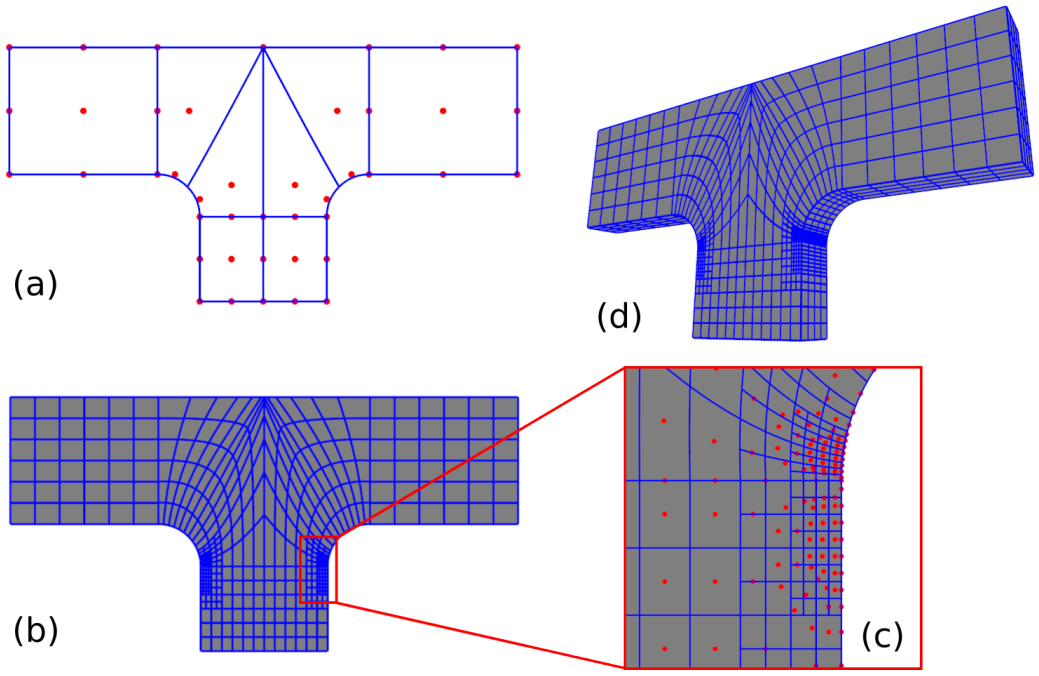

Figure 6.11: The evolution of the T-joint mesh in each steps of modeling: (a) 2D mesh where the orientation values are assigned to the control points; (b) 2D mesh after global and local refinement; (c) magnified view of locally refined area; red dots are control points; (d) 3D mesh ready for analysis after extrusion.

refinement level of $k = 2$ is chosen, and figure 6.5 (c) shows the magnified view of the mesh at the local refined region. As a last step for the model generation procedure, 2D spline surface is extruded to provide four layers on the laminate. The knot vector in out-of-plane direction, $\boldsymbol{\zeta} = [0, 0, 1, 1]$ is used to produce a single layer thickness with two control points: $c1 = (0, 0, 0, 1)$ and $c2 = (0, 0, 1, 1)$ in homogeneous coordinate system. Then, three knots ($\zeta_1 = 0.25$, $\zeta_2 = 0.50$, and $\zeta_3 = 0.75$) are inserted to obtain four layers. The resultant mesh that are ready for analysis is shown in Fig. 6.11 (d).

First, the analysis was performed on the laminate with straight fibers in a cross-ply configuration to set the reference for comparison with the optimized results. Figure 6.12 (a) shows the contour of the stress component in y-direction. A region of stress concentration is identified, and the localized cracks are placed for a fractured simulation. Figure 6.6 (b) shows the contour of the stress component in y-direction on the same structure with the

cracks that have a length, $a = 0.25$ mm.

The first optimization study is to minimize the maximum principal stress. In this optimization problem, an argument is a vector consisting of twelve orientation values, $\mathbf{\Theta} = \{\theta_1, \theta_2, ...\theta_{19}\}$, to be assigned to the control points in the spline surface shown in Fig. 6.11 (a), and the objective function, y_i is the maximum of principal stress from the simulation. To set up a Gaussian process regression model for Bayesian optimization step, 4000 pairs of $(\mathbf{\Theta}_i, y_i)$ are prepared using Sobol sequences. Once the training step is done, 500 iterations of Bayesian optimization loop are performed followed by a gradient-based optimization described in the previous section. The total run time for this optimization is about 6 hours.

Figure 6.13 (a) shows the contour of maximum principal stress of the optimized result. In the reference case, the largest maximum principal stress is found to be around 422 MPa. After the optimization, it is dropped to 1361 MPa. The largest value of the maximum principal stress is reduced by a factor of 3. Similar to the previous study, the stress contour of the optimized laminate exhibits a well distribution of load across the structure. The optimal fiber paths of the cross-ply laminate is shown in Fig. 6.13 (b) and (c). Focusing on the fiber paths in Fig. 6.13 (b), the curvy feature on fiber paths seems to make the region compliant and reduce the stress build up around the corners.

The other optimization study is to minimize the energy release rate. Similarly, a total of 4000 training data is generated using Sobol sequences. 500 iterations of Bayesian optimization loop are performed followed by a gradient-based optimization to fine tune the optimal fiber paths. The total run time for this optimization is about 12 hours.

Figure 6.14 (a) and (b) show the contours of stress component in y-direction from the optimized laminate without the crack and with the crack, respectively. Following observations are consistent with the optimization study perfomed with the other geometry. The stress contour is almost identical to each other as there is a negligible crack opening displacement. The optimizer finds the fiber paths that does not induce positive strain where the crack is likely to occur. As a result, outstanding result of $G = 0.004$ N/mm is obtained. For the reference case, the energy release rate is found to be 0.88 N/mm. The optimal laminate exhibits well distributed stress contour. Figure 6.15 (a) and (b) show the optimal

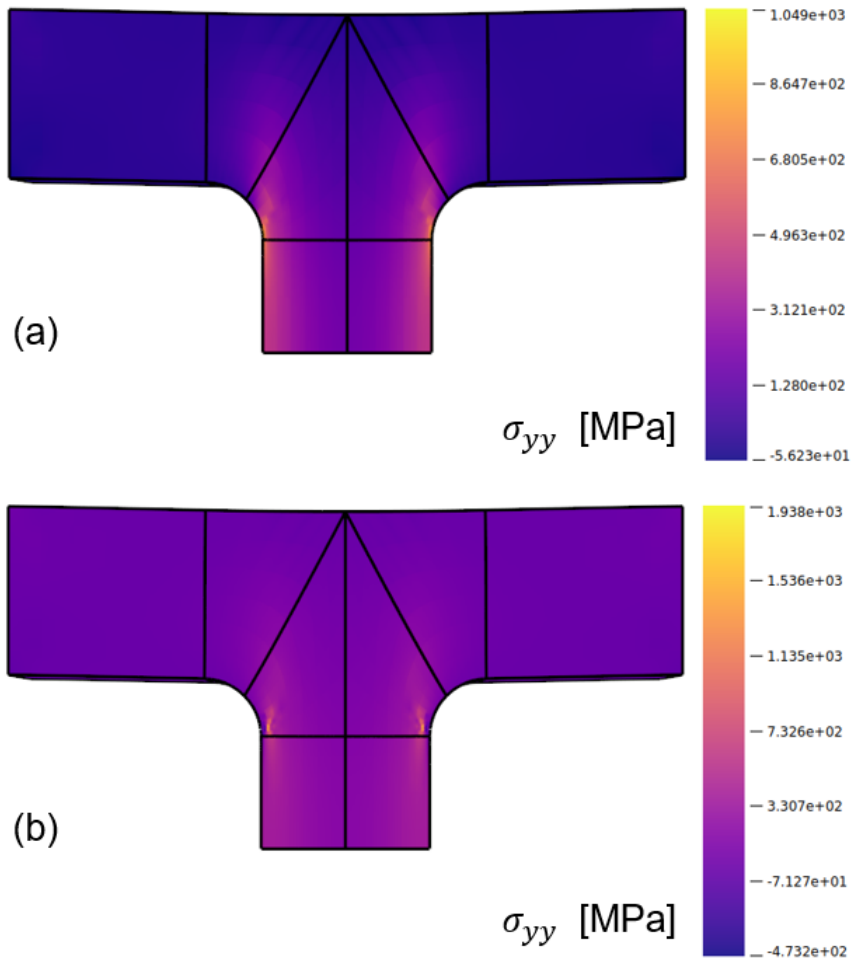

Figure 6.12: The result from isogeometric analysis on the cross-ply laminate with straight fibers: (a) contour plot of a stress component in y-direction; (b) contour plot of a stress component in y-direction after a crack is inserted at the region of stress concentration.

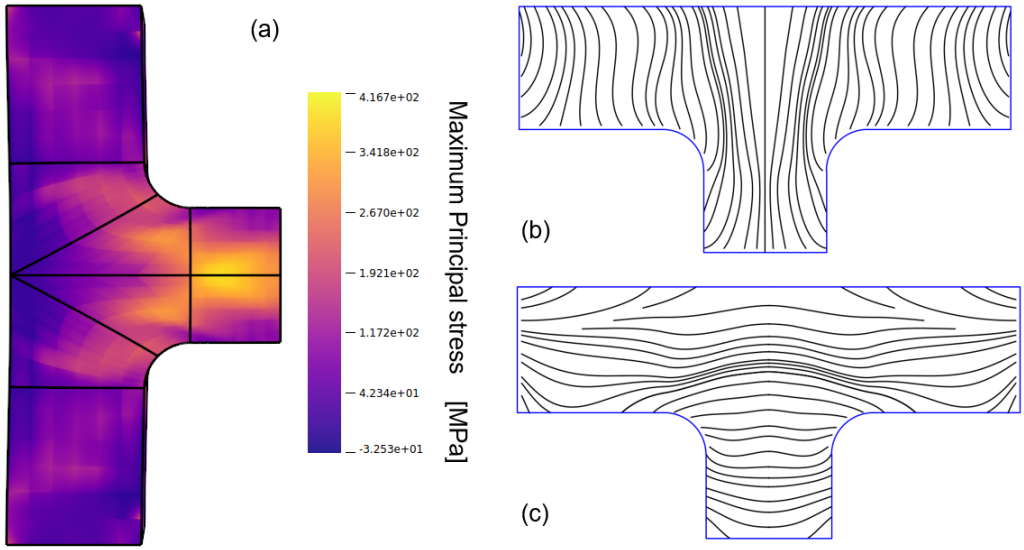

Figure 6.13: The optimization result for minimizing the maximum principal stress on the T-joint: (a) contour of the maximum principal stress of the laminate with optimal fiber placement; (b) optimal fiber paths in the outer layers; (c) optimal fiber paths in the inner layers, which are 90° offsets of fibers in the outer layers to retain a cross-ply configuration.

fiber paths of the cross-ply laminate. Focusing on the fiber paths in Fig. 6.15 (b), fibers near the tip of notch approximately forms a circular paths centered around the tip. This was already observed with the plate with a semi-circular notch. The optimizer consistently places circular paths which trap the crack, and the enclosing arcs reduces the local stiffness around the crack. This mechanism efficiently makes the crack stealthy from the tensile load. The fiber paths near the corners try to embrace the contour of the T-joint. Fibers straighten out for those are away from the corners

Revisiting the possibility of change in G_f, the enclosing fiber paths are very close to being orthogonal to the direction of the crack propagation as shown in Fig. 6.15 (b). In this optimization problem, there were no constraint that can induce this condition. It seems to worth investigating the enclosure of the cracks provides a mechanism of minimizing the energy release rate of a general structures. In this optimization result, orthogonal placement of fibers along the crack path allows to conclude that the G_f stays uniform in the direction of the crack growth, and the minimization of G is relevant to the increase of fracture resistance.

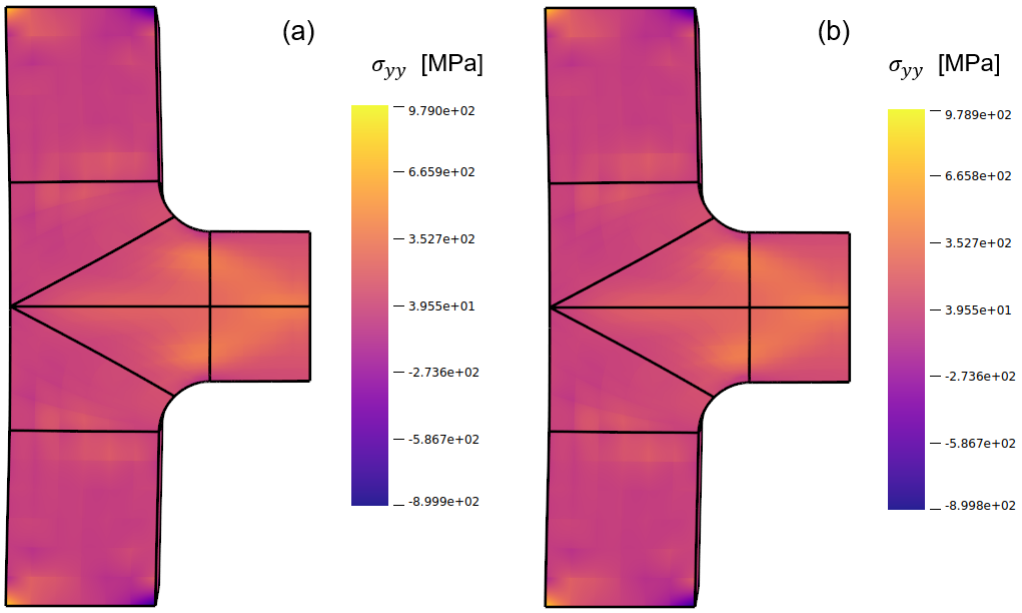

Figure 6.14: The optimization result for minimizing the energy release rate of the T-joint: (a) contour of the stress component in y-direction without a crack; (b) contour of the identical stress component with the cracks at the locations of stress concentration found with straight fibers.

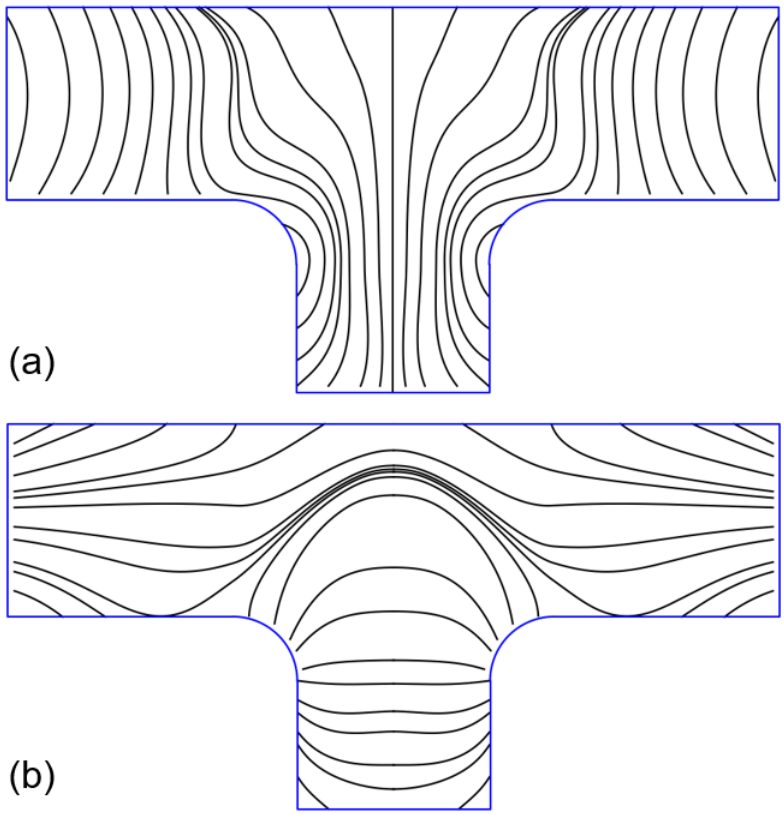

Figure 6.15: The optimal fiber paths for minimizing the energy release rate of the T-joint: (a) placed in the outer layers; (b) placed in inner layers which are 90° offsets of fibers in the outer layers to retain a cross-ply configuration.

Chapter 7

A NOVEL FRAMEWORK IN DAMAGE MODELING OF FIBER-REINFORCED COMPOSITES FEATURING CTI

The optimization studies in the previous chapter was able to utilize a linear solver since it was focusing on the asymptotic regions in type II SEL of quasibrittle materials. The fracture behavior of composites in the transition zone requires more sophisticated computational model because damage initiation and progression in FPZ need to be properly described in order to predict the ultimate failure of composite materials. This chapter is intended to present a novel discrete approach called the Discrete Model for Composites (DM4C) in modeling 3D printed fiber-reinforced composites featuring CTI.

In this chapter, main components of the new discrete approach such as model generation, discrete kinematics and governing laws, and constitutive laws for discrete composite description which includes elastic and nonlinear behavior are explained. Then, the material properties of a 3D printed continuous fiber composite is provided followed by calibration results. Lastly, 3D printed composite laminates featuring CTI with sinusoidal waviness are modeled using the novel approach. To examine the fracture behavior, a center crack is inserted to each laminate. Damage mechanisms of simulated laminates are discussed.

7.1 Model generation

In DM4C framework [14-17], fiber tows extruded from a 3D printer are explicitly modeled as Timoshenko beams. Internal nodes from beam elements with the boundary nodes are used to construct a tetrahedral mesh to represent the surrounding matrix material. The modeling procedure is highly efficient and parallelizable and the geometry generation algorithm is summarized as follows:

1. A polygon mesh that resembles a printed geometry is constructed and provides a geometric information such as vertices, edges, and faces.
2. Examining the cross-section of the structure, the centroidal locations of filaments are

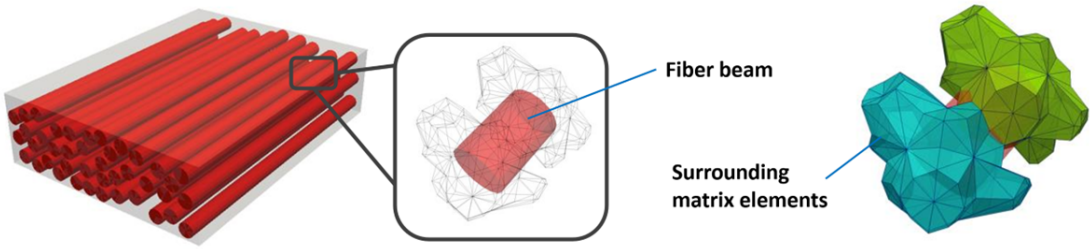

Figure 7.1: A rectangular specimen with straight fiber tows which are represented with Timoshenko beam elements; the surrounding matrix cells represent the matrix material.

extracted from the printing profile. Nodal locations for beam elements are obtained by extruding along the printing paths. The lengths of beam elements are approximately 20 % longer than the diameter of filaments. This ensures that the aspect ratios of tetrahedral elements are reasonable after a tessellation process performed in the next step.

3. The polygon mesh with the coordinates of beam elements is exported to either Tetgen [28] or GMSH [29]. Delaunay triangulation is performed to produce a tetrahedral mesh.
4. Voronoi tessellation is used on the tetrahedral mesh to generate facets that surrounds the beam elements.

Figure 7.1 shows a simple rectangular specimen of composite parts modeled in DM4C framework. Rendered red cylinders represent the fiber tow beams. As can be seen, groups of facets form cells and surround the fiber beams.

7.2 Discrete kinematics and governing laws

The mechanical behavior of fiber tows is described at the integration points of beam elements. The kinematic relations are formulated in a discrete manner to provide information on the deformation of structure. Similarly, the governing laws follows a discrete formulation to provide a loading condition to fiber beams and matrix elements. Fortunately, discrete beams resembles Timoshenko beam formulation. The mechanical behavior of a matrix material is defined on the facets. DM4C utilizes the discrete kinematic relation of nodes in a

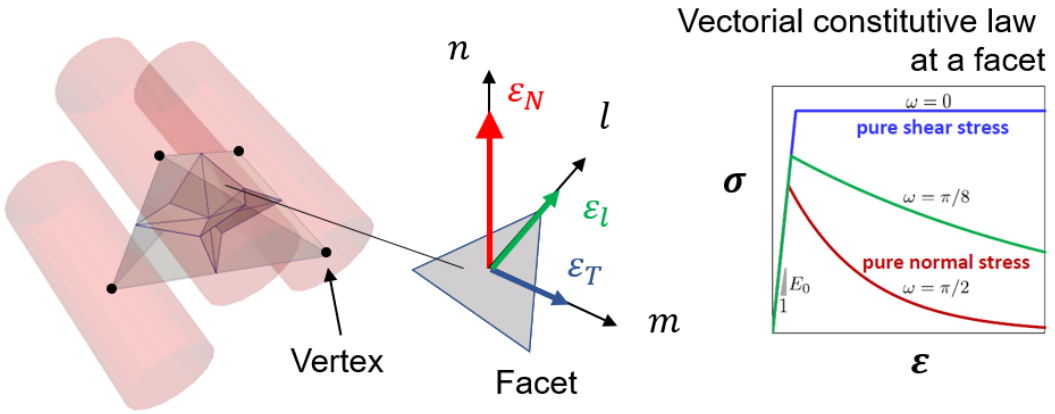

Figure 7.2: Four internal nodes from beams form a single tetrahedral element; a strain vector is computed at each facet, and the strain vector is used to compute the stress vector at the facet following the vectorial constitutive law.

tetrahedron to compute the strain vector of a facet embedded inside the associated tetrahedron. A single tetrahedral elements have a total of twelve facets as shown in Fig. 7.2. The strain vectors of these twelve facets are derived from the deformation of the tetrahedron. The volume of a tetrahedron is subdivided into four regions by facets inside of it. The displacement field in side the tetrahedron is derived from the kinematic relations in these four regions. At the end, a strain vector can be computed at each facet from the displacement field.

The displacement field $\boldsymbol{u}$ inside each element is defined following the kinematic relation of nodes as follows:

$$\boldsymbol{u}(\boldsymbol{x}) = \boldsymbol{u}_i + \boldsymbol{\theta}_i \times (\boldsymbol{x} - \boldsymbol{x}_i) = \boldsymbol{A}_i(\boldsymbol{x})\boldsymbol{Q}_i \tag{7.1}$$

where

$$\boldsymbol{A}_i(\boldsymbol{x}) = \begin{bmatrix} 1 & 0 & 0 & 0 & x_3 - x_{3i} & x_{2i} - x_3 \\ 0 & 1 & 0 & x_{3i} - x_3 & 0 & x_1 - x_{1i} \\ 0 & 0 & 1 & x_2 - x_{2i} & x_{1i} - x_1 & 0 \end{bmatrix} \tag{7.2}$$

The vector $\boldsymbol{x}$ is the Cartesian coordinate inside the element, and the vector $\boldsymbol{x}_i$ represents the coordinate of node i. The vector $\boldsymbol{Q}_i^T = \left[\boldsymbol{u}_i^T, \boldsymbol{\theta}_i^T\right]$ is the ordered pair of the vector $\boldsymbol{u}_i^T = [u_{1i}, u_{2i}, u_{3i}]$ and the vector $\boldsymbol{\theta}_i^T = [\theta_{1i}, \theta_{2i}, \theta_{3i}]$, which are the translational and rotational degrees of freedom of node i.

Stress vector and strain vector at individual facet are computed following the Lattice Discrete Particle Model (LDPM) [163, 164]. The strain components in each projected facet are computed following Eqs. 7.3–7.5.

$$\varepsilon_{Nk} = \boldsymbol{B}_N^{jk}\boldsymbol{Q}_j - \boldsymbol{B}_N^{ik}\boldsymbol{Q}_i \tag{7.3}$$

$$\varepsilon_{Mk} = \boldsymbol{B}_M^{jk}\boldsymbol{Q}_j - \boldsymbol{B}_M^{ik}\boldsymbol{Q}_i \tag{7.4}$$

$$\varepsilon_{Lk} = \boldsymbol{B}_L^{jk}\boldsymbol{Q}_j - \boldsymbol{B}_L^{ik}\boldsymbol{Q}_i \tag{7.5}$$

where $\boldsymbol{B}_N^{pk} = (1/\ell_e)\,\boldsymbol{n}_k^T\boldsymbol{A}_p(\boldsymbol{x}_{Ck})$, $\boldsymbol{B}_M^{pk} = (1/\ell_e)\,\boldsymbol{m}_k^T\boldsymbol{A}_p(\boldsymbol{x}_{Ck})$, and $\boldsymbol{B}_L^{pk} = (1/\ell_e)\,\boldsymbol{l}_k^T\boldsymbol{A}_p(\boldsymbol{x}_{Ck})$ for $p = i, j$. The vectors $\boldsymbol{n}_k = (\boldsymbol{x}_j - \boldsymbol{x}_i)/\ell_e$, $\boldsymbol{m}_k$, and $\boldsymbol{l}_k$ compose a set of mutually orthogonal axes for the plane of the projected facet.

The stress vectors at the projected facets comes from the constitutive relation. The Principle of Virtual Work (PVW) states that the sum of the internal work from all the facets is equivalent to the total external work applied to the structure. As a result, the internal energy associated with the facet k can be expressed shown in Eq. 7.6.

$$\delta W_k = \ell_k A_k \boldsymbol{\sigma}_k^T \delta\boldsymbol{\varepsilon}_k = \ell_k A_k \left(\sigma_{Nk}\delta\varepsilon_{Nk} + \sigma_{Mk}\delta\varepsilon_{Mk} + \sigma_{Lk}\delta\varepsilon_{Lk}\right) \tag{7.6}$$

where A_k is the area of a projected facet k.

The relations between strain components and the nodal degrees of freedom in Eqs. 7.3–7.5 can be substituted, and the following expressions are obtained to compute the nodal

force vectors, $\boldsymbol{F}_{ik}$ and $\boldsymbol{F}_{ik}^{T}$, for nodes i and j associated to the facet k:

$$\delta W_k = \boldsymbol{F}_{ik}^{T}\delta\boldsymbol{Q}_i + \boldsymbol{F}_{jk}^{T}\delta\boldsymbol{Q}_j, \quad \text{where} \tag{7.7}$$

$$\boldsymbol{F}_{ik}^{T} = -\ell_k A_k \left(\sigma_{Nk}\boldsymbol{B}_N^{ik} + \sigma_{Mk}\boldsymbol{B}_M^{ik} + \sigma_{Lk}\boldsymbol{B}_L^{ik}\right) \tag{7.8}$$

$$\boldsymbol{F}_{jk}^{T} = \ell_k A_k \left(\sigma_{Nk}\boldsymbol{B}_N^{jk} + \sigma_{Mk}\boldsymbol{B}_M^{jk} + \sigma_{Lk}\boldsymbol{B}_L^{jk}\right) \tag{7.9}$$

7.3 Constitutive laws for discrete fiber model

In this section, the constitutive law for fiber beams is introduced. In DM4C, the constitutive law is defined at the integration points of each beam element. In the elastic regime, the axial stress σ_f follows a elastic Hooke's Law as a function of axial strain ε_f shown in Eq. 7.10:

$$\sigma_f = E_f \varepsilon_f \tag{7.10}$$

where E_f is the parameter associated to the modulus of the fiber bundle, and the value is determined in calibration process so that it matches the longitudinal modulus of a composite material.

A simple linear softening law describes the degradation in the fiber modulus once the axial stress goes over the strength limit, σ_c. The equation 7.11 is the expression for the linear boundary.

$$\sigma_f(\delta) = \max\left[0, \sigma_c\left(1 - \frac{\delta - \delta_c}{\delta_f - \delta_c}\right)\right] \tag{7.11}$$

In Eq. 7.11, δ is the elongation of a beam element, $\delta_c = \sigma_c L_0/E_f$, with L_0 being the length of the beam element, is the elastic limit displacement which determines the initiation of the linear softening. Complete softening is reached when $\delta_f > (2G_f)/\sigma_c$ where G_f is the fracture energy of fibers and δ_f the beam element length. In such a case, the axial stress becomes zero.

7.4 Constitutive laws for discrete matrix model

In this section, the constitutive behavior of the matrix defined at the facet is introduced. The equations for the elastic and inelastic behaviors are described in the following subsections. One major difference compared to other models that define a constitutive law between stress and strain tensors is that stress and strain are vectorial quantity in DM4C framework. Therefore, there is one normal component and two tangential components.

7.4.1 Elastic behavior

In the elastic regime, each component of strain and stress vectors follows the linear Hooke's law in one-dimension as expressed in Eqs. 7.12, and .

$$\sigma_N = E_0 \varepsilon_N \tag{7.12}$$

$$\sigma_M = \alpha E_0 \varepsilon_M \tag{7.13}$$

$$\sigma_L = \alpha E_0 \varepsilon_L \tag{7.14}$$

where E_0 is effective mesoscale normal modulus, and α is a shear-normal coupling parameter. E_0 and α are the DM4C-matrix properties defined at the facet level. They are determined in the calibration process so that the model has a matching the macroscopic elastic properties of a composite material in the transverse direction.

7.4.2 Fracture behavior in tension

A facet in tension experience the fracturing behavior once it reaches the critical condition, which is characterized with the effect strain, ε, and the effective stress, σ, as defined in Eqs. 7.15 and 7.16. This relation follows the LDPM formulation [163].

$$\varepsilon = \sqrt{\varepsilon_N^2 + \alpha \left(\varepsilon_M^2 + \varepsilon_L^2 \right)} \tag{7.15}$$

$$\sigma = \sqrt{\sigma_N^2 + \left(\sigma_M^2 + \sigma_L^2 \right) / \alpha} \tag{7.16}$$

The increment of the effective stress is proportional to the increment of the effective strain. The effective stress develops linearly until it reaches the tensile boundary, σ_{bt}, as expressed in Eq. 7.17:

$$\sigma_{bt}(\varepsilon,\omega) = \sigma_0(\omega)\exp\left(-H_0(\omega)\frac{\langle\varepsilon_{max}-\varepsilon_0(\omega)\rangle}{\sigma_0(\omega)}\right) \tag{7.17}$$

where the bracket follows the Macaulay's notion: $\langle x\rangle = \max(x,0)$. The tensile boundary provides the exponential decay as a function of the normal-shear ratio variable, ω, and the history-dependent maximum effective strain, ε_{max} The normal-shear ratio variable ω is computed as:

$$\tan\omega = \frac{\varepsilon_N}{\sqrt{\alpha}\varepsilon_T} \tag{7.18}$$

where $\varepsilon_T = \sqrt{\varepsilon_M^2+\varepsilon_L^2}$. This variable indicates the degree of interaction between shear and normal load in a facet. The strength limit of the effective stress, $\sigma_0(\omega)$, is computed as:

$$\sigma_0(\omega) = \sigma_t\frac{-\sin(\omega)+\sqrt{\sin^2(\omega)+4\alpha\cos^2(\omega)/r_{st}^2}}{2\alpha\cos^2(\omega)/r_{st}^2} \tag{7.19}$$

where $r_{st} = \sigma_s/\sigma_t$ is the ratio between the shear strength σ_s and the tensile strength σ_t. The elastic limit $\varepsilon_0(\omega)$ is the ratio: $\sigma_0(\omega)/E_0$.

The rate of decay in the tensile boundary is determined by the function, $H_0(\omega)$, which is defined as

$$H_0(\omega) = H_t\left(\frac{2\omega}{\pi}\right)^{n_t} \tag{7.20}$$

where $H_t = 2E_0/(\ell_t/\ell-1)$ and $\ell_t = 2E_0G_t/\sigma_t^2$.

In Equation 7.20, ℓ is the edge length of the tetrahedron element related to the facet in the evaluation, and G_t is the fracture energy of the matrix. The set of parameters, σ_s, σ_t,

ℓ_t, and n_t, need to be determined in the calibration process in order to capture the tensile strength and the fracture energy of the matrix material modeled in DM4C.

7.4.3 Hardening behavior in compression

A facet in compression experiences hardening behavior on its normal component of stress vector after it passes the elastic regime. The hardening behavior is a function of the volumetric strain ε_V and the deviatoric strain $\varepsilon_D = \varepsilon_N - \varepsilon_V$ as proposed in LDPM formulation [163, 165]. After the elastic limit, the normal stress follows the compressive boundary $\sigma_{bc}(\varepsilon_D, \varepsilon_V)$ expressed as follows:

$$\sigma_{bc}(\varepsilon_D, \varepsilon_V) = \begin{cases} \sigma_{c0} & \text{for} \quad -\varepsilon_{DV} \leq 0 \\ \sigma_{c0} + \langle -\varepsilon_{DV} - \varepsilon_{c0} \rangle H_c(r_{DV}) & \text{for} \quad 0 \leq -\varepsilon_{DV} \leq \varepsilon_{c1} \\ \sigma_{c1}(r_{DV}) \exp((-\varepsilon_{DV} - \varepsilon_{c1}) H_c(r_{DV}) / \sigma_{c1}(r_{DV})) & \text{otherwise} \end{cases} \tag{7.21}$$

where σ_{c0} is the compressive yielding strength of a facet, H_c is the initial hardening modulus, and σ_{c1} is the normal stress value at the onset of the rehardening.

In the compressive boundary, $\varepsilon_{DV} = \varepsilon_V + \beta\varepsilon_D$, and $\varepsilon_{c0} = \sigma_{c0}/E_0$. When the magnitude of ε_{DV} exceeds the parameter $\varepsilon_{c1} = \kappa_{c0}\varepsilon_{c0}$, the facet exhibits the rehardening behavior. The rehardening stress has the following expression: $\sigma_{c1}(r_{DV}) = \sigma_{c0} + (\varepsilon_{c1} - \varepsilon_{c0}) H_c(r_{DV})$.

In the compressive boundary, $H_c(r_{DV})$ is the initial hardening modulus and has the following expression:

$$H_c(r_{DV}) = \frac{H_{c0} - H_{c1}}{1 + \kappa_{c2} \langle r_{DV} - \kappa_{c1} \rangle} + H_{c1} \tag{7.22}$$

where H_{c0}, H_{c0}, and H_{c0} are matrix properties in facet level and $H_{c1} = \kappa_{c3} E_0$.

In Equation 7.22, the deviatoric and volumetric dependent variable, r_{DV}, is computed as follows:

$$r_{DV} = \begin{cases} -\dfrac{|\varepsilon_D|}{\varepsilon_V - \varepsilon_{V0}} & \text{for} \quad \varepsilon_V \leq 0 \\ \dfrac{|\varepsilon_D|}{\varepsilon_{V0}} & \text{for} \quad \varepsilon_V > 0 \end{cases} \tag{7.23}$$

where $\varepsilon_{V0} = \kappa_{c3}\varepsilon_{c0}$.

In this work, β is assumed to be zero, and $\kappa_{c3} = 0.1$. The set of parameters, σ_{c0}, H_{c0}, ε_{c1}, κ_{c1} and κ_{c2} are to be determined in the calibration process in order to capture the proper normal behavior of facets under a compressive load in DM4C.

7.4.4 Frictional behavior in compression

A facet in compression experiences a frictional behavior which modifies the shear strength. The shear boundary under compression depends on the effective shear stress, which is express as:

$$\sigma_T = \sqrt{\sigma_M^2 + \sigma_L^2}. \tag{7.24}$$

The effective shear stress develops incrementally proportional to the effective shear strain until it reaches the shear boundary σ_{bs} defined as follows:

$$\sigma_{bs} \quad = \quad \sigma_s \; + \; \alpha\left(\mu_0 - \mu_\infty\right)\sigma_{N0} \; - \; \alpha\mu_\infty\sigma_N \; - \; \alpha\left(\mu_0 - \mu_\infty\right)\sigma_{N0}\exp\left(\frac{\sigma_N}{\sigma_{N0}}\right) \tag{7.25}$$

where σ_s is the shear strength of a facet under pure shear loading condition. In Equation 7.25, σ_{N0} determines the transition from the initial friction coefficient μ_0 to the asymptotic friction coefficient μ_∞.

The set of parameters, σ_s, σ_{N0}, μ_0 and μ_∞ are to be determined in the calibration process in order to capture the proper shearing behavior of facets under a compressive load in DM4C.

7.5 Material choice and properties

In this work, Composer A3, a desktop printer from Anisoprint SARL, was used to manufacture composite parts. The Anisoprint desktop printer co-extrudes a 0.35mm diameter,

continuous 1.5k CF tow, and a polyamide matrix material to create composite structures one tow at a time. From the coupon testing following the ASTM standard D3039, the four tensile properties of the 3D printed composites from the Composer A3 printer are measured and listed in Table 7.1.

Table 7.1: Mechanical properties of 3D printed composite material from the Anisoprint desktop printer

Property	Value
Longitudinal modulus, E_1, (GPa)	50.8
Transverse modulus, E_2, (GPa)	0.420
Longitudinal tensile strength, X_T (MPa)	611
Transverse tensile strength, Y_T, (MPa)	2.53

7.6 Calibration results

Rectangular specimens measuring 28 mm in width and 95 mm in length are modeled to simulate the longitudinal tension test and the transverse tension test. To calibrate longitudinal properties, a laminate comprising four layers at 0 degrees is utilized, while a laminate with four layers at 90 degrees is used to calibrate transverse properties. Both laminates have a thickness of 2 mm and a fiber tow volume fraction of 50%. The tow beams' diameter is 0.4 mm.

7.6.1 Longitudinal tension

The calibration process for longitudinal properties provides the following results. Figure 7.3 (a) illustrates the stress-strain response, with the black dashed lines representing the longitudinal Young's modulus and tensile strength of 3D printed composites from an Anisoprint desktop printer. As can be noticed, the calibration results closely match the target properties obtained from the experiment. The main damage mechanism observed in a longitudinal tension simulation is shown in Fig. 7.3 (b). The primary load drop occurs after the fiber tow beams break. Additionally, there is evidence of matrix failure in tension around the tow beams throughout the specimen as the nominal stress reaches the criti-

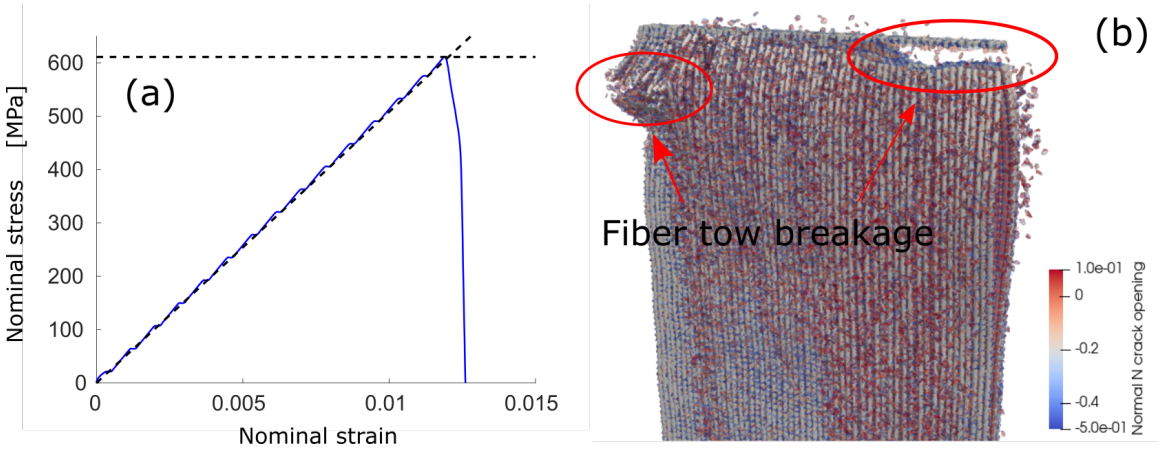

Figure 7.3: Calibration result for longitudinal properties: (a) Nominal stress versus nominal strain plot; dashed black lines represent the target Young's modulus and the target tensile strength; (b) Damage morphology in longitudinal tension; load drop is mainly due to the broken fiber tows.

cal value. This behavior is commonly observed in unidirectional composites experiencing failure under a longitudinal tensile load. Therefore, DM4C demonstrates the capability of accurately capturing the strength of composites with an appropriate damage mechanism in the longitudinal direction.

7.6.2 Transverse tension

The calibration process for transverse properties provides the following results. Figure 7.4 (a) shows the stress-strain response, with the black dashed lines representing the transverse Young's modulus and tensile strength of 3D printed composites from an Anisoprint desktop printer. As can be noticed, the calibration results closely match the target properties obtained from the experiment. In Figure 4 (b), the main damage mechanism observed in a transverse tension simulation is depicted. The transverse strength is achieved when the matrix elements fail in tension. As shown in Fig. 7.4 (b) and (c), a distinct localized region of facets failed in tension, a behavior commonly observed in unidirectional composites experiencing failure under a transverse tensile load. Therefore, DM4C is capable of accurately capturing the strength of composites with an appropriate damage mechanism in the

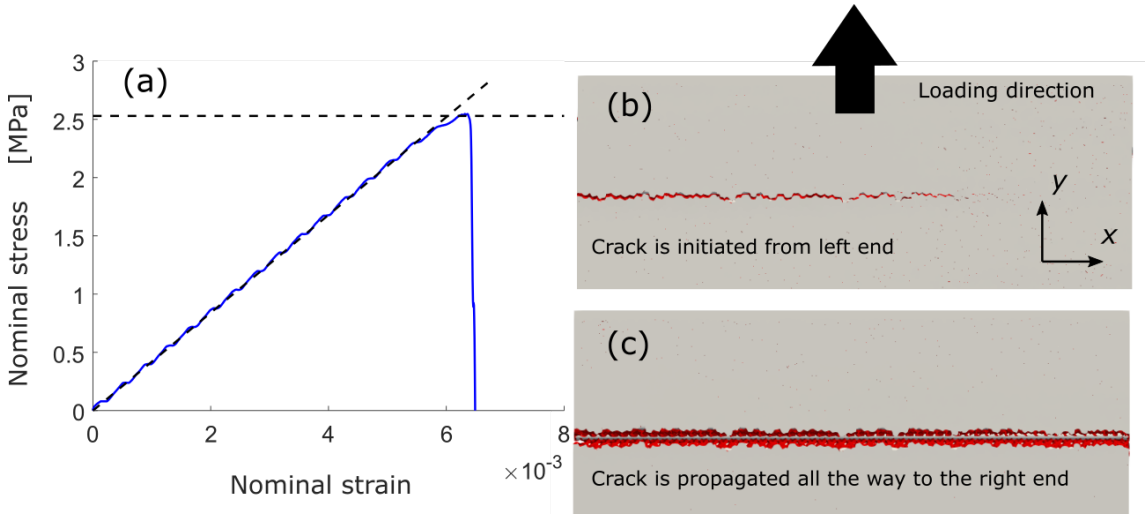

Figure 7.4: Calibration result for transverse properties: (a) Nominal stress versus nominal strain plot; dashed black lines represent the target Young's modulus and the target tensile strength; (b) The frame at which the localized crack is propagating from the left end; (c) The frame at which the crack is fully propagated to the right end.

transverse direction as well.

7.7 Effect of wavy reinforcement on toughness

To assess the strength of the 3D printed composites, a CCT specimen, as shown in Fig 7.5 (a), is created with the same dimensions as the tensile specimen used in calibration. The crack length is set to 30 % of the width. As a comparison, a cross-ply laminate comprising four layers, [0, 90, 90, 0], is simulated under a tensile load. To explore the impact of in-plane waviness, three specimens with fiber tows following sinusoidal waves, each having different amplitudes, are modeled. The in-plane waviness is applied exclusively to the transverse layers, and an illustration of wavy reinforcement can be seen in Fig. 7.5 (b). All three wavy reinforcements share the same period of 10 mm.

7.7.1 Cross-ply laminate

The tensile simulation of the cross-ply laminate with a center crack provides the following results. The nominal stress-strain plot is presented in Fig. 7.6 (a), while the overall specimen

Figure 7.5: Specimen for fracture simulations: (a) CCT specimen modeled in DM4C; (b) Magnified view of an example of wavy reinforcement near the crack.

view of the damage morphology can be seen in Fig. 7.6 6 (b). Dispersed matrix cracking is observed on the outer layer, where longitudinal fiber tows are arranged. The load decreases as a localized crack initiates from the tip of the pre-inserted crack. Subsequently, this single localized crack propagates in a straight path across the width of the cross-ply laminate, leading to the ultimate failure.

7.7.2 Wavy reinforcement 1

The first wavy variant contains sinusoidal fiber tow reinforcement with an amplitude equal to the diameter of the tows (0.4 mm). The simulation outcome is illustrated in Figure 7. The nominal stress-strain plot is shown in Fig. 7.7 (a). It indicates a marginal enhancement in fracture toughness when applying the waviness to the transverse layers. The nominal stress maintains an almost linear behavior up to the peak. However, there is still widespread matrix cracking observed on the outer layers. As shown in Fig. 7.7 (c), the crack propagates approximately along the paths defined by the in-plane waviness.

7.7.3 Wavy reinforcement 2

The second wavy variant contains sinusoidal fiber tow reinforcement with an amplitude twice as large as the diameter of the tows. The simulation outcome is presented in Figure 8. There is not a significant improvement in strength by doubling the amplitude compared to the diameter of the fiber tows. Nevertheless, the post-peak response indicates that the energy dissipation during crack propagation increases, as the waviness of the crack path is

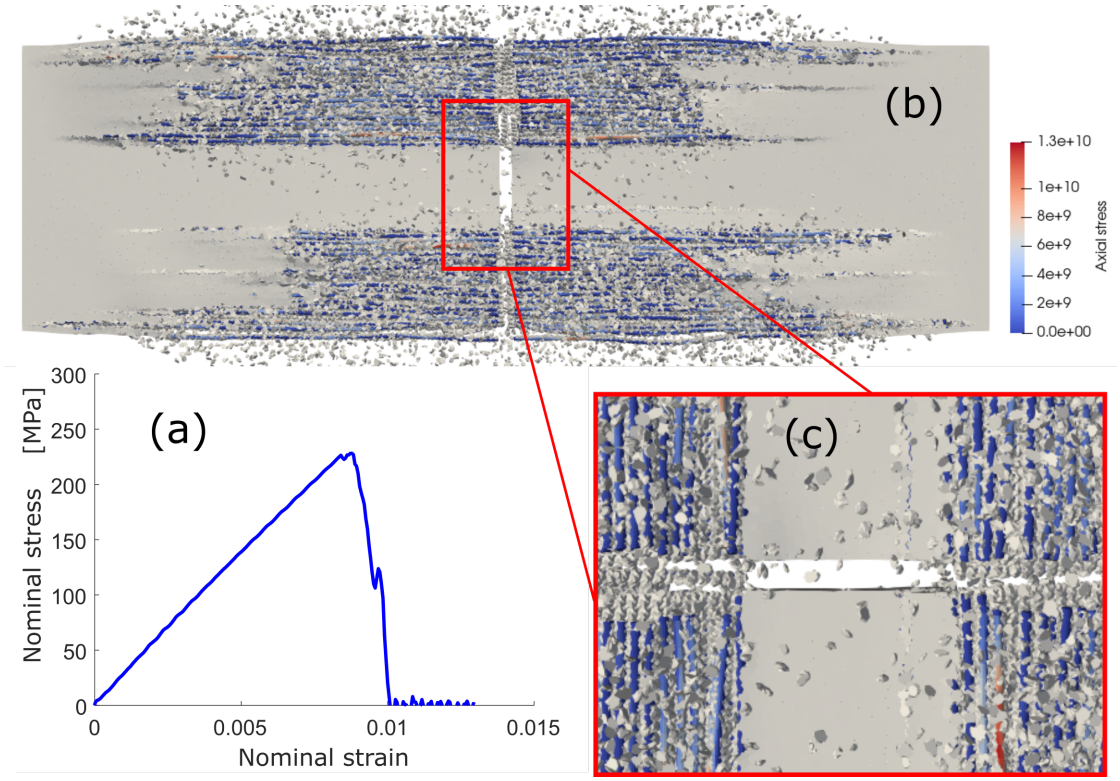

Figure 7.6: Simulations results on the straight cross-ply laminate: (a) Nominal stress versus nominal strain from the tensile simulation; (b) Full specimen view of damage morphology; (C) Magnified view of damage near the pre-inserted center crack.

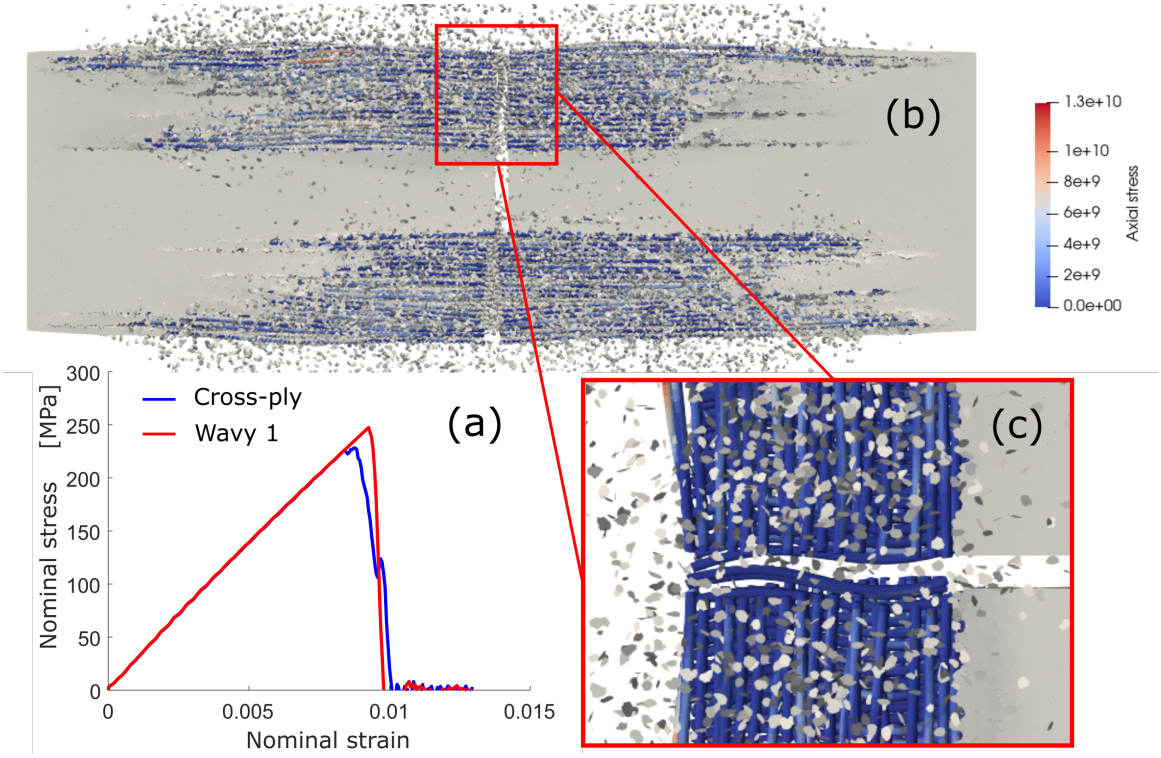

Figure 7.7: Simulations results on the first wavy laminate: (a) Nominal stress versus nominal strain from the tensile simulation of first wavy variant; (b) Full specimen view of damage morphology; (c) Magnified view of damage near the one end of the pre-inserted center crack.

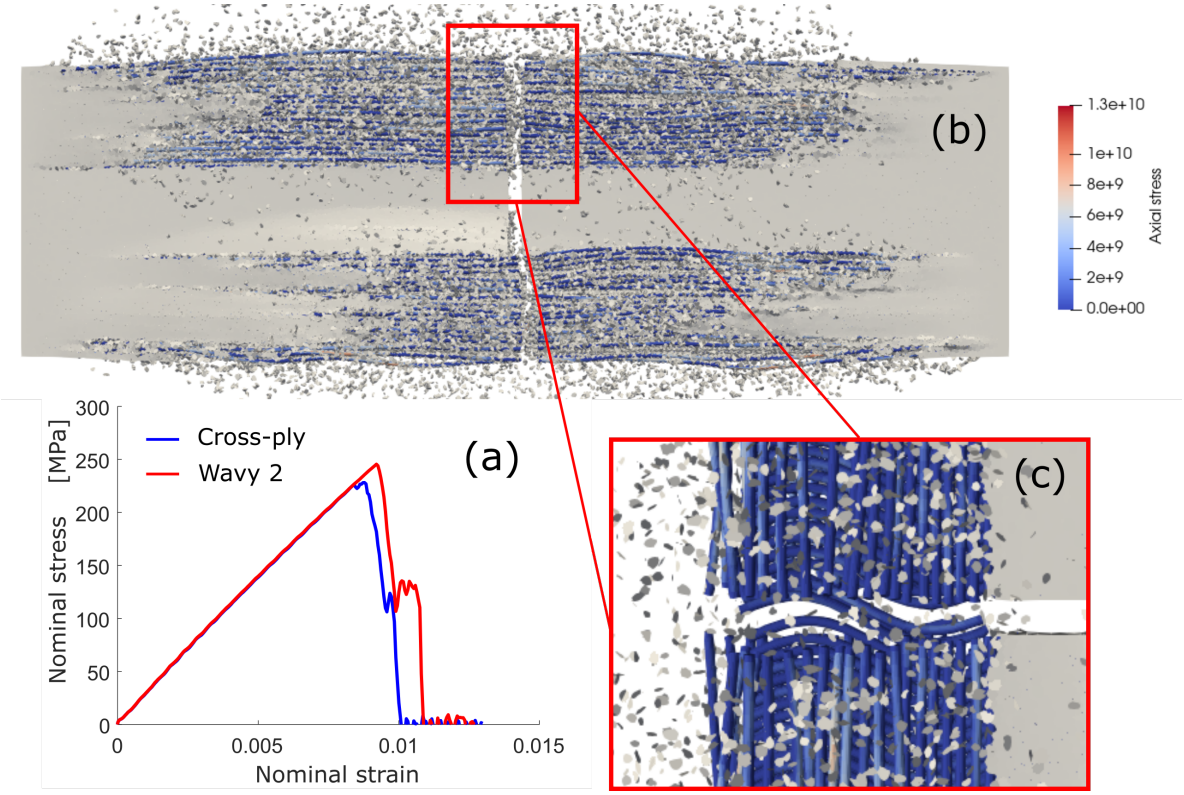

Figure 7.8: Simulations results on the second wavy laminate: (a) Nominal stress versus nominal strain from the tensile simulation of second wavy variant; (b) Full specimen view of damage morphology; (c) Magnified view of damage near the one end of the pre-inserted center crack.

enhanced. Figure 7.8 (c) illustrates this enhancement, where matrix fragments are omitted to provide better visibility of the fiber tows.

7.7.4 Wavy reinforcement 3

The last wavy variant contains sinusoidal fiber tow reinforcement with an amplitude four times as large as the diameter of the tows. The simulation result is shown in Figure 9. In contrast to the marginal improvement observed in the previous waviness, a significant increase in structural strength is observed when the amplitude exceeds a certain threshold, as shown in Fig. 7.9 (a). For this specific model, the critical threshold appears to be around four times the diameter. The strength achieved with this wavy reinforcement is 25 % higher

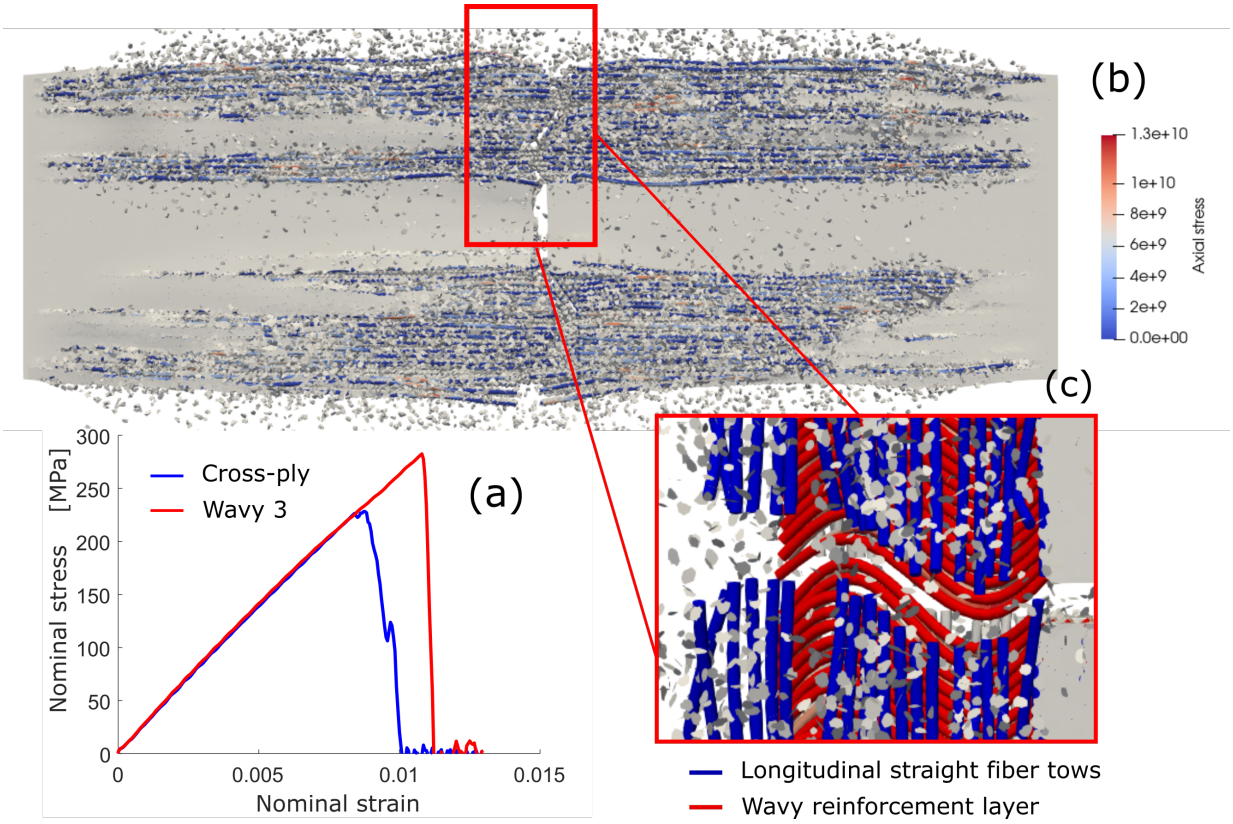

Figure 7.9: Simulations results on the third wavy laminate: (a) Nominal stress versus nominal strain from the tensile simulation of third wavy variant; (b) Full specimen view of damage morphology; (c) Magnified view of damage near the one end of the pre-inserted center crack.

than that of the cross-ply laminate. Once the nominal stress reaches its peak, there is a rapid drop in the load. In figure 7.9 (c), it can be noticed that longitudinal fiber tows break approximately following the path of the wavy reinforcement placed inside during the crack propagation.

At this amplitude of waviness, the initiation of crack propagation occurs slightly above the right end of the pre-inserted crack, as illustrated in Fig. 7.10. Upon closer examination of this region, it becomes evident that the wavy paths possess uphill slopes, enabling them to bear the load in shear. This mechanism contributes to an enhanced toughness of the laminate, particularly in the presence of neighboring defects.

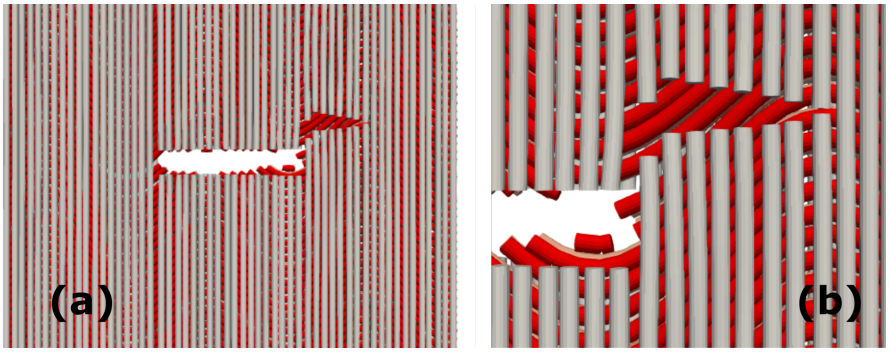

Figure 7.10: Damage morphology at the onset of the load drop: (a) The initiation of the crack occurs above from the right end of the pre-inserted center crack; (b) Magnified view of the crack initiation.

7.8 Concluding remarks

In this chapter, a novel discrete approach of modeling fiber-reinforced composites is presented and demonstrated its capability of capturing the damage mechanisms well noticed from composite literature. Most of lab testing specimens and composite parts fall inside the transition zone in type II SEL. It is important to choose the right modeling technique to accurately predict the fracturing behavior of composites by including the effect of nonlinear behavior in FPZ. DM4C framework provides a high resolution damage model suitable for analyzing the sophisticated fracturing behavior of composites featuring CTI.

Chapter 8

CONCLUSIONS AND FUTURE WORKS

8.1 Conclusions

In this work, a methodical investigation into the impact of curvilinear reinforcement within a composite structure is provided. The study delves into the influence of curvilinear reinforcement across two primary scenarios: 1) enhancing functional attributes of composites in electrostatic problem, and 2) improving mechanical performance focusing on the fracture resistance of composite structures. Following list is the summary of the findings:

1. Theoretical framework is expanded to provide a exact, closed-form solution for the electrostatic problem involving a finite electric current source within a CTI material system. Additionally, a numerical approach is introduced to acquire the most suitable fiber paths for any given geometry, serving as an illustration of how CTI materials can be applied effectively in damage detection.
2. The superiority of CTI media in damage detection surpasses isotropic and straight fiber material systems thanks to two key factors: 1) fiber breakage via crack propagation, and 2) deviations in initial fiber paths caused by updated field lines during crack propagation. Additionally, the exceptional health monitoring capacity of CTI material systems is achieved through the piezoresistive behavior of the fibers. It outperforms traditional fiber-reinforced composites such as woven composites. This presents an intriguing multi-objective optimization challenge for CTI material systems in applications involving health monitoring and damage detection.
3. From the simulation of media with curvilinear anisotropy utilizing the Isogeometric Analysis (IGA) framework, following observation is made. Leveraging precise geometric representation and enhanced continuity among elements, the NURBS-based IGA surpasses standard Finite Element Analysis (FEA) in computational efficiency, runtime, and the accuracy of field variable depiction while maintaining an equivalent

number of degrees-of-freedom.

4. The gradient-based optimization study is performed with the fiber path defined with polynomials. Through the optimization of fiber paths within a plate containing a semi-circular notch, a noteworthy outcome was achieved. The stress concentration factor, Kt, was successfully diminished to 1.28, with the highest stress point located at the notch tip. This result highlights a substantial 82 % decrease when compared to the conventional longitudinal fiber reinforcement, and 58 % decrease when compared from the isotropic case. In order to improve the optimization scheme, a broader definition of fiber paths seem to be necessary. Moreover, a global optimization method can be used to ensure that the optimal result is not a local minimum.
5. In-house IGA software package which utilizes LR B splines definition is developed to adapt IGA suitable for geometries with trimmed features. Local refinement technique is added to improve the accuracy of simulations and to model a local discontinuity such as a crack at the notch tip. With this new development, isogeometric optimization framework is proposed to take advantage of spline definition of mesh in representing a design space for optimization problems.
6. The optimization studies are performed following the isogeometric framework. Bayesian optimization step is added before the gradient-based method in order to improve the probability of finding a global optimum. Two composite structures are considered: 1) rectangular plate with a semi-circular notch and 2) T-joint. Both are laminated structures with the cross-ply layup sequence. The first objective is to minimize the maximum principal stress. For the rectangular plate, the maximum principal stress is reduced by a factor greater than 7. For T-joint structure, the maximum principal stress is reduced by a factor of 3. The other objective is to minimize the energy. For both structures, the energy release rate is reduced close to zero which indicates that the crack is not likely to form at the notch.
7. A novel, discrete modeling approach for fiber-reinforced composites (DM4C) is introduced. Its proficiency in accurately depicting the damage mechanisms of fiber reinforced composite is highlighted by simulating the center-cracked coupons with wavy reinforcements.

Fibers are explicitly modeled using Timoshenko beams which are embedded in a tetrahedral conforming mesh that characterizes the matrix. The facet-based formulation enables discrete fracture modeling, and prevents the element erosion. Additionally, the explicit representation of fibers and matrix allows a simple and distinct definition of material parameters thanks to the constitutive laws grounded in physics rather than in empirical curve fitting.

8.2 Future works

While many aspects of composites featuring CTI are explored in this work, there remain numerous unanswered questions. The following list includes the suggested future works that can be derived on from the current investigation.

1. Thanks to the advancement in the additive manufacturing technology in composite materials, the optimal fiber paths obtained from the optimization studies can be printed using several methods such as AFP and 3D printing of continuous fibers. Experimental validation of those results can evaluate mechanical performance of the optimal laminates compare to the standard design.
2. It is expected that the additively manufactured composite parts are likely to underperform because of the inherent defects from manufacturing process. The processing modeling can be incorporate to the design and analysis of composite structures featuring CTI.
3. In this work, the electrostatic problem and mechanical problem in composites are investigated, separately. However, in a practical design, both attributes may need to be considered for a given structure. Employing a multi-objective optimization approach, one can find the optimal fiber paths for a laminated configuration to enhance both the functional and mechanical properties. Similarly, multi-objective idea can be used to consider multiple loading conditions such as compression to prevent a design prone to other type of failure (e.g. buckling from compression).
4. The prediction of the ultimate strength of a composite structures requires a higher order damage models such as DM4C because the progression of multiple damage mechanisms may need to be captured in a right manner. However, the evaluation on these

models are often numerically expensive. Therefore, there are not many of optimization study that uses these models for the objective function. A data-driven approach such as Bayesian optimization can be applied to handle computationally intensive objective functions, enabling the identification of the optimal laminate configuration that maximizes the load capacity of a given structure.

5. As noticed in the previous chapter, there is no theoretical and experimental work done to investigate the change in fracture energy depending on the fiber orientation. In future, it is probable that a more complex design utilizing composite materials will emerge. In order to have a good understanding of the fracturing behavior of those composite designs, it is significant to know how to compute the proper fracture energy for them. Furthermore, the size of fracture process zone may be investigated with curvilinear reinforcement to see if damage mechanisms in 3D printed parts may affect the nature of crack formation and propagation.
6. The optimization in this study assumes the idealized manufacturing condition. As a future work, it is suggested to perform optimization studies with manufacturing constraints such as radius of curvatures that the printer head can travel. Moreover, it can be noticed that there are regions where fibers get compact and regions where fibers tend to diverge based on the vector field represented with splines. In real world, fibers have finite diameter; therefore, a fiber filament need to be cut before colliding others. These manufacturing constraints can be considered in the optimization study to find an optimal configuration that is more practical to be made. Ultimately, it would be interesting to apply the optimization framework to the real structures such as laminate design for aircraft wing-box with manufacturing constraints extending the work from Poort [166].

BIBLIOGRAPHY

[1] Thomas JR Hughes, John A Cottrell, and Yuri Bazilevs. Isogeometric analysis: Cad, finite elements, nurbs, exact geometry and mesh refinement. *Computer methods in applied mechanics and engineering*, 194(39-41):4135–4195, 2005.

[2] Thomas W Sederberg, Jianmin Zheng, Almaz Bakenov, and Ahmad Nasri. T-splines and t-nurccs. *ACM transactions on graphics (TOG)*, 22(3):477–484, 2003.

[3] Thanh Ngan Nguyen. Isogeometric finite element analysis based on bézier extraction of nurbs and t-splines. Master's thesis, Norges teknisk-naturvitenskapelige universitet, Fakultet for . . . , 2011.

[4] Wenyan Wang, Yongjie Zhang, Michael A Scott, and Thomas JR Hughes. Converting an unstructured quadrilateral mesh to a standard t-spline surface. *Computational Mechanics*, 48(4):477–498, 2011.

[5] Hyun-Jung Kim, Yu-Deok Seo, and Sung-Kie Youn. Isogeometric analysis for trimmed cad surfaces. *Computer Methods in Applied Mechanics and Engineering*, 198(37-40):2982–2995, 2009.

[6] Dominik Schillinger, Luca Dede, Michael A Scott, John A Evans, Michael J Borden, Ernst Rank, and Thomas JR Hughes. An isogeometric design-through-analysis methodology based on adaptive hierarchical refinement of nurbs, immersed boundary methods, and t-spline cad surfaces. *Computer Methods in Applied Mechanics and Engineering*, 249:116–150, 2012.

[7] Kjetil André Johannessen, Trond Kvamsdal, and Tor Dokken. Isogeometric analysis using lr b-splines. *Computer Methods in Applied Mechanics and Engineering*, 269:471–514, 2014.

[8] Michael Lange, Lawrence Mitchell, Matthew G Knepley, and Gerard J Gorman. Efficient mesh management in firedrake using petsc dmplex. *SIAM Journal on Scientific Computing*, 38(5):S143–S155, 2016.

[9] J Austin Cottrell, Thomas JR Hughes, and Yuri Bazilevs. *Isogeometric analysis: toward integration of CAD and FEA*. John Wiley & Sons, 2009.

[10] Zdenek P Bažant, Jia-Liang Le, and Marco Salviato. *Quasibrittle fracture mechanics and size effect: A first course*. Oxford University Press, 2021.

[11] Jiacheng Chen. *Comprehensive Investigation of Quasibrittle Fracture of IM7/977-3 Laminates via Size Effect Analysis*. PhD thesis, University of Washington, 2023.

[12] Doug Beason. Aircraft started with the wright materials. *MRS Bulletin*, 20(5):67–67, 1995.

[13] Walter James Boyne. Airplane. `https://www.britannica.com/technology/airplane`. Online; accessed 23 March 2021.

[14] Andrew R Goetz and Brian Graham. Air transport globalization, liberalization and sustainability: post-2001 policy dynamics in the united states and europe. *Journal of Transport Geography*, 12(4):265–276, 2004.

[15] David L Greene and Michael Wegener. Sustainable transport. *Journal of Transport Geography*, 5(3):177–190, 1997.

[16] John Whitelegg. Aviation: the social, economic and environmental impact of flying. *Ashden Trust, London*, 2000.

[17] Y KUEN. *Composite materials: materials, manufacturing, analysis, design and repair*. CreateSpace, 2015.

[18] Isaac M Daniel, Ori Ishai, Issac M Daniel, and Ishai Daniel. *Engineering mechanics of composite materials*, volume 1994. Oxford university press New York, 2006.

[19] William G Roeseler, Branko Sarh, Max U Kismarton, J Quinlivan, J Sutter, and D Roberts. Composite structures: the first 100 years. In *16th International Conference on Composite Materials*, pages 1–41. Japan Society for Composite Materials Kyoto, Japan, 2007.

[20] FAST (Flight Airworthiness Support Technology)—Special Edition A350 XWB. *Airbus Technical Magazine*, June 2013.

[21] N Amsc and A AREA CMPS. Composite materials handbook. *Polymer matrix composites materials usage, design, and analysis*, 2002.

[22] Yong Han Noel Kim, Seunghyun Ko, Wei-Siang Lay, Jingmeng Tian, Paochen Chang, Seiji Umeda Thielk, Hyung-Joon Bang, and Jinkyu Yang. Effects of shallow biangle, thin-ply laminates on structural performance of composite wings. *AIAA Journal*, 55(6):2086–2092, 2017.

[23] Bruno Vermes, Stephen W Tsai, Aniello Riccio, Francesco Di Caprio, and Surajit Roy. Application of the tsai's modulus and double-double concepts to the definition of a new affordable design approach for composite laminates. *Composite Structures*, 259:113246, 2021.

[24] H Reissner and M Morduchow. Reinforced circular cutouts in plane sheets. Technical report, POLYTECHNIC INST OF BROOKLYN NY, 1949.

[25] EH Mansfield. Neutral iioles in plane sheet—reinforced iioles which are elastically equivalent to the uncut sheet. *The Quarterly Journal of Mechanics and Applied Mathematics*, 6(3):370–378, 1953.

[26] Maya Jacob John and Sabu Thomas. Biofibres and biocomposites. *Carbohydrate polymers*, 71(3):343–364, 2008.

[27] Kalpana S Katti, Chunju Gu, and Dinesh R Katti. Biomimetics: Inspiration from the structural organization of biological systems. *Natural Polymers*, 1:8–36, 2012.

[28] Huajian Gao, Baohua Ji, Ingomar L Jäger, Eduard Arzt, and Peter Fratzl. Materials become insensitive to flaws at nanoscale: lessons from nature. *Proceedings of the national Academy of Sciences*, 100(10):5597–5600, 2003.

[29] W Wagermaier, H S. Gupta, A Gourrier, M Burghammer, P Roschger, and P Fratzl. Spiral twisting of fiber orientation inside bone lamellae. *Biointerphases*, 1(1):1–5, 2006.

[30] Structure and Function of the Haversian System Explained With Diagrams. `https://bodytomy.com/haversian-system-structure-diagram-function`. Online; accessed 23 March 2021.

[31] Elizabeth A Zimmermann, Bernd Gludovatz, Eric Schaible, Neil KN Dave, Wen Yang, Marc A Meyers, and Robert O Ritchie. Mechanical adaptability of the bouligand-type structure in natural dermal armour. *Nature communications*, 4(1):1–7, 2013.

[32] Wen Yang, Vincent R Sherman, Bernd Gludovatz, Mason Mackey, Elizabeth A Zimmermann, Edwin H Chang, Eric Schaible, Zhao Qin, Markus J Buehler, Robert O Ritchie, et al. Protective role of arapaima gigas fish scales: structure and mechanical behavior. *Acta biomaterialia*, 10(8):3599–3614, 2014.

[33] SN Patek and RL Caldwell. Extreme impact and cavitation forces of a biological hammer: strike forces of the peacock mantis shrimp odontodactylus scyllarus. *Journal of Experimental Biology*, 208(19):3655–3664, 2005.

[34] James C Weaver, Garrett W Milliron, Ali Miserez, Kenneth Evans-Lutterodt, Steven Herrera, Isaias Gallana, William J Mershon, Brook Swanson, Pablo Zavattieri, Elaine DiMasi, et al. The stomatopod dactyl club: a formidable damage-tolerant biological hammer. *Science*, 336(6086):1275–1280, 2012.

[35] Nicholas A Yaraghi, Nicolás Guarín-Zapata, Lessa K Grunenfelder, Eric Hintsala, Sanjit Bhowmick, Jon M Hiller, Mark Betts, Edward L Principe, Jae-Young Jung, Leigh Sheppard, et al. A sinusoidally architected helicoidal biocomposite. *Advanced Materials*, 28(32):6835–6844, 2016.

[36] Jolie Frketic, Tarik Dickens, and Subramanian Ramakrishnan. Automated manufacturing and processing of fiber-reinforced polymer (frp) composites: An additive review of contemporary and modern techniques for advanced materials manufacturing. *Additive Manufacturing*, 14:69–86, 2017.

[37] Guillaume Rousseau, Roudy Wehbe, Joshua Halbritter, and Ramy Harik. Automated fiber placement path planning: A state-of-the-art review. *Computer-Aided Design and Applications*, 16(2):172–203, 2019.

[38] A Sawicki and P Minguett. The effect of intraply overlaps and gaps upon the compression strength of composite laminates. In *39th AIAA/ASME/ASCE/AHS/ASC Structures, Structural Dynamics, and Materials Conference and Exhibit*, page 1786, 1998.

[39] Kaven Croft, Larry Lessard, Damiano Pasini, Mehdi Hojjati, Jihua Chen, and Ali Yousefpour. Experimental study of the effect of automated fiber placement induced defects on performance of composite laminates. *Composites Part A: Applied Science and Manufacturing*, 42(5):484–491, 2011.

[40] Kazem Fayazbakhsh, Mahdi Arian Nik, Damiano Pasini, and Larry Lessard. Defect layer method to capture effect of gaps and overlaps in variable stiffness laminates made by automated fiber placement. *Composite Structures*, 97:245–251, 2013.

[41] O Falcó, JA Mayugo, CS Lopes, N Gascons, and J Costa. Variable-stiffness composite panels: Defect tolerance under in-plane tensile loading. *Composites Part A: Applied Science and Manufacturing*, 63:21–31, 2014.

[42] Supratik Mukhopadhyay, Mike I Jones, and Stephen R Hallett. Compressive failure of laminates containing an embedded wrinkle; experimental and numerical study. *Composites Part A: Applied Science and Manufacturing*, 73:132–142, 2015.

[43] Supratik Mukhopadhyay, Mike I Jones, and Stephen R Hallett. Tensile failure of laminates containing an embedded wrinkle; numerical and experimental study. *Composites Part A: Applied Science and Manufacturing*, 77:219–228, 2015.

[44] Xiaodong Xu, Mike I Jones, Hafiz Ali, Michael R Wisnom, and Stephen R Hallett. Effect of out-of-plane wrinkles in curved multi-directional carbon/epoxy laminates. *Composites Science and Technology*, page 108282, 2020.

[45] Marine Lan, Denis Cartié, Peter Davies, and Christophe Baley. Influence of embedded gap and overlap fiber placement defects on the microstructure and shear and compression properties of carbon–epoxy laminates. *Composites Part A: Applied Science and Manufacturing*, 82:198–207, 2016.

[46] Minh Hoang Nguyen, Avinkrishnan A Vijayachandran, Paul Davidson, Damon Call, Dongyeon Lee, and Anthony M Waas. Effect of automated fiber placement (afp) manufacturing signature on mechanical performance of composite structures. *Composite Structures*, 228:111335, 2019.

[47] Stratasys. . `https://www.stratasys.com/`.

[48] Markforged. . `https://markforged.com/`.

[49] Frank Van Der Klift, Yoichiro Koga, Akira Todoroki, Masahito Ueda, Yoshiyasu Hirano, Ryosuke Matsuzaki, et al. 3d printing of continuous carbon fibre reinforced thermo-plastic (cfrtp) tensile test specimens. *Open Journal of Composite Materials*, 6(01):18, 2016.

[50] Ryosuke Matsuzaki, Masahito Ueda, Masaki Namiki, Tae-Kun Jeong, Hirosuke Asahara, Keisuke Horiguchi, Taishi Nakamura, Akira Todoroki, and Yoshiyasu Hirano. Three-dimensional printing of continuous-fiber composites by in-nozzle impregnation. *Scientific reports*, 6(1):1–7, 2016.

[51] Xiaoyong Tian, Tengfei Liu, Chuncheng Yang, Qingrui Wang, and Dichen Li. Interface and performance of 3d printed continuous carbon fiber reinforced pla composites. *Composites Part A: Applied Science and Manufacturing*, 88:198–205, 2016.

[52] Kentaro Sugiyama, Ryosuke Matsuzaki, Masahito Ueda, Akira Todoroki, and Yoshiyasu Hirano. 3d printing of composite sandwich structures using continuous carbon fiber and fiber tension. *Composites Part A: Applied Science and Manufacturing*, 113:114–121, 2018.

[53] Pedram Parandoush, Levi Tucker, Chi Zhou, and Dong Lin. Laser assisted additive manufacturing of continuous fiber reinforced thermoplastic composites. *Materials & Design*, 131:186–195, 2017.

[54] Marco Salviato and Michele Zappalorto. A unified solution approach for a large variety of antiplane shear and torsion notch problems: Theory and examples. *International Journal of Solids and Structures*, 102:10–20, 2016.

[55] Marco Salviato, Michele Zappalorto, and Lucio Maragoni. Exact solution for the mode iii stress fields ahead of cracks initiated at sharp notch tips. *European Journal of Mechanics-A/Solids*, 72:88–96, 2018.

[56] Michele Zappalorto, Marco Salviato, and Lucio Maragoni. Analytical study on the mode iii stress fields due to blunt notches with cracks. *Fatigue & Fracture of Engineering Materials & Structures*, 42(3):612–626, 2019.

[57] Marco Salviato and Sean E Phenisee. Enhancing the electrical and thermal conductivities of polymer composites via curvilinear fibers: An analytical study. *Mathematics and Mechanics of Solids*, 24(10):3231–3253, 2019.

[58] Igor Sevostianov and Mark Kachanov. Connections between elastic and conductive properties of heterogeneous materials. In *Advances in applied mechanics*, volume 42, pages 69–252. Elsevier, 2009.

[59] K Schulte, , and Ch Baron. Load and failure analyses of cfrp laminates by means of electrical resistivity measurements. *Composites science and technology*, 36(1):63–76, 1989.

[60] Xiaojun Wang and DDL Chung. Self-monitoring of fatigue damage and dynamic strain in carbon fiber polymer-matrix composite. *Composites Part B: Engineering*, 29(1):63–73, 1998.

[61] Ruediger Schueler, Shiv P Joshi, and Karl Schulte. Damage detection in cfrp by electrical conductivity mapping. *Composites science and technology*, 61(6):921–930, 2001.

[62] Shoukai Wang and DDL Chung. Self-sensing of flexural strain and damage in carbon fiber polymer-matrix composite by electrical resistance measurement. *Carbon*, 44(13):2739–2751, 2006.

[63] A Boschetti-de Fierro, R Pardey, V Savino, and AJ Müller. Piezoresistive behavior of epoxy matrix-carbon fiber composites with different reinforcement arrangements. *Journal of Applied Polymer Science*, 111(6):2851–2858, 2009.

[64] Akira Todoroki, Yusuke Samejima, Yoshiyasu Hirano, and Ryosuke Matsuzaki. Piezoresistivity of unidirectional carbon/epoxy composites for multiaxial loading. *Composites Science and Technology*, 69(11-12):1841–1846, 2009.

[65] E. H. Mansfield. Neutral holes in plane sheet: Reinforced holes which are elastically equivalent to the uncut sheet. *Quarterly Journal of Mechanics and Applied Mathematics*, 6(3):370–378, 1953.

[66] H-JA Lukaszewicz Dirk, Carwyn Ward, and Kevin D Potter. The engineering aspects of automated prepreg layup: History, present and future. *Composites Part B: Engineering*, 43(3):997–1009, 2012.

[67] Kaven Croft, Larry Lessard, Damiano Pasini, Mehdi Hojjati, Jihua Chen, and Ali Yousefpour. Experimental study of the effect of automated fiber placement induced defects on performance of composite laminates. *Composites Part A: Applied Science and Manufacturing*, 42(5):484 – 491, 2011.

[68] Wei Gao, Yunbo Zhang, Devarajan Ramanujan, Karthik Ramani, Yong Chen, Christopher B. Williams, Charlie C.L. Wang, Yung C. Shin, Song Zhang, and Pablo D. Zavattieri. The status, challenges, and future of additive manufacturing in engineering. *Computer-Aided Design*, 69:65 – 89, 2015.

[69] M.W. Hyer and R.F. Charette. Innovative Design of Composite Structures: Use of Curvilinear Fiber Format to Improve Structural Efficiency. Technical report, University of Maryland, 1987.

[70] M. W. Hyer and H. H. Lee. The use of curvilinear fiber format to improve buckling resistance of composite plates with central circular holes. *Composite Structures*, 18(3):239–261, 1991.

[71] Levend Parnas, Süha Oral, and Ümit Ceyhan. Optimum design of composite structures with curved fiber courses. *Composites science and technology*, 63(7):1071–1082, 2003.

[72] Stephen W Tsai. *Theory of composites design*. Think composites Dayton, OH, 1992.

[73] Shahriar Setoodeh, Mostafa M Abdalla, and Zafer Gürdal. Design of variable–stiffness laminates using lamination parameters. *Composites Part B: Engineering*, 37(4-5):301–309, 2006.

[74] Cláudio S Lopes, Pedro Ponces Camanho, Zafer Gürdal, and Brian F Tatting. Progressive failure analysis of tow-placed, variable-stiffness composite panels. *International Journal of Solids and Structures*, 44(25-26):8493–8516, 2007.

[75] Z. Gürdal, B. F. Tatting, and C. K. Wu. Variable stiffness composite panels: Effects of stiffness variation on the in-plane and buckling response. *Composites Part A: Applied Science and Manufacturing*, 39(5):911–922, 2008.

[76] Samuel T IJsselmuiden, Mostafa M Abdalla, and Zafer Gurdal. Optimization of variable-stiffness panels for maximum buckling load using lamination parameters. *AIAA journal*, 48(1):134–143, 2010.

[77] Zafer Güdal and Reynaldo Olmedo. Composite laminates with spatially varying fiber orientations-'variable stiffness panel concept'. In *33rd Structures, Structural Dynamics and Materials Conference*, page 2472, 1992.

[78] Mahdi Arian Nik, Kazem Fayazbakhsh, Damiano Pasini, and Larry Lessard. Surrogate-based multi-objective optimization of a composite laminate with curvilinear fibers. *Composite Structures*, 94(8):2306–2313, 2012.

[79] H. K. Cho and R. E. Rowlands. Reducing tensile stress concentration in perforated hybrid laminate by genetic algorithm. *Composites Science and Technology*, 67(13):2877–2883, 2007.

[80] H. K. Cho and R. E. Rowlands. Optimizing fiber direction in perforated orthotropic media to reduce stress concentration. *Journal of Composite Materials*, 43(10):1177–1198, 2009.

[81] S Honda, K Owatari, and Y Narita. Minimization of stress concentration for laminated composite plates with curvilinearly shaped fibers. *Japan Society of Mechanical Engineers, Part A*, 76(769):1139–1146, 2010.

[82] Shinya Honda, Teruki Igarashi, and Yoshihiro Narita. Multi-objective optimization of curvilinear fiber shapes for laminated composite plates by using nsga-ii. *Composites Part B: Engineering*, 45(1):1071–1078, 2013.

[83] AV Malakhov and AN Polilov. Design of composite structures reinforced curvilinear fibres using fem. *Composites Part A: Applied Science and Manufacturing*, 87:23–28, 2016.

[84] Hamed Akhavan and Pedro Ribeiro. Natural modes of vibration of variable stiffness composite laminates with curvilinear fibers. *Composite Structures*, 93(11):3040–3047, 2011.

[85] Zahra Zamani, Hassan Haddadpour, and Mohammad-Reza Ghazavi. Curvilinear fiber optimization tools for design thin walled beams. *Thin-Walled Structures*, 49(3):448–454, 2011.

[86] Hassan Haddadpour and Zahra Zamani. Curvilinear fiber optimization tools for aeroelastic design of composite wings. *Journal of Fluids and Structures*, 33:180–190, 2012.

[87] Senthil Murugan and MI Friswell. Morphing wing flexible skins with curvilinear fiber composites. *Composite Structures*, 99:69–75, 2013.

[88] Marco Montemurro and Anita Catapano. A general b-spline surfaces theoretical framework for optimisation of variable angle-tow laminates. *Composite Structures*, 209:561–578, 2019.

[89] Anita Catapano and Marco Montemurro. Strength optimisation of variable angle-tow composites through a laminate-level failure criterion. *Journal of Optimization Theory and Applications*, 187(3):683–706, 2020.

[90] GA Fiordilino, MI Izzi, and M Montemurro. A general isogeometric polar approach for the optimisation of variable stiffness composites: Application to eigenvalue buckling problems. *Mechanics of Materials*, 153:103574.

[91] Thi D Dang, Rakesh K Kapania, Wesley CH Slemp, Manav Bhatia, and Sham P Gurav. Optimization and postbuckling analysis of curvilinear-stiffened panels under multiple-load cases. *Journal of Aircraft*, 47(5):1656–1671, 2010.

[92] Karanpreet Singh, Wei Zhao, Mohamed Jrad, and Rakesh K Kapania. Hybrid optimization of curvilinearly stiffened shells using parallel processing. *Journal of aircraft*, 56(3):1068–1079, 2019.

[93] Balakrishnan Devarajan and Rakesh K Kapania. Thermal buckling of curvilinearly stiffened laminated composite plates with cutouts using isogeometric analysis. *Composite Structures*, 238:111881, 2020.

[94] Kenta Suzuki. Isogeometric Computational Modeling of Curvilinear Fiber Composites. Master's thesis, University of Washington, 2019.

[95] Kenta Suzuki, Sean E Phenisee, and Marco Salviato. An isogeometric framework for the modeling of curvilinear anisotropic media. *Composite Structures*, 266:113771, 2021.

[96] MJ Turner. Stiffness and deflection analysis of complex structures. *Journal of the Aeronautical Sciences*, 23(9):805–823, 1956.

[97] David F Rogers. *An introduction to NURBS: with historical perspective*. Elsevier, 2000.

[98] Chien H Thai, AJM Ferreira, Stephane Pierre Alain Bordas, Timon Rabczuk, and H Nguyen-Xuan. Isogeometric analysis of laminated composite and sandwich plates using a new inverse trigonometric shear deformation theory. *European Journal of Mechanics-A/Solids*, 43:89–108, 2014.

[99] L Beirao Da Veiga, Annalisa Buffa, C Lovadina, M Martinelli, and G Sangalli. An isogeometric method for the reissner–mindlin plate bending problem. *Computer Methods in Applied Mechanics and Engineering*, 209:45–53, 2012.

[100] Navid Valizadeh, Sundararajan Natarajan, Octavio A Gonzalez-Estrada, Timon Rabczuk, Tinh Quoc Bui, and Stéphane PA Bordas. Nurbs-based finite element analysis of functionally graded plates: static bending, vibration, buckling and flutter. *Composite Structures*, 99:309–326, 2013.

[101] Daryl L. Logan. *A first course in the finite element method*. Cengage Learing, Boston, 6th edition edition, 2016.

[102] Les Piegl and Wayne Tiller. *The NURBS book*. Springer Science & Business Media, 2012.

[103] Carl De Boor. On calculating with b-splines. *Journal of Approximation theory*, 6(1):50–62, 1972.

[104] Wolfgang Boehm. Inserting new knots into b-spline curves. *Computer-Aided Design*, 12(4):199–201, 1980.

[105] Michael E. Mortenson. *Geometric Modeling*. John Wiley and Sons, Ltd., New York, 1985.

[106] Gerald Farin. *Curves and Surfaces for Computer-Aided Geometric Design- A Practical Guide*. Academic Press, INC., Boston, 4th edition, 1993.

[107] David F Rogers and J. Alan Adams. *Mathematical Elements for Computer Graphics*. McGraw-Hill, New York, 1986.

[108] Les Piegl and Wayne Tiller. *The NURBS book*. Springer-Verlag, 1997.

[109] K.J. Versprille. *Computer-Aided Design Applications of the Rational B-Spline Approximation Form*. PhD thesis, Syracuse University, 1975.

[110] Wayne Tiller. Rational b-splines for curve and surface representation. *IEEE Computer Graphics and Applications*, 3(6):61–69, 1983.

[111] Les Piegl. On NURBS: A Survey. *IEEE Computer Graphics & Applicntions*, 10(1):55–71, 1991.

[112] Ronald F. Gibson. *Principles of Composite Material Mechanics*. McGraw-Hill, New York, 1994.

[113] László P. Kollár and George S. Springer. *Mechanics of Composite Structures*. Cambridge University Press, New York, 01 2003.

[114] Vinh Phu Nguyen, Cosmin Anitescu, Stéphane PA Bordas, and Timon Rabczuk. Isogeometric analysis: an overview and computer implementation aspects. *Mathematics and Computers in Simulation*, 117:89–116, 2015.

[115] Jasbir S. Arora. *Introduction to Optimum Design*. Elsevier Inc., 3 edition, 2012.

[116] Jorge Nocedal and Stephen J. Wright. *Numerical Optimization*. Springer, 2 edition, 2006.

[117] *Optimization Toolbox™ User 's Guide*. The MathWorks, Inc., Natick, Massachusetts, United States, 2020.

[118] Stephen W. Tsai and Edward M. Wu. A General Theory of Strength for Anisotropic Materials. *Journal of Composite Materials*, 5(1):58–80, 1971.

[119] Z.P. Bažant. Scaling theory for quasibrittle structural failure. *Proceedings of the National Academy of Sciences*, 101(37):13400–13407, 2004.

[120] Marco Salviato, Shiva Esna Ashari, and Gianluca Cusatis. Spectral stiffness microplane model for damage and fracture of textile composites. *Composite Structures*, 137:170–184, 2016.

[121] Marco Salviato, Kedar Kirane, Shiva Esna Ashari, Zdeněk P Bažant, and Gianluca Cusatis. Experimental and numerical investigation of intra-laminar energy dissipation and size effect in two-dimensional textile composites. *Composites Science and Technology*, 135:67–75, 2016.

[122] Marco Salviato, Kedar Kirane, Zdeněk P Bažant, and Gianluca Cusatis. Mode i and ii interlaminar fracture in laminated composites: a size effect study. *Journal of Applied Mechanics*, 86(9), 2019.

[123] Yuta Kumagai, Sota Onodera, Marco Salviato, and Tomonaga Okabe. Multiscale analysis and experimental validation of crack initiation in quasi-isotropic laminates. *International Journal of Solids and Structures*, 193-194:172–191, 2020.

[124] Marco Salviato and Sean E Phenisee. Enhancing the electrical and thermal conductivities of polymer composites via curvilinear fibers: An analytical study. *Mathematics and Mechanics of Solids*, 03 2019.

[125] Zeger Bontinck, Jacopo Corno, Sebastian Schöps, and Herbert De Gersem. Isogeometric analysis and harmonic stator–rotor coupling for simulating electric machines. *Computer Methods in Applied Mechanics and Engineering*, 334:40–55, 2018.

[126] Scott Lipton, John A Evans, Yuri Bazilevs, Thomas Elguedj, and Thomas JR Hughes. Robustness of isogeometric structural discretizations under severe mesh distortion. *Computer Methods in Applied Mechanics and Engineering*, 199(5-8):357–373, 2010.

[127] Laura De Lorenzis, Peter Wriggers, and Thomas JR Hughes. Isogeometric contact: a review. *GAMM-Mitteilungen*, 37(1):85–123, 2014.

[128] Ning Liu and Ann E Jeffers. A geometrically exact isogeometric kirchhoff plate: Feature-preserving automatic meshing and c 1 rational triangular bézier spline discretizations. *International Journal for Numerical Methods in Engineering*, 115(3):395–409, 2018.

[129] Avinkrishnan A. Vijayachandran, Paul Davidson, and Anthony M. Waas. Optimal fiber paths for robotically manufactured composite structural panels. *International Journal of Non-Linear Mechanics*, 126(July):103567, 2020.

[130] Avinkrishnan A Vijayachandran, Paul Davidson, and Anthony M Waas. Optimal steered fiber paths for maximizing biaxial buckling load of a flat plate manufactured using AFP. In *AIAA Scitech 2020 Forum*, 2020.

[131] Kedar Kirane, Marco Salviato, and Zdeněk P. Bažant. Microplane triad model for simple and accurate prediction of orthotropic elastic constants of woven fabric composites. *Journal of Composite Materials*, 50(9):1247–1260, 2016.

[132] Kedar Kirane, Marco Salviato, and Zdenek P. Bazant. Microplane-Triad Model for Elastic and Fracturing Behavior of Woven Composites. *Journal of Applied Mechanics, Transactions ASME*, 83(4):1–14, 2016.

[133] Yao Qiao, Qiwei Zhang, and Marco Salviato. Effects of In-situ Stress State on the Plastic Deformation, Fracture, and Size Scaling of Thermoset Polymers and Related Fiber-reinforced Composites. In *ASC 35th Technical Conference*, number July, 2020.

[134] Lei Liu, Yongjie Jessica Zhang, and Xiaodong Wei. Handling extraordinary nodes with weighted t-spline basis functions. *Procedia Engineering*, 124:161–173, 2015.

[135] Hyun-Jung Kim, Yu-Deok Seo, and Sung-Kie Youn. Isogeometric analysis with trimming technique for problems of arbitrary complex topology. *Computer Methods in Applied Mechanics and Engineering*, 199(45-48):2796–2812, 2010.

[136] Ruben Sevilla, Sonia Fernández-Méndez, and Antonio Huerta. Nurbs-enhanced finite element method (nefem). *International Journal for Numerical Methods in Engineering*, 76(1):56–83, 2008.

[137] Dominik Schillinger, Martin Ruess, Nils Zander, Yuri Bazilevs, Alexander Düster, and Ernst Rank. Small and large deformation analysis with the p-and b-spline versions of the finite cell method. *Computational Mechanics*, 50(4):445–478, 2012.

[138] Ernst Rank, Martin Ruess, Stefan Kollmannsberger, Dominik Schillinger, and Alexander Düster. Geometric modeling, isogeometric analysis and the finite cell method. *Computer Methods in Applied Mechanics and Engineering*, 249:104–115, 2012.

[139] Martin Ruess, Dominik Schillinger, Ali I Oezcan, and Ernst Rank. Weak coupling for isogeometric analysis of non-matching and trimmed multi-patch geometries. *Computer Methods in Applied Mechanics and Engineering*, 269:46–71, 2014.

[140] Tor Dokken, Tom Lyche, and Kjell Fredrik Pettersen. Polynomial splines over locally refined box-partitions. *Computer Aided Geometric Design*, 30(3):331–356, 2013.

[141] Xin Li, Jianmin Zheng, Thomas W Sederberg, Thomas JR Hughes, and Michael A Scott. On linear independence of t-spline blending functions. *Computer Aided Geometric Design*, 29(1):63–76, 2012.

[142] Michael A Scott, Michael J Borden, Clemens V Verhoosel, Thomas W Sederberg, and Thomas JR Hughes. Isogeometric finite element data structures based on bézier extraction of t-splines. *International Journal for Numerical Methods in Engineering*, 88(2):126–156, 2011.

[143] Michael J Borden, Michael A Scott, John A Evans, and Thomas JR Hughes. Isogeometric finite element data structures based on bézier extraction of nurbs. *International Journal for Numerical Methods in Engineering*, 87(1-5):15–47, 2011.

[144] Lisandro Dalcin, Nathaniel Collier, Philippe Vignal, AMA Côrtes, and Victor M Calo. Petiga: A framework for high-performance isogeometric analysis. *Computer Methods in Applied Mechanics and Engineering*, 308:151–181, 2016.

[145] Michael Lange, Matthew G Knepley, and Gerard J Gorman. Flexible, scalable mesh and data management using petsc dmplex. *arXiv preprint arXiv:1505.04633*, 2015.

[146] Thomas JR Hughes. *The finite element method: linear static and dynamic finite element analysis*. Courier Corporation, 2012.

[147] Patrick R Amestoy, Iain S Duff, Jean-Yves L'Excellent, and Jacko Koster. A fully asynchronous multifrontal solver using distributed dynamic scheduling. *SIAM Journal on Matrix Analysis and Applications*, 23(1):15–41, 2001.

[148] Patrick R Amestoy, Alfredo Buttari, Jean-Yves L'excellent, and Theo Mary. Performance and scalability of the block low-rank multifrontal factorization on multicore architectures. *ACM Transactions on Mathematical Software (TOMS)*, 45(1):1–26, 2019.

[149] Joey De Vries. Learn opengl. *Licensed under CC BY*, 4, 2015.

[150] Mark Ainsworth and J Tinsley Oden. A procedure for a posteriori error estimation for hp finite element methods. *Computer Methods in Applied Mechanics and Engineering*, 101(1-3):73–96, 1992.

[151] Phillip L Gould and Yuan Feng. *Introduction to linear elasticity*, volume 2. Springer, 1994.

[152] Zdeněk P Bažant. Instability, ductility, and size effect in strain-softening concrete. *Journal of the engineering mechanics division*, 102(2):331–344, 1976.

[153] Zdeněk P Bažant and Luigi Cedolin. Blunt crack band propagation in finite element analysis. *Journal of the engineering mechanics division*, 105(2):297–315, 1979.

[154] Zdeněk P Bažant and Byung H Oh. Crack band theory for fracture of concrete. *Matériaux et construction*, 16:155–177, 1983.

[155] Zdeněk P Bažant and MT Kazemi. Determination of fracture energy, process zone longth and brittleness number from size effect, with application to rock and conerete. *International Journal of fracture*, 44:111–131, 1990.

[156] Zdeněk P Bažant and Jaime Planas. *Fracture and size effect in concrete and other quasibrittle materials*. Routledge, 2019.

[157] Zdeněk P Bažant. *Scaling of structural strength*. CRC Press, 2002.

[158] Carl Edward Rasmussen, Christopher KI Williams, et al. *Gaussian processes for machine learning*, volume 1. Springer, 2006.

[159] Kevin P Murphy. *Machine learning: a probabilistic perspective*. MIT press, 2012.

[160] Peter I Frazier. A tutorial on bayesian optimization. *arXiv preprint arXiv:1807.02811*, 2018.

[161] Maximilian Balandat, Brian Karrer, Daniel R. Jiang, Samuel Daulton, Benjamin Letham, Andrew Gordon Wilson, and Eytan Bakshy. BoTorch: A Framework for Efficient Monte-Carlo Bayesian Optimization. In *Advances in Neural Information Processing Systems 33*, 2020.

[162] Stephen B Clay and Philip M Knoth. Experimental results of quasi-static testing for calibration and validation of composite progressive damage analysis methods. *Journal of Composite Materials*, 51(10):1333–1353, 2017.

[163] Gianluca Cusatis, Daniele Pelessone, and Andrea Mencarelli. Lattice discrete particle model (ldpm) for failure behavior of concrete. i: Theory. *Cement and Concrete Composites*, 33(9):881–890, 2011.

[164] Gianluca Cusatis, Andrea Mencarelli, Daniele Pelessone, and James Baylot. Lattice discrete particle model (ldpm) for failure behavior of concrete. ii: Calibration and validation. *Cement and Concrete composites*, 33(9):891–905, 2011.

[165] Chiara Ceccato, Marco Salviato, Carlo Pellegrino, and Gianluca Cusatis. Simulation of concrete failure and fiber reinforced polymer fracture in confined columns with different cross sectional shape. *International Journal of Solids and Structures*, 108:216–229, 2017.

[166] Gregorius Egbertus Gerardus Poort. *Composite Aircraft Structural Optimization and the Implementation of Manufacturing Constraints*. PhD thesis, University of Washington, 2009.

Appendix A

CONTROL POINTS USED IN MODEL GENERATION

The control points used to model the initial surface of the rectangular laminate with a semi-circular notch is listed in Table A.1.

Table A.1: Homogeneous coordinates of control points for a plate with a semi-circular notch

Control point	x	y	z	w
1	0	1	0	1
2	$1-\sqrt{2}$	1	0	$\left(1+1/\sqrt{2}\right)/2$
3	-1	$\sqrt{2}-1$	0	$\left(1+1/\sqrt{2}\right)/2$
4	-1	0	0	1
5	-1	$1-\sqrt{2}$	0	$\left(1+1/\sqrt{2}\right)/2$
6	$1-\sqrt{2}$	-1	0	$\left(1+1/\sqrt{2}\right)/2$
7	0	-1	0	1
8	0	2.5	0	1
9	-0.75	2.5	0	1
10	-2.5	0.75	0	1
11	-2.5	0	0	1
12	-2.5	-0.75	0	1
13	-0.75	-2.5	0	1
14	0	-2.5	0	1
15	0	4	0	1
16	-4	4	0	1
17	-4	4	0	1
18	-4	0	0	1
19	-4	-4	0	1
20	-4	-4	0	1
21	0	-4	0	1

The control points used to model the initial surface of T-joint laminate is listed in Table A.2 and Table A.3.

Table A.2: Homogeneous coordinates of control points for left half of T-joint surface

Control point	x	y	z	w
1	-6	1	0	1
2	-4.25	1	0	1
3	-2.5	1	0	1
4	$\sqrt{2}-3.5$	1	0	$\left(1+1/\sqrt{2}\right)/2$
5	-1.5	$\sqrt{2}-1$	0	$\left(1+1/\sqrt{2}\right)/2$
6	-1.5	0	0	1
7	-1.5	-1	0	1
8	-1.5	-2	0	1
9	-6	2.5	0	1
10	-4.25	2.5	0	1
11	-2.5	2.5	0	1
12	-1.75	2.5	0	1
13	-0.75	0.75	0	1
14	-0.75	0	0	1
15	-0.75	-1	0	1
16	-0.75	-2	0	1
17	-6	4	0	1
18	-4.25	4	0	1
19	-2.5	4	0	1
20	0	4	0	1
21	0	4	0	1
22	0	0	0	1
23	0	-1	0	1
24	0	-2	0	1

Table A.3: Homogeneous coordinates of control points for left half of T-joint surface

Control point	x	y	z	w
1	6	1	0	1
2	4.25	1	0	1
3	2.5	1	0	1
4	$3.5-\sqrt{2}$	1	0	$\left(1+1/\sqrt{2}\right)/2$
5	1.5	$\sqrt{2}-1$	0	$\left(1+1/\sqrt{2}\right)/2$
6	1.5	0	0	1
7	1.5	-1	0	1
8	1.5	-2	0	1
9	6	2.5	0	1
10	4.25	2.5	0	1
11	2.5	2.5	0	1
12	1.75	2.5	0	1
13	0.75	0.75	0	1
14	0.75	0	0	1
15	0.75	-1	0	1
16	0.75	-2	0	1
17	6	4	0	1
18	4.25	4	0	1
19	2.5	4	0	1
20	0	4	0	1
21	0	4	0	1
22	0	0	0	1
23	0	-1	0	1
24	0	-2	0	1

VITA

Sean Eunsik Phenisee was born in Cheongju, South Korea, and came to United States when he was 13 years old. He earned his B.S. in Aeronautics and Astronautics degree from the University of Washington in 2016. Then, he joined the Laboratory for Multi-scale Analysis of Materials & Structures (MAMS) led by Professor Marco Salviato (chair) in the Autumn of 2016. In Summer of 2023, he earned his Ph.D. degree in Aeronautics and Astronautics from the University of Washington.